Study of the Microstructural Refinement of a High Niobium Microalloyed Steel Under Controlled Hot Deformation

Eduardo Pineda Martinez

Thesis Submitted for the Degree of Doctor of Philosophy

Department of Materials Science and Engineering

The University of Sheffield

July 2020

Abstract

A current trend within the oil and gas field is towards the development of steel grades exhibiting higher strength and toughness; the need for linepipe components with superior mechanical properties constantly mounts pressure on steel manufacturers to innovate or develop products with such improvements. This is the case of the high-temperature processing (HTP) steel alloy developed for the API X80 steel grade used in the East-West transmission pipeline project (the largest in the world) in China within the last decade. The resulting alloy is based on a high Nb content (~0.1 wt%) which allows for controlled hot rolling due to its ability to retard the recrystallisation of the deformed austenite. The HTP steel alloy enable the possibility to achieve highly refined microstructures with superior strength and toughness over conventional steels.

Grain refinement of the microstructure is a fundamental mechanism by which the steel's strength and toughness can be increased. One of the finest microstructures observed in steel is that arising from the deformation-induced ferrite transformation (DIFT) which can produce grain sizes on the order of 1 – 2 μm. In the present research, a series of plane strain compression tests were performed in order to simulate different thermomechanical controlled processing (TMCP) routes for obtaining the finest possible microstructure following hot deformation. It was found that an adequately designed multi-pass finish rolling can lead to a remarkable grain refinement within the HTP alloy: a simulation that consisted of two finishing passes at 950°C plus two additional passes at 810°C (imparting strains of 0.22 with each pass) produced a microstructure comprising a mixture of highly deformed austenite and 30.7% DIFT. The former had an average grain size of 84 μm and an aspect ratio of around 10, whilst the latter showed a dominant polygonal morphology of size of ~1 μm.

A thorough characterisation of the DIFT using various methods was undertaken to yield new findings that help elucidate on the characteristics of this phase. The results obtained indicated that the mechanism of DIFT was the same at temperatures both above and below the critical temperature Ae_3; additionally, a transitory ferrite morphology was observed in microstructures corresponding to all the deformation conditions which helps to explain the evolution of DIFT phase from plates to polygonal grains.

Acknowledgements

The author acknowledges the “Consejo Nacional de Ciencia y Tecnologia” (CONACYT) for the full funding provided for the PhD studies.

I would like to express my sincere thanks to my research supervisor Professor Eric J. Palmiere for his constant support and guidance during my PhD. His patience, encouragement and immense knowledge were fundamental for the successful completion of my studies. I will always remember those periodic meetings which included very enjoyable conversations and exiting discussions about the results of my research.

I am very grateful as well with all the university staff who helped me carry out the experimental part of my research and trained me in different skills, special thanks to Dean Haylock, Colm O'Regan, Dawn Bussey and Tesoro Morgan. This work would not have been possible without their support.

My sincere thanks also goes to my colleagues Marta Muñiz, Bhushan Raske and Luis Romano for their invaluable support, encouragement, mentoring and friendship during the PhD. Thanks to their talent and team spirit, we formed a fantastic research group full of support and synergy.

I would like to express my deepest gratitude to my parents and brothers for all the unconditional support and encouragement in this stage of my life, I will always be indebted to them for all the support provided during my PhD. I dedicate this thesis to them.

Thanks to my beloved wife Miriam Mendoza for her unwavering support, patience and encouragement. She is the source from where I take the strength and inspiration to achieve my goals. I also dedicate this work to you.

Table of contents

Abstract ..... **I**

Acknowledgements ..... **II**

Chapter 1. Introduction, aims and objectives. **1**

Chapter 2: Literature review **5**

2.1. Restoration mechanisms in metals 5

2.1.1. Recovery 5

2.1.2. Recrystallisation 9

2.1.2.1. The laws of recrystallisation 9

2.1.2.2. Dynamic recrystallisation (DRX). 10

2.1.2.3. Static recrystallisation. 12

2.1.3. Grain growth 13

2.2. Microalloyed steels 14

2.2.1. Niobium microalloyed steels 18

2.2.1.1. Effect on microstructural evolution. 20

2.2.1.2. Precipitation 22

2.3. Deformation strain induced ferrite transformation (DIFT) 27

2.3.1. Evidence of DIFT 29

2.3.2. Transformation mechanism 32

Chapter 3. Experimental procedure and methods **41**

3.1. Material 41

3.2. Austenitising heat treatment 41

3.3. Estimation of the temperatures A_{e3} and A_{r3}. 42

3.4. Thermomechanical testing 43

3.4.1. Rough rolling simulation 46

3.4.2. Finish rolling simulations 48

3.5. Sample preparation 51

3.6. Prior austenite grain boundaries (PAGBs) analysis 51

3.7. Metallography 51
3.8. Scanning Electron Microscopy (SEM) 52
3.8.1. Electron backscattering diffraction (EBSD) analysis 52
3.9. Transmission Electron Microscopy (TEM) 53
3.9.1. Carbon extraction replicas 53
3.9.2. Thin foils 56
3.10. X-Rays diffraction 56
3.11. Nanohardness and contact scanning probe microscopy (SPM) 57
3.11.1. Validation and quantification of DIFT. 58
3.12. Vickers Microhardness 64

Chapter 4. Rough rolling simulation 65
4.1. Introduction 65
4.2. Initial state of the HTP alloy prior to rough rolling 66
4.3. Modelling Precipitation-Time-Temperature (PTT) diagrams 69
4.4. Results 72
4.4.1. Flow behaviour and critical strains for DIFT and DRX 72
4.4.2. Morphology of prior austenite grains 78
4.4.3. Microstructure 80
4.4.4. Characterisation and quantification of DIFT by scanning probe microscopy and nanoindentation. 83
4.4.5. Niobium precipitation 89
4.4.6. Microhardness 93
4.5. Discussion 95
4.5.1. Estimations on the recrystallisation of austenite and critical strains for DIFT and DRX 95
4.5.2. The dynamic transformation of ferrite 100
4.5.3. Scanning probe microscopy and nanoindentation, a useful tool for the analysis and quantification of DIFT. 103
4.5.4. Selection of the rough rolling temperature 112
4.6. Summary 113

Chapter 5. Finish rolling simulation 115
5.1. Introduction 115
5.2. Precipitation-time-temperature diagram for a strain of 0.22 116

5.3. Results 117
5.3.1. X-Rays diffraction 117
5.3.2. Finish rolling simulation at 950°C. 119
5.3.2.1. Flow behaviour and estimation of critical strains for DIFT and DRX 119
5.3.2.2. Morphology of the prior austenite grain boundaries. 123
5.3.2.3. Microstructure 125
5.3.2.4. EBSD analysis 129
5.3.2.5. TEM thin foils 139
5.3.2.6. TEM carbon extraction replicas 141
5.3.2.7. SPM and nanohardness evaluation 143
5.3.2.8. DIFT quantification. 145
5.3.3. Finish rolling simulation at 810°C 147
5.3.3.1. Flow behaviour and estimation of critical strains for DIFT and DRX 147
5.3.3.2. Morphology of the prior austenite grain boundaries. 149
5.3.3.3. Microstructure 150
5.3.3.4. EBSD analysis 153
5.3.3.5. TEM thin foils 156
5.3.3.6. SPM and nanohardness evaluation 158
5.3.3.7. DIFT quantification 159
5.3.4. Finish rolling simulation at 950°C and 810°C. 161
5.4. Discussion 163
5.4.1. Recrystallisation behaviour of the HTP alloy during the finish deformation. . 163
5.4.2. Characteristics of DIFT at 950°C and 810°C 166
5.5. Summary 168

Chapter 6. Industrial application 170
6.1. Rough deformation temperature 170
6.2. Controlling the microstructural evolution during finish rolling 172
6.3. Limitations of the TMCP 176

Chapter 7. Conclusions 180
7.1. Austenitising Treatment. 180
7.2. Single pass rough rolling 180
7.3. Multipass finish rolling 181
7.4. Characteristics of DIFT 182

7.5. Testing methods to evaluate DIFT.....185

Chapter 8. Future work.....186

8.1. Controlled cooling after the finish rolling simulations. 186

8.2. Study of the strain induced precipitation of Nb at the different stages of the TMCP simulations. 186

8.3. Evaluation of DIFT in Atomic Force Microscopy (AFM). 187

References.....188

Chapter 1. Introduction, aims and objectives.

The current objective in the oil and gas sector to exploit new reservoirs is complex, with access to hydrocarbon reserves becoming increasingly scarce in many regions. Difficulties are arising due to the demanding operating conditions required to reach new deposits, including high pressures, low temperatures and corrosive environments. The development and improvement of linepipe (LP) components capable of withstanding such conditions is of paramount importance to the safety and success of these operations.

LPs are tubular steel components utilised in the construction of transmission lines which transport natural gas or crude oil from oil fields to ports or refineries [1], such components must possess high strength and high toughness in order to resist extreme conditions during service. Around four decades ago, the development of microalloyed steels (MAS) emerged as an alternative to manufacture LPs with substantially better mechanical properties than conventional steels, since then, this type of steels has been widely exploited and their application is massive nowadays. MAS also enjoy popularity in the manufacture of other high strength products, such as automotive components [2], hulls for naval ships [3], structures for submarines [4] and other structural components used in civil engineering [5], [6].

A typical MAS contains a low carbon content (around 0.05 to 0.25 wt%) with small additions of microalloying elements (generally less than 0.15 wt%) [7], [8]. The low C content allows for excellent weldability, while the microalloying elements (MAEs), generally Nb, Ti and V, provide grain refinement within the microstructure, improving both the strength and toughness of the material.

The manufacturing process of MAS alloys plays a fundamental role in the final mechanical properties of components – the most effective method for achieving highest grain refinement appears to be thermomechanical controlled processing (TMCP), which consists of a series of controlled hot deformations combined with thermal processes of controlled heating and cooling

at various rates. One of the major issues during the TMCP of LP plates is the low finish-rolling temperature (< 815°C [9]), which requires the use of higher loads to deform the material to compensate, and the concomitant impacts on the energy consumption and overall efficiency of the process. Low temperatures are however necessary during finish rolling to prevent the recrystallisation process which has a substantial effect on the refining of austenite grains.

In order to mitigate the negative effects caused by the low finish-rolling temperatures during the TMCP, a new concept called high temperature processing has been introduced, giving rise to a new class of steels of the same name. The chemical composition of the HTP concept is based on a low carbon content and a high amount of niobium (~0.10 wt%), the latter possessing the ability to supress or retard the recrystallisation of austenite at high rolling temperatures. This new processing route allows for finish rolling at temperatures around 100 – 200°C higher than those in conventional thermomechanical rolling without affecting the final mechanical properties of the steel, leading to a significant reduction in the rolling loads and mitigating shaping issues during the process which consequently benefits productivity [9], [10].

The HTP concept has been widely accepted in the manufacture of high strength LPs; such is the case of the API 5L X80 steel grade. This steel has a minimum yield strength of 550 MPa and was used extensively during the construction of the second West-East gas pipeline in China (2007 – 2012), which spanned a distance of 7,000 km – making it the longest in the world [11].

A key point in the successful development of the X80 steel grade using the HTP alloy, is the excellent grain refinement achieved in the final microstructure which consists of a mixture of ferrite (proeutectoid) and acicular ferrite (AF) [10], [12]. This type of microstructures possess superior strength, toughness [13], [14], H_2S corrosion resistance [15], [16] and fatigue resistance [17] to the conventional ferrite-pearlite microstructures typically found in LP steels[12]. While the development of the HTP-alloy grade X80 steel represents an important progress in the innovation of LP components, there remains much work to produce steel grades with increasingly better mechanical properties given the trend in industry to strive towards higher operating pressures and higher strength steels in turn.

Grain refinement is of critical importance for the development of LP components with superior mechanical properties given it is the only means by which both the strength and toughness of

the steel can be increased in simultaneously. The relationship between the grain size, d, and the yield strength, σ_y, of a material is expressed mathematically by the Hall-Petch equation [18], [19]:

$$\sigma_y = \sigma_0 + kd^{-1/2}$$

where σ_0 and k are material constants. It is clear from this relationship that the development of finer microstructures will yield steels of superior strength.

One of the finest known microstructures possible in steels is that of deformation induced ferrite transformation (DIFT) which occurs during hot rolling and produces ultrafine polygonal grains with diameters on the order of 1 – 2 μm [20]. In contrast to the conventional proeutectoid ferrite transformations that occur during the cooling of austenite, DIFT proceeds much faster when the load is still applied during rolling. Furthermore, the transformation can take place at very high temperatures completely within the austenite phase field [21]. Thus, a suitable TMCP regime could enable the tailoring of the DIFT structure at conventional rolling temperatures and lead to a final microstructure with a remarkable degree of refinement.

The DIFT microstructure has attracted much attention in recent decades due to its large potential for industrial applications. Currently, there are many gaps surrounding the mechanisms of its transformation; consequently, a global effort comprising a diverse range of research groups is underway to better understand the parameters that govern it. Much of the research performed so far has focused on understanding the effect of the key rolling variables on DIFT formation within a single deformation pass. However, this is not applicable to industrial conditions where multiple deformations are required to obtain the final plate geometries.

In the present research, various TMCP simulations were carried out by means of plane strain compression tests to study the microstructural evolution of the HTP alloy in a multi-pass deformation scheme. These simulations consisted of a single rough deformation at conventional roughing temperatures and a strain of 0.3, followed by finishing passes at different temperatures and strains of 0.22. The microstructures obtained from the various

simulations were analysed extensively using several techniques, and the results were discussed thereafter.

The aim of the project contained within this thesis is to find a TMCP design for the HTP alloy that is capable of producing the finest possible microstructure following hot deformation, i.e. a combination of unrecrystallised and highly deformed austenite mixed with the largest possible volume fraction of DIFT grains. This aim has been decomposed into the following objectives:

- Make use of available models to construct Precipitation-Time-Temperature (PTT) diagrams so as to study the interactions between the recrystallisation of austenite and the strain-induced precipitation of Nb in the HTP alloy during rough and finish rolling.

- Identify an optimised rough rolling temperature for the HTP alloy achieving a strain of 0.3 at a rate of $10s^{-1}$ which leads to the best austenite refinement via recrystallisation.

- Perform a TMCP simulation with finish rolling at the highest possible temperature within the non-recrystallisation zone and investigate the resistance of the HTP alloy to recrystallisation after several finishing passes.

- Validate the presence of DIFT phase through different characterisation methods and identify a methodology sufficient for quantitative analysis.

- Correlate the main rolling variables to the evolution of DIFT phase in a multi-pass deformation scheme.

- Compare and analyse the microstructural characteristics of DIFT phase obtained using deformations at $T > Ae_3$ and at temperatures intermediary to Ae_3 and the Ar_3.

Chapter 2: Literature review

2.1. Restoration mechanisms in metals

Within the metals processing industry, most of the real rolling processes apply large deformations at high temperatures and high strain rates in the material to achieve specific shapes and dimensions in the final product. When the material undergoes such conditions, a significant change in the microstructure takes place due to the massive introduction of dislocations, the deformation or/and fragmentation of grains, the formation of deformation bands, etc., these microstructural changes are followed by restoration processes that reduce the stored energy in the deformed material and hence, counteract the effect of the work hardening.

There are three well know mechanisms of restoration during the plastic deformation of metals; recovery, recrystallisation and grain growth. These processes involve diffusion to rearrange dislocations and grain boundaries, thus, they are triggered by thermal activation and the temperature is fundamental to determine which process is favoured. Recovery and recrystallisation also depend on the extent of plastic deformation, while grain growth is mainly dependant on temperature and occurs once recovery and recrystallisation are complete, during grain growth the material is restored by reducing its surface energy in the grain boundaries [22].

2.1.1. Recovery

Recovery is the first restoration process that happens after the plastic deformation of the material, it involves the release of the stored energy generated during deformation by the annihilation and rearrangement of dislocations. Recovery is generally classified in two categories; dynamic (DRV) and static (SRV). Dynamic recovery takes place during deformation, while static recovery happens afterwards during the deformation interpass time or during the annealing process following cold working. The main microstructural change during recovery is the formation of substructures within the deformed grains, the dislocations

introduced during the deformation rearrange themselves and form polygonal arrays, such changes cause softening in the material. Figure 1 shows the evolution of recovery within the grain and Figure 2 shows the polygonisation process of dislocations.

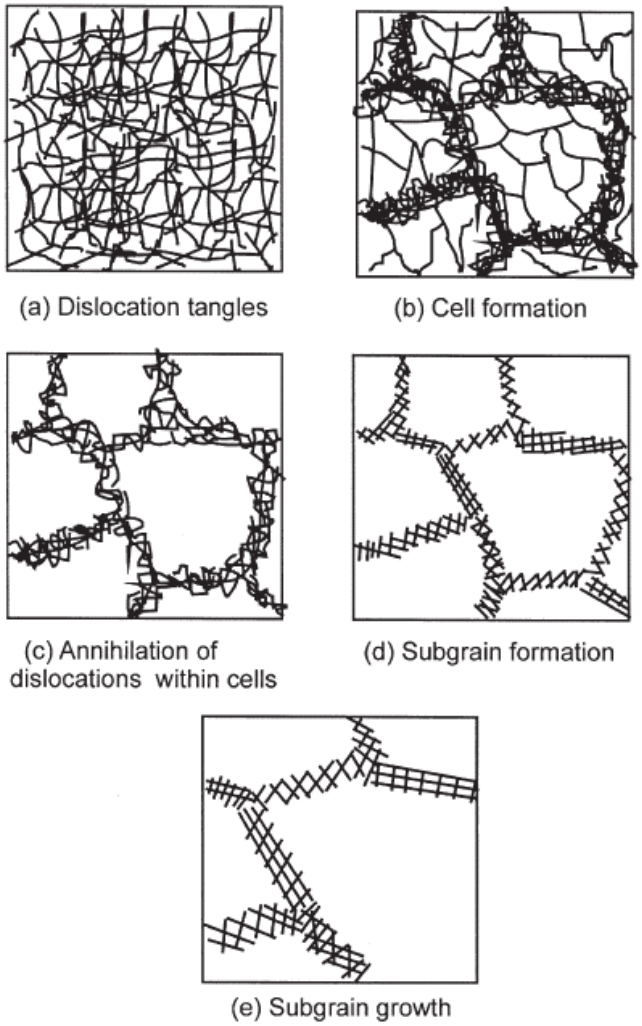

Figure 1. Stages of recovery of a plastically deformed material [23].

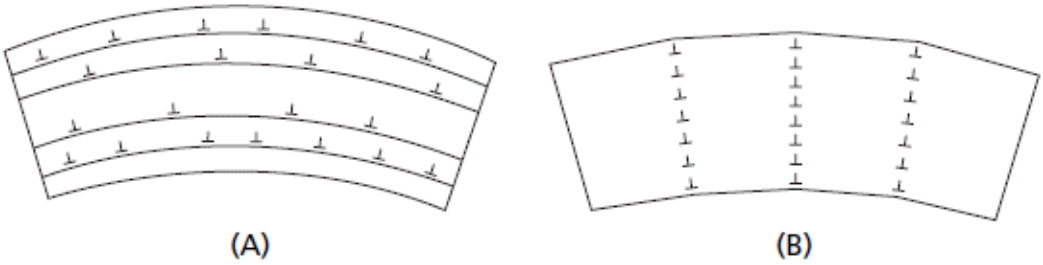

Figure 2. Rearrangement of edge dislocations through polygonisation. A) multiple dislocations move on the active slip planes within the deformed grain. B) New arrangement of dislocations due to polygonisation [24].

Despite being a restoration process, recovery does not cause significant changes in the mechanical properties of the material, the yield strength and hardness experience a subtle change when the deformed microstructure recovers. Some properties such as the density and the electrical resistivity can be affected during deformation, nevertheless, during recovery they only show slight changes as shown in Figure 3.

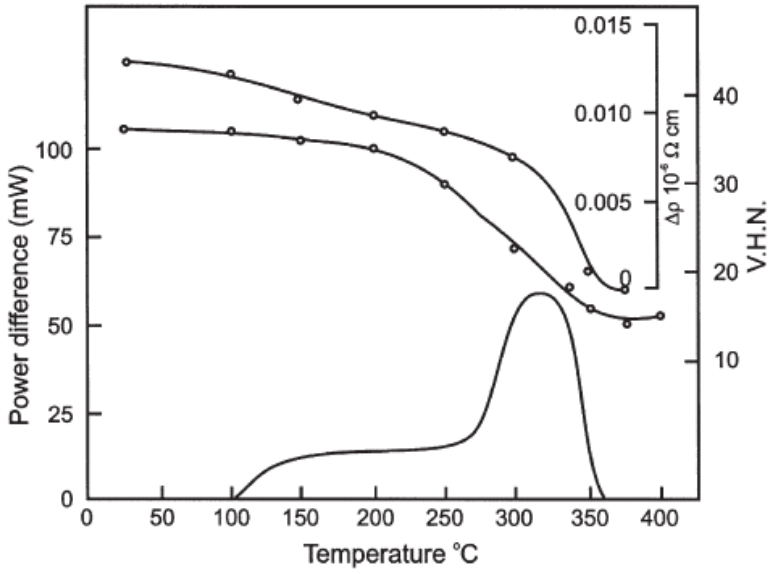

Figure 3. The recovery of 99.998% aluminium deformed 75% in compression, measured by calorimetry, electrical resistivity and hardness. Heating rate 6 °C/min [23].

Another important variable to consider during recovery is the stacking fault energy of the material. The stacking fault determines the ease of dislocations to dissociate into partial dislocations, therefore, the rate of dislocation climb and cross slip (mechanisms necessaries for polygonisation) is strongly influenced by the stacking fault energy. Metals with low stacking fault such as copper, α-brass and austenitic stainless steel show poor recovery softening when deformed, in these metals dislocation climb is difficult and the restoration mechanism that dominates is the recrystallisation. On the other hand, in metals with high stacking fault energy such as aluminium and α-iron, cross slip is easy and significant recovery can take place as shown in Figure 4.

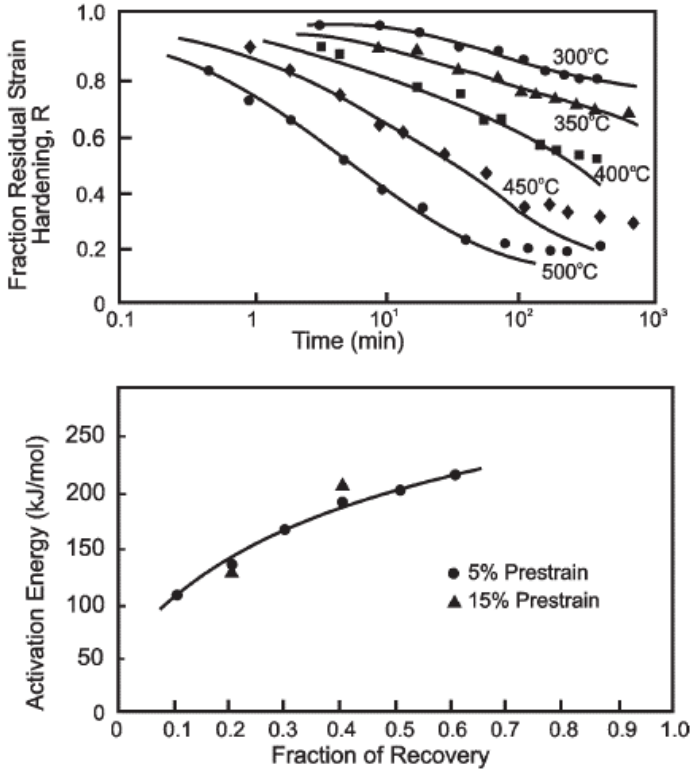

Figure 4. Isothermal recovery of iron deformed 5% at 0°C. (a) Recovery of hardness as a function of logarithmic time, (b) Change of activation energy during recovery [23].

2.1.2. Recrystallisation

Recrystallisation is another restoration process that consists in the replacement of the deformed grains by new relatively defect-free grains, it is accompanied by nucleation and grain boundaries migration. The original deformed matrix is consumed by recrystallised grains until a new microstructure free of deformation is fully formed. This process generally shows a stronger softening effect than recovery and causes significant changes in the strength, hardness and ductility of the material. Like recovery, when recrystallisation occurs during deformation it is referred to as dynamic recrystallisation (DRX), and it is correspondingly called static recrystallisation (SRX) when it occurs after the deformation. Recrystallisation can be a continuous restoration mechanism (CDRX) preceded by recovery, but in some metals at certain conditions of stress and temperature of deformation, if the recovery is slow, the accumulation of defects and the local gradients of dislocation density can lead to the formation of nuclei for recrystallisation without previous recovery, this last path is also known as discontinuous dynamic recrystallisation (DDRX) [25], [26].

2.1.2.1. The laws of recrystallisation

Based on the results obtained after a large amount of experimental work, several empirical laws have been formulated so as to rationalise the recrystallisation behaviour of materials, they can be summarised as follows [23], [27]:

i) **A minimum amount of deformation is necessary to initiate recrystallisation.** There must be a critical strain able to provide the necessary energy to form a nucleus for the recrystallisation and its subsequent growth.

ii) **A minimum temperature is needed to initiate recrystallisation.** The nucleation of new strain-free grains and its subsequent growth are thermally activated processes, hence, there is a critical temperature required to start the recrystallisation.

iii) **Increasing the strain reduces the critical temperature for recrystallisation.** The stored energy increases with strain, thus, nucleation and grain growth are more rapid or occur at lower temperature when the material is more deformed.

iv) **Increasing the annealing time decreases the recrystallisation temperature**. The relationship between the temperature and the recrystallisation rate is given by the Arrhenius equation.

v) **The deformation affects the recrystallised grain size, high deformations and low temperatures lead to smaller grains**. Higher strains provide more nuclei per unit volume which results in a smaller final grain size.

vi) **Coarser microstructures require higher deformation and/or higher temperatures to trigger recrystallisation.** Grain boundaries are preferential nucleation sites, thus, in a material with large initial grain size the nucleation rate is lowered and the recrystallisation is slower or occurs at higher temperatures due to fewer nucleation sites.

vii) **The amount of deformation required to give an equivalent amount of work hardening increases with increasing the temperature of deformation**. The amount of dynamic recovery increases with the deformation temperature, thus, at higher deformation temperatures less energy is stored resulting in a reduction in the work hardening.

2.1.2.2. Dynamic recrystallisation (DRX).

During plastic deformation at high temperatures there is a competition between the hardening and softening in the material. The deformation massively introduces dislocations that harden the microstructure, however, dynamic restoration processes can act in parallel to counteract the work hardening by eliminating dislocations and consequently softening the microstructure. In materials with low stalking fault energy such as austenite in steel, the recovery is relatively slow due to the difficulty of the fcc (face centred cubic) structures to cross slip, thus, the accumulation of defects can create sites with enough energy to form new nuclei dynamically recrystallised without prior recovery. Figure 5 shows a typical stress-strain curve when dynamic recrystallisation occurs. As the stress is applied, plastic deformation hardens the material until a critical strain ε_c is reached and the DRX starts, after this point, the competition between softening and hardening takes place and a maximum peak strain ε_p is achieved. The fraction dynamically recrystallised continues increasing with the strain causing a gradual drop in the curve until a steady state (ε_{ss}) is reached at a constant stress, σ_{ss}.

During DRX new grains are nucleated in triple points and grain boundaries, as the stain continues the new grains are deformed until they reach the critical strain necessary to recrystallise once again, this leads to a steady state in which a “cascade” of events of nucleation and limited growth occur [28].

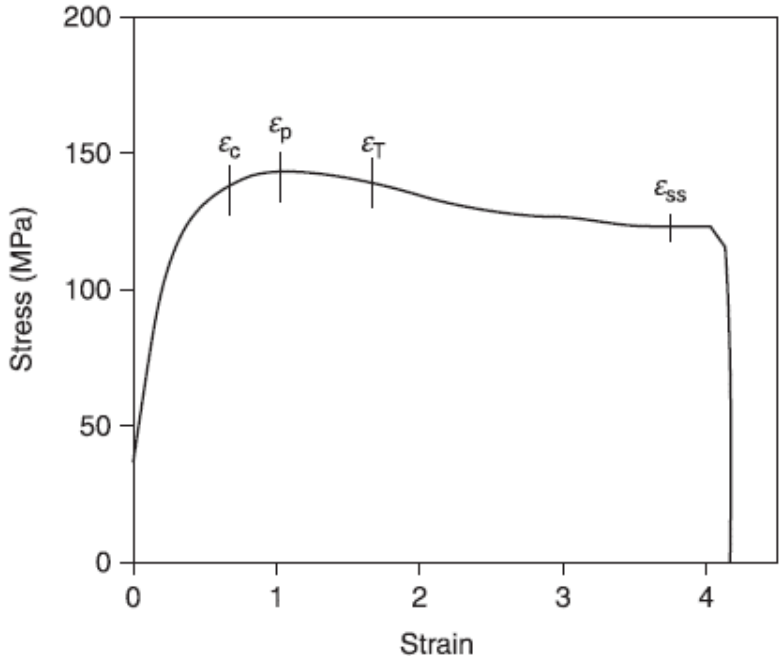

Figure 5. Example of a stress-strain curve of austenite showing the different stages of DRX [28].

The grains evolution during DRX is illustrated in Figure 6, the old grain boundaries serve as nucleation sites for new grains and a “necklace-like” structure is formed, the new grains grow through the grain boundary until they impinge each other, then more grains are formed through the new grain boundaries within the old matrix until the material become fully recrystallised [23].

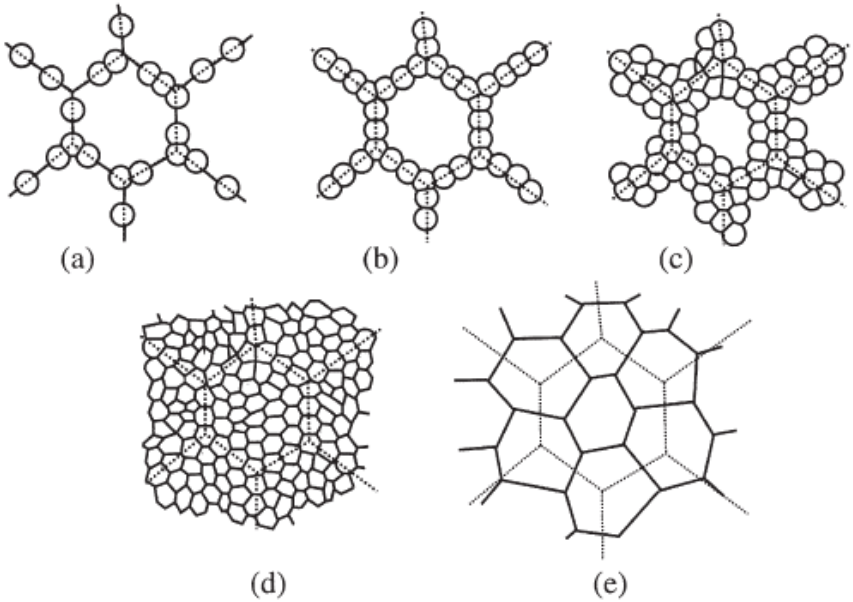

Figure 6. Microstructural evolution during DRX. (a)-(d) Large initial grain size, (e) small initial grain size. The dotted lines show the prior grain boundaries [23].

2.1.2.3. Static recrystallisation.

During hot working of austenite when the deformation does not reach the critical strain for DRX and the recovery is very limited, static recrystallisation (SRX) can occur after the deformation, this form of restauration generally takes place during the interpass intervals. SRX is a function of time and also involves the nucleation and growth of new grains in the deformed matrix.

The fraction recrystallized (X) increases with time according to the Avrami equation,

$$X = 1 - exp\left\{-ln\ 2 \cdot \left(\frac{t}{t_{0.5x}}\right)^n\right\} \qquad (1.1)$$

where t is time, $t_{0.5x}$ is the time required to recrystallise a fraction of 50% and n is the Avrami coefficient. For static recrystallisation in austenite the value of the coefficient n typically ranges around 1 and 2 [26], [28].

2.1.3. Grain growth

Once the recrystallisation is complete the microstructure tends to further reduce its energy by decreasing the grain boundaries area per unit volume. Usually the grain growth under isothermal conditions is described by:

$$D^n = D_{RX}^n + B \cdot t_q \cdot exp\left(-\frac{Q_{gg}}{RT}\right) \qquad (1.2)$$

where D_{RX} is the fully recrystallised grain size, t_q is the time after complete recrystallisation, normally it is assumed to be the time to achieve a 95% recrystallisation fraction, Q_{gg} is apparent activation energy for grain growth, and n and B are constants depending on the chemical composition of the steel.

Grain growth can be divided in two categories; normal grain growth and abnormal grain growth or secondary recrystallisation. Normal grain growth is considered a continuous process in which the grains grow homogenously in a narrow range of sizes and shapes as shown in Figure 7 a. In contrast, during abnormal grain growth a bimodal distribution of grain sizes is observed as a result of the growth of some grains at the expense of smaller grains within the microstructure, the bimodal distribution of grain sizes as a function of time is shown in Figure 7 b.

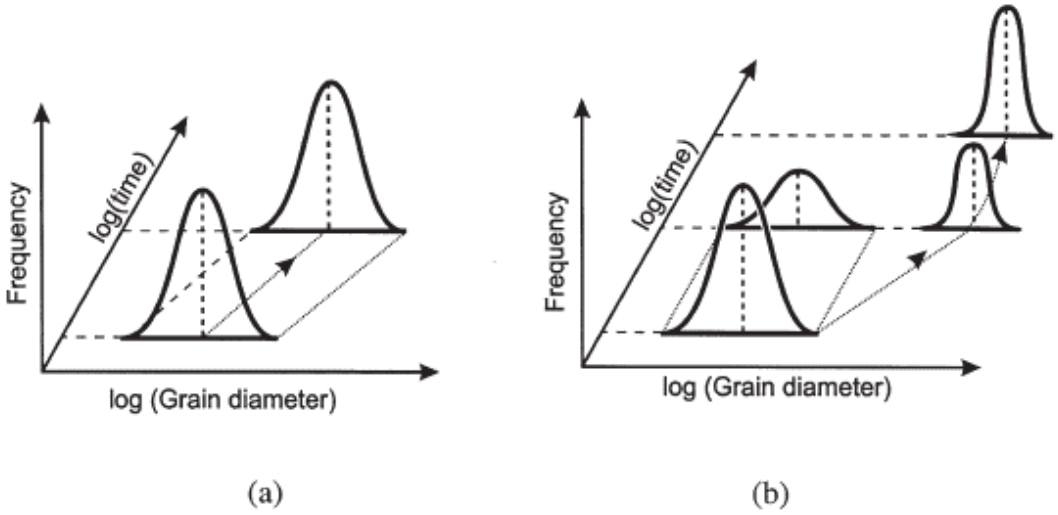

Figure 7. Grain size distributions during normal and abnormal grain growth [23].

Grain growth is strongly affected by the temperature since the kinetics of the high angle grain boundaries migration relies mainly on temperature. The higher the temperatures, the higher the boundary migration and the coarser the grain. Another important variable is the presence of solutes and particles within the matrix, grain growth can be supressed by the interference of solute elements and second phase particles dispersed along the microstructure. Solute elements and particles can act as pinning sites that stop the grain boundary motion, such is the case of microalloy elements in HSLA steels like Nb, V and Ti that possess the ability to refine the microstructure by hindering the grain growth [23].

2.2. Microalloyed steels

The beginning of microalloyed steels (MAS), also named High Strength Low Steels (HSLA), dates back to the late 1950's when small amounts of niobium (0.005 to 0.03%) where added to ordinary C-Mn steels. These relatively low cost Nb additions brought a remarkable improvement in the mechanical properties of the steel (GLX-60W grade), the yield strength was increased from 300 MPa to 415 MPa and a superior toughness and weldability was achieved [29]. During the next two decades, MAS were mainly exploited to produce components with microstructures consisting of ferrite–pearlite (F-P) manufactured by conventional hot rolling followed by air cooling, the chemical composition of MAS was based on relatively high carbon and moderate Mn levels. However, at the beginning of the 80s the development of MAS gained momentum since the linepipe and automotive industries started to demand steel grades with a yield strength higher than 420 MPa. This historical moment represents an inflection point in the development of modern MAS, the change from F-P microstructures to lower temperature transformation products such as acicular ferrite, bainite, martensite or a mixture of them was the obvious choice to attain the high strengths required in the steel. The rolling mills had to evolve to achieve high cooling rates after hot rolling and as a result, new processing routes such as Interrupted Accelerated Cooling (IAC) and Interrupted Direct Quenching (IDQ) where developed. The benefits of faster cooling rates allowed for the development of steel grades with higher levels of strength with lower carbon concentrations.

Nowadays, a suitable combination of processing routes and specific chemical compositions in the steel can lead to the manufacture of microalloyed steels with very high strength, such is the case of the X100 linepipe grades which possess a yield strength in excess of 690 MPa [30] or the automotive grades ALFORM700M and ALFORM900M which have minimum yield strength values of 700 MPa and 900 MPa respectively [31].

Microalloyed steels occupy a privileged position in the world of materials for engineering, they can achieve optimal combinations of mechanical and metallurgical properties which are fundamental for the development of diverse technologies with high social and environmental impact. One of their primary characteristics is that they can possess both high strength and high toughness due to their notable grain refinement achieved during controlled processing. Additionally, they exhibit high resistance to corrosion and have good weldability. The combination of mechanical properties of MAS brings important economic benefits, the increase of toughness and strength allows a reduction in the thickness and consequently lighter steel products can be manufactured, the reduction of weight is then reflected in savings in the operation costs, transport, handling and welding.

The application of MAS is massive and is not limited only to the automotive and oil sectors, there is also an important consumption in the shipbuilding, extraction and construction industries [7]. At present, the estimated annual world production of MAS is approximately 200 million tonnes, which is around the 12% of the whole steel production including all the classes [8].

As for the chemical composition, MAS generally contain less than 0.15 wt% of microalloying elements (MAE) which usually do not exceed 0.10% individually, they also have a low carbon content (0.05 to 0.25% C) to achieve good weldability and formability, manganese contents up to 2% and other elements in small quantities such as chromium, nickel, molybdenum, copper, nitrogen, and zirconium [8], [32]. MAE are those able to a) refine the grain size, b) cause precipitation hardening and c) increase the hardenability when in solid solution. Niobium, vanadium and titanium are MAE by definition [33]. Table 1 shows the ranges of alloying elements which are usually found in MAS.

Table 1. Alloying elements used in microalloyed steels [8]

Element	wt-% in steel	Influence
C	<0.25	Strengthener
Mn	0.5–2.0	Delays austenite decomposition during accelerated cooling Decreases ductile to brittle transition temperature Strong sulphide former
Si	0.1–0.5	Deoxidiser in molten steel Solid solution strengthener
Al	<0.02	Deoxidiser Limits grain growth as AlN
Nb	0.02–0.06	Very strong ferrite strengthener as Nb(C,N) Delays $\gamma \rightarrow \alpha$ transformation
Ti	0–0.06	γ grain size control by TiN Strong ferrite strengthener
V	0–0.10	Strong ferrite strengthener by V(C,N)
Zr	0.002–0.05	γ grain size control [Zr(C,N)] Strong sulphide former
N	<0.012	Forms nitrides and carbonitrides with
Mo	0–0.3	Promotes bainite formation Ferrite strengthener
Ni	0.0.5	Increases fracture toughness
Cu	0–0.55	Improves corrosion resistance Ferrite strengthener
Cr	0.1.25	With Cu, increases atmospheric corrosion resistance
B	0.0005	Promotes bainite formation

MAE are transition metals that readily react with the nitrogen and carbon present in the steel to form nitrides, carbides or carbonitrides. The precipitates are B1 NaCl type fcc (face centred cubic) compounds and have a lattice parameter larger than austenite and ferrite, the lattice mismatch is the reason to find them always located on crystalline defects such as dislocations, grain boundaries and subgrain boundaries. The strains caused by the misfit between the particles and the matrix (either austenite or ferrite) cause strengthening by the Orowan-Ashby mechanism [30]. According to the stage of the process at which the precipitates are formed, the nitrides and carbides are classified into three categories [8]:

I. Type 1. Precipitates formed at high temperatures, they can precipitate in the liquid phase, in the liquid/solid interphase during solidification and in the delta ferrite after the solidification. These precipitates are very stable and large, during the reheating of the slabs they tend to coarsen and only the smallest truly contribute suppression of the austenite grain growth. Titanium belongs to this category since it forms very stable and coarse nitrides that do not dissolve during the reheating of the slab before hot rolling.

II. Type 2. These precipitates play a remarkable role in the austenite refining during thermomechanical controlled processing. Through a solution heat treatment at temperatures in the austenitic region, the precipitates dissolve and the microalloy element is brought back into solid solution. Afterwards, during controlled hot rolling the deformation induces its dynamic precipitation, this phenomenon is called strain induced precipitation (SIP) because the energy required for precipitation is provided by the deformation. SIP has a profound effect in the austenite refining for the particles formed are small and dispersed, this gives them the ability to significantly retard the recrystallisation since the grain boundaries mobility is hindered by the Zener pinning effect [34]. The most representative MAE within this group is Nb, since its supersaturation in austenite can occur at the conventional hot rolling temperatures making it prone to precipitate due to deformation.

III. Type 3. The precipitates of this group are formed during or after the austenite to ferrite transformation, the nucleation takes place in the austenite/ferrite interphase and in ferrite. Fine and dispersed particles provide precipitation strengthening to the ferrite matrix, Niobium and Vanadium fall in this category.

Microalloy elements can increase the strength of the steel in form of precipitates or in solid solution, however, the strengthening mechanism for which MAE are very well known, is the grain size refining. Figure 8 shows the reheating of a cold slab or billet to different temperatures in the austenitic phase, the ability of the different microalloying elements to refine the austenitic grain size is clearly notable for each element at certain range of temperatures.

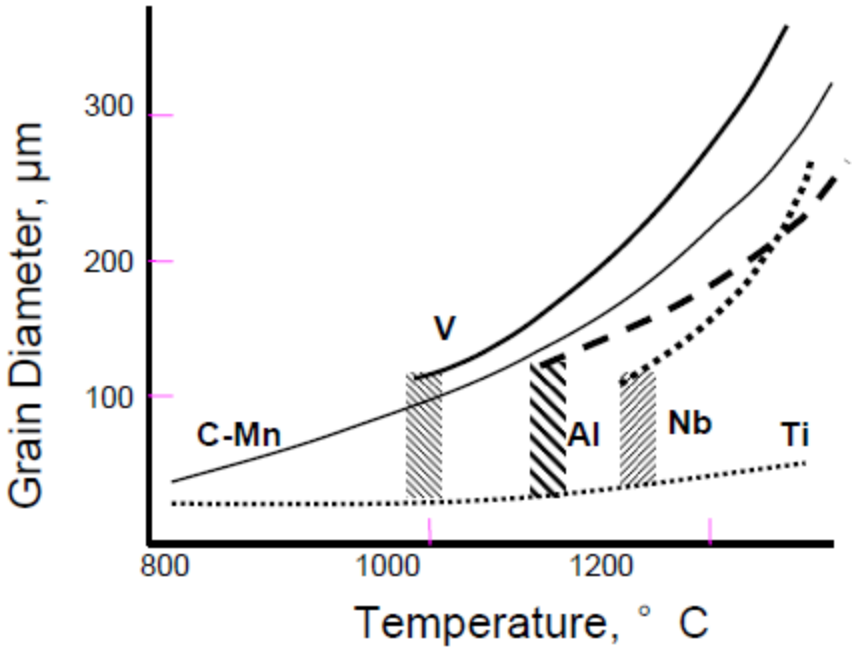

Figure 8. Effect of different steel microalloys on the austenitic grain size in a C-Mn steel at different temperatures [33].

2.2.1. Niobium microalloyed steels

Niobium is perhaps the element most extensively studied within the microalloying elements, and its ability to control the recrystallisation of austenite during hot rolling is vastly exploited in thermomechanical controlled processing. Compared to other microalloys, Nb shows superior refining properties, smalls additions cause a profound effect on the recrystallisation temperature of austenite as shown in Figure 9. Either in solid solution form or as a precipitate, Nb can play a very positive role in the microstructural evolution of the steel, besides, the range of temperatures at which Nb dissolves or precipitates in austenite has a good match with the conventional hot rolling temperatures as shown in Figure 10. Due to these characteristics Nb is preferred microalloy used to tailor the microstructure during controlled hot rolling nowadays.

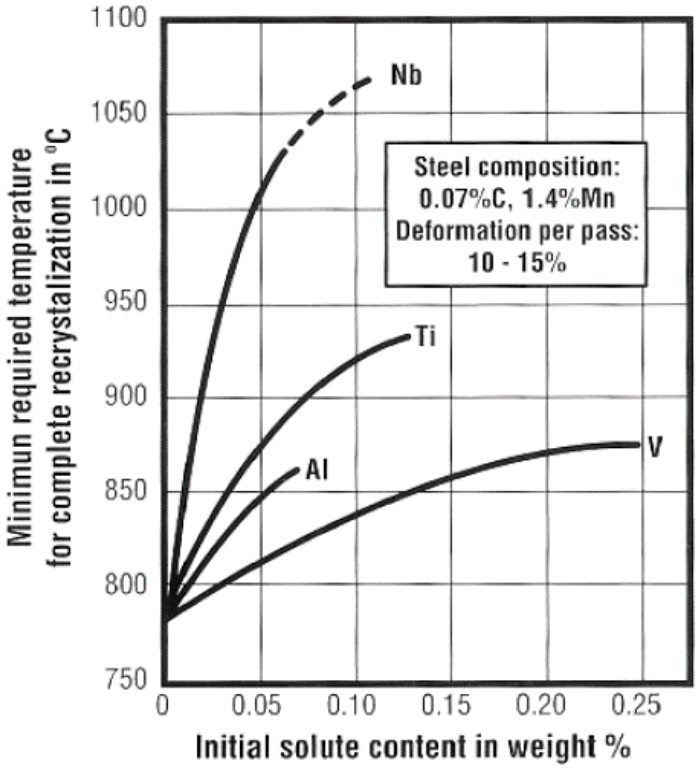

Figure 9. Effect of different additions to steel on austenite temperature recrystallization [35].

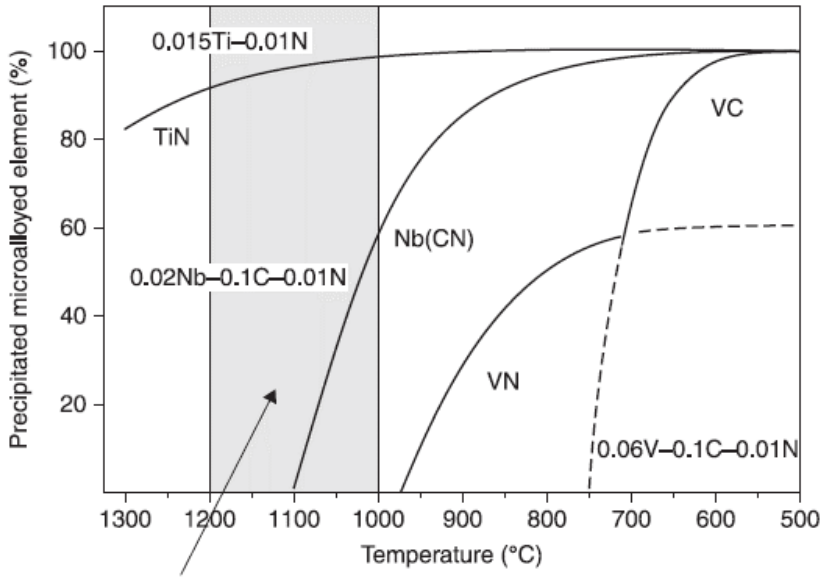

Figure 10. Percentage fraction of precipitation of different austenite microalloys as function of temperature under equilibrium conditions [23].

2.2.1.1. Effect on microstructural evolution.

The ability of Nb as a microstructural refiner has been reported at the early stages of the steel production during the solidification and casting of steel [33], during the dendritic growth of the delta ferrite, the solute Nb segregates into the vicinity of the delta-delta boundaries, as the cooling continues and further transformation of austenite takes place, the nucleation on the delta ferrite grain boundaries leads to a remarkably refined austenite as shown in Figure 11, the Nb rich delta boundaries are responsible for the austenite growth suppression.

In general, Niobium is recognised for three effects on austenite [36]–[39]: (i) the inhibition grain coarsening during reheating, (ii) the suppression or retardation of the static recrystallisation after deformation (iii) and the precipitation hardening after the austenite decomposition to lower temperature transformation products.

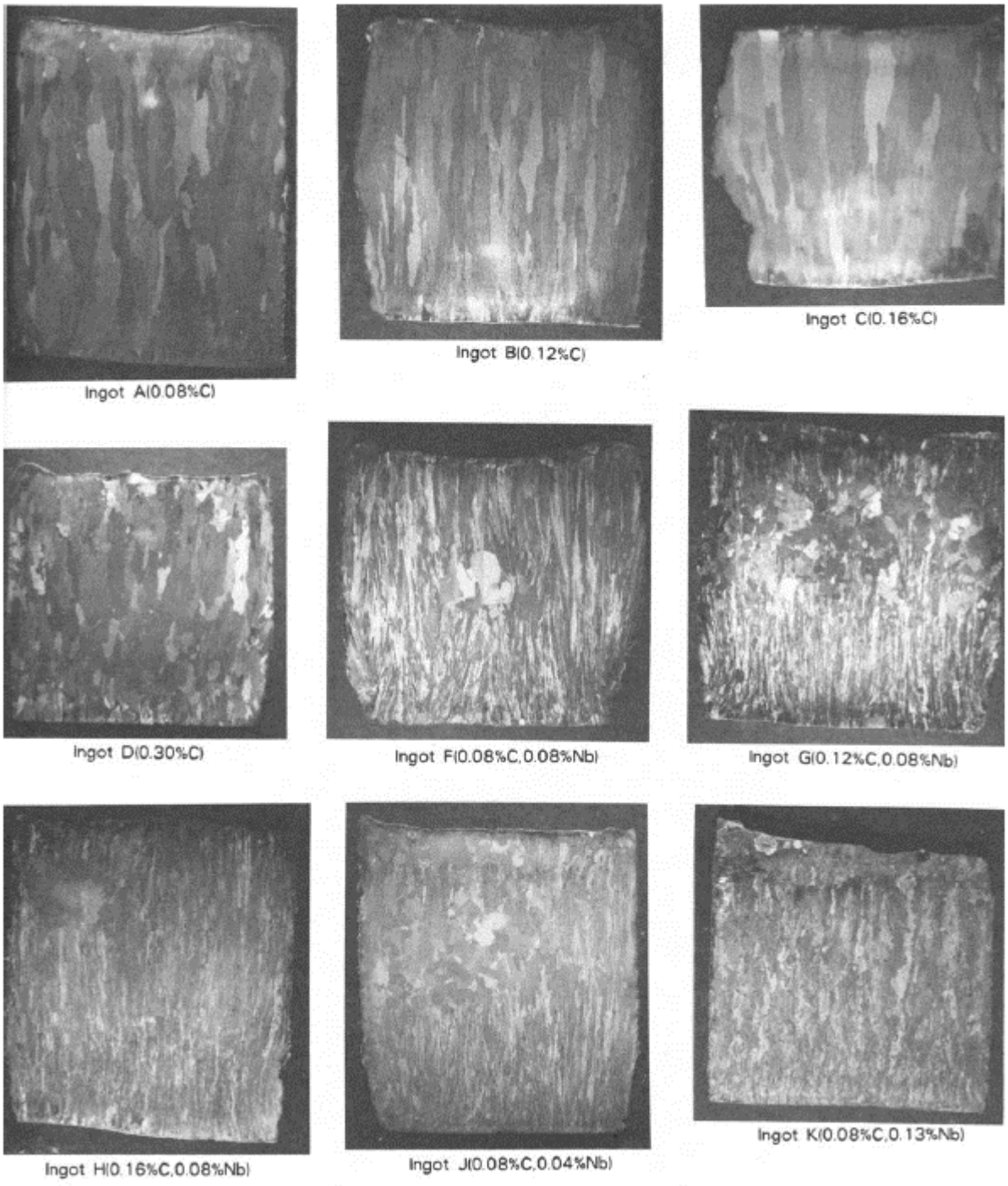

Figure 11. Effect of Nb addition on the macrostructure of unidirectional solidified ingots, water quenched before the austenite to ferrite transformation. The chilled surfaces are at the bottom [33].

Nb also has an influence on the hardenability of steel, the incubation time of allotriomorphic ferrite is longer in niobium-containing steels, soluble Nb segregates to the prior austenite grain boundaries and reduces the grain boundary energy [40], this mechanism improves the hardenability and compensates the low carbon concentrations found in MAS. The higher the Nb concentration in solid solution, the lower the critical temperature Ar_3, low temperature transformation products are achievable when high Nb concentrations and fast cooling rates are combined.

2.2.1.2. Precipitation

Niobium belongs to the group of transition metals which have the characteristic to possess unfilled inner shells inside the outer or valence shell. Compared to non-transition metals, transition metals can dissolve much more readily small atoms such as nitrogen and carbon to form interstitial solid solutions [24]. Nb is a strong carbides and nitrides former but shows poor tendencies to form oxides and sulphides, this characteristic distinguishes it from Titanium which forms carbides until all the available oxygen, sulphur and nitrogen are consumed by initial additions of titanium [35] or other elements. Ti can form large non-metallic inclusions with oxygen and sulphur (particles which are in most of the cases negative for the mechanical properties), while Nb is confined to form much smaller precipitates which somehow or other contribute to the strengthening of steel.

The precipitation of Nb in steel results in three main compounds with a B1 (NaCl) type fcc crystal structure, their stoichiometry can be represented as NbC_x, NbN_x and NbC_xN_y. In the first two systems NbC_x and NbN_x x is equal to the C/Nb and N/Nb mole ratios respectively, whereas in NbC_xN_y x is the C/Nb ratio, y is the N/Nb ratio, and $1 – (x + y)$ is the mole ratio of vacancies. This type of precipitates are of most interest in Nb microalloyed steels, however, it is important to mention that other compounds can be found in some steels, such is the case of the precipitate Nb_2C that has an hcp (hexagonal closed packed) crystal structure, this compound has been observed in steels with high Nb/C ratios [35].

The lattice parameter of the compounds varies according to their stoichiometry, for instance, the carbon solubility in NbC_x reported at 1100°C falls in the range $0.72 < x < 1$, since the lattice

parameter increases with *x*, the pure stoichiometric NbC has a lattice parameter of 4.470 Å while in $NbC_{0.7}$ the lattice parameter is about 4.43 Å [35], [41]. The NbN shares very similar characteristics with NbC, in fact, these two compounds can easily combine to form carbonitrides type NbC_xN_y. The composition of the carbonitrides varies with the chemical composition of the steel, the N/C ratio plays a primary roll, the larger the ratio the higher the content of nitrogen in the precipitates. Other nitrides formers such as Ti and Al affect the composition of the carbonitrides. (hereinafter, NbC_xN_y will be denoted as Nb(CN) for simplification).

The precipitation of niobium occurs on preferential crystallographic directions of the matrix, thus certain orientations relationships between the matrix and the precipitates are conserved. Due to the NaCl type crystal structure of the Nb precipitates, the precipitation in the parent austenite follows the next relationships [35]:

$$[100]_{M(CN)} \parallel [100]_{\gamma}$$
$$[010]_{M(CN)} \parallel [010]_{\gamma}$$

whereas in ferrite or martensite, the NbC_xN_y precipitation obeys the Baker-Nutting orientation relationship [42].

$$[100]_{NbC} \parallel [100]_{\alpha}$$
$$[011]_{NbC} \parallel [010]_{\alpha}$$

These orientation relationships (OR) are useful to determine whether the Nb precipitation happened in austenite or in its further transformations, i.e. ferrite or martensite. When the austenite transforms on cooling, it does so with the Kurdjumov-Sachs (K-S) OR [43].

$$(111)_{\gamma} \parallel (110)_{\alpha}$$
$$[110]_{\gamma} \parallel [111]_{\alpha}$$

Therefore, the origin of the precipitation can be traced back by analysing the crystallographic orientation relationships between the matrix and the precipitates at room temperature, if the ferrite and the precipitates are related by the K-S OR, the precipitates were formed in austenite,

otherwise, if they obey Baker-Nutting OR, it means that the precipitation occurred during or after the transformation from austenite to ferrite. If none of these orientation relationships between the matrix and the particles is accomplished, then the precipitation happened in austenite and further recrystallisation erased the crystallographic correlations between the matrix and the precipitates. It is important to notice that recrystallisation of austenite is not very frequent the after the Nb(CN) precipitation, most of the precipitates formed in the parent austenite are strain induced and have a strong effect on the retardation of the recrystallisation.

The precipitation of Nb(CN) on the steel matrix generates a significant lattice mismatch as shown in Table 2. The misfit strains around the particles strengthen the matrix and provide precipitation hardening, besides, the lack of registry is large enough that the coherency between the particles and the matrix within the grains is not possible, that is the reason why the precipitates nucleate only in the grain or subgrain boundaries and other crystalline defects.

Table 2. Lattice mismatch for Nb(CN) precipitates in austenite and ferrite [35].

Orientation relationship	Required linear strain in matrix, %*		
	NbC	$NbC_{0·8}$	$NbN_{0·8}$
γ matrix			
$[100]_{ppt} \parallel [100]_{\gamma}$	25·5	26·6	23·0
$[010]_{ppt} \parallel [101]_{\gamma}$	25·5	26·6	23·0
$[001]_{ppt} \parallel [001]_{\gamma}$	25·5	26·6	23·0
α matrix			
$[100]_{ppt} \parallel [100]_{\alpha}$	56·3	57·7	53·1
$[011]_{ppt} \parallel [010]_{\alpha}$	10·5	11·5	8·4
$[011]_{ppt} \parallel [001]_{\alpha}$	10·5	11·5	8·4

*All matrix strains are tensile (+).

The precipitation of Nb(CN) shows three typical distributions and morphologies: i) general precipitation, ii) interphase precipitation and iii) strain induced precipitation. The general and interphase precipitation occurs in ferrite when the remaining soluble Nb precipitates during or after the austenite transformation. The solubility of niobium in ferrite is around 20 times lower than in austenite, thus, a sudden supersaturation of soluble Niobium and a significant increase in the driving force for precipitation is expected when the γ to α transformation occurs. As for

the strain induced precipitation in austenite, the Nb(CN) precipitates are formed dynamically during the deformation, this type of precipitation is of major interest in thermomechanical controlled processing due to the austenite conditioning provided by the fine precipitated particles.

The general or homogeneous precipitation of Nb in ferrite occurs at the lowest temperatures during hot strip coiling or tempering of a quenched steel. The precipitates are very fine and homogenously dispersed in the matrix, after prolonged holding at high temperatures the precipitates remain fine and do not show a dramatic coarsening [44]. These precipitates are responsible for the precipitation hardening effect of Nb(CN) [35]. An example of the homogeneous precipitation of NbC in a microalloyed steel is shown in Figure 12.

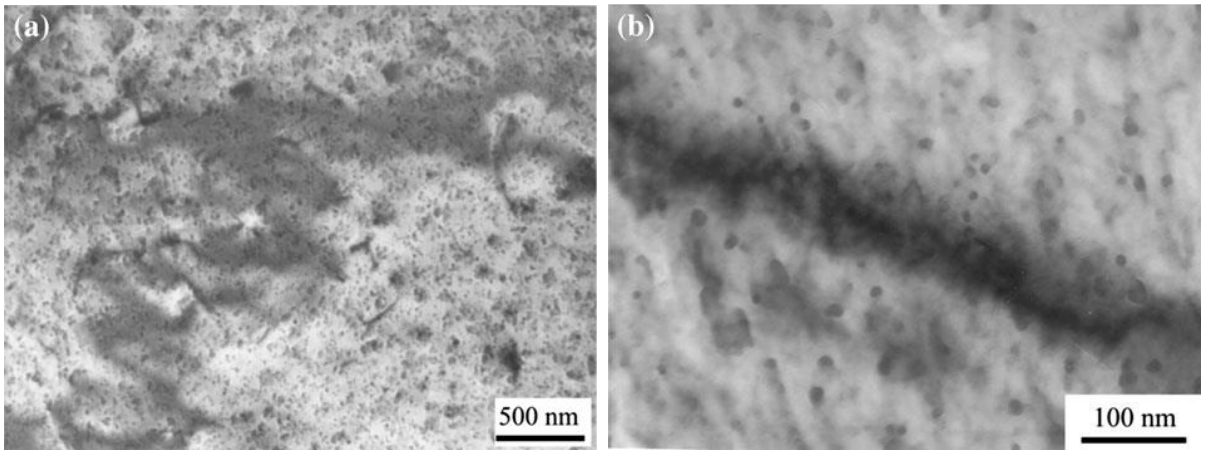

Figure 12. Thin foil bright field TEM images showing homogenous precipitation of NbC in a steel containing 0.06C-0.056Nb (wt%) [44].

Interphase precipitation on the other hand, is observed at higher temperatures and lower cooling rates, the advance of the transformation front must be slow enough to allow for the nucleation of precipitates at the α-γ interphase. As the phase boundary moves to a new location, fine and spherical NbC precipitates are left behind in parallel rows as can be seen in Figure 13, the spacing among the rows depends on the temperature. Similarly, to general precipitation, the rows of fine precipitates strengthen the ferrite matrix.

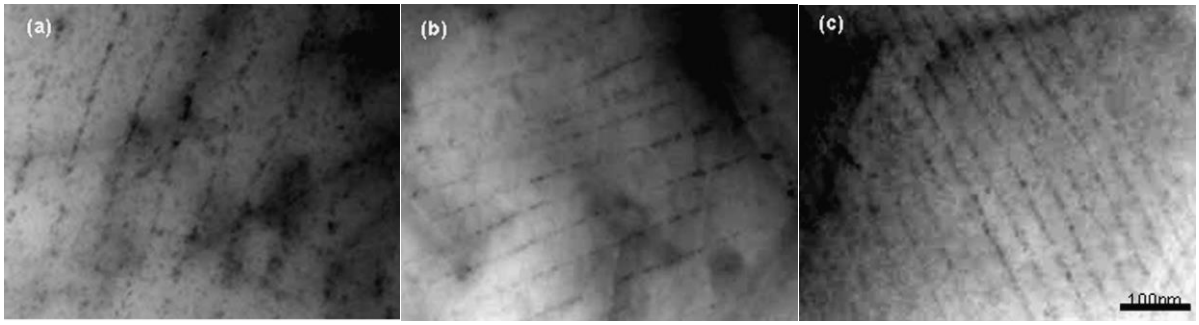

Figure 13. STEM Bright field image showing the interphase precipitation of NbC at a) 750°C, b) 700°C and c) 650°C in a steel containing 0.052C-0.05Nb (%wt) [45].

As previously mentioned the solubility of Nb in austenite is significantly higher than in ferrite, in fact, in undeformed austenite the precipitation of Nb is a very sluggish process which is a disadvantage for the hot rolling process, since the benefits of Nb as precipitate can be exploited only when the precipitation occurs sufficiently rapid. However, the kinetics of precipitation can be dramatically affected by deformation, the massive introduction of dislocations in the austenite as the strain increases provides nucleation sites to bring about the SIP of Nb. The morphology and distribution of SIP precipitates are optimal for the austenite refining since the particles are very small and dispersed, the size of precipitates has been measured in multiple studies and although there are some differences in the sizes reported, SIP precipitates observed just after the deformation are very fine and their average diameter ranges from a few nanometres to around 25 nm [46]–[50].

A proper combination of multiple deformation passes, strains, interpass times, and deformation temperatures can be designed for microalloyed steels to obtain the maximum strain induced precipitation of niobium, as the strain accumulates during the deformation passes, the volume fraction of precipitates increases and the austenite is shaped into an elongated body in the rolling direction with negligible recrystallisation, this is the principle of “austenite conditioning” which is the basis for microstructural refining in controlled rolling. Figure 14 shows an example of strain induced precipitates of niobium in a microalloyed steel with 0.02 wt% of Nb, the size of precipitates varies from 10 to 12 nm.

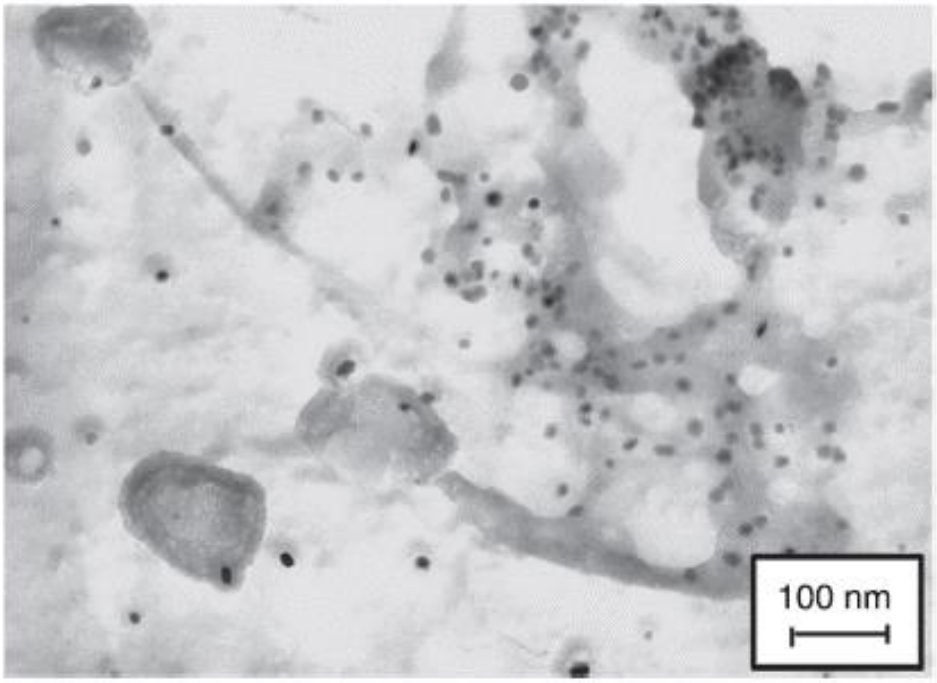

Figure 14. Strain induced precipitates of Nb observed in a carbon extraction replica obtained from a microalloyed steel [23].

2.3. Deformation strain induced ferrite transformation (DIFT)

Within the last five decades, an extensive research has been focused to improve the ferrite grain size refinement, the increasing demand of structural steels with higher strength and toughness has produced a global trend towards the research and development of steels with microstructures as fine as possible. The γ to α dynamic transformation during deformation seems to be a promising alternative to produce ultrafine grained microstructures, a proper combination of deformation variables and alloy design could lead to microstructures with a grain size on the order of 1 μm or even smaller.

The first observations of the dynamic transformation of austenite to ferrite were reported by Yada et al [51] in the 1980s, large deformations of at least 75% of reduction divided in one or two passes in common C-Mn steels were carried out at temperatures at approximately the Ar_3, the final microstructure consisted of 70% or more of equiaxed ferrite grains with a size of 4 μm or less, which was significantly finer than that produced by conventional hot rolling. Two

important findings were observed during deformation; the increase of the Ar_3 temperature that allowed for the dynamic transformation of austenite to ferrite, and the dynamic recrystallisation of the deformation induced ferrite in subsequent passes. The new ultrafine microstructure showed significant industrial advantages compared to that produced by conventional rolling, such as high strength without the use of a special alloying elements (which also reduces the production costs), predictable superior toughness due to the improved grain refinement, and higher ductility and workability than conventional steels. Besides, at temperatures between 600°C and 800°C, the elongation and welding friction were excellent due to the superplasticity of the material. In a later work [52], the dynamic transformation of ferrite was observed in plain carbon steels at temperatures around 65 °C above the Ae_3 (900°C) and a strain of 0.69, however, ferrite grains were unstable at such temperature and the reversion to austenite began a few seconds after the deformation. A second pass was added before the beginning of the retransformation of ferrite to austenite and an ultrafine ferrite with a grain size of 2 μm was obtained. In another research, Yada and co-workers could demonstrate that the dynamic transformation of ferrite can occur at temperatures as much as 150°C above the Ae_3 [53].

Extensive research has been carried out after the pioneering work of Yada and co-workers and different names have been adopted to call the dynamic transformation of austenite to ferrite, for the present work, the term Deformation Induced Ferrite Transformation (DIFT) will be used after Dong et al [54]. An example of the presence of DIFT in a microalloyed low carbon steel containing 0.094%C–0.29%Si–1.42%Mn–0.045%Nb is shown in Figure 15, the steel was deformed to a strain of 0.92 at 766 °C (above the Ar_3) followed by rapid water quenching to preserve the DIFT, abundant equiaxed and polygonal ferrite grains can be observed mainly along the prior austenite grain boundaries.

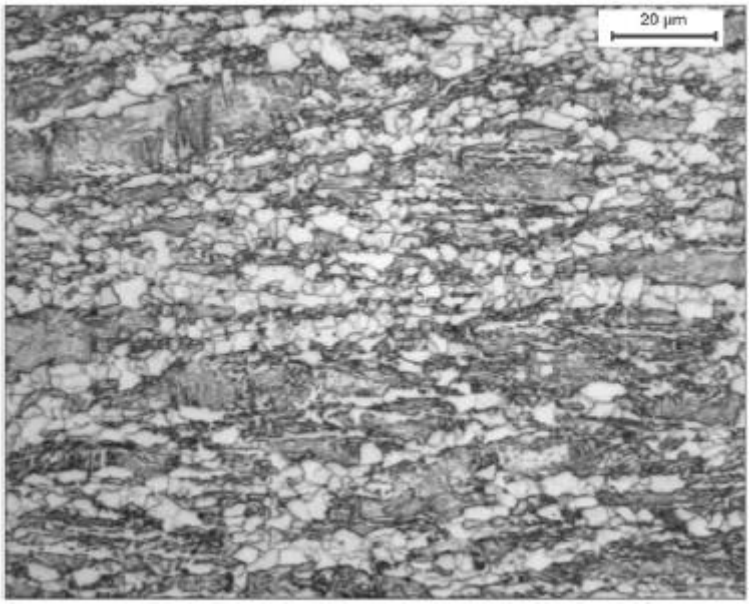

Figure 15. Presence of DIFT in a low carbon microalloyed steel in a quenched sample after deformation [54].

2.3.1. Evidence of DIFT

The validation of the occurrence of DIFT has been a polemic topic, most of the evidence reported has been based on the analysis of the microstructure of quenched samples after the deformation, however, since there is an interval of time between the deformation and the quenching of the sample, this method has failed to prove with accuracy whether the ferrite is formed during deformation or during quenching. The first experiments that succeeded in proving DIFT in real testing time were conducted by Yada et al [55] in 2000, in their work, torsion tests were performed in a Fe-6%Ni-(0.0008 ~ 0.29)%C alloy and in-situ X-Ray diffraction was used to detect the main crystallographic planes diffracting in the sample during the test. When the deformation was applied, lines corresponding to the planes $(1\ 1\ 0)_{\alpha Fe}$ and $(1\ 1\ 1)_{\gamma Fe}$ appeared as shown in Figure 16, these results proved that the γ to α transformation happened dynamically during the deformation in a wide range of temperatures, even above the paraequilibrium temperature Ae^{p}_{3} (local equilibrium temperature at the migrating α-γ interphase).

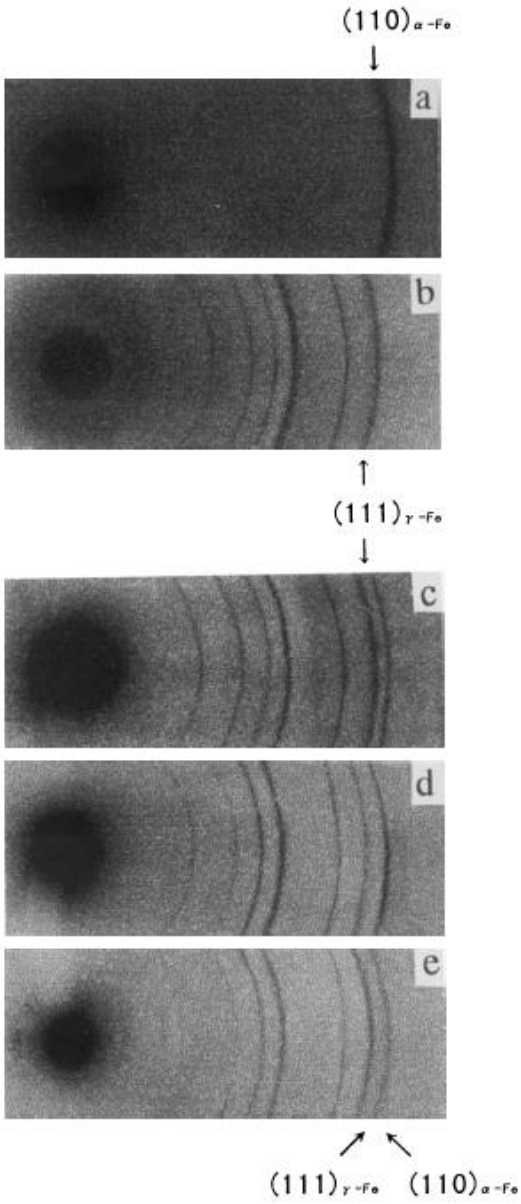

Figure 16. Typical X-Ray diffractions patterns observed in the Fe-6%Ni-0.96%C alloy at different conditions; before heat treating a), austenitised at 790°C and then cooled and held at 640°C b), austenitised at 790°C and then cooled and deformed at 640°C c), 680°C d) and 720°C e) [55].

Furthermore, a substantial deviation in the expected deformation stress was observed as shown in Figure 17, the abnormality in the plastic behaviour cannot be attributed solely to recrystallisation or recovery effects, the most consistent explanation is found in the DIFT given that ferrite is much softer than austenite, thus, as the strain increases the deviation in the flow behaviour becomes more evident due to the increase in the volume fraction of ferrite.

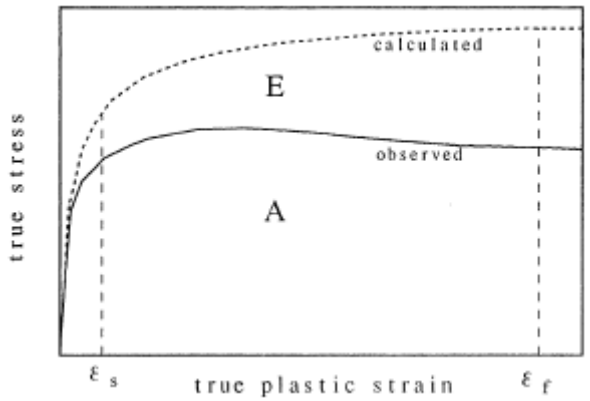

Figure 17. Comparison between the expected (calculated) and the observed flow stress curves [55].

In more recent researches, flow curves were also analysed to prove the occurrence of DIFT during torsion tests above the Ae_3 in common and Nb microalloyed steels [56]–[58], the real flow stress showed a deviation from the expected values in multipass deformation simulations as shown in Figure 18, it can be observed that the increase in the stresses is slower than expected as more passes are added, this can be related to the progressive ferrite transformation happening in each pass.

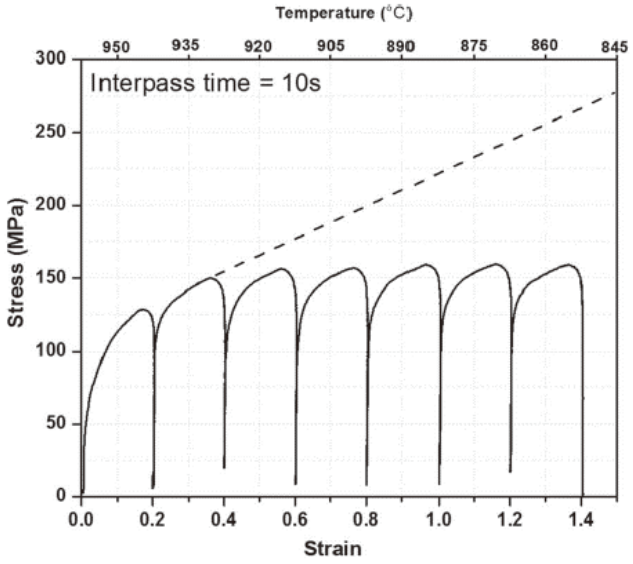

Figure 18. Stress-strain curves obtained from a simulation consisting of 7 passes at temperatures from 950°C to 860°C, using a strain of 0.2 applied at a strain rate of $1s^{-1}$ and interpass times of 10 seconds, in a steel containing Fe-1.56%Mn-0.047%C-0.25%Si-0.092%Nb. The broken line represents the expected stress [57].

2.3.2. Transformation mechanism

There is still debate regarding the transformation mechanism of DIFT, at least four different approaches can be found in the literature to describe the transformation phenomena. The first explanation was provided by Yada et al [55], who proposed a massive transformation in which long-range diffusion of carbon does not occur during the γ to α phase change. Their conclusions were based on previous evidence of abundant ultrafine ferrite formation found at strain rates up to $250s^{-1}$. The fast ferrite formation rates cannot be related to the pro-eutectoid ferrite transformation, however, evidence was not provided with respect to whether the ferrite was formed during the holding or cooling after the deformation.

A different mechanism consisting in long distance diffusion controlled transformation has been supported by various researchers, in this hypothesis the transformation is basically the same as that of pro-eutectoid ferrite transformation. The experimental evidence supporting this transformation mechanism is detailed below [20], [59]:

1. The effect of alloying elements in DIFT is the same as that in proeutectoid ferrite, thus, niobium, manganese and carbon in solution retard the dynamic transformation.
2. Carbon is rejected from ferrite during DIFT, there is clear evidence of the presence of carbides at the austenite grain boundaries and edges after DIFT, this indicates that the precipitation occurs in the final carbon rich austenite. The enrichment of austenite also increases its hardenability.
3. As in pro-eutectoid ferrite, DIFT produces the conventional Kurdjumov-Sachs orientation relationships between austenite and ferrite, differently to massive transformation where orientation between ferrite and austenite is random.

A third transformation mechanism was proposed by Weng et al [60], who classified DIFT as a new kind of transformation different from both massive and pro-eutectoid transformations. Their interpretation is based on the finding of cementite precipitates with sizes smaller than 20 nm within DIFT grains, according to their hypothesis, the precipitates are formed after DIFT due to the supersaturation of carbon in a process of limited diffusion and far from the equilibrium state. In addition, DIFT grains possess low dislocation density and dynamic

recovery is presumed to happen during the transformation, observations in TEM showed the rearrangement of some dislocations to form low angle grain boundaries around DIFT grains as shown in Figure 19. Despite the evidence supporting this transformation hypothesis, it is not clear whether the cementite precipitates were formed during the DIFT or during cooling.

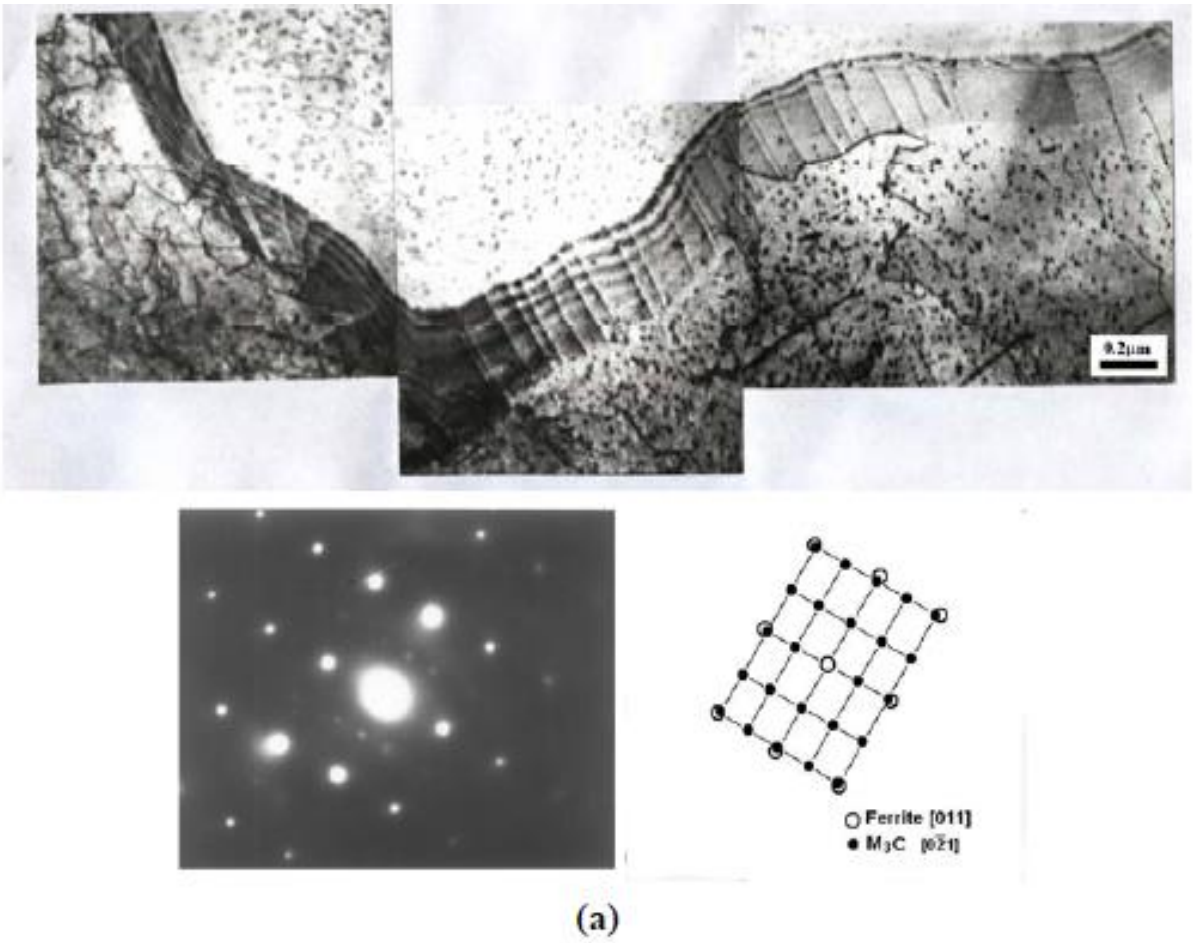

(a)

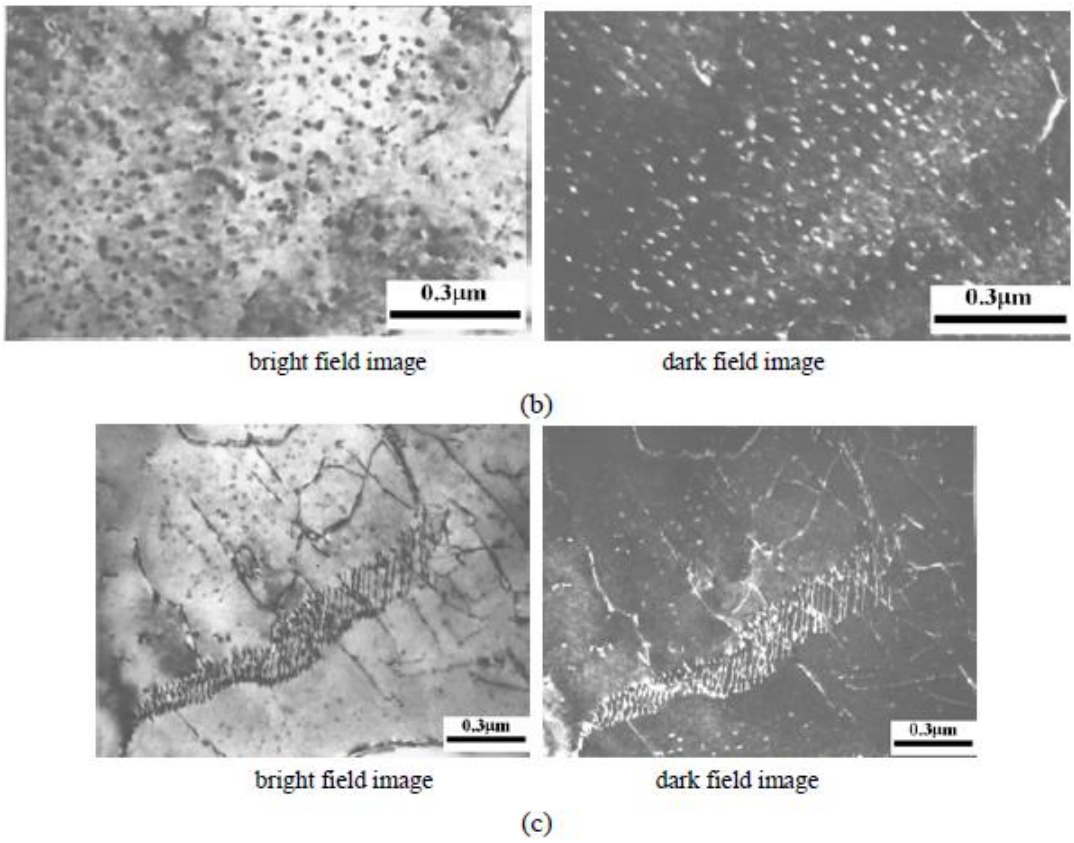

Figure 19. TEM Images of DIFT in two low carbon steels containing 0.09%C-0.51%Mn-0.25%Si-0.017%Nb a), and 0.12%C-0.34%Mn-0.22%Si b) and c) [60].

Another transformation mechanism proposed to explain the dynamic transformation of ferrite was published by Basabe et al [61], who carried out torsion tests above the Ae_3 temperature at strains from 0.5 to 2 in a steel containing 0.09%C-1.3%Mn-0.02%Si-0.036%Nb, according to their findings, the deformation causes the displacive transformation of thin Widmanstätten ferrite plates of about 200 nm wide that then merge by coalescence and evolve into polygonal grains, Figure 20 a) illustrates the stages of the dynamic transformation of ferrite according to this mechanism. Ferrite plates appear aligned in a single direction showing the influence of the stress during the deformation, the nucleation can occur at the prior austenite grain boundaries but also intragranulary as shown in Figure 20 b) and c) respectively. EBSD analysis showed that the angular misorientation between adjacent plates is very small (less than or around 1°), which accounts for the rapid coalescence of plates that leads to polygonal grains formation. Basabe et al used the term "dynamic transformation" (DT) to name transformations that occur above the Ae_3 temperature caused by the deformation.

a)

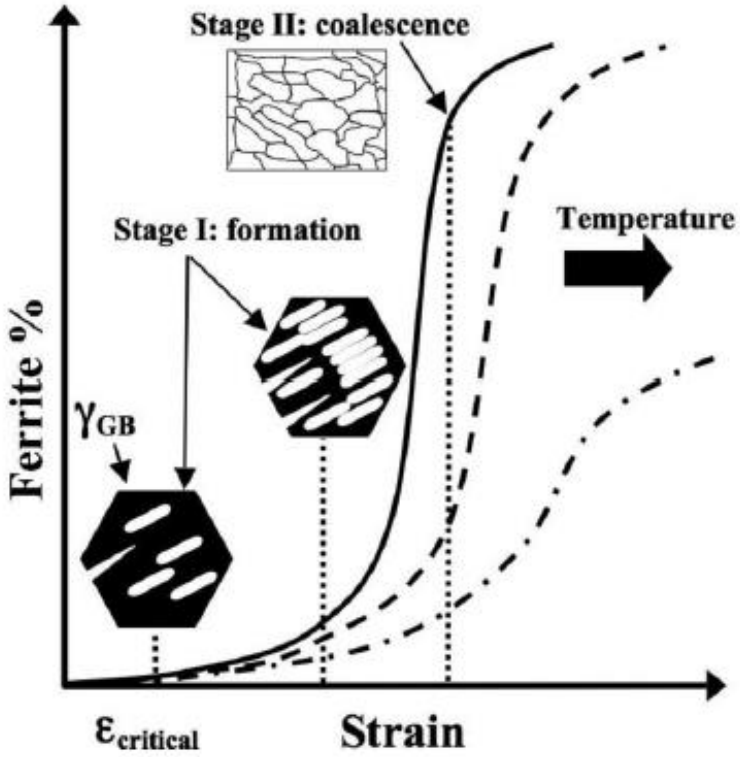

b) c)

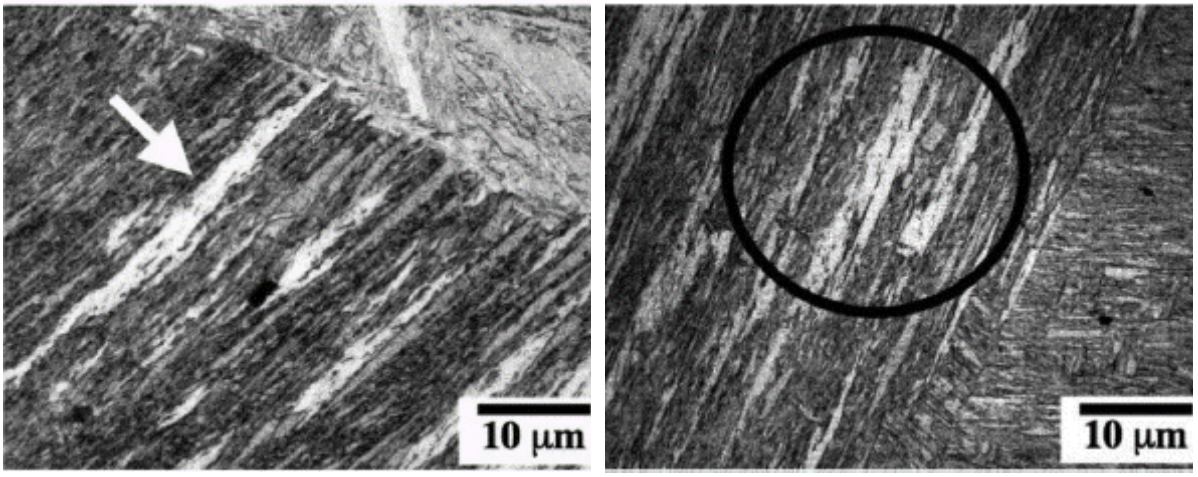

Figure 20. Stages in the formation of dynamically transformed ferrite as a function of strain at temperatures above the Ae_3 a), and evidence of the formation of ferrite plates at the grain boundaries b) and intragranulary c) [61].

The DT mechanism has received increased attention and numerous papers have been published in the last years around this hypothesis. Gosh et al [62] performed torsion tests in a range of temperatures above Ae_3 up to 160°C in steels with different carbon content, the flow curves were analysed and the double differentiation method was used to detect the initiation of the DT

of Widmanstätten ferrite. The critical strain for the DT appeared even at lower strains than for DRX and increased with temperature. In a latter work [63], the effect of high contents of carbon (0.79%) on the DT was studied, it was found that the critical strain to form ferrite and cementite above Ae_3 was about 0.20, and the volume fractions of Widmanstätten ferrite and cementite increased with strain but decreased with temperature. Besides, despite the high carbon content there was enough time for the interstitial diffusion during the dynamic transformation but substitutional diffusion did not occur.

A model to describe the DT of the Widmanstätten ferrite plates was developed by Jonas et al [64], according to their work, the transformation occurs by mechanical activation and forms pairs of self-accommodating plates of near-identical orientation [65]. The stress provides the energy required to accommodate the shear of the parent austenite into Widmanstätten plates as well as the volume change or dilatation needed for the ferrite formation. Figure 21 shows an schematic diagram of the dynamic formation of a pair of ferrite plates by mechanical activation, the application of a shear stress conducts to the formation of a ferrite plate that forces the adjacent austenite to shear along with one of the sides of the plate, then the strained austenite transforms into a second ferrite plate, forming a pair of self-accommodating plates with opposite shears that cancel each other out. The introduction of dilatation and shear work to the model helped explain the dynamic transformation at low critical strains of about 0.1 reported in previous works [62], [66].

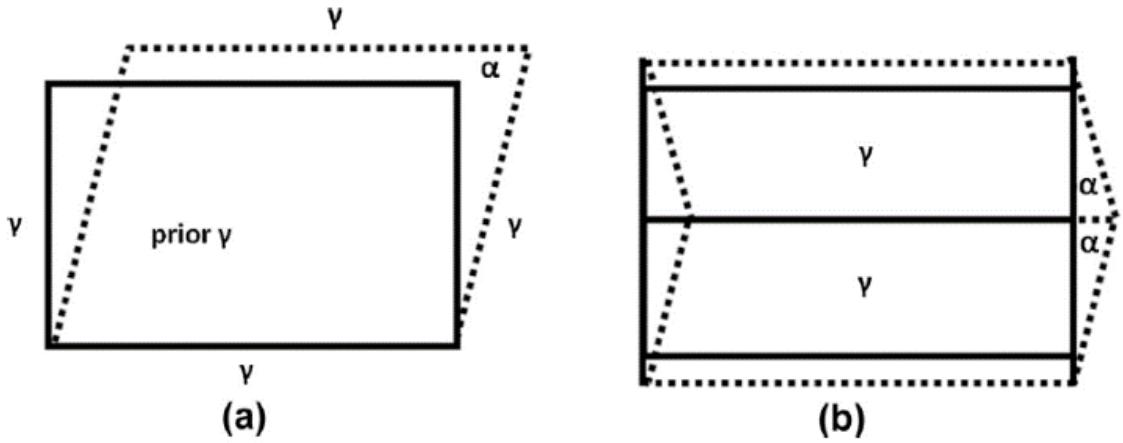

Figure 21. a) The application of a shear stress causes the transformation of a rectangle of prior austenite into a parallelogram of Widmanstätten ferrite. The lattice dilation (shown exaggerated) takes place in a direction perpendicular to the habit plane. The austenite adjacent to the upper surface of the ferrite plate is forced to shear along with the ferrite, and part of energy provided by the deformation is consumed by the accommodation work. (b) The geometry associated with the formation of a pair of "self-accommodating" plates. Here the adjacent austenite above and below the ferrite plates is undisturbed and the austenite to the left and the right of the growing plates has to accommodate shears ranging from 0 to 0.36 with an average value of 0.18 [64].

Evidence has been provided in recent years to support the DT proposed by Basabe, Grewal et al [21] demonstrated that the dynamic transformation can occur in the whole austenite phase field, even up to the δ-ferrite formation temperature. In their work, Vickers microhardness was performed in specific regions of quenched samples after a compression at 0.3 of strain in a plain C-Mn steel containing 0.06%C-0.3%Mn-0.02%Si. The dynamic polygonal and Widmanstätten ferrite showed average hardness values of 170 HV and 203 HV respectively, whereas the martensite hardness was 263 HV. Figure 22 shows the indents and hardness values of the different phases.

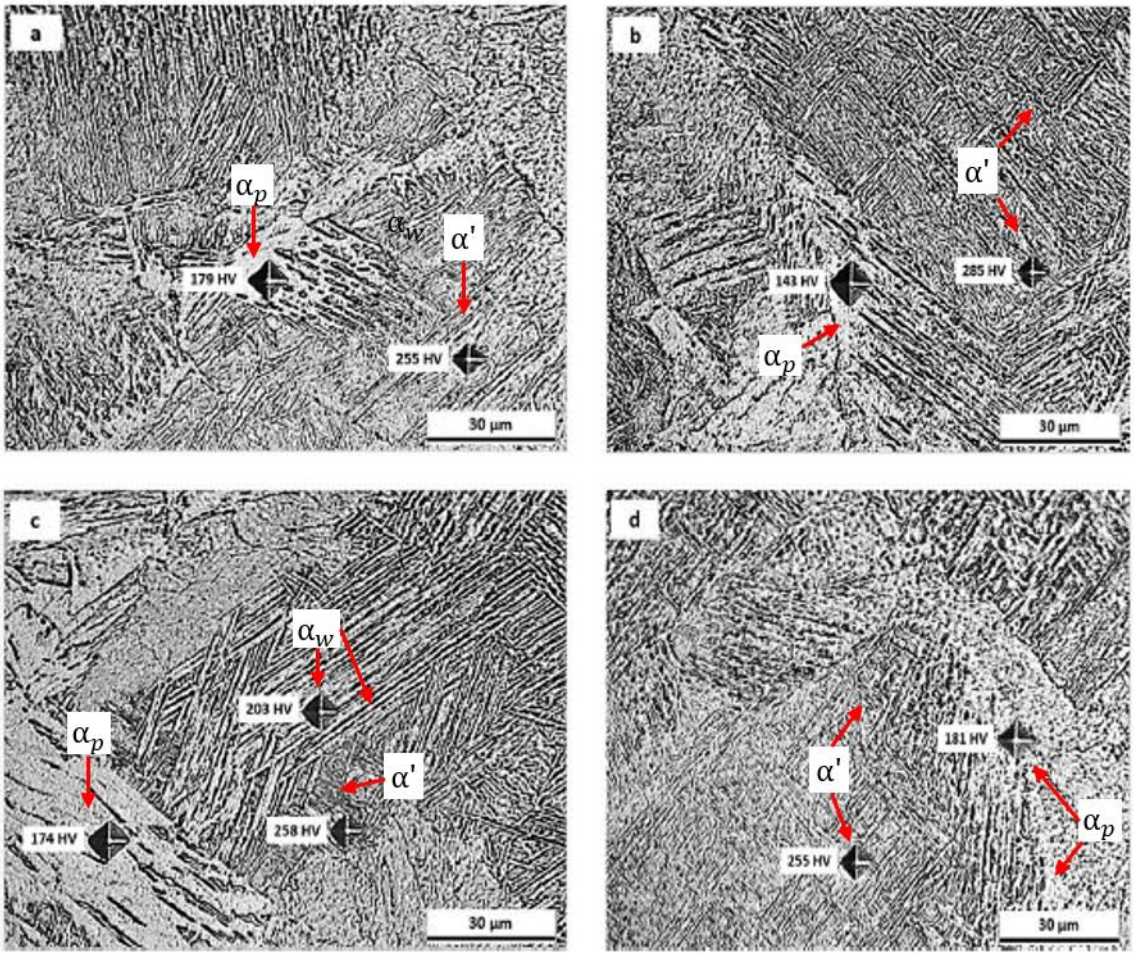

Figure 22. Indents and microhardness values of polygonal ferrite (α_p), Widmanstätten ferrite (α_w) and martensite (α') in samples strained to 0.3 at a) 1200°C, b) 1250°C, c) 1300°C and d) 1350°C.

In the last years, an extensive effort has been carried out in the study of the DT of ferrite in multipass deformation schemes in linepipe steels [58], [65], [67]–[70], firstly the X70 and X80 grades. The analysis of the flow curves has shown a decrease in the expected flow stress between deformation passes as previously shown in Figure 18, these observations indicate that the dynamic transformation occurred during the deformation passes since ferrite is softer than austenite. One of the central topics in the study of DT in multipass deformation, is the reversion of the ferrite to austenite during the holding time between passes for ferrite is unstable above the Ae_3 temperature. When the retransformation back into austenite takes place, the benefits in the grain refinement are lost. Solutions to prevent such reversion might be possible by reducing the holding time between passes, the addition of Nb also appears as an alternative since it has been reported that Nb can retard significantly the reversion of ferrite [68].

There is still polemic about the formation mechanism of the dynamically transformed ferrite, in fact, there is not even a unified criterion to classify and name such transformation. Beladi et al [71], used the term "dynamic strain induced transformation" (DSIT) to call the dynamic ferrite transformed at temperatures between the Ae_3 and Ar_3. On the other hand, expression "dynamic transformation" (DT) has been extensively used in numerous publications to refer to the Widmanstätten ferrite transformation that occurs above the Ae_3 [61], [66], [72]. However, it is likely that DSIT and DT might be governed by the same transformation mechanism, but there is not enough research to confirm it so far. Ghosh et al [73], highlighted the similarities existing between DSIT and DT in a review of diverse investigations, the gaps in the research to demonstrate that both mechanisms might be very similar, seem to narrow as shown in Table 3.

In the current work, the acronym DIFT was adopted after Dong et al [54], [60], to name in the same manner the ferrite transformation in both ranges of temperatures, i.e. above the Ae_3 and between the Ae_3 and Ar_3.

Table 3. Similarities between DSIT and DT, and knowledge gaps to validate whether both transformations follow the same mechanism.

	DSIT (Between the Ar_3 and the Ae_3)	**DT (Above the Ae_3)**	**Knowledge gap**
Transformation mechanism	Diffusion-controlled [59], [74]	Displacive, although carbon diffusion is also involved the in transformation [63], [75]	During the DT there is not partitioning of substitutional elements between ferrite and austenite, determining if partitioning occurs during DSIT would validate that both processes are displacive.
			The Kurdjumov–Sachs (K–S) orientation relationships (OR) are conserved between ferrite and the parent austenite in DSIT [76] (which also suggests that the transformation is displacive). A validation that the same OR are obeyed between DT ferrite and the parent austenite would demonstrate the similarity between DT and DSIT.
Morphology of ferrite	Polygonal grains	Widmanstätten ferrite plates that then coalesce and evolve into polygonal grains [61], [63], [72]	Most of the experiments that demonstrated the presence of DSIT ferrite were carried out at large strains, thus, there is scarce evidence available about the early stages of the transformation. Experiments at low strains below the Ae_3 might demonstrate whether the formation and coalescence of Widmanstätten plates also occur at DSIT conditions.
Flow curves	No correlations with DSIT reported	Exhibit softening during deformation due to the DT of ferrite. The curves have been used to determine the critical strain for DT using the double differentiation method.	The procedure to obtain the critical strain for DT is also applicable for DSIT, the estimation of the critical strain for DSIT would reveal if the mechanisms are similar or not.

Chapter 3. Experimental procedure and methods

3.1. Material

An API X80 steel grade was used for the experiments of this research project, real sections of a finished pipe (from the West-East II China high pressure pipeline) with a wall thickness of 12 mm were provided by Companhia Brasileira de Metalurgia e Mineração (CBMM). The material analysed is an High Temperature Processing (HTP) concept steel and the chemical composition reported by the manufacturer is shown in Table 4.

Table 4 Chemical composition (wt%) of the linepipe steel.

C	Mn	Si	S	P	Nb	Cr	Ni	Cu	Ti	N
0.045	1.43	0.14	0.003	0.01	0.09	0.21	0.12	0.21	0.01	0.0039

3.2. Austenitising heat treatment

Before thermomechanical testing, the steel sections underwent an austenitising heat treatment at 1300°C with a holding time of 2 hours and then were rapidly quenched in cold water. The objective of the heat treatment was to dissolve the niobium precipitates existing in the steel plate in order to exploit the benefits of niobium as a solute element during the deformation tests, the heat treatment also erased the thermomechanical history of the steel sections. The dissolution temperature of Nb was calculated using the solubility product of Equation 3.1, such equation is suitable to use for the current chemical composition of the samples due to low levels of nitrogen in the HTP alloy [38]. According to the Nb and C contents, the lowest temperature required to fully dissolve the NbC is 1232°C.

$$log[Nb][C] = 2.06 - \frac{6700}{T} \quad (3.1)$$

3.3. Estimation of the temperatures A_{e3} and A_{r3}.

The critical temperatures A_{e3} and A_{r3} were estimated so as to select the deformation temperatures for the thermomechanical testing presented in Section 3.4.1 and Section 3.4.2. The equilibrium temperature Ae_3, defined as the highest temperature at which austenite and ferrite can coexist in equilibrium [77], was calculated with the software JMatPro 7.0 [78] using the chemical composition of the HTP alloy and the resulting value was 849.5°C. The Ar_3, defined as the start temperature of the transformation from austenite to ferrite on continuous cooling, was estimated by dilatometry in an induction coil dilatometer model thermos-conductor simulator UT2-250. Cylindrical samples with a length 150 mm and a diameter of 15 mm were machined and drilled at the half of its length to form a hole of about 6 mm of depth and 1 mm of diameter, then, a K-type thermocouple was welded within the hole in order to measure the temperature from the bulk of the sample. The samples were continuously heated in the induction coil dilatometer at a rate of 10 °C/s from room temperature to 1000°C, then held 2 minutes for homogenisation, and finally cooled down to room temperature at a rate of 10 °C/s. The temperature and sample dilatation (strain) were recorded every second, and the Ar_3 was determined from the change in the slope of strain versus temperature plot shown in Figure 23. The average value of the A_{r3} was 680°C after testing two samples that showed good repeatability.

It is important to mention that the expected microstructure in the HTP steel alloy used in this work obtained at a cooling rate of 10°C/s is primarily bainite as reported in a previous work [79], therefore the main transformation occurs at the temperature Bs (bainite starts) at around 625°C, however, the dilatometric diagram shows a subtle change at 680°C which allowed for the detection of A_{r3}.

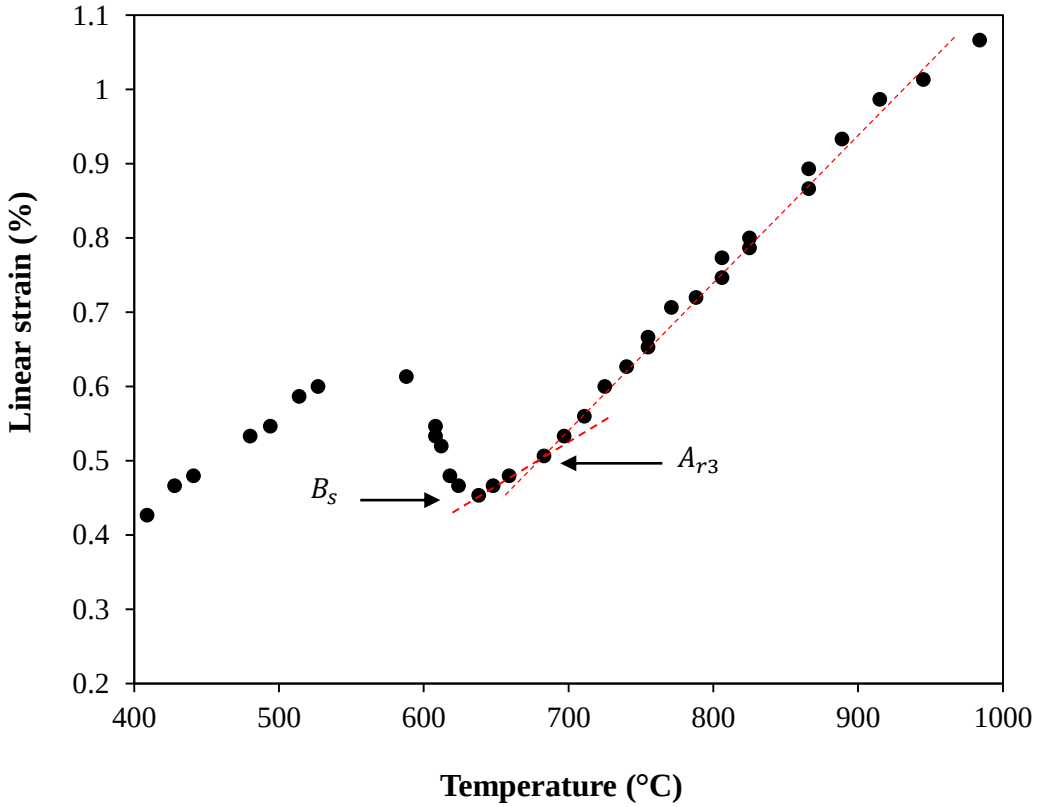

Figure 23. Cooling dilatometric curves showing the linear strain (dilatation) in the sample as a function of the temperature.

3.4. Thermomechanical testing

In order to simulate the hot rolling of the HTP alloy in different thermomechanical controlled processing (TMCP) schemes, a series of plane strain compression (PSC) tests in specimens with standard dimensions (10x30x60 mm) were conducted at diverse temperatures in the austenite phase. The tests were performed in a servo-hydraulic Thermomechanical Compression (TMC) machine in accordance to the God Practice Guide for Hot (isothermal) Plane Strain Compression Test [80]. The technical capabilities of the TMC machine are summarised in Table 5 and an schematic representation of the PSC test is illustrated in Figure 24.

Table 5. Main features of the servo-hydraulic Thermomechanical Compression machine.

	Machine characteristics
Actuators	Servo-hydraulic
Maximum strain	~2
Maximum strain rate	150 - 200 1/s
Maximum deformation temperature	1200°C
Maximum load	500 kN
Machine Stiffness	410 kN/mm
Maximum FTTU reheating temperature	1300°C
Full quench start time	< 0.5 second from the end of derformation
Controllable cooling variables	Forced air, mist and water quench
Reheating rate	Rapid and controlled heating (up to 1300°C)
Atmosphere control	None (natural air)
Temperature measurement	Up to 3 thermocouples inside in the PSC specimen

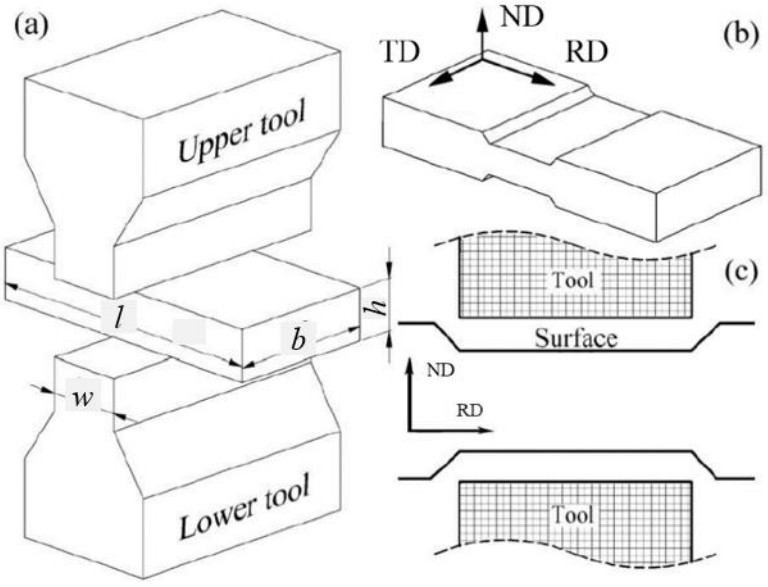

Figure 24. Schematic representation of the plain strain compression test, a) position of the tools and the specimen (*l*, *b* and *h* are the length, breadth and height of the testpiece respectively and *w* is the platen width), b) testpiece after the deformation and c) plane of interest for all the microstructural characterisation (Normal direction – Rolling direction) [81].

The equivalent true strains and equivalent stress during the PSC tests were calculated using the expressions 3.2 and 3.3 respectively [80]:

$$\bar{\varepsilon} = \frac{2}{\sqrt{3}}(\varepsilon_2^2 + \varepsilon_2\varepsilon_3 + \varepsilon_3^2)^{\frac{1}{2}} \quad (3.2)$$

where ε_3=ln(h/h$_o$) and ε_2=ln(b/b$_o$)

$$\bar{\sigma} = \bar{\boldsymbol{p}}/(f_1(\mu).f) \quad (3.3)$$

where $f_1(\mu)$ and f are correction factors for friction and for effective stress respectively, and $\bar{\boldsymbol{p}}$ is the pressure defined as the Force, *F*, at any time during the test divided by the cross sectional area, A, of the testpiece at any instant of time.

$$\bar{\boldsymbol{p}} = F/wb \quad (3.4)$$

The simulations consisted of combinations of different rolling variables (strains, interpass times, deformation temperatures, number of passes and cooling rates), the values for each variable are adequate to realistically simulate the TMCP of steel in a plate-mill. In general, the true strains applied in each pass during rough or finish rolling in a plate-mill can vary from 0.05 to 0.35 and the strain rates can go from 1 to 40 s^{-1}, the latter is not constant during the period of a hot reduction and usually decreases with the progress of deformation [82]. The number of passes depends on the percentage of reduction pursued in final thickness of the plates, and the deformations are performed in different ranges of temperatures according to the stage of the process; during rough rolling the deformations are carried out at high temperatures above the non-recrystallisation temperature of austenite ($T_{95\%}$ or also called T_{nr}), the objective in this stage of the process is to apply relatively large reductions at temperatures in which the deformed austenite recrystallises completely between the rolling passes, such recrystallisation leads to austenite grain refinement. Conversely, during finish rolling smaller reductions (per pass) are applied to the steel plates until the final thickness and length are achieved, the passes are executed at lower temperatures in order to prevent the recrystallisation of austenite, after finish rolling the austenite ends in "pancake" shape, i.e. deformed and elongated along the rolling direction.

In the TMCP of steel plates for welded linepipe steel grades (such as the X80 HTP) an accepted industrial practice is to perform rough rolling with reductions between 20 to 35% per pass at temperatures above 1070°C, the deformation can accumulate up to 60% of reduction depending on the number of passes. Then, after rough rolling the slabs are transferred to the finish rolling mill where the passes are commonly executed with gradually decreasing reductions per pass from 40% to 10% within a temperature window that ranges from 50~100°C below the $T_{95\%}$ to 20~70°C above the Ar_3, generally the accumulated reduction during finish rolling can be as much or even more than 70% [83], [84].

Based on the industrial practices to manufacture linepipe steels through TMCP, the rough rolling was simulated performing a single pass at an equivalent strain of 0.30 and 1100°C, whereas the finish rolling simulation consisted of various passes at a constant strain of 0.22 at 810°C and 950°C, after each finishing pass an isothermal holding time of 10 seconds was added in order to allow time for the strain induced precipitation of Niobium. The holding time of the simulation matches well with the interpass times used during the finish rolling in plate-mills, which commonly range from 8 to 20 s [82], [85].

3.4.1. Rough rolling simulation

A schematic representation of the rough rolling simulation is shown in Figure 25, samples were heated to 1200°C at a rate of 10°C/s, held 2 minutes for equilibration, then cooled at a rate of 10 °C/s to five different deformation temperatures, after which a strain of 0.3 was applied to each sample at a constant true strain rate of $10s^{-1}$. After deformation, the samples were immediately quenched in cold water to room temperature.

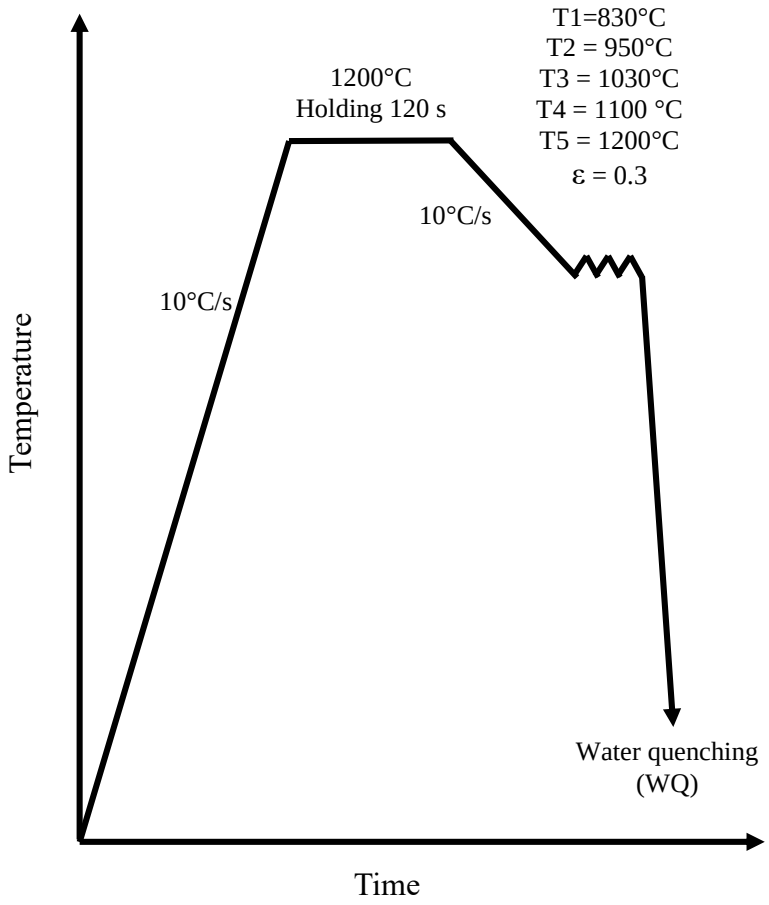

Figure 25. Experimental design to simulate rough rolling.

The temperatures for the rough rolling simulation were selected to deform the material in the following conditions:

i) at 830°C in the metastable austenite region above Ar_3 but 20°C below equilibrium temperature Ae_3.

ii) in the austenitic region below the recrystallisation-stop temperature ($T_{5\%}$) at 950°C.

iii) in the partial recrystallisation zone between $T_{5\%}$ and the full recrystallisation temperature ($T_{95\%}$) at 1030°C, and

iv) in the fully recrystallised austenite at 1100°C and 1200°C. Two temperatures were chosen in this region to compare the effect of temperature on the prior austenite grain size.

The temperatures $T_{5\%}$ and $T_{95\%}$ were extracted from the Precipitation-Time-Temperature diagram constructed for the HTP alloy (details in Section 4.3). For a strain of 0.30 and a holding time of one second (approximate delay between the deformation and quenching), $T_{5\%}$ and $T_{95\%}$ were 1020°C and 1080°C respectively.

Although the rough rolling temperatures of interest for industrial applications are above the full recrystallisation temperature (at 1100°C and 1200°C), simulations in the non-recrystallisation and partial recrystallisation zones were performed merely for research purposes so as to understand the dynamic transformations (DIFT and DRX) in the HTP alloy.

3.4.2. Finish rolling simulations

Two TMCP simulations were carried out in order to study the microstructural evolution of the HTP alloy deformed in multiple finishing passes at different temperatures. Both simulations included the same initial rough deformation pass at 1100°C and a strain of 0.3, the conditions for the rough deformation were selected based on the results obtained in Chapter 4, in which it was shown that a single deformation at 1100°C led to significant austenite grain refinement due to recrystallisation. After the rough deformation, finishing passes were added at 950°C (simulation A) and 810°C (simulation B), at a strain of 0.22 followed by isothermal holding times of 10 seconds. The simulation at 950°C, was carried out so as to simulate the industrial high temperature processing of the HTP steel alloy, the deformation is performed 30°C below the beginning of the recrystallisation but 100°C above the critical temperature Ae_3. Whereas in the simulation at 810°C, the finish deformation is carried out in the metastable austenite region 40°C below the Ae_3 but 30°C above the Ar_3. Note that the Ar_3 temperature was obtained by dilatometry in undeformed austenite at a cooling rate of 10°C/s, such conditions are analogous to those present after the rough deformation, during the cooling of the specimens to the finishing temperatures.

The parameters used in simulation A and the testing sequence are illustrated in Figure 26, after the rough deformation at 1100°C specimens were cooled down at a rate of 10°C/s to 950°C to be deformed in three passes at a strain of 0.22 and a constant strain rate of $10s^{-1}$. Holding times of 10 seconds were added after each finishing pass. After each deformation pass or holding

time, the specimens were quenched in cold water to analyse the microstructure. An additional specimen was deformed in a single finishing pass at a strain ε_5=0.66 to serve as reference for the calculation of the fractional softening of the microstructure during the finish rolling, this test is called “monotonic finishing test”.

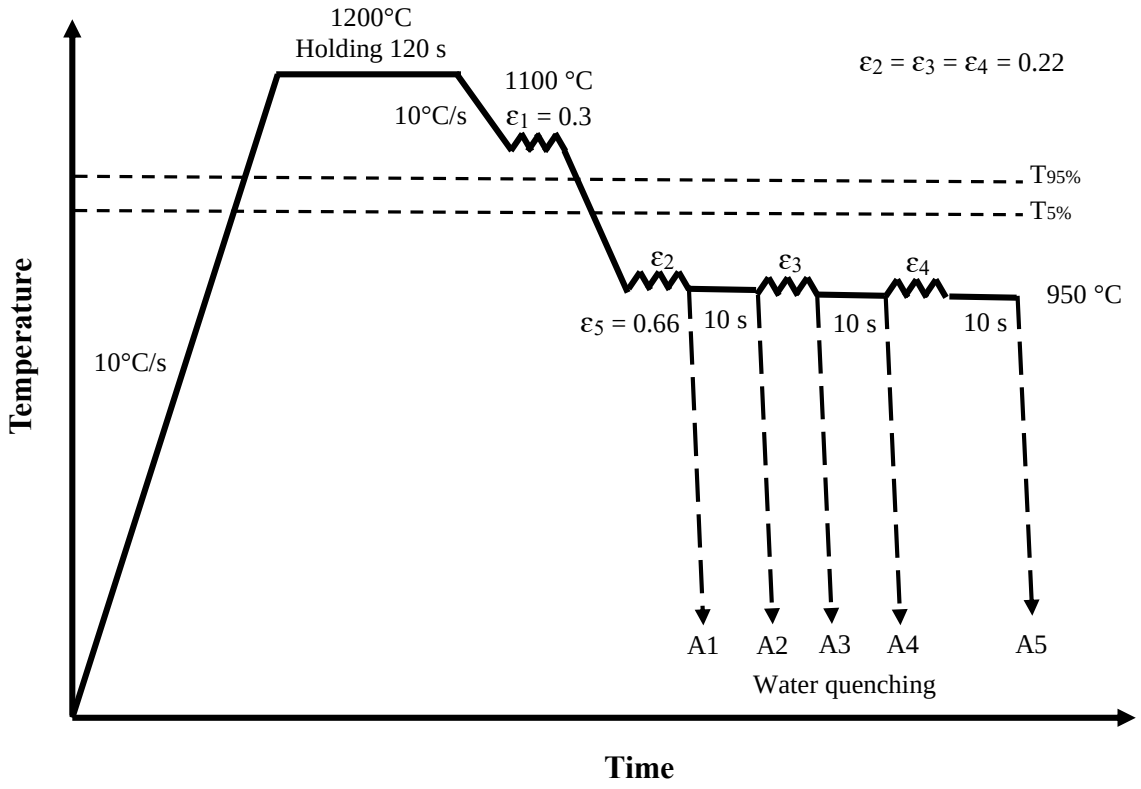

Figure 26. Testing sequence for the finishing simulation at 950°C. The specimens were labelled with the letter A in a consecutive order as the simulation progressed.

To ensure that the finish deformation is performed below the recrystallisation temperature (at least in the first finishing pass), Dutta, Palmiere & Sellars’ model [36], [86] was used to calculate the recrystallisation stop temperature ($T_{5\%}$). For a single pass, a strain of 0.22 and a grain size of 25 μm (resulting from the rough deformation), the $T_{5\%}$ was 974°C. Finishing passes followed by holding times were added to the TMCP simulation until evident recrystallisation happened (based on PAGs observations), after the holding time of the third finishing pass 20% of the microstructure was recrystallised, thus the TMCP consisted of only 3 finishing passes at 950°C. One of the purposes of the simulation A, was to find the number

of finishing passes at 950°C that the HTP allow can withstand without presenting significant recrystallisation.

As for the simulation at 810°C, the test sequence was the same as that for 950°C, however, only two finishing passes were considered since the scope of this simulation is to study primarily the DIFT at a temperature between the Ae_3 and the Ar_3. The strain induced precipitation of Nb was not studied in this simulation, since, it is predictable to have a superior SIP at 810°C than at 950°C due to the higher supersaturation of Nb at lower temperatures. Figure 27 schematises the sequence of the simulation at 810°C.

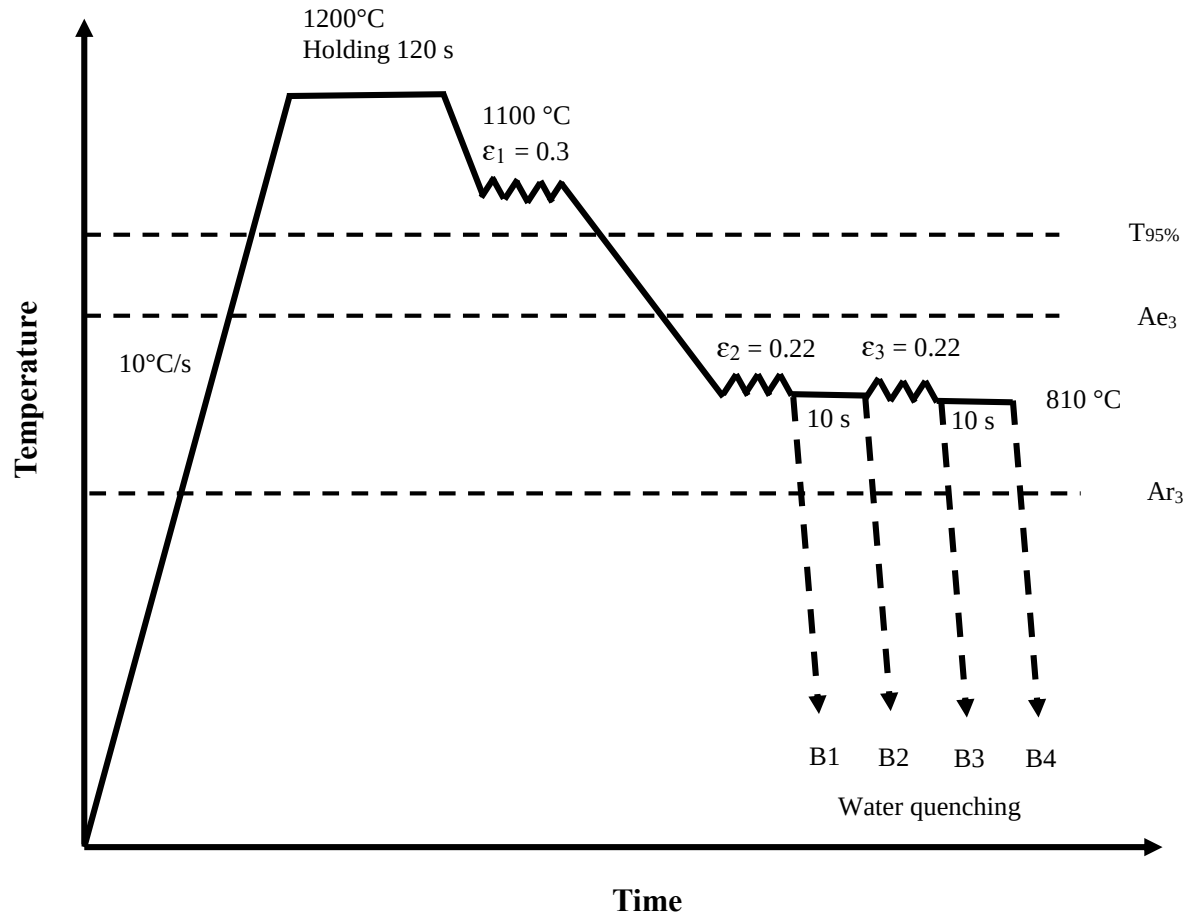

Figure 27. Testing sequence for the finishing simulation at 810°C.

3.5. Sample preparation

The deformed PSC specimens were sectioned in the rolling plane (ND-RD shown in Figure 24) and mounted in conductive Bakelite for automatic preparation in a grinder-polisher machine. The surface of interest was successively grinded using 120, 220, 320, 600 and 1200 grit silicon carbide papers and water was applied to provide lubrication. Final polishing was carried out with two monocrystalline diamond suspensions of 3 μm and 1 μm until visible scratches were removed and a mirror-like finish was achieved.

3.6. Prior austenite grain boundaries (PAGBs) analysis

PAGBs were revealed in order to observe the morphology of the prior austenite grains at each stage of the TMCP simulations. Polished samples were etched between 1 and 3 minutes in a saturated aqueous picric acid solution at 80°C until PAGBs were revealed, the solution was prepared with 100 ml of distilled water, 1.5 gr of Sodium dodecyl sulphate as a surfactant and 5 to 7 drops of HCl. The PAGBs were observed in a Nikon Eclipse LV150 optical microscope and the average grain size was measured using the linear intercept method with ASTM E-112 [87]. Due to the low carbon and low phosphorus of the HTP steel, the etching of PAGBs turns out to be very laborious, the immersion times to reveal the grain boundaries can vary importantly from sample to sample. It is recommendable to observe the progression of the etching in intervals of 30 seconds after the first minute of immersion to avoid overetching and subsequent rework.

3.7. Metallography

Traditional metallographic methods were used so as to observe the microstructure of the material after each test. Samples were polished and then immersed around 15 seconds in 2% Nital solution until the steel phases were clearly revealed. The microstructure was observed with optical microscopy up to 1000x magnification.

3.8. Scanning Electron Microscopy (SEM)

In order to observe micrometric phases in the microstructure that cannot be resolved in light microscopy, secondary electrons imaging was carried out in scanning electron microscopy. Samples were polished and etched with Nital 2% and observed in FEI Inspect F and FEI Inspect F50 instruments at a voltage of 20kV and magnifications between 2000x and 10,000x.

3.8.1. Electron backscattering diffraction (EBSD) analysis

EBSD analysis was performed in order to study the crystal lattice orientation and microtexture of selected PSC specimens, this technique is able to perform orientation mapping over large areas automatically which makes it very suitable for microstructural analysis of deformed materials. In the current work, the lattice misorientation was analysed in detail so as to elucidate the morphology and transformation mechanism of DIFT, besides, the separation of ferrite from martensite in the multiphase microstructures was achieved using the relative quality of the EBSD pattern. The latter analysis is one of main advantages of EBSD compared to other characterisation techniques, ferrite and martensite tend to show very different contrast in the pattern quality (PQ) maps making possible the separation and quantification of phases [88], [89].

Specimens were prepared as described in Section 3.5, however, a meticulous polishing from 15 to 30 minutes with 0.06 μm colloidal silica was added to the procedure to improve surface quality, the colloidal silica absorbed on the polished surface was removed with an ultrasonic cleaning for at least 30 minutes. The analysis was conducted in a FEI inspect F50 microscope with an accelerating voltage of 20kV, a working distance of 152.4 mm and the specimen tilted around RD to 70° to the horizontal plane. For microtexture and grain misorientation analysis a step size of one-tenth of the average grain size is frequently used [90], thus, the sample with the coarse microstructure obtained after the austenitising heat treatment was analysed with a step size of 1 μm, whereas, the specimens with deformed and unrecrystallised austenite were scanned with step sizes of 0.2 μm and 0.1μm. The indexing rate in most of the analysis was moderately steady and ranged from 80 to 86%. The EBSD data was post-processed and analysed in the HKL Chanel 5 Flamenco Package.

3.9. Transmission Electron Microscopy (TEM)

Various TEM instruments were used in order to observe and analyse the individual phases in the steel and the nanometric precipitates, Table 6 shows the TEMs used and the analysis carried out in them. Bright field (BF) imaging was performed up to 1 million magnifications and the chemical analysis was performed with energy-dispersive X-Ray spectroscopy (EDS) in standard mode and in scanning transmission electron microscopy (STEM) mode.

Table 6. TEMs and techniques used to analyse the microstructure of the steel phases and the precipitates.

Microscope	Voltage (kV)	Techniques	Magnifications
Phillips 420	120	BF imaging	Up to 300Kx
Tecnai 20	200	BF imaging	Up to 300Kx
JEOL R005	300	High resolution TEM (HRTEM), BF imaging and EDS	Up to 500Kx
JEOL JEM-200	200	High resolution TEM (HRTEM), BF imaging, EDS and STEM	Up to 1 Million x

3.9.1. Carbon extraction replicas

With the objective of doing statistical analysis of the size and distribution of SIP in the microstructure in the different simulations, carbon extraction replicas were prepared. In this technique, a substrate of carbon extracts the precipitates embedded on steel matrix producing a replica that contains the precipitates formerly located on the steel sample. Since the carbon replica is thin and amorphous, the former distribution and shape of the precipitates on the steel can be promptly observed without interference from electron scattering. This replication method allows for more accurate statistical analysis of the precipitates formed in the steel matrix.

Figure 28 illustrates the process to make extraction replicas. A substrate of carbon is applied on the steel sample surface, then, the steel sample with the carbon layer is etched with acid

causing the dissolution of the underlying steel, and finally, during the etching the carbon film floats off and extracts the precipitates from the steel [91].

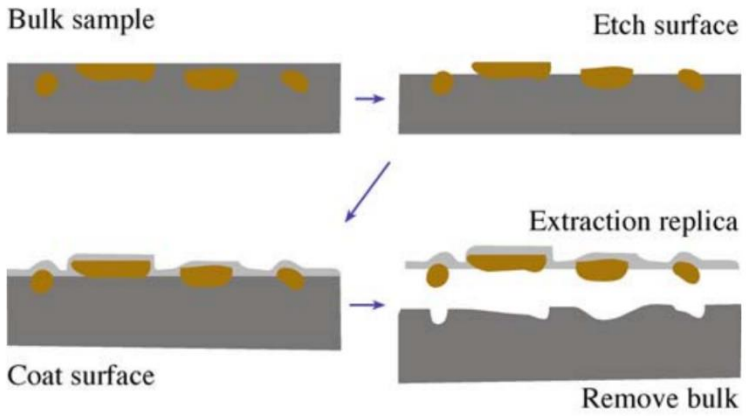

Figure 28. Illustration of the process to make carbon extraction replicas. Particles embedded in the steel are revealed by etching with Nital 2% which leaves the particles exposed on the surface, then a carbon film is evaporated over the surface and finally the acid dissolves the steel surface leaving the particles adhering to the carbon film [91].

The carbon extraction replicas were prepared with the following methodology. Samples were polished as described in Section 3.5 and slightly etched in Nital 2% to expose the precipitates on the surface. The carbon substrate was deposited over the steel surface by a high vacuum carbon coating devise, then a grid was made manually in the area of interest with a scalpel to produce squares of around 1x1 mm. The coated samples were etched in a solution of Nital 10% until the carbon film started to detach, then the etched samples were immersed in isopropanol to leave the replicas float away. Finally, the replicas were collected with 400 mesh cupper grids and dried for further analysis in TEM.

The replicas were observed at high magnifications in TEM and images were taken at random positions, then, a minimum of 3 images at the same magnification were post-processed and analysed using the software ImageJ to obtain statistics about the precipitates. Figure 29 shows an example of the features that were considered as precipitates for the statistical analysis.

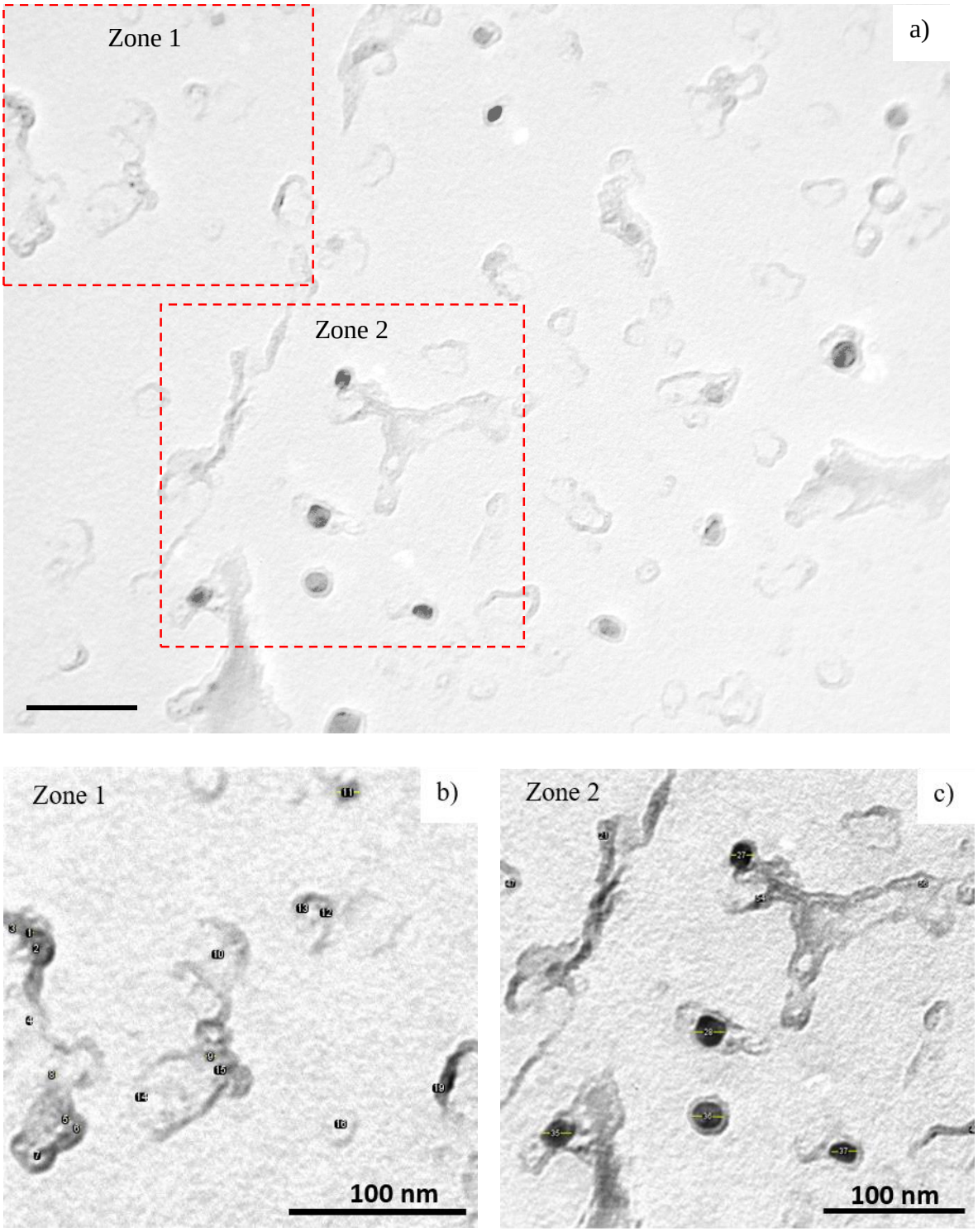

Figure 29. Example of the features classified as precipitates for the statistical analysis of particles. a) TEM image at 105000x showing the presence of strain induced precipitates, b) and c) segments of the image post processed in the software ImageJ displaying the particles considered for the analysis.

3.9.2. Thin foils

Thin foils were prepared in order to observe the nanometric precipitates and the individual steel phases present in the steel at very high magnifications in TEM, this analysis is fundamental to study the morphology and the transformation mechanism of DIFT, for Widmanstätten ferrite laths, micrometric grains, dislocations and carbides can be observed in great detail in dark field imaging.

For the preparation of thin foils, specimens were sectioned in the rolling plane to obtain sheets with a thickness of around 1 mm, then the sheets were ground down to approximately 400 µm with 120 and 220 grit silicon carbide grinding papers until a smooth and flat surface was achieved. The preliminary sheets were punched to make 3 mm diameter disks, then the disks were thinned to around 60 - 80 µm with 360 and 600 grit grinding papers. Finally, the discs were perforated electrolitically (without mechanical deformation) in a TenuPol-5 twin-jet automatic electropolisher using an electrolytic solution that contained 5% perchloric acid, 35% butoxyethanol and 60% methanol at -40°C and a voltage from 30 to 32 mA.

3.10. X-Rays diffraction

X-Ray diffraction analysis was carried out using a Bruker D2 Phaser diffractometer with CuK_{α} radiation (1.5406Å). A 2θ range from 30° to 120, step size 0.2 and a voltage of 30 kV were selected for the analysis. Two specimens were analysed; a) the sample after the austenitising heat treatment and b) a sample deformed to an accumulated strain of 1.2. The objective in this analysis was to measure the lattice length in specimens with very different microstructural characteristics. The microstructure of the sample with the austenitising heat treatment consisted of an untempered martensite with a body centred tetragonal (bct) lattice and carbon in solid solution, whereas the microstructure of the second sample with extensive deformation, showed a mixture of martensite, DIFT and cementite, these last two microstructures have body centred cubic (bcc) and orthorhombic lattices respectively. Significant differences in the lattice parameters between the bcc and bct crystal structures can considerably ease the separation of phases in EBSD in microstructures containing both ferrite and martensite

3.11. Nanohardness and contact scanning probe microscopy (SPM)

Nanohardness tests and SPM were performed so as to identify and quantify the DIFT present in the microstructures. Most of the deformed samples showed a microstructure that consisted of a combination of DIFT and martensite, the separation and quantification of such phases represent a real challenge using the methods known nowadays, i.e. metallographic methods and EBSD maps, since their accuracy is quite debatable. In the current work, SPM was used in order to map the topography of the different phases of the microstructure, then, nanoindentation was conducted to evaluate the nanohardness in each phase, a detailed description of the methodology used in this research to identify and quantify DIFT is presented in the following Section 3.11.1.

Both the nanohardness test and SPM were performed in a Hysitron TI Premier with a Berkovich indenter which operates at a normal load range from 75 nN to 30 mN and has a depth resolution of 0.2 nm. Samples were prepared as described in Section 3.5, and then electro-etched following the standard guide for electrolytic polishing of metallographic specimens ASTM E1558 [92]. A solution containing 6% perchloric acid, 14% distilled water and 80% ethanol (formula I1 ASTM E1558) at room temperature was used as electrolyte, the electrolysis cell was set in and electrolytic polishing and etching machine table that operates with controlled power supply. The samples were immersed in intervals from 10 to 20 seconds in the in the electrolytic cell using a voltage from 10 to 15V until the microstructure was slightly observed in optical microscopy as shown in Figure 30. The objective of electrolytic etching was to remove work hardened layer on the surface caused by the sample preparation, very slight disturbances or cold work on the surface can lead to large variations in the nanohardness results, the electrolytic etching of the specimens is essential to measure the hardness when very low loads are used in the test. Several attempts were carried out to evaluate the nanohardness of specimens etched with 2% Nital (at least 200 indents were performed per specimen), however, the results showed unrealistic hardness distributions in all the cases.

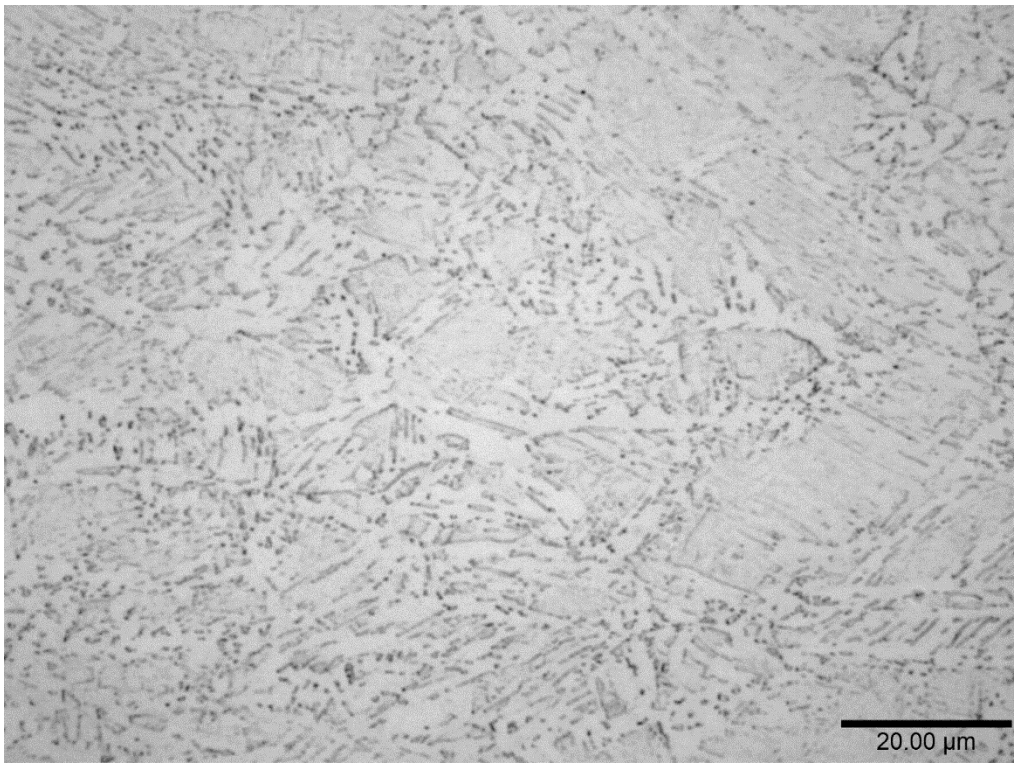

Figure 30. Microstructure observed in optical microscope after electrolytic etching.

The topography and surface gradient of the etched samples were observed in real time in SPM by reverse and forward scans at a scan rate of 0.5 and 1 Hertz, then, specific positions were chosen to perform indents to obtain the hardness in individual phases. Since the ultrafine ferrite is reported to have a grain size from around 1 to 2 µm [20], a low load of 500 µm was used to ensure that the indentation mark do not go beyond the grain boundaries of a single ferrite grain of 1 µm diameter. Load and displacement curves were obtained for each indent and the nanohardness was calculated using the area functions proposed by Oliver et al [93].

3.11.1. Validation and quantification of DIFT.

The specimen B4 of Figure 27 was chosen to validate the presence of DIFT, such specimen was deformed in two finishing passes at 810°C (above Ar_3 but below Ae_3) applying a strain of 0.22, at such deformation conditions the DIFT is very predictable in the microstructure. The specimen was prepared as described in Section 3.11 and SPM imaging and Nanohardness indents were carried out in regions with different morphology to identify the DIFT.

In SPM the DIFT was observed as a micrometric phase with a higher surface relief as shown in Figure 31 a-c), 15 indents were performed on DIF grains and the hardness ranged from 1.41 to 2.7 GPa with an average of 2.0 GPa. Figure 32 illustrates the similarities in the size and distribution of DIFT between SPM and optical microscopy.

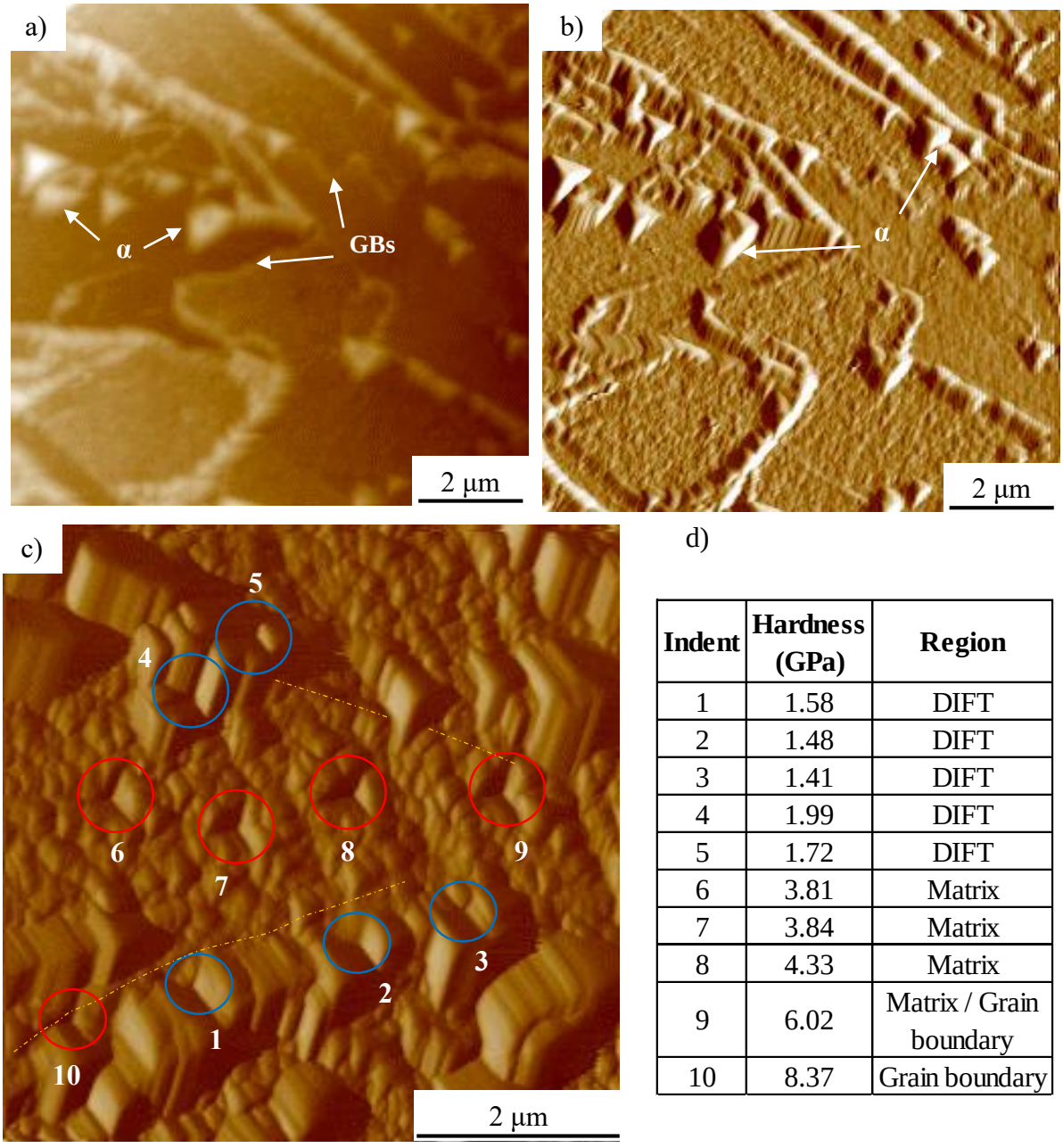

d)

Indent	Hardness (GPa)	Region
1	1.58	DIFT
2	1.48	DIFT
3	1.41	DIFT
4	1.99	DIFT
5	1.72	DIFT
6	3.81	Matrix
7	3.84	Matrix
8	4.33	Matrix
9	6.02	Matrix / Grain boundary
10	8.37	Grain boundary

Figure 31. Validation of DIFT by SPM and nanohardness. Forward topographic a) and gradient b) images showing the presence of DIFT and grain boundaries (GBs). Reverse gradient image c) showing the indents in the ferrite grains (blue circles), grain boundaries (yellow dashed arrows) and matrix (red circles) and their respective Nanohardness values d).

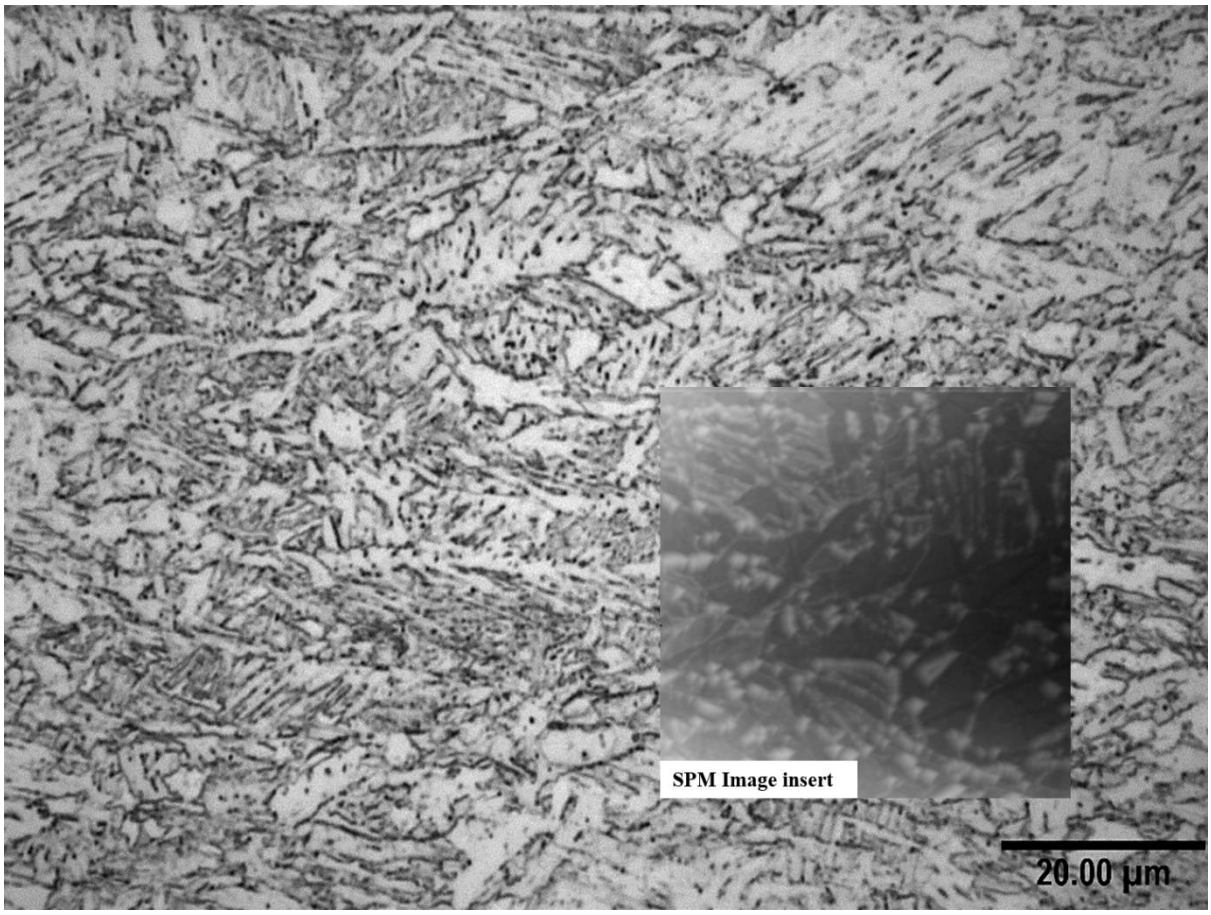

Figure 32. Comparison between the SPM and optical microscopy showing the similarities in the size and distribution of DIFT.

It is important to mention that the morphology of the ferrite grains observed in the SPM images is affected by a phenomenon known as tip convolution or tip imaging, this inaccuracy in the topographic mapping is common in SPM imaging when the features are very small and tip is very blunt (as the Berkovich tip is) [94], this explains why DIFT grains images do not show a clear polygonal shape and instead, show shapes influenced by the Berkovich tip. The tip convolution was greater in larger ferrite grains due to the higher surface height.

Figure 33 shows how the aspect of a grain of ultrafine ferrite is affected by the convolution effect in SPM imaging. As the Berkovich tip moves across the ferrite grain, the sides of the tip come into contact with the grain sooner than the apex of the tip, thus, the real tip-grain contact occurs on the tip side and not at the tip apex as shown in Figure 33 a). Since the detector and feedback system respond to the tip-sample contact, the *x* and *y* dimensions of the grain are

broadened and consequently, the feature shows a shape highly influenced by the tip geometry as shown in the ferrite grain depicted in Figure 33 b).

a)

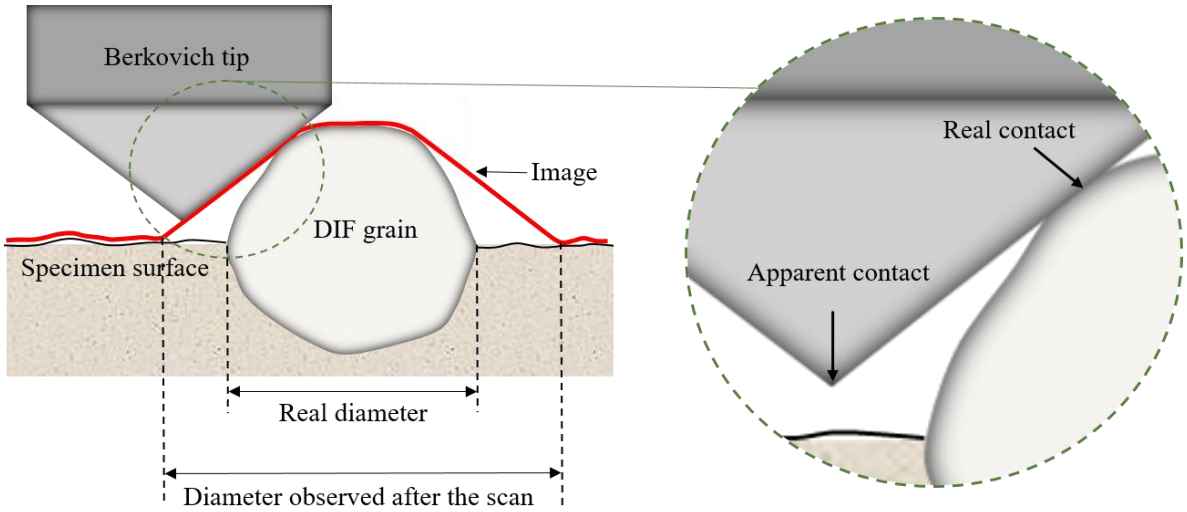

b)

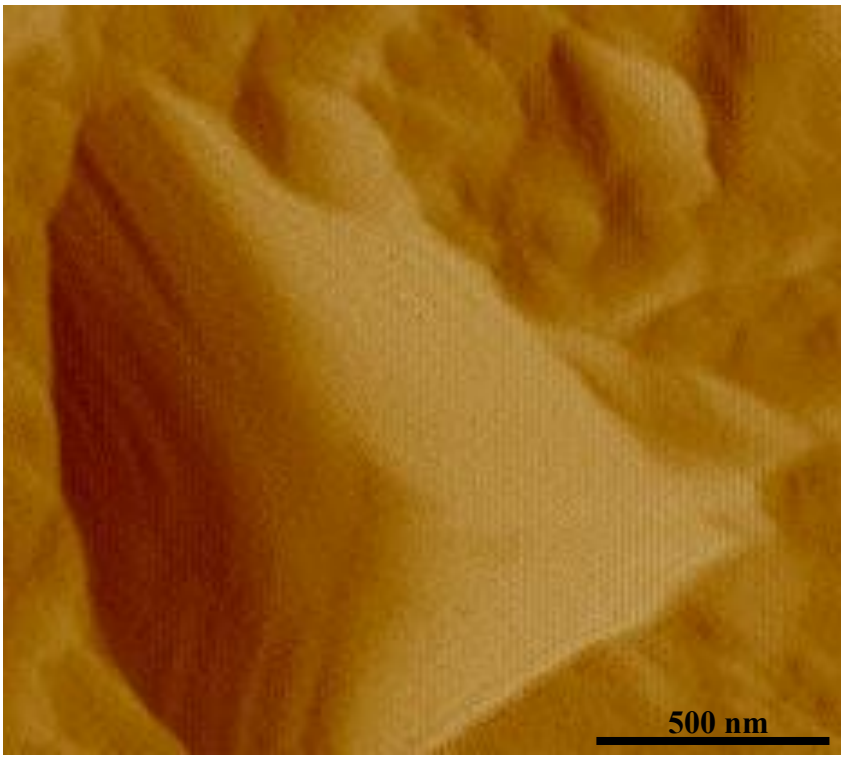

Figure 33. Tip convolution effect in contact-SPM imaging. a) Illustration of convolution between the Berkovich tip and a grain of ultrafine ferrite, b) SPM topographic image showing the appearance of a ferrite grain affected by the convolution.

As for the quantification of the volume fraction of DIFT, a minimum of 3 images of 40 x 40 μm were obtained in different regions of the area of interest and then post-processed in the software Hysitron TriboView as shown in Figure 34. Finally, the software ImageJ was used to estimate the area fraction which is equal to the volume fraction on a two dimensional cross section by stereological relation [95], [96].

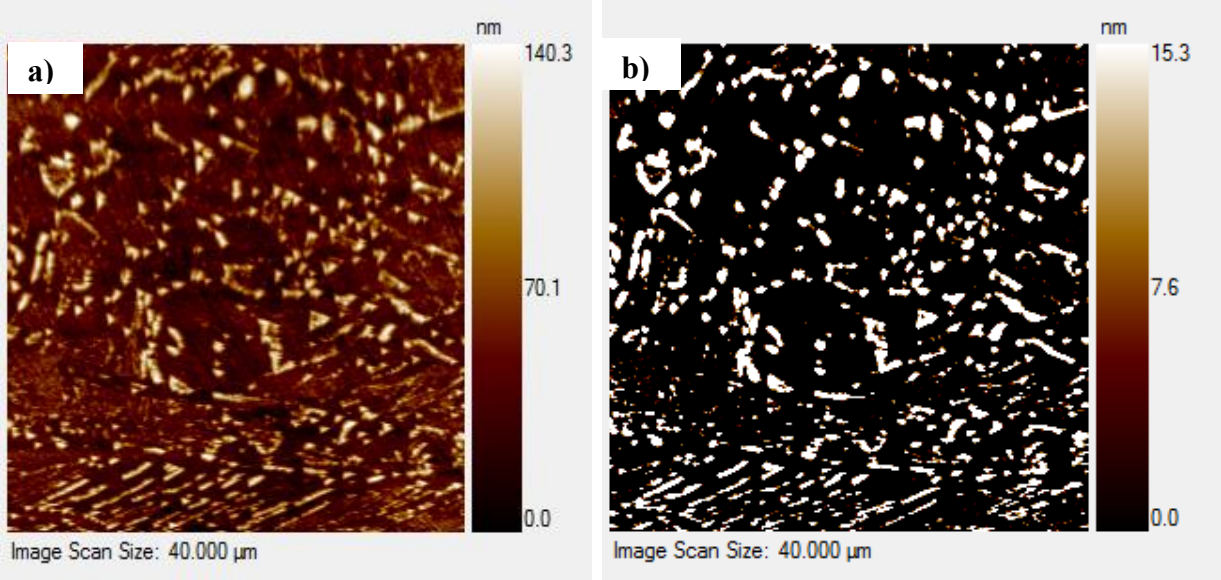

Figure 34. SPM images post-processing for the estimation of area fraction of DIFT. a) Forward Topographic scan with background extracted by linear regression and b) change in the height scale to separate DIFT from the matrix. The area fraction estimated with ImageJ was 18.9%.

It is important to mention that the estimated volume fraction of DIFT using this methodology might be just slightly different to the real volume fraction. The estimation implies the discrimination of a thin layer of around 10 to 20 nm of surface height in the SPM images in order to produce the contrast shown in Figure 34, such discrimination eliminates part of the convolution in the grains and consequently reduces the error in the quantification. Therefore, in microstructures with ultrafine ferrite grains where the convolution effect is minor, the estimation of DIFT tends to be more accurate.

An outstanding microstructural characterisation can be achieved with the use of nanoindentation and SPM, the topography and nanohardness of individual microconstituents

can be obtained allowing for the identification and quantification of the steel phases. Both techniques possess high sensitivity and are able to analyse very small features such as the ultrafine ferrite, however, it is important to take into account some drawbacks in the operation and precision of the nanoindentation/SPM instruments.

Modern SPMs can have very high sensitivity and operate at extreme magnifications ranging from 10^3 to 10^9 in the x, y and z directions, besides, exceptional resolutions of less than 0.1 nm can be achieved in contact mode [97]. However, the tip convolution can substantially affect the imaging of small features and lead to significant imprecisions in the measurement of the size of the particles, for instance, DIFT grains appear evidently affected by the tip convolution in the SPM images as showed in Figure 33 b), thus, estimations of the average grain size using SPM images would inevitably include an error since the grains appear broader than they are.

The magnitude of the error depends on the characteristics of both the tip and the feature; the larger the radius and the opening angle of the tip, the greater the convolution, and, the larger the ferrite grain size, the greater the convolution as well. The latter correlation is due to larger ferrite grains also show higher surface height and consequently are more affected by the tip convolution. A detailed analysis about the error in the measurement of the ferrite grain size is presented in Section 4.5.3, very fine ferrite grains with diameters of around 760 nm are just slightly affected by the tip convolution, it was demonstrated that such grains broaden less than 4% in the SPM images, conversely, coarser grains are substantially affected by the convolution, at least a 35% of broadening was observed in grains with diameters as of 2.8 μm.

The accuracy in the quantification of the volume fraction of DIFT using SPM imaging is strongly related to the average ferrite grain size, the finer the grain, the better the quantification. Conveniently, the hot deformation of the HTP alloy at temperatures below the initiation of the recrystallisation ($T_{5\%}$) leads the formation of fine DIFT grains of around 1 μm average diameter as reported in the Chapter 4 and Chapter 5 of this thesis. Therefore, SPM images can be used to estimate the volume fraction of DIFT grains produced during the finish rolling of the HTP alloy with reasonable accuracy.

As for the nanoindentation, typical instruments are so sensitive that they can detect very subtle changes in the operating environment such as temperature fluctuations and mechanical vibrations from the floor. The depth resolution is the most striking feature since indentations can be performed at a penetration depth as low as 0.03 nm, this permits the analysis of very small features at nanometric scale with great precision [98].

Despite the high sensitivity of the nanoindenter instrument utilised in this work (Hysitron TI Premier with a depth resolution of 0.2 nm), the nanohardness measurements performed in the ferrite grains were not useful to characterise the nanomechanical properties of such phase. Due to the electrolytic etching, ferrite grains appear as reliefs with higher heights than the martensitic matrix as showed in Figure 31, the heights of the grains ranged from around 150 to 500 nm depending on the ferrite grain size (the larger the grain the greater the height). This peculiarity in the topography of ferrite causes misleading results in nanohardness test, since the nanohardness is strongly related to the grain height and thus to ferrite grain size as well. The correlation between the grain size and the nanohardness is discussed in detail in Section 4.4.4.

However, although the nanoindentation cannot be used to obtain consistently the nanohardness of DIFT, this technique is very useful in the identification of phases, the difference in nanohardness between ferrite and martensite is huge as shown Figure 31 c) and d). Thus nanoindentation is a powerful tool to identify the ferrite by its topography, which is a tremendous advantage for the characterisation of the phases of steel phases.

3.12. Vickers Microhardness

Vickers microhardness tests were performed in order to evaluate the bulk mechanical properties in the PSC specimens. Samples were prepared as indicated in Section 513.5 and then evaluated in a Durascan 70 micro-hardness tester using a load of 1N and 15 seconds of dwelling time. At least 9 indents were carried out on the area of interest of the specimen in accordance to ASTM E384 [99].

Chapter 4. Rough rolling simulation

4.1. Introduction

This chapter is dedicated to the presentation of results and analysis of the rough rolling simulation whose main aim is to find the most suitable path to begin the austenite conditioning. The rough rolling plays a vital role in the microstructural evolution of the TMCP, the austenite grain size together with the size and distribution of precipitates after rough rolling unavoidably have a strong effect on the subsequent finish rolling. Ideally, the rough deformation ought to provide a homogeneous microstructure with the finest possible grain size, however, the deformation temperature must be high enough to prevent the use of high rolling loads which increase the production costs and cause other quality issues such as cracks and defects on the slabs. An optimal relationship between the deformation temperature and grain refinement must be pursued so as to design roughing routes able to perform large reductions that lead to extensive austenite refinement without the issues aforementioned.

In the last decades the deformation induced ferrite transformation (DIFT) during hot rolling has received increased attention due to its industrial importance, various investigations have reported the occurrence of DIFT at conventional rough rolling temperatures and TMCP simulations have shown that it is possible to design processing routes capable to retain volume fractions of ferrite from around 5 to 8% prior to finish rolling [57], [58], [69]. Tailoring the DIFT since the rough rolling stage might bring important benefits to the final microstructural refinement of the material, however, at temperatures above the Ae_3 the reversion of ferrite to austenite during the interpass times is still a challenge to overcome considering that the industrial hot rolling take place at such temperatures.

For the present chapter PSCTs were conducted at various temperatures at a strain of 0.3 and a constant rate of $10s^{-1}$, the aim of the experiments is to study the dynamic transformations (SIP, DIFT and DRX) and austenite refinement that takes place at different rough rolling conditions. The main objective is to find a deformation temperature able to provide the best microstructural characteristics for subsequent grain refinement during finish rolling, although the rolling temperatures of interest for industrial applications are above the recrystallisation temperature,

deformations in the non-recrystallisation and partial recrystallisation zones were performed merely for research purposes so as to understand the dynamic transformations (DIFT and DRX) in the HTP alloy.

4.2. Initial state of the HTP alloy prior to rough rolling

After the austenitising heat treatment, the material was characterised to study the initial state of the microstructure and precipitates prior to rough rolling. Coarse and polygonal PAGBs with an average size of 87 µm and a standard deviation of 25 µm were found as shown in Figure 35.

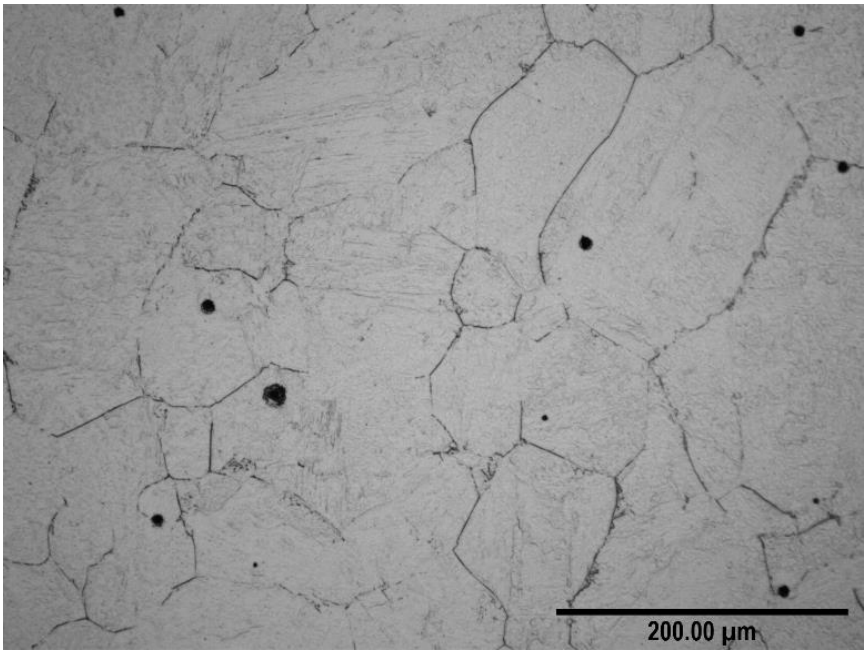

Figure 35. Prior austenite grain boundaries of the HTP alloy after the austenitising heat treatment.

The material exhibited a dominant martensitic microstructure (α') with some bainitic (α_B) regions as shown in the OM image of Figure 36 a) and b). As expected, no reconstructive transformations took place during the quenching of the samples due to the rapid cooling, instead, martensite laths with high density of dislocation (Figure 36 d)) were formed at the grain boundaries permitting the observation of PAGBs in SEM as shown in Figure 36 c). The grains misorientation distribution presented in Figure 37 shows the texturisation typically observed in martensitic and/or bainitic microstructures in steel [88], [100], it is important to

notice that the misorientation frequency in the range between 20 and 49° is negligible, which means that only displacive transformations took place in the microstructure during quenching. The analysis of the grain misorientation is a useful reference to validate the presence of DIFT grains within the martensitic matrix, since DIFT grains are expected to show a random texturisation similar to that in the non-displacive transformations.

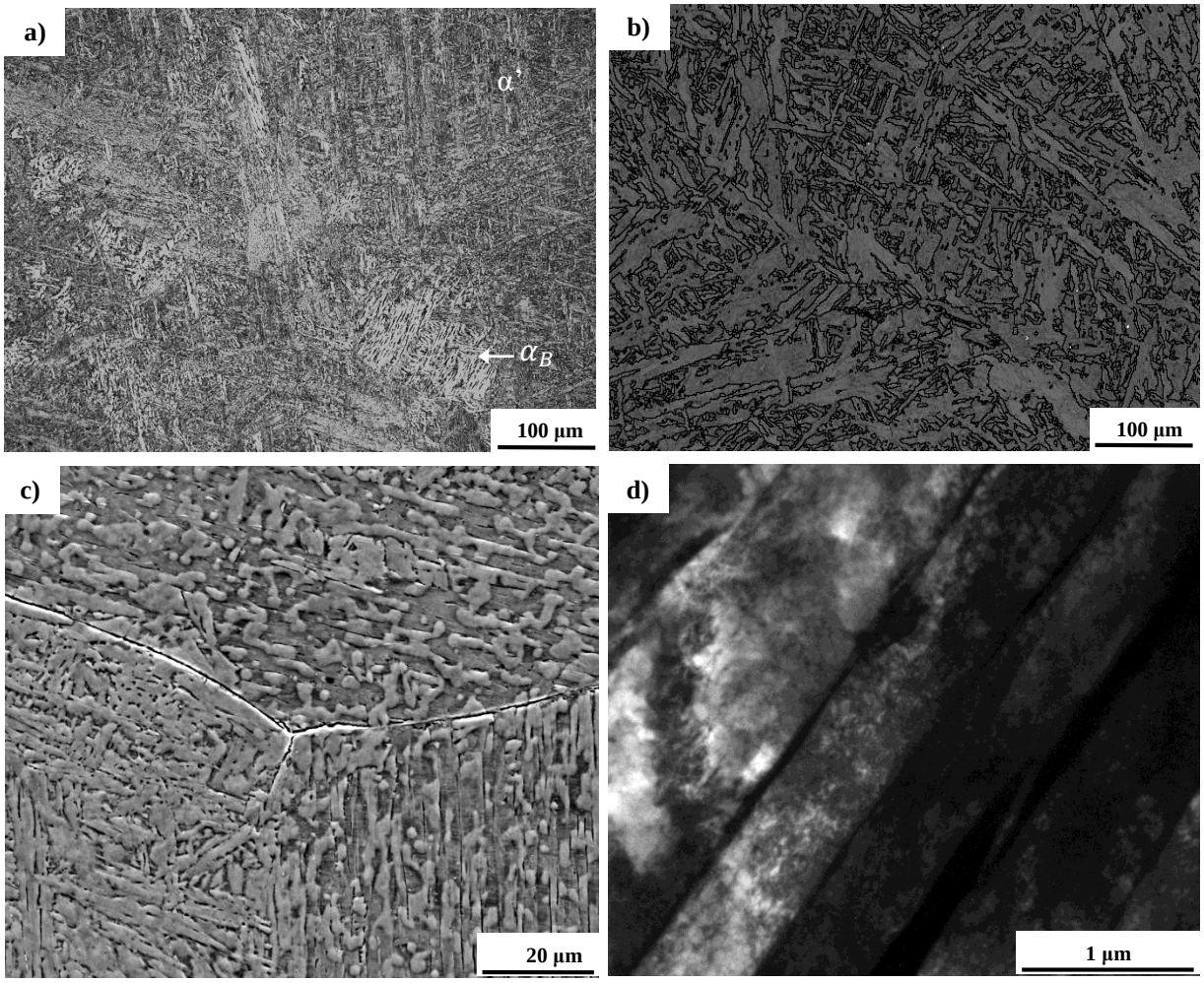

Figure 36. Characterisation of the HTP alloy after the austenitising heat treatment. Martensite microstructure observed by a) optical microscopy, b) band contrast in EBSD, c) secondary electrons SEM and d) TEM bright field.

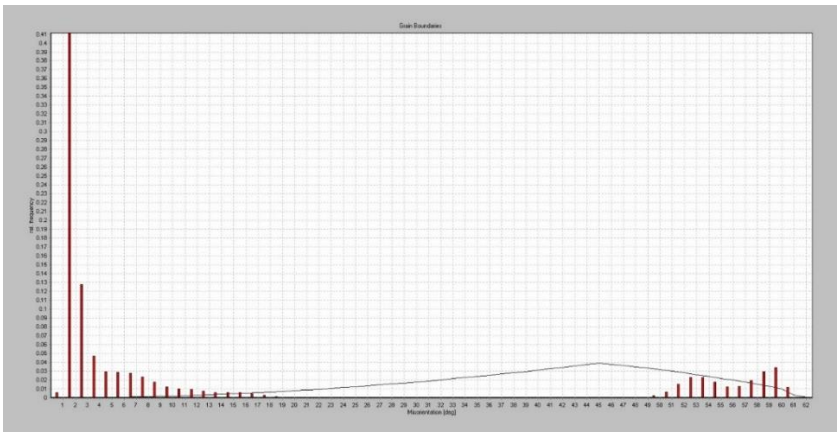

Figure 37. Grain misorientation distribution histogram of the austenitising heat treated material.

As for the state of niobium in the treated sample, carbon extraction replicas were made in order to analyse the morphology and chemical composition of precipitates in TEM and EDS. Most of the area in the replicas was free of precipitates, and the few particles found were mainly coarse cuboid TiN distributed randomly as shown in Figure 38 a), however, some Ti rich (Ti,Nb)(C,N) precipitates showed that the Nb was not fully dissolved after the austenitising heat treatment (Figure 38 b)), these type of precipitates form at high temperatures during or after the solidification process and have high stability during the reheating of the steel [101][102]. The dissolution of (Ti,Nb)(C,N) cannot occur at the austenitising temperature (1300°C) used in the heat treatment, and therefore a small fraction of Nb remains undissolved. However, only some particles were observed and it can be assumed that must of the niobium is in solid solution available to precipitate during the TMCP simulation.

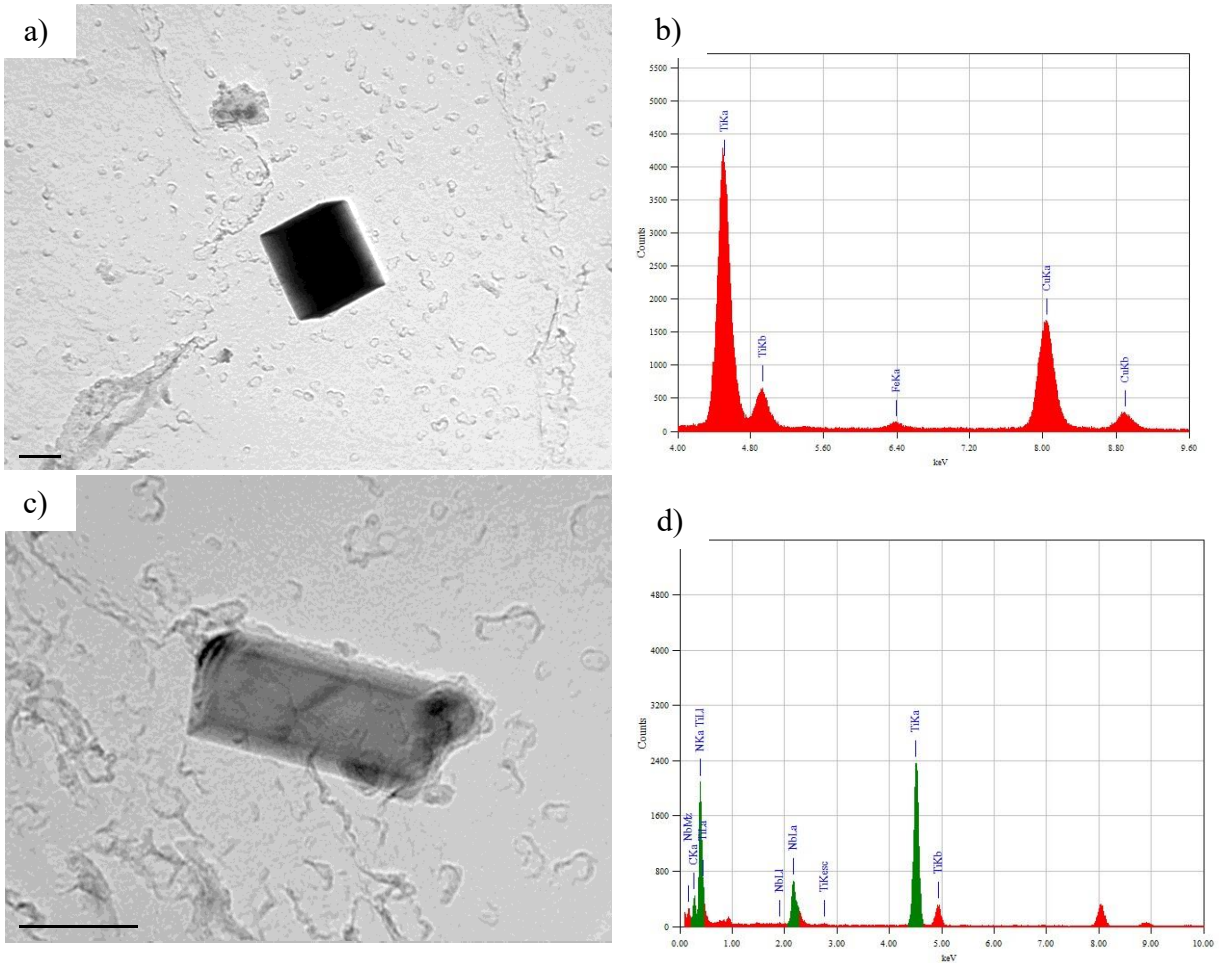

Figure 38. TEM bright field and EDS analysis in carbon extraction replicas obtained after the austenitising heat treatment. Coarse TiN a) and (Ti,Nb)(C,N) b) precipitates with their respective EDS spectrums b) and d).

4.3. Modelling Precipitation-Time-Temperature (PTT) diagrams

PTT diagrams were constructed so as to model the effect of Nb on the recrystallisation during the rough deformation simulation. The diagrams show the interaction between the initiation of the strain induced precipitation and the fraction of recrystallisation as a function of time and temperature at a given constant strain [28]. Two important temperatures can be found in the PTT diagram; the full recrystallisation temperature $T_{95\%}$ at which the static recrystallisation is almost complete, and the recrystallisation stop temperature $T_{5\%}$ where the initiation of the strain induced precipitation stops the onset of the recrystallisation. Below $T_{5\%}$ the material remains

deformed and unrecrystallised, between $T_{5\%}$ and $T_{95\%}$ the recrystallisation is partial and above $T_{95\%}$ the static recrystallisation is complete.

The times for the start and end of both recrystallisation and SIP have been conventionally defined by their partial fractions; 5% has been used for the start and 95% for the end. Thus, when the curves $t_{0.05X}$ (onset of recrystallisation) and $t_{0.05}$ (start of SIP) converge, $T_{5\%}$ is found. On the other hand, when $t_{0.95X}$ (full static recrystallisation) and $t_{0.05}$ intersect $T_{95\%}$ is defined.

The kinetics of initiation of both SIP ($t_{0.05}$) and recrystallisation ($t_{0.05x}$) in Nb microalloyed deformed austenite has been modelled by Dutta, Palmiere and Sellars [36][86], according to their model the Equations 4.1 and 4.2 can predict the times at which the SIP and recrystallisation achieve a fraction of 5%:

$$t_{0.05} = 3 \times 10^{-6}[Nb]^{-1}\varepsilon^{-1}Z^{-0.5} \times exp\frac{2700}{RT}\, exp\frac{2.5\times10^{10}}{T^3(ln\, k_s)^2} \tag{4.1}$$

$$t_{0.05x} = 6.75 \times 10^{-20} d_o^2 \varepsilon^{-4} \times exp\frac{300000}{RT} \times exp\left\{\left(\frac{2.75\times10^5}{T}\right)[Nb]\right\} \tag{4.2}$$

where $[Nb]$ is the percentage of Nb in solution, Z is the Zener-Hollomon parameter, R the universal gas constant, d_o is the initial grain size in μm and k_s is the supersaturation ratio at the deformation temperature defined as:

$$ks = [Nb][C + 12N/14]_{sol}/10^{2.26-6770/T} \tag{4.3}$$

the kinetics for complete recrystallisation ($t_{0.95x}$) can be modelled by an Avrami-type equation using an exponent k = 2, which generally fits well with the kinetics of static recrystallisation [36], [103] thus, assuming that Nb is in solid solution the Avrami equation can be written as:

$$X = 1 - exp\left(-\ln(0.95)\left(\frac{t}{ts}\right)^2\right) \tag{4.4}$$

where X is the recrystallised fraction at a time t, and t_s is the recrystallisation start time which in this case is assumed to be $t_{0.05X}$. For a recrystallised fraction of 0.95 the Equation 4.4 can be simplified as follows:

$$t_{0.95X} = 7.64 t_{0.05X} \quad (4.5)$$

The PTT diagram for the HTP alloy with an initial austenite grain size of 87 µm and a strain of 0.3 was constructed using the Equations 4.1, 4.2 and 4.5 as illustrated in Figure 39. The points T1 to T5 within the diagram, represent the conditions (deformation temperature and holding time) at which the simulations were carried out. The $T_{5\%}$ and $T_{95\%}$. temperatures where located at the coordinates 997°C, 2.4 seconds and 1020°C, 7.5 seconds respectively.

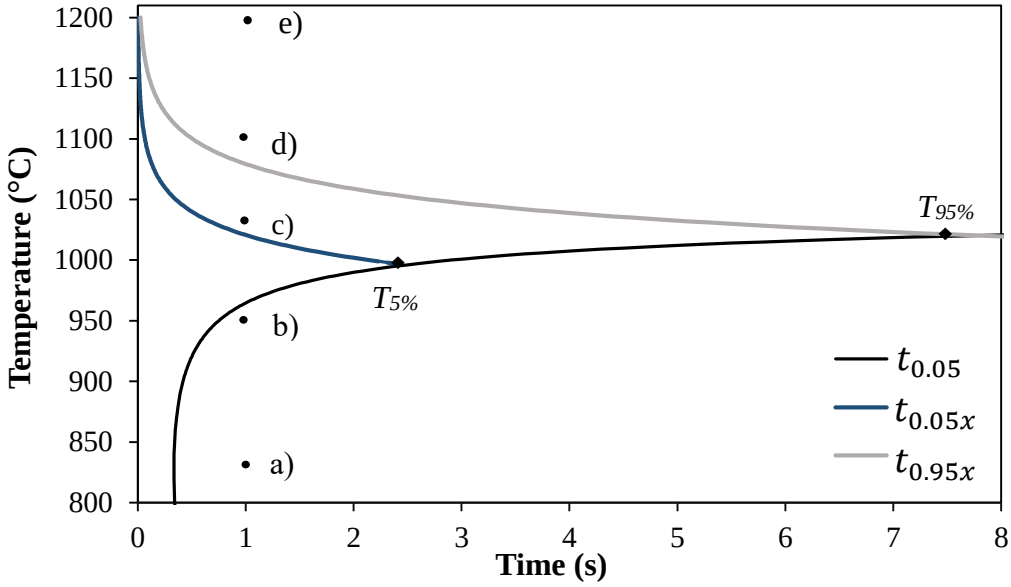

Figure 39. Precipitation-Time-Temperature diagram of the HTP steel alloy at a strain of 0.3 and a strain rate of $10s^{-1}$. The diagram also shows the temperatures at which the simulations where carried out; T1=830°C, T2=950°C, T3=1020°C, T4=1100°C, T5=1200°C.

4.4. Results

4.4.1. Flow behaviour and critical strains for DIFT and DRX

The flow behaviour of all the simulations is shown in Figure 40, at the beginning of the deformation the flow stress increases with strain but then slows down gradually, in the tests at higher temperatures the curves show a plateau in the flow stress after certain value of strain, the deceleration in the strain hardening can be related to dynamic softening processes such as DIFT and the onset of dynamic recrystallisation.

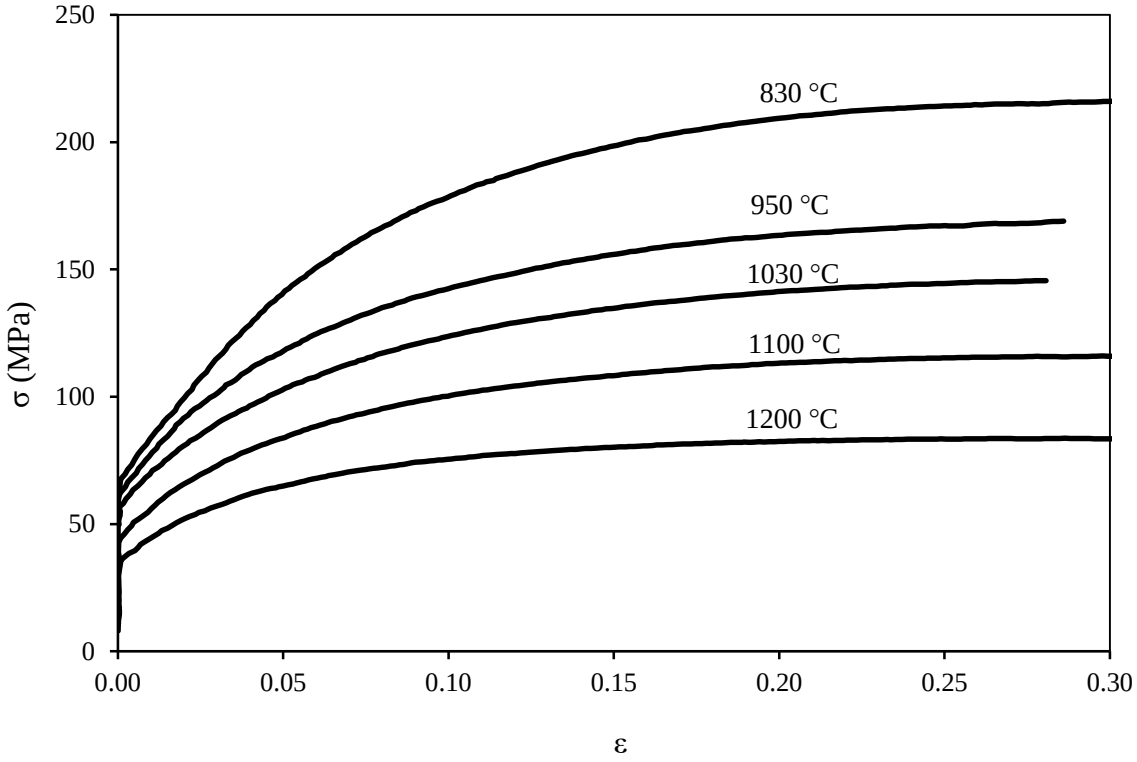

Figure 40. True stress-strain curves of the for five rough deformation temperatures.

The double differentiation method developed by Poliak and Jonas[104] was used to detect the onset of DRX and DIFT from the experimental flow curves. This method has been successfully used in the past to analyse the occurrence of DRX [104] and DIFT [105], [106] in steel, and high sensitivity can be achieved when high order polynomials are used to fit the flow curves

[66], [107]. A discussion of the accuracy and sensitivity of the double differentiation method is provided Section 4.5.1.

According to this model the initiation of DRX or DIFT corresponds to the following condition:

$$\frac{\partial}{\partial\sigma}\left(-\frac{\partial\theta}{\partial\sigma}\right) = 0 \tag{4.6}$$

where θ is the strain hardening rate ($\partial\sigma/\partial\varepsilon$). According to the Equation 4.6 the onsets of DIFT or DRX correspond to an inflection point in the θ-σ curve and with minima in the -($\partial\theta/\partial\sigma$) versus σ curve. The experimental stress-strain curves were fitted using the MATLAB software from the 0.2% of the flow stress to the peak stress using a 9th order polynomial as shown in Figure 41 a), then the work hardening rate $\theta = \partial\theta/\partial\varepsilon$ was obtained with the first derivative of the fitted curves and plotted as a function of stress (Figure 41 b), finally, the second derivative of the stress ($\partial\theta/\partial\sigma$) was plotted against the stress to identify the minimums that represent the onsets of DIFT and/or DRX as shown in Figure 41 c).

Three inflection points can be identified in the curve -($\partial\theta/\partial\sigma$) versus σ, the first point (the first minima) appears due to the onset of DIFT, then the curve increases until a second inflection point is reached, this maximum indicates that rate of DIFT has decreased to below a certain level, the third point is finally located at the second minima of the plot and is caused by the initiation of DRX.

a)

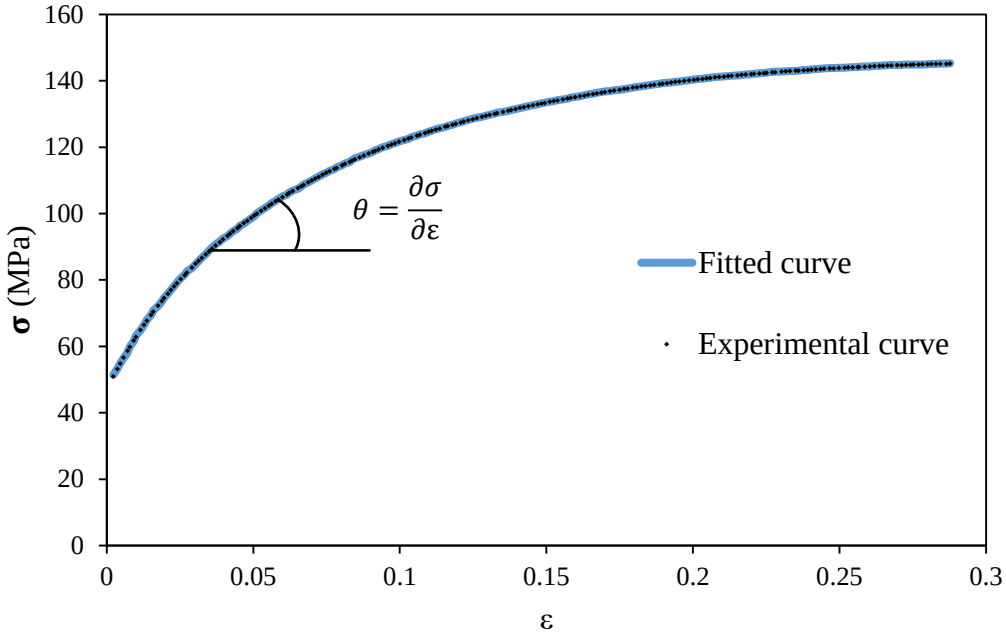
160
140
120
100
80
60
40
20
0
σ (MPa)
0
0.05
0.1
0.15
0.2
0.25
0.3
ε
$\theta = \frac{\partial \sigma}{\partial \varepsilon}$
Fitted curve
Experimental curve

b)

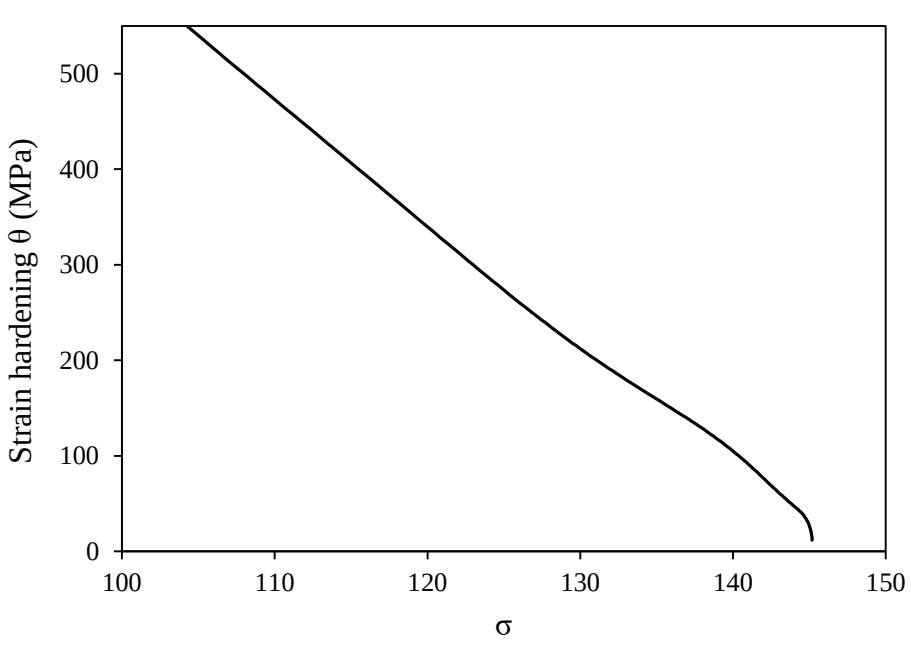
500
400
300
200
100
0
Strain hardening θ (MPa)
100
110
120
130
140
150
σ

c)

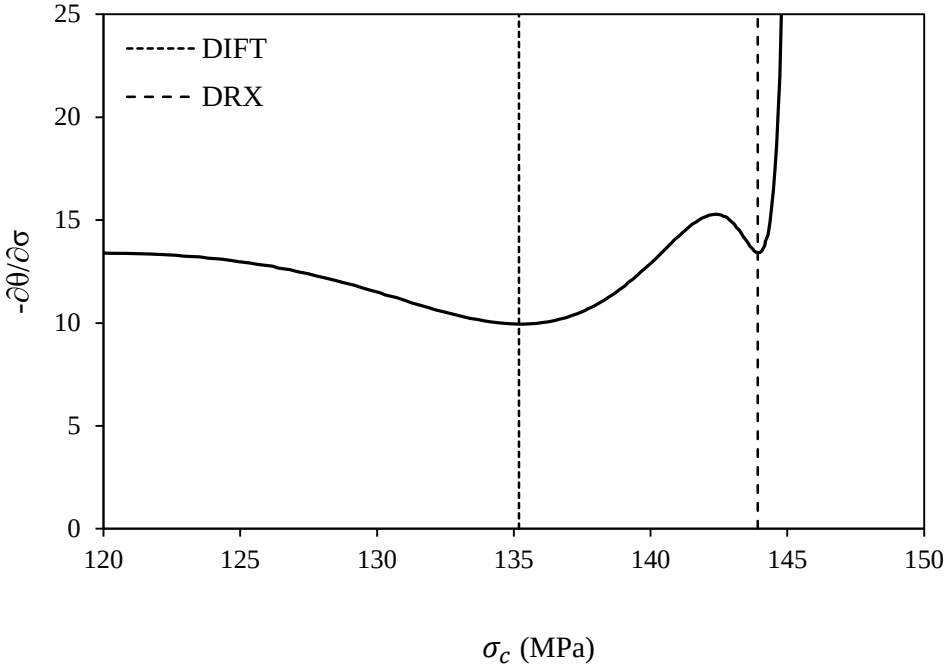

Figure 41. Double differentiation method used to estimate the critical stresses for the onsets of DIFT and DRX in the simulation carried out at 1030°C. a) experimental curve fitted with a 9th order polynomial and definition of strain hardening rate, b) first derivative to obtain the strain rate (θ) versus stress plot and b) second derivative showing -($\partial\theta/\partial\sigma$) versus σ plot and location of the minimum stresses that represent the onsets for DIFT and DRX.

The load utilised in all the deformation tests was high enough to reach the critical strain for DIFT, although dynamic recrystallisation only occurred at temperatures as of 950°C as shown in Figure 42 a). DRX is a thermally activated process and it would be expected to observe the onset of recrystallisation at lower strains and stresses as the temperature increases, in Figure 42 b) a strong correlation between the critical stress and temperature is observed, however, the critical strain for DRX do not show the same behaviour. It appears that the onset of DIFT affects the onset of DRX, that explains why the expected correlation between the critical strain for DRX and the temperature is not accomplished. Other works have shown similar behaviour in the onset of DRX at different temperatures [21], [62], [108].

a)

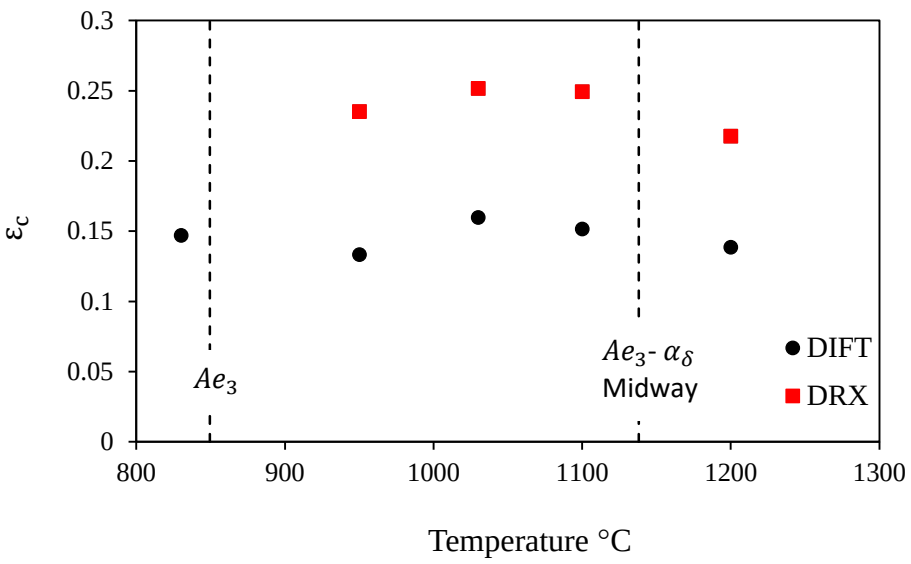

b)

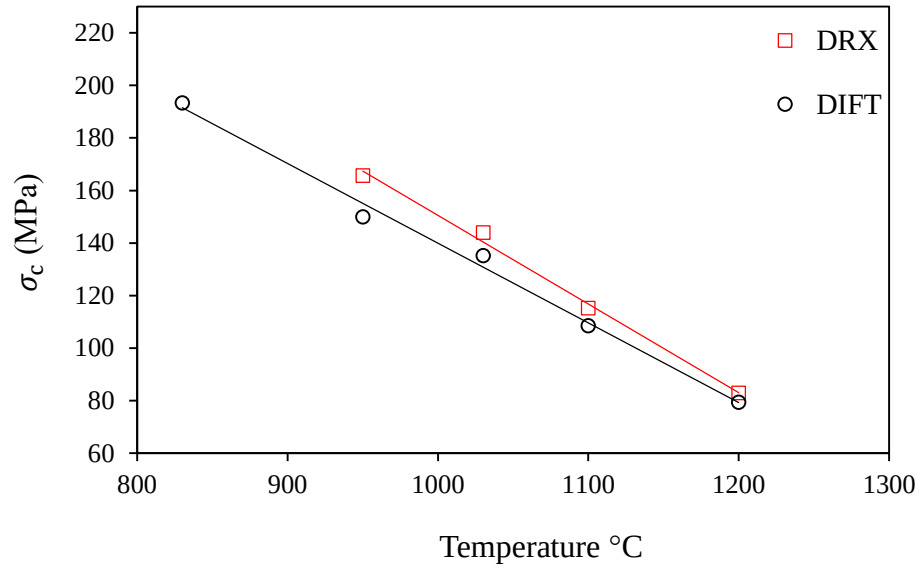

Figure 42. Critical strain a) and critical stress b) required to achieve to the onset of DIFT and DRX as function of the deformation temperature.

As for DIFT, the critical strain varied subtly from around 0.13 to 0.16 which matches well with values reported in steels with relatively similar chemical composition [62], [66]. In general, there is not a clear correlation between the critical strain for DIFT and the deformation temperature, it is commonly accepted that the critical strain decreases with temperature although the correlation has shown to be weak [66]. According to Grewal et al [21], the driving force for dynamic transformation is the lowest at the midway temperature between Ae_3 and δ-ferrite phase field, thus, the critical strain for DIFT increases gradually from Ae_3 to the midway

temperature until a maximum is achieved, then, the critical strain decreases slowly as the deformation temperature recedes from the midway temperature as illustrated in Figure 43.

Nevertheless, despite showing a general trend in the whole range of temperatures, the correlation is weak at various segments of the temperature range since very similar critical strains can be found at significantly different temperatures. The critical strains for DIFT obtained in the current work (Figure 42 a)) are not necessarily in disagreement with Grewal et al, but more tests might be necessary to confirm whether there is similarity between both works.

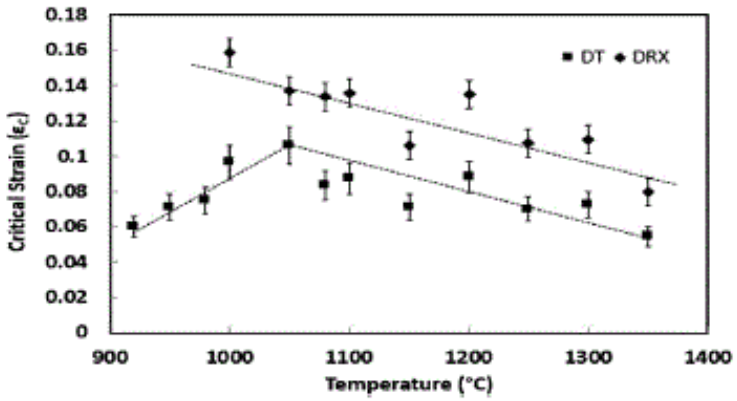

Figure 43. Critical strain for dynamic transformation (DT) and dynamic recrystallization (DRX) in the austenite phase field [21].

The apparent insensitive behaviour of the critical strain for DIFT to temperature is also observed at the simulation below Ae_3, at this point of metastable equilibrium, the chemical driving force for γ to α transformation increases and the deformation is expected to trigger the onset of DIFT at lower strains, however, the critical strain seems not to be affected and showed a value similar to those above Ae_3.

4.4.2. Morphology of prior austenite grains

Figure 44 shows the prior austenite grains morphology after deformations at a) 830°C, b) and c) 950°C, d) 1030°C, e) 1100°C and f) 1200°C. The specimen tested at 830°C shows deformed austenite grains elongated in the rolling direction with a "pancake"-like shape, no evident traces of recrystallisation are observable. As the deformation temperature increases to 950°C, most of the microstructure still remains deformed but a very small amount of recrystallised grains start to appear mainly at triple points of the deformed grains, such grains are likely to be formed during deformation which concurs with the results obtained with the double differentiation method that detected DRX in the flow curve. Another important feature observed in this specimen is the vanishing of some austenite grain boundaries due to the dynamic ferrite transformation, for instance, a pair of adjacent deformed grains showed in Figure 44 b) is displayed at higher magnification in Figure 44 c), it is noticeable that most of the boundary amongst the grains disappeared, besides, there are reliefs suggesting the presence of fine plates oriented in a single direction within the grains. Such evidence is a clear indicator of the presence DIFT in form of Widmanstätten ferrite plates and polygonal grains at the PAGBs, the correlation between DIFT plates and grains is explained in detail afterwards. The same features aforementioned were also observed in the PAGBs of the specimen deformed at 830°C, and in the remaining deformed grains of the simulation at 1030°C.

As the deformation temperature increases the recrystallisation cannot be deterred as shown in Figure 44 d), the micrograph of the specimen deformed at 1030°C shows an important partial recrystallisation where new grains expand all over the microstructure consuming the deformed grains. The deformations performed at 1100°C and 1200°C share similar characteristics, under these conditions full recrystallisation occurred and the grains exhibit a polygonal shape. The specimen deformed at 1200°C has a slightly larger grain size than that deformed at 1100°C (27 μm vs 25 μm), nevertheless, it is important to note that the samples were quenched in around 0.45 seconds immediately following deformation, therefore, the time for coarsening was almost insignificant.

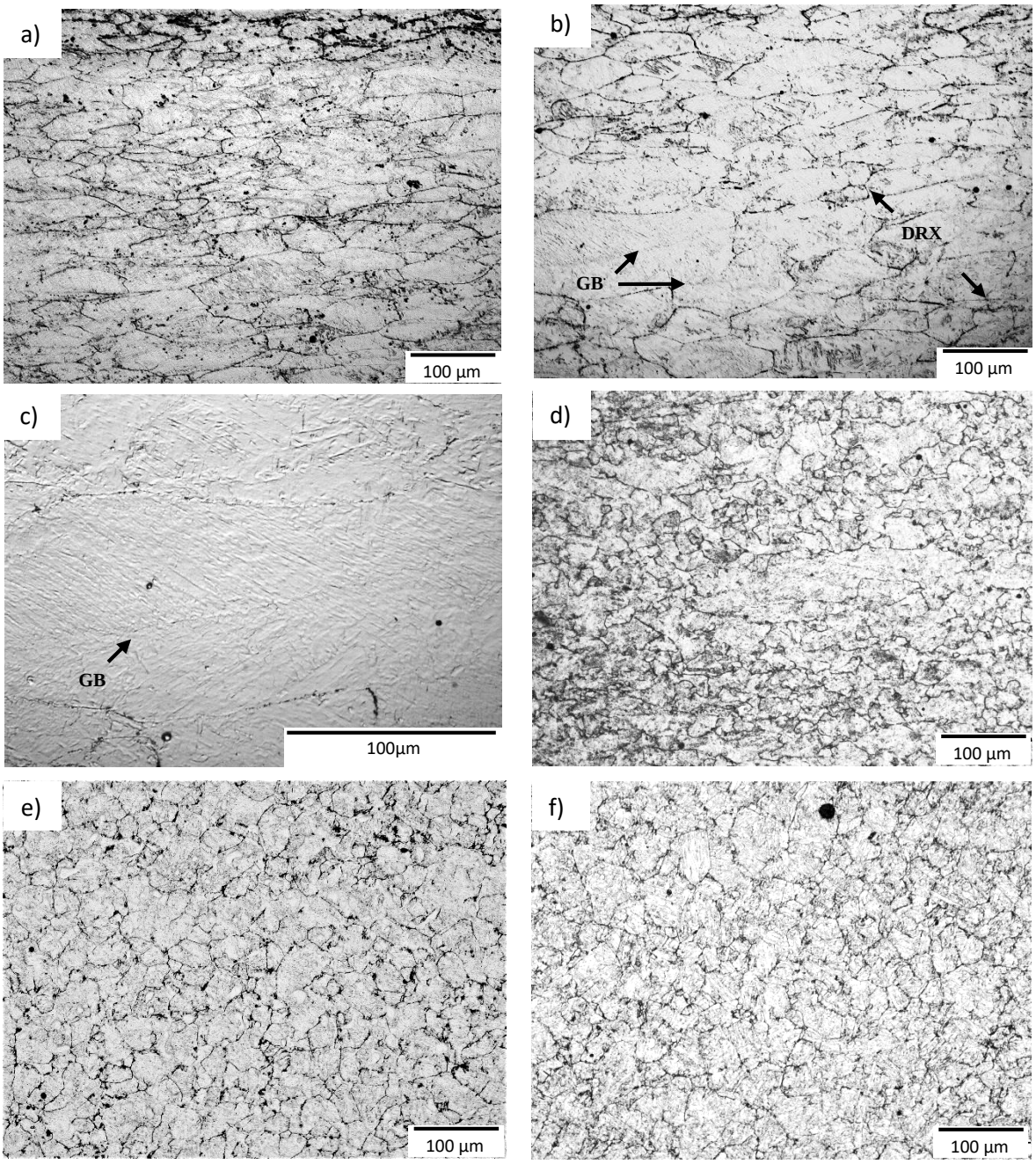

Figure 44. Prior-austenite grain boundaries after a deformation at a strain of 0.3 and a temperature of a) 830°C, b) and c) 950°C, d) 1030°C, e) 1100°C and f) 1200°C. The samples were quenched 1 second after the deformation.

4.4.3. Microstructure

The microstructure in all the simulations is shown in Figure 45, a mixture of Widmanstätten ferrite (α_w), ultrafine polygonal ferrite (α), and martensite (α') is observed in the specimens deformed at 830°C, 950°C and 1030°C, then at 1100°C, the microstructure surprisingly changed to ferrite bainite (α_b), and finally, at 1200°C the microstructure consisted of ferrite (plates and grains), bainite and martensite.

The microstructures in the simulations performed in the non-recrystallisation zone at 830°C and 950°C (Figure 45 a) and b)) show evident formation of ferrite in the grain boundaries, besides, colonies of Widmanstätten ferrite plates appear aligned in the same direction as a reminiscence of the influence of the stress on the dynamic transformation during deformation. As the deformation temperature increases up to the partial recrystallisation region at 1030°C, the α_w plates become sharper and larger, but the amount of ferrite in the grain boundaries seems to decrease. As for the microstructures transformed from fully recrystallised austenite, at 1100°C the Widmanstätten ferrite is no longer observed, instead, a dominant bainitic matrix mixed with random martensite regions is revealed, few ferrite polygonal grains of a diameter of approximately 2 to 3 μm appear surrounding some of the grain boundaries. Finally, the microstructure in the deformation condition at 1200°C shows again a mixture of phases, waved grain boundaries are observed due to the formation of ultrafine ferrite on the PAGBs, and large Widmanstätten plates grow inside some grains.

It is important to mention that the polygonal ferrite and the α_w plates cannot be formed by the classical transformation mechanism of proeutectoid ferrite on austenite cooling below Ae_3, the dynamic ferrite transforms in less than a millisecond [63], [73] whereas the allotriomorphic ferrite takes from 8 to 10 seconds to transform to allow for the partitioning of Mn and Si between the austenite and ferrite [67], in the current work the holding time between the deformations and the quenching was 1 second and the cooling rate on water quenching varied from 65°C/s to 105°C/s, thus, the holding times in the temperature range between Ae_3 and the bainite finish temperature (around 550°C) varied from 3 to 5 seconds. The only possible mechanism that explains the presence of ferrite after the rapid quenching of the specimens, is that proposed by Basabe et al [61], where the deformation causes the nucleation of ferrite plates followed by coalescence that transforms the plates into polygonal grains. Furthermore,

intragranular polygonal ferrite is frequently found mainly in the tests at lower temperatures, which is also a characteristic of the dynamic transformation according to Basabe.

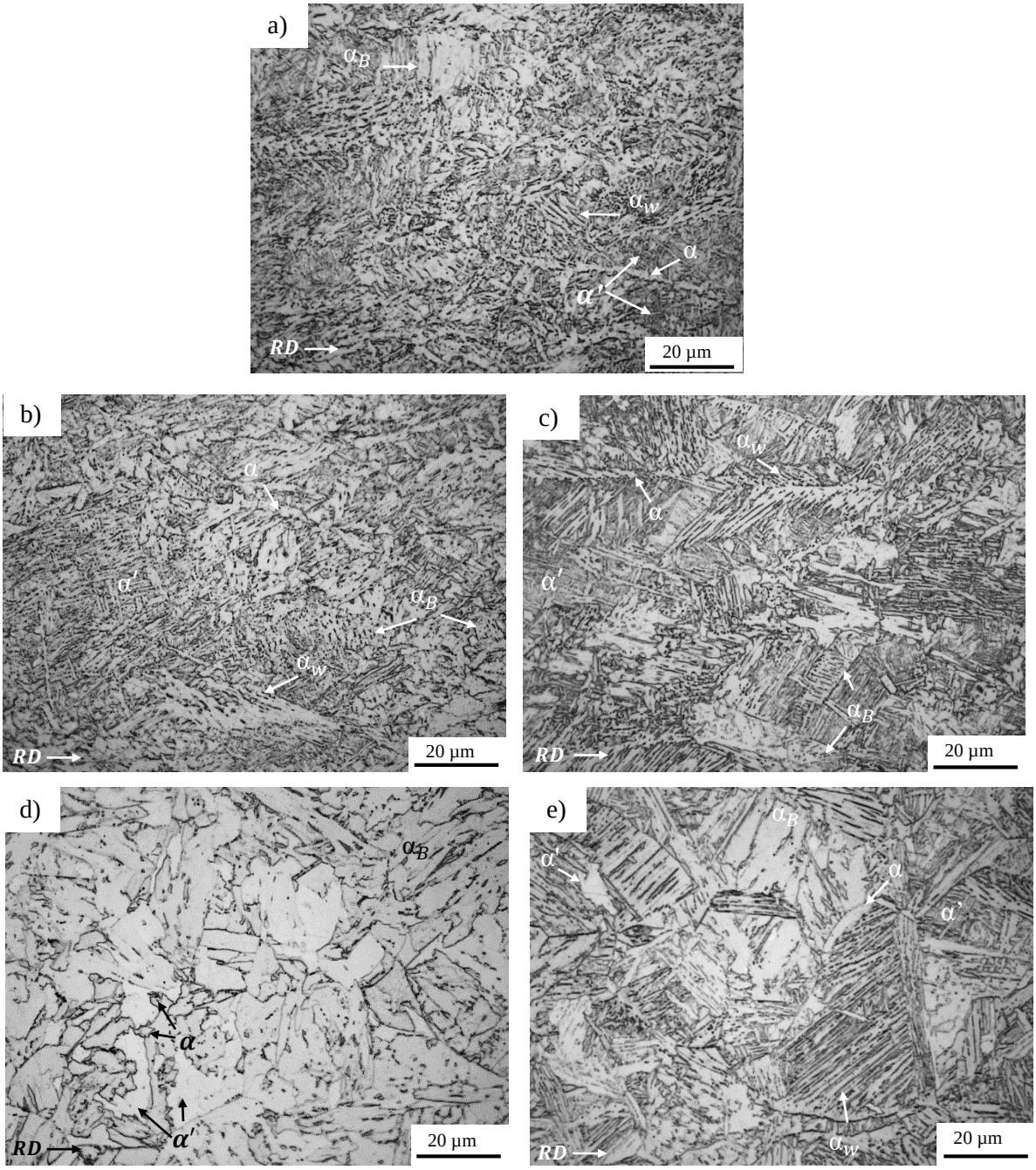

Figure 45. Optical micrographs at 1000x showing the RD-ND plane of quenched PSC specimens deformed at a strain of 0.3 at a)830°C, b) 950°C, c) 1020°C, d) 1100°C and d) 1200°C.

SEM imaging was carried out to observe the microstructure in some simulations at higher resolution, a similar trend in the microstructure was observed compared to the findings in OM. At 1200 °C a small amount of DIFT was observed in some waved grain boundaries as shown in Figure 46 a), very fine plates of Widmanstätten ferrite can be found adjacent to the ferrite formations but most of the microstructure consists of a mixture of bainite and martensite, at lower temperature at 1100°C the presence of DIFT is difficult to observe, however, some polygonal micrometric grains can be found in some regions as depicted in Figure 46 b), at the lowest deformation temperature at 830°C (Figure 46 c)), the microstructure remains deformed and the presence of DIFT is evident along the grain boundaries, large colonies of Widmanstätten ferrite grow within the prior austenite grains. At higher magnifications (Figure 46 d)) the coalescence of Widmanstätten plates and formation of new polygonal grains with diameter smaller than a micron can be observed. Another relevant characteristic revealed in the microstructure by SEM is the presence of cementite carbides and small islands of martensite-austenite surrounding the ferrite. Due to the low carbon content of the HTP alloy the formation of ferrite grains occurs rapidly, according to Ghosh et al [109], in steels with carbon contents below about 0.15% the carbides formation is not necessary during the dynamic transformation of ferrite plates and the transformation is entirely displacive, thus, the plate growth and the subsequent formation of polygonal grains is not retarded by carbon diffusion. The few carbides observed in the ferrite grain boundaries in the SEM image are likely to be formed post-dynamically during the merging of plates after the deformation, these particles also serve as pining sites that hinder the coarsening of the polygonal ferrite grains. More evidence of the formation of cementite is presented in the further chapter in the finish rolling simulations where the presence of cementite is more abundant in the microstructures with larger volume fraction of DIFT.

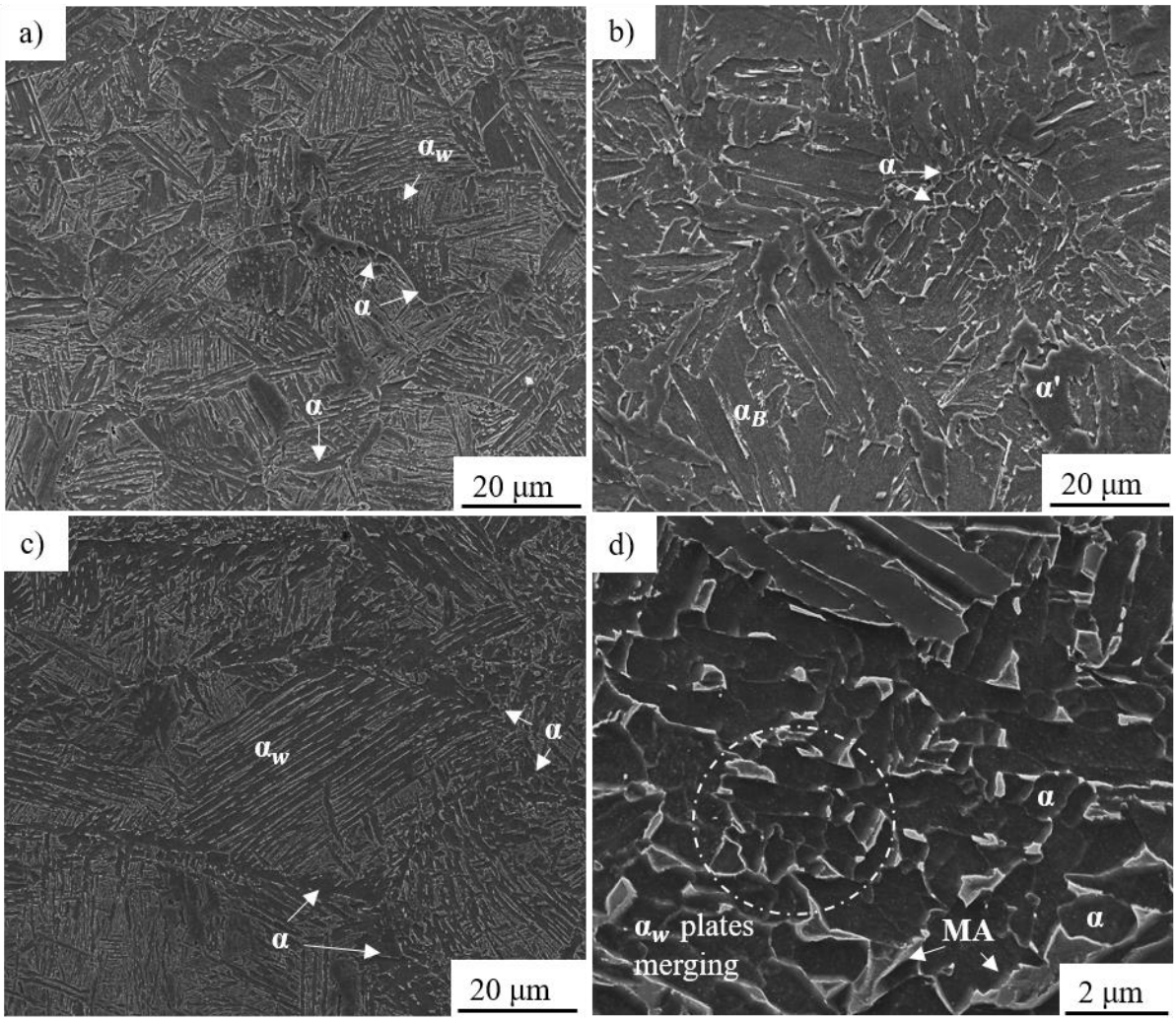

Figure 46. Secondary electrons imaging in SEM showing the microstructural characteristics of the tests carried out at a) 1200°C, b)1100°C, c) and d)830°C.

4.4.4. Characterisation and quantification of DIFT by scanning probe microscopy and nanoindentation.

The presence and volume fraction of DIFT was observed and quantified by SPM as described in Section 3.11, Figure 47 displays the topography of different deformation conditions evaluated on the area of interest, images of the simulation at 1030°C are not presented since the morphology and distribution of DIFT is very similar to that found in the conditions deformed at 830°C and 950°C. At lower deformation temperatures the formation of dynamic ferrite is abundant (more than 20% of the volume fraction) as shown in Figure 47 a) and b), the

deformed PAGBs served as effective nucleation sites for DIFT and the grains are ultrafine, must of them are even smaller than 1μm. As the temperature increases in the full recrystallisation zone at 1100°C (Figure 47 c), the occurrence of DIFT drops drastically, most of the features with higher surface relief correspond to micrometric islands of martensite-austenite (MA) (one indent was done in each of the two islands shown in Figure 47 c), the hardness values were 7.9 and 6.6 GPa while the surrounding matrix gave an average value of 3.8 GPa after 5 indents), the matrix consists mainly of granular bainite and grains of DIFT are scarce. Finally, the topography in the simulation at 1200°C showed a moderate amount of DIFT (8%) despite the high deformation temperature, Widmanstätten plates are easier to observe in SPM due to the undeformed PAGBs that allow the growth of larger ferrite plates. Important features that can be observed in the scan of Figure 47 d); the coalescence of adjacent Widmanstätten ferrite plates (which is the second stage in the dynamic transformation of ferrite [61]) and the intragranular formation of a ferrite grain.

A summary of the volume fraction of DIFT at the different simulation temperatures is presented in Figure 48, it can be seen that the amount of ferrite decreases subtly as the temperature increases from 830°C to 1030°C, then at 1100°C there is a significant decrease in the transformed ferrite and the volume fraction is only 2%, finally at 1200 °C the amount of ferrite increases again to 8%. A minimum in the fraction of the dynamic transformation has been previously reported at similar temperatures, such minimum is related with the midway between Ae_3 and the δ – ferrite phase field, as the deformation temperature approaches to both Ae_3 or the δ – ferrite phase, the energetic obstacle for the dynamic transformation of Widmanstätten ferrite becomes easier to overcome since the austenite require less work hardening to transform to ferrite. The middle point between Ae3 and the δ – ferrite phase field for the current HTP alloy is 1139.5°C, this explains the very low amount of DIFT found at 1100°C.

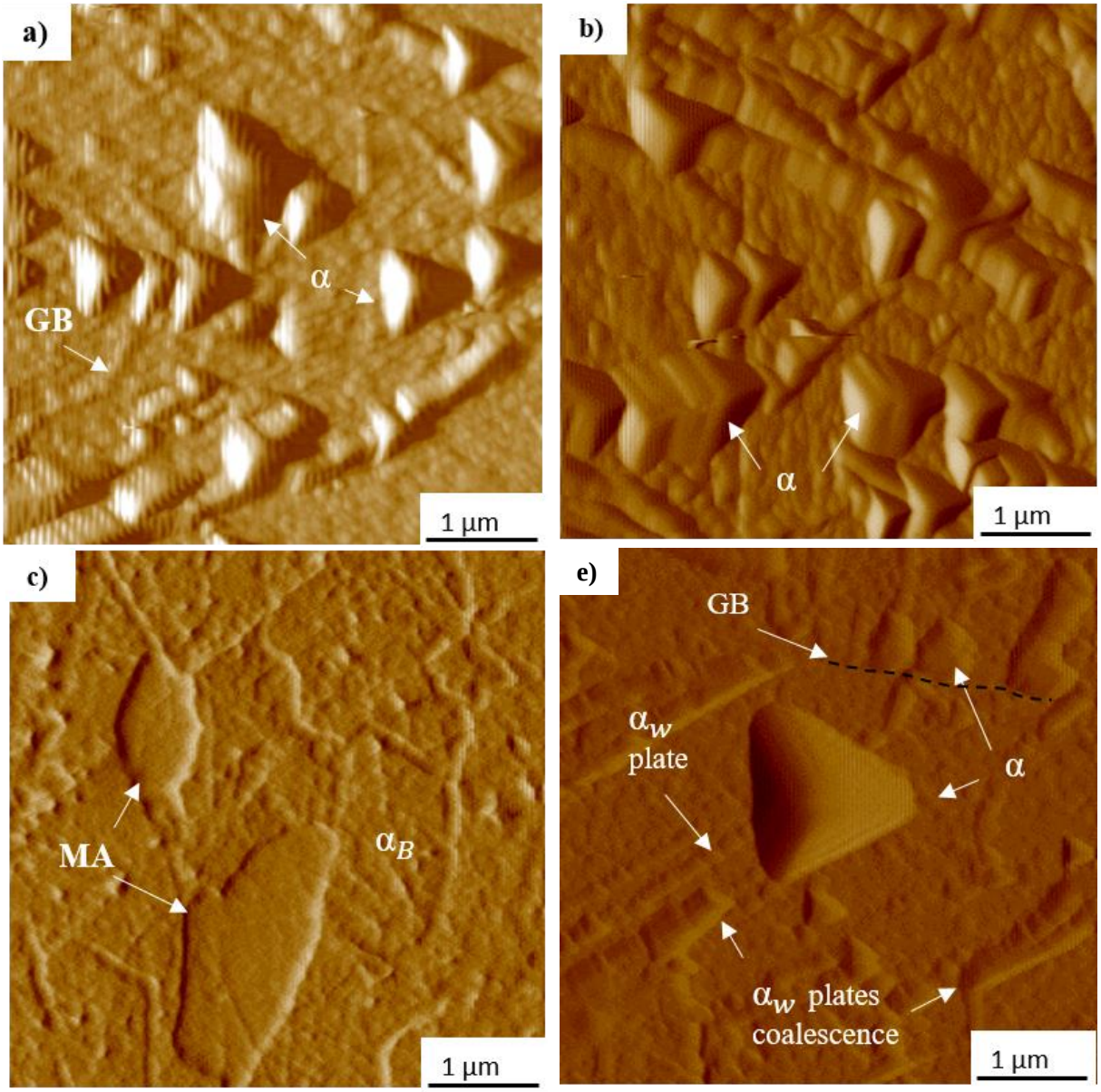

Figure 47. Gradient scan SPM Images of the tests performed at a) 830°C, b) 950°C, c)1100°C and d) 1200°C.

The effect of deformation temperature on the DIFT grain size was evaluated by measuring the diameter of at least 10 polygonal grains in each deformation condition, Figure 49 shows that the ferrite grains become finer as the deformation temperature decreases, at high temperatures in the recrystallisation region (1100°C and 1200°C) the largest ferrite grains show a size of almost 6 µm, the coarsening of the ferrite grains at high temperatures is promoted by the recrystallisation process that removes dislocations that might hinder the grain boundary mobility of the transformed ferrite. The average DIFT grain size for the simulations at 1200°C

and 1100°C was 2.8 and 1.9 µm respectively nevertheless, the range of sizes is wider as the temperature increases, the largest grains showed a size of almost 6 µm at 1200°C and 3.2 at 1100°C.

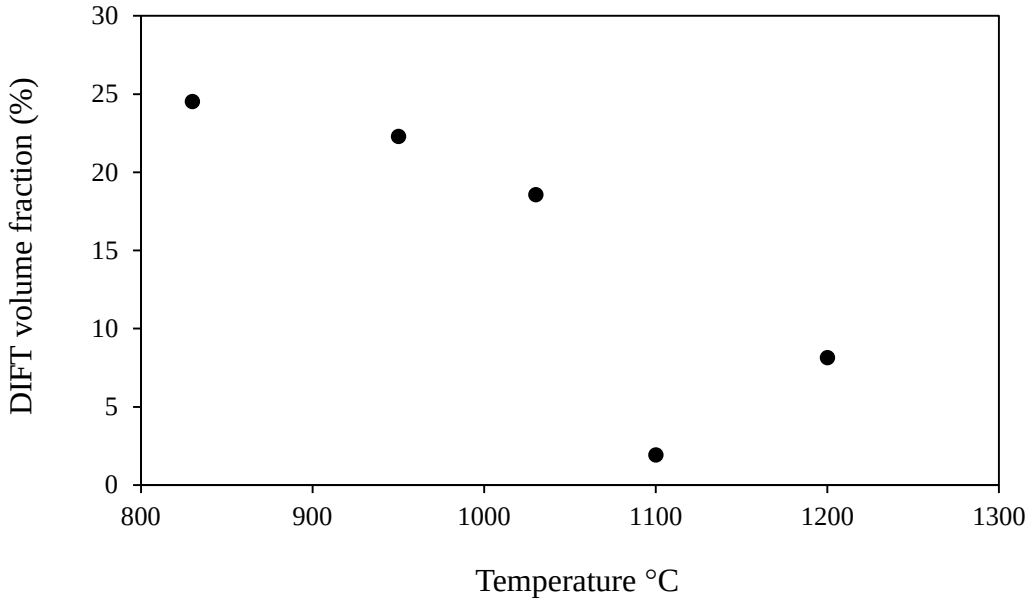

Figure 48. DIFT volume fraction as a function of deformation temperature.

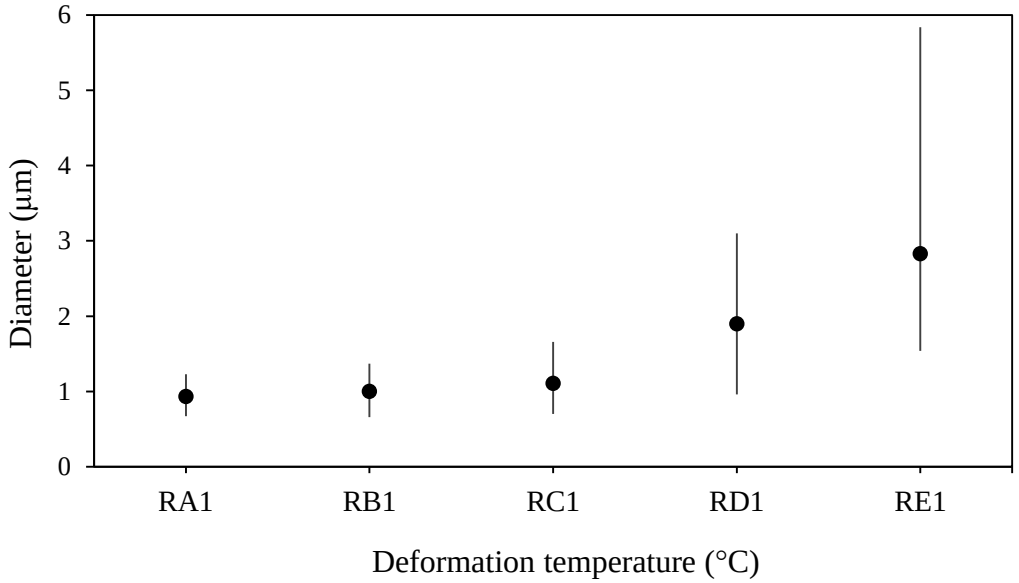

Figure 49. Effect of deformation temperature on DIFT grain size.

Conversely, at lower temperatures in the partial and non recrystallisation region, the coarsening of the dynamic ferrite is limited and the average ferrite grain size is around 1μm. The presence of defects and dislocations caused by the deformation in the unrecrystallised austenite and the harder austenite matrix (due to the low temperature) constrain the ferrite grain growth. The term ultrafine ferrite is therefore applicable only for the phase formed at deformations below the full recrystallisation temperature.

As for the Nanohardness evaluation, it was found that the hardness decreases significantly as the ferrite grain increases, this trend is even observed in ferrite grains located in the same sample and same scanning region, Figure 50 displays the hardness of single ferrite grains found in two different simulations; the 1 pass hardness values correspond to the simulation carried out at 1200°C (which produced an 8% of DIFT and relatively "coarse" grains) and the 2 passes values come from a simulation (the one used in Section 2.12 to validate DIFT) that consisted of one rough deformation pass at 1100 °C (which lead to almost insignificant DIFT) plus a second finishing pass at 810 °C and 0.2 strain that produced ultrafine grains smaller than 1 μm.

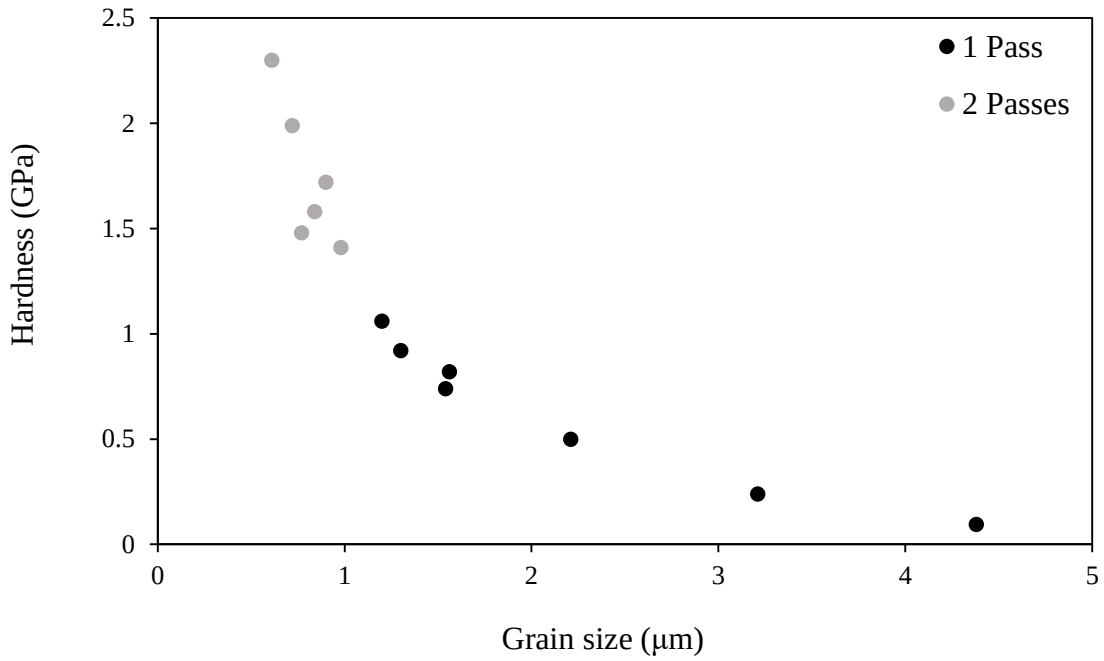

Figure 50. Effect of DIFT grain size on the Nanohardness.

The explanation for the unexpected correlation between the nanohardness and the ferrite grains size can be found analysing the surface topography of the specimen, after the electrolytic etching DIF grains appear as bulges on the somewhat flat matrix with heights from around 150 to 500 nm depending on the ferrite grain size (the larger the grain the higher the bulge). In the case of coarse grains, since there is a large superficial area in form of bulge or protrusion free of neighbouring grains, the plastic zone generated by the deformation of the indentation does not reach the grain boundaries as illustrated in Figure 51 a), the grain responds to the indentation as a single crystal in which the deformation resistance is provided only by dislocations within the grain. The indentation prompts the nucleation of two types of dislocations; geometrically necessary dislocations (shown in Figure 51) that reaccommodate the material displaced during the indentation and allow for the permanent shape change at the surface, and statistically stored dislocations which trap each other randomly during the deformation [110].

In small grains, apart from the dislocations created during the indentation previously described, an additional contribution to the nanohardness is given by the pile up of dislocations in the ferrite grain boundaries as schematised in Figure 51 b), in this case the plastic zone can cross segments of the grain boundaries leading to local hardening. The interaction of dislocations and grain boundaries can also be inferred by the analysis of the load and displacement curves, in coarse grains the curve shows a smooth increase in the load as the indentation progresses as shown in Figure 51 c), low loads cause large displacements at the beginning of the test but the constant nucleation of dislocations hardens the material and the load raises rapidly at certain point of the curve. On the other hand, the indentation of an ultrafine grain shows a rough curve (Figure 51 d)) with subtle pop in events (sudden displacement jumps) caused by dislocations pile up and transitions across grain boundaries, these interactions between dislocations and grain boundaries accounts for the significant increase in the nanohardness in ultrafine grains. The relation between a single pop in event in the load and displacement curves during nanoindentation and the presence of a grain boundary has been previously reported elsewhere [111], in the case of the indentation of a polygonal grain of ultrafine ferrite, the advancing plastic zone generated by the deformation can have multiple encounters with the grain boundaries and generate pile up of dislocations in different sites, that accounts for the shape of the curve.

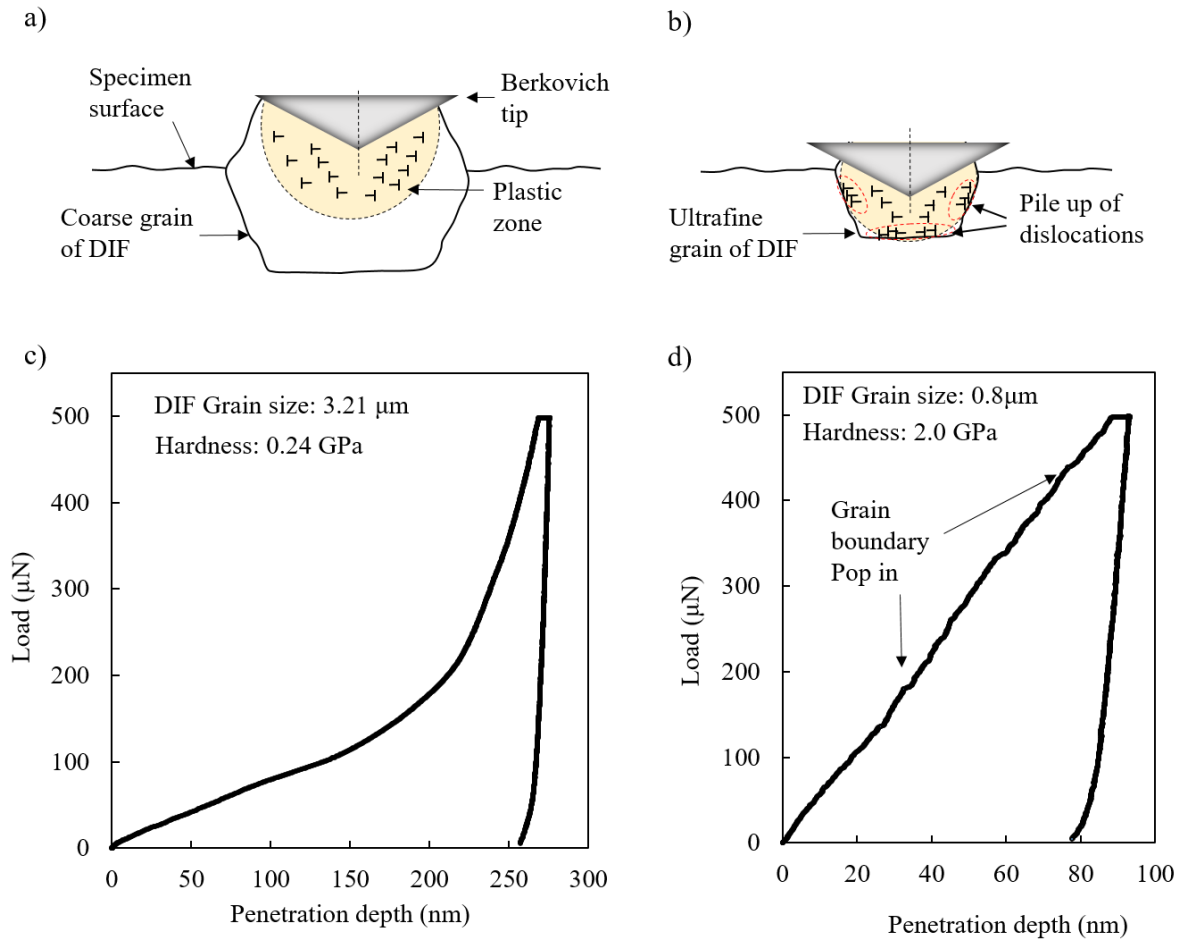

Figure 51. Schematic representation of the interaction between dislocations and grain boundaries during the nanoindentation of a) coarse and b) ultrafine ferrite grains and an example of a load and penetration depth curve for each case respectively c) and d).

4.4.5. Niobium precipitation

For practical reasons, only simulations performed at 950°C, 1100°C and 1200°C were evaluated with carbon extraction replicas by TEM, the simulations at 830 and 1030°C temperatures are impractical for industrial application for rough rolling and SIP is predictably higher as the deformation temperature decreases. Although 950°C is also a temperature unusual for rough rolling, the precipitation behaviour was analysed to understand the results obtained with the double differentiation method in Section 4.4.1.

At 1200°C the SIP of Nb was negligible, very few spherical particles with sizes of around 8 nm where observed in the whole region of the replica, it can be assumed then that the SIP of NbC is insignificant at this temperature, the main particles found consisted of large cuboid TiN precipitates distributed randomly in the carbon matrix of the replica, some of them showed epitaxial growth of NbC as shown in Figure 52 a), the EDS analysis on chemical composition showed characteristic peaks of Nb and Ti in the precipitate as shown in Figure 52 b), the peak of Cu in the spectrum is from the copper grid supporting carbon replica and the silicon peak is from the TEM sample holder. In contrast, the deformations at 1100°C and 950°C conducted to strain induced precipitation of nanometric spherical shaped NbC as can be seen in in the replicas showed in Figure 52 c), e), and f).

An important difference is noticeable in the size and extent of SIP between both deformation temperatures; at 1100°C precipitates appear coarser but the precipitation is more abundant at 950°C as shown in Figure 53 a). Most of the precipitates observed in both conditions have diameters from 3 to 8 nm and the average sizes are 8.9 and 8.4 nm for the deformations at 1100°C and 950°C respectively. The size distribution shows a different tendency in both simulations, at 1100°C the curve exhibits a bimodal distribution with peaks at 3.5 and 17.1 nm, whereas at 950°C the frequency increases as the particle size decreases.

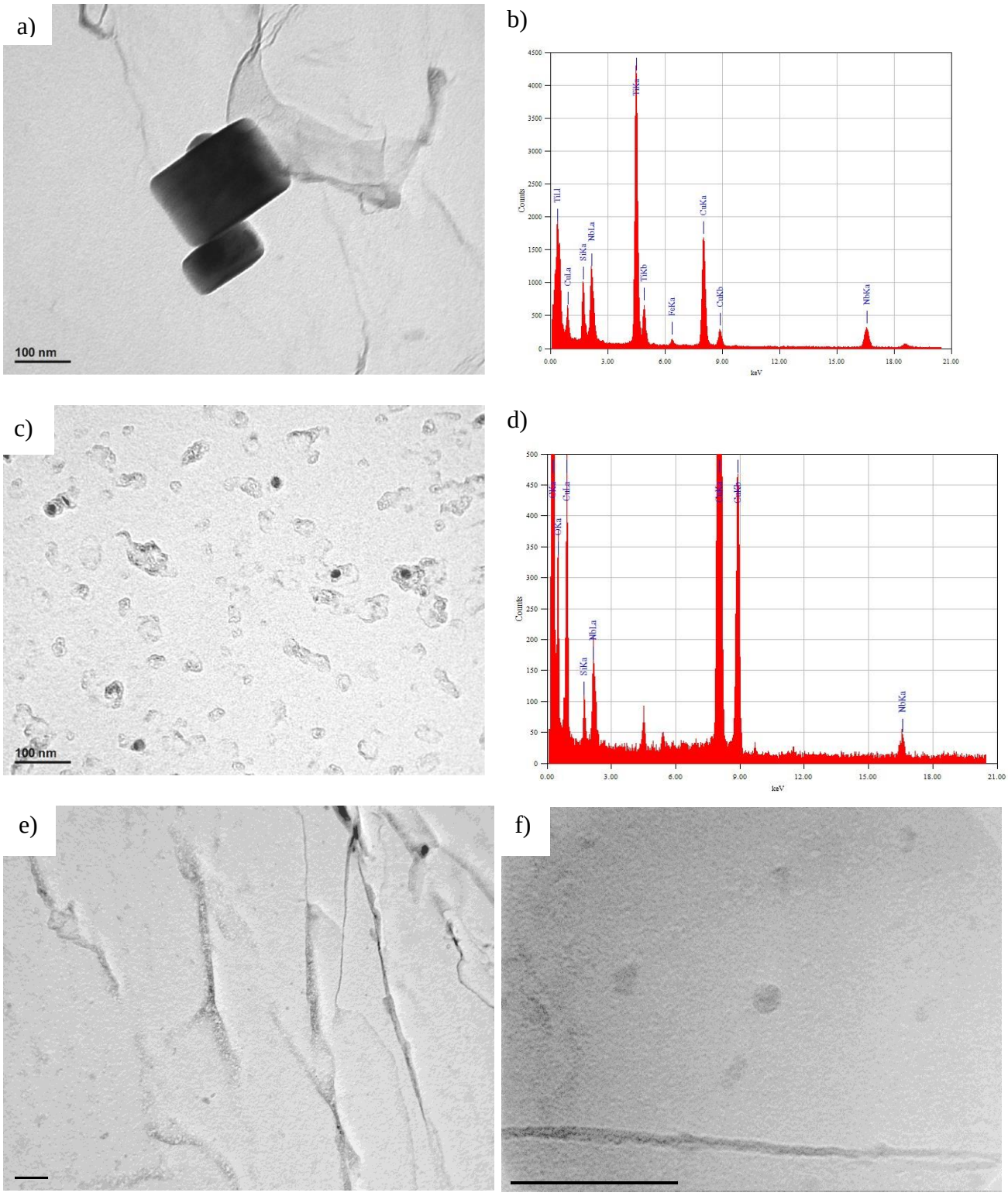

Figure 52. TEM images of the Nb precipitates found in the simulations carried out at a) 1200°C, c) 1100°C and e) and f) 950°C and EDS spectrum of a) and b).

a)

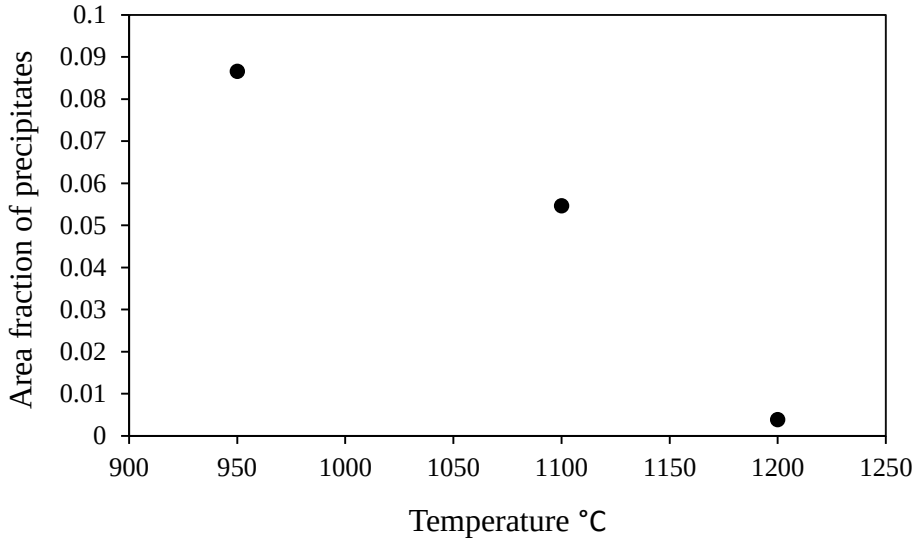

b)

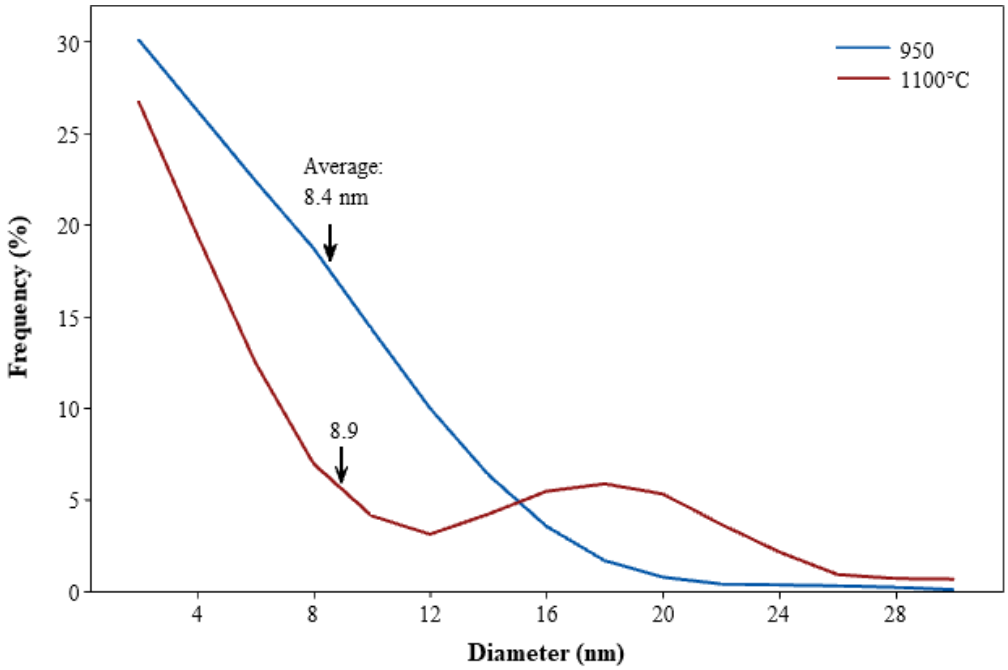

Figure 53. a) Area fraction of precipitates as function of temperature and b) particle size distribution of SIP in the simulations performed at 950 (blue line) and 1100°C (red line).

The difference in the particle size distribution could be related with the nucleation sites for precipitation, the first stage of precipitation occurs rapidly after the deformation at the prior austenite grain boundaries and deformation bands, these precipitates coarsen quickly on further holding, if recrystallisation does not occur, the deformation leads to the formation of sub boundaries that provide new nucleation sites for a second stage of more general precipitation

[47], this might account for the difference in the precipitates size distribution in both conditions, the frequency of small particles is high in the simulation at 950°C since the precipitation takes places not only in PGABs at the initial stage of precipitation, but also in sub boundaries caused by the deformation wherein small precipitates nucleate and have shorter times to coarsen after the nucleation, besides, the low temperatures increase the supersaturation of Nb that lead to a progressive precipitation in multiple sites . On the other hand, at 1100°C the lack of sub boundaries due to the recrystallisation confines the nucleation of precipitates to the PAGBs, some of the precipitates formed at the early stages of precipitation (probably dynamically during deformation) can coarsen in the interval of time which includes the delay of 1 second between deformation and quenching plus the cooling time from 1100°C to the temperature at which the coarsening of precipitates stops.

4.4.6. Microhardness

The microhardness values at different deformation temperatures is shown in Figure 54. Although the hardness is also influenced by the state of niobium (either in solid solution or precipitate) and the grain refinement, there is a direct correlation with the fraction of phases obtained after quenching, in the range of temperatures from 830°C to 1030°C the phases consisted mainly of dynamically transformed ferrite during deformation and martensite transformed during quenching, the hardness increases gradually with temperature in a similar mode that the volume fraction of DIFT decreases (see Figure 48), however, the predominant phase is martensite since the fraction of DIFT varied from 25 to 19% and only few packets of bainite can be seen in the microstructure (Figure 45 a), b) and c)), thus the high hardness values are associated with the high volume fraction of martensite. A dramatic change in the microstructure and a substantial drop in the hardness is observed in the simulation at 1100°C, in this case the microstructure is dominantly bainitic, despite the volume fraction of DIFT (which is the softest phase) is too small, the transition from martensite to bainite in the phase transformation accounts for the significant drop in the hardness. Finally, at 1200°C the hardness increases to values relatively similar to those measured at the deformations below 1100°C, despite having only 8% of DIFT the hardness is not higher due to a moderate amount of bainite in the microstructure.

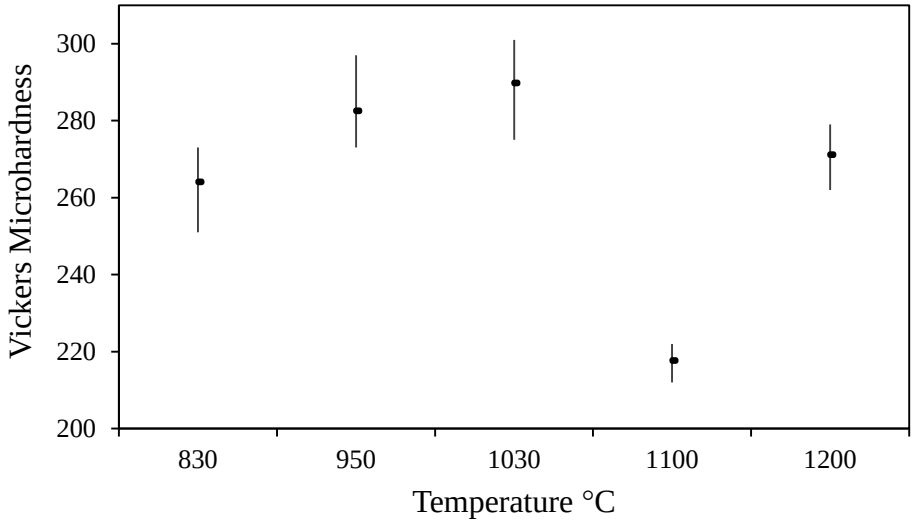

Figure 54. Vickers microhardness as function of the deformation temperature.

An important correlation can be seen as well between the variation of hardness and the amount of DIFT at each deformation temperature, the conditions that presented higher amount of dynamic transformation also show more variation in the hardness, due to the contrasts in the soft and hard phases present in the microstructure.

It is important to mention that the Vickers microhardness values are substantially lower than those obtained by nanoindentation due to the indentation size effect, the hardness increases as the indentation size decreases specially in the sub-micrometre depth regime [110]. Nanoindentation gives a very localised hardness while the microhardness gives the average hardness of a large area, this implies that the nanoindentation is much more sensitive to the heterogeneities in the material and large variations in the hardness even in the same phase are common. Table 7 compares the hardness between both methods, the nanoindentation was performed in a region of 20 μ^2 without indents in the DIF grains.

Table 7. Comparison in the micro and nanohardness in the simulation performed at 1200°C.

	Vickers microhardness				**Nanohardness (GPa)**				**Conversion of GPa to Vickers**		
Temperature	**Indents**	**Min**	**Max**	**Average**	**Indents**	**Min**	**Max**	**Average**	**Min**	**Max**	**Average**
1200°C	9	262	279	**271**	14	4.3	5.8	4.86	439	592	**496**

4.5. Discussion

4.5.1. Estimations on the recrystallisation of austenite and critical strains for DIFT and DRX

The PTT diagrams constructed with the Dutta & Sellars precipitation model provided a good estimation of the extent of recrystallisation in the HTP alloy at different deformation temperatures, Figure 39 and Figure 44 show a good match between the model and PAGBs observed after quenching, however, the model underestimates the start of the SIP of Nb at 1100°C since precipitation was observed at this condition as shown in Figure 52 c), according to model the time required for the initiation of SIP at 1100°C is excessively long even at larger strains as shown in Figure 55, while in this work SIP is observed in the quenched specimen. Due to the high content of Nb in the HTP alloy the recrystallisation at 1100°C and SIP can occur simultaneously, this might represent an advantage for finish rolling in TMCP if the times between rough and finish rolling are not long enough to cause significant coarsening of SIP, the precipitation observed at 1100°C does not prevent the recrystallisation thus, additional roughing passes could be probably added to increase the volume fraction of SIP and still conserve a recrystallised and finer austenite, in subsequent deformation passes at lower temperatures during finishing, the prior formation of precipitates during roughing could enhance the grain refinement along with the fresh strain induced precipitates formed during finishing. It is well known that Nb in solid solution retards the recrystallisation by solute drag effect, if Nb(C,N) precipitation occurs during rough rolling without suppressing the recrystallisation, the effectivity of soluble Niobium to retard the recrystallisation will decrease in subsequent deformations due to the reduction in the content of dissolved niobium, however, the formation of fine and evenly dispersed Nb(C,N) precipitates can outweigh the loss of the solute drag effect on the retardation of recrystallisation, precipitates can act as potent pining sites able to impede or retard the recrystallisation, there is evidence that Nb(C,N) precipitation has a stronger effect on the recrystallisation kinetics than soluble niobium [47], the incubation time for austenite recrystallisation is increased and the recrystallisation growth rate is much slower due to the pinning effect of Nb(C,N) precipitates.

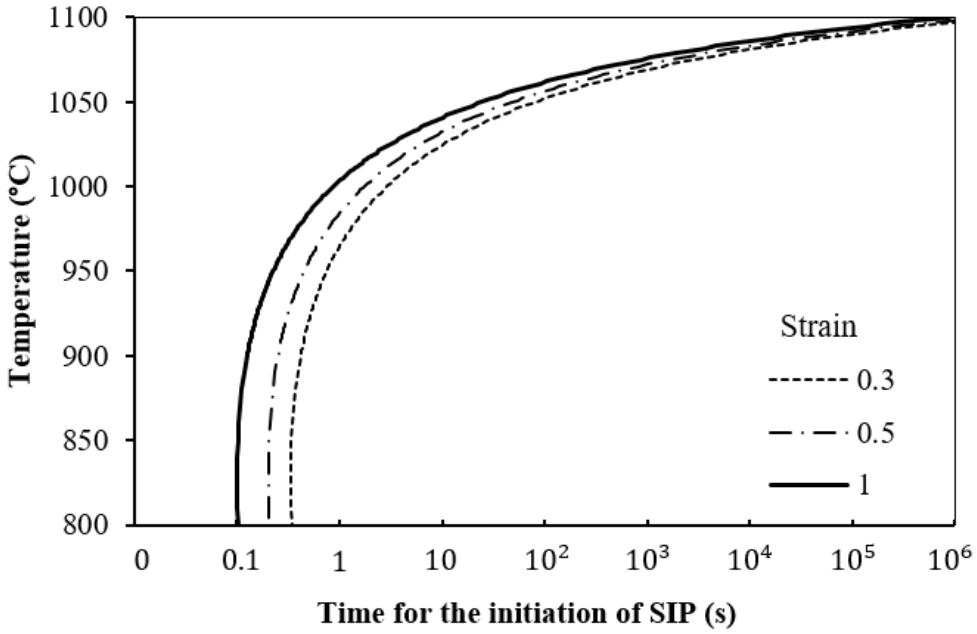

Figure 55. Time required for the initiation of SIP at different deformation temperatures and strains according to the model.

The double differentiation method was useful to detect the onset of DIFT and DRX at different simulation temperatures, however, it is necessary to use high order polynomials to fit the experimental flow curves so as to obtain more reliable results. According to Jonas et al [66], [107], who analysed 63 flow curves obtained by hot compression tests on a 0.019%C plain C, a 0.11%C Nb microalloyed and a 1.56%Mn-1.56%Si Nb-modified TRIP steel, when the fitting procedure only considers the initial part of the flow curve (such as the procedure in this research) a polynomial of at least 8th order must be used, on the other hand, when the fitting contemplates the entire flow curve a polynomial of at least 11th order is necessary, lower order polynomials may fail to detect the initiation of DIFT and even of DRX. The critical strains can be obtained with great precision when the rules aforementioned are followed, for the onset of DIFT and DRX were determined to accuracies of about +/– ½% and +/– 2% respectively [63].

However, differently to Jonas et al, in this research the flow curves were obtained by plain strain compression test, it was found that the onset for DIFT and DRX can be easily detected using 6th order polynomials as well, nevertheless, the critical strains obtained showed unexpected trends that did not show good agreement with the amounts of DIFT and recrystallisation observed. 9th order polynomials on the other hand, showed more plausible

critical strains that fitted more consistently with the microstructures observed. The variation between the values of the critical strains estimated using 6^{th} and 9^{th} order polynomials ranged from 4 to 16% for DIFT, and 1 to 4% for DRX. Thus, although 6^{th} order polynomials show a good correspondence with the real flow curves and DIFT and DRX are detectable, it is recommendable to use higher order polynomials to detect the critical strains with better accuracy.

The comparison between the results obtained with the double differentiation method and the PTT diagram constructed with Dutta & Sellars model showed good match in most of the conditions, it is important to remember that there is a fundamental difference in the definition of the beginning of the recrystallisation between both methods, the double differentiation method finds the onset of DRX by detecting changes in the strain hardening in the flow curves, whereas the model of Dutta & Sellars defines the initiation of recrystallisation (t_{05x}) as the time required for deformed austenite to achieve a 5% of recrystallisation, thus t_{05x} occurs after the onset of DRX. For instance, while the double differentiation method detects DRX at 1030°C and 1100°C, the PTT diagram estimates t_{05x} at 0.7 and 0.07 seconds after the deformation at 1030°C and 1100°C respectively, both methods provided a good predictions confirmed by microstructural observation. However, the simulation at 950°C showed contrasting results between both methods with regards to the initiation of the recrystallisation, DRX was detected by the double differentiation method while the PTT diagram shows the t_{05x} curve far away from 950°C. A careful examination of the PAGBs showed in Figure 44 b) revealed the presence of a few small polygonal grains located mainly at the junction of three grains which can be an evidence that DRX occurred to some extent, the recrystallised fraction was 3.2% after the evaluation of two micrographs at 200x with the point counting method [112]. Although the PTT diagram predicts well the suppression of the recrystallisation due to the initiation of SIP, it seems that curve that define the initiation recrystallisation is underestimated, it is possible as well that the suppression of recrystallisation occurs at lower fractions than 5% of SIP in the HTP alloy.

It was unexpected to detect DRX at 950°C with the double differentiation method, there is evidence reported in the literature that no recrystallisation occurred in steels with 0.09% of Nb deformed in a single pass at temperatures below 1000°C [113], besides, the analysis of particles in the carbon extraction replicas showed that the deformation at 950°C conducted to important

strain induced precipitation (Figure 53), however, it is probable that a small amount DRX has been suppressed by the immediate formation of SIP during and after the deformation.

An explanation of the findings in the simulation at 950°C can be provided by analysing the curve obtained with the double differentiation method showed in Figure 56 a). As described in Section 4.4.1, the expected curves show three inflection points when DIFT and DRX occur during deformation, the two minimums indicate onset of DIFT and DRX while the maximum in between is associated with a decrease in the rate of DIFT [62], after the second minimum (the onset of DRX), $-(\partial\theta/\partial\sigma)$ is expected to increase rapidly as the peak stress is approached [104] (as shown in Figure 41 c). In the condition deformed at 950°C, a fourth in inflection point (a second maximum) was detected almost immediately after the onset of DRX as shown in Figure 56 a), this change in $-(\partial\theta/\partial\sigma)$ might indicate a sudden decrease in the softening caused by the strain induced precipitation of Nb that supresses the progress of DRX and provides precipitation strengthening, this is in agreement with the very small amount of recrystallised grains observed in the PAGBs and the abundant strain induced precipitates observed in the carbon extraction replicas. An analogous trend is also observed in the simulation at 830°C (Figure 56 b) where DRX did not happen, after the first minimum that indicates the onset of DIFT, the curve reaches a short plateau at a stress of around 210 MPa due to the deceleration of the dynamic transformation, then a maximum is reached at 213.6 MPa accompanied with an accelerated decrease in $-(\partial\theta/\partial\sigma)$. The drastic drop $-(\partial\theta/\partial\sigma)$ in the curves obtained with the double differentiation method could be related to the onset of SIP at a stress below the critical stress.

a)

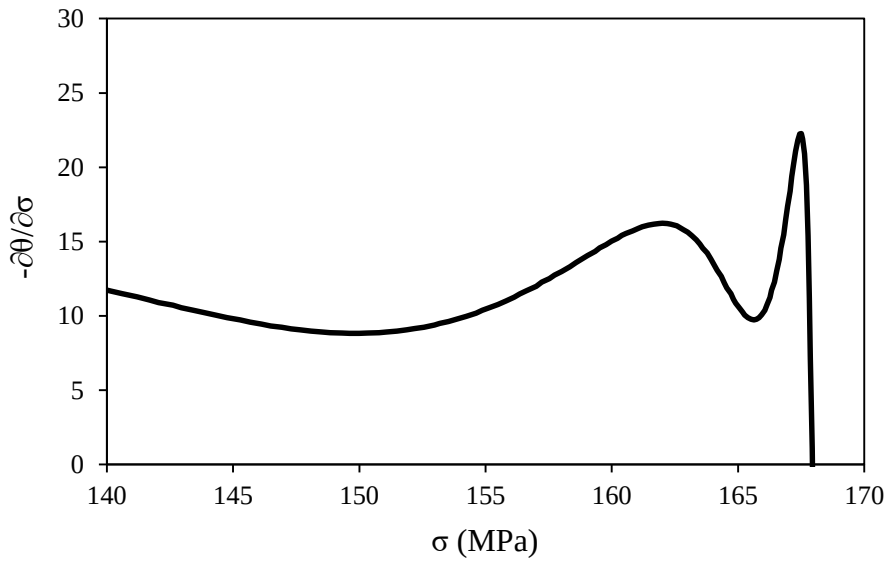

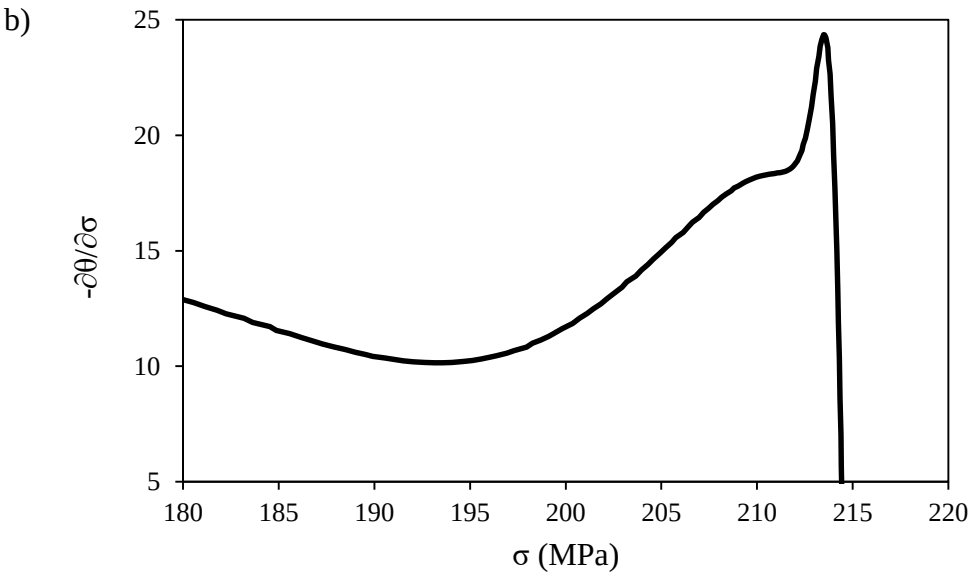

Figure 56. Curves obtained with the double differentiation method showing the second derivative -($\partial\theta/\partial\sigma$) versus σ, the plots were obtained from the experimental stress-strain curves of the simulations performed at a) 950°C and b) 830°C.

Dynamic strain induced precipitation at 950°C is likely to occur in the HTP alloy in an extent enough stop the insipient DRX, this finding could be a hot topic since the formation of precipitates large enough to supress the recrystallisation requires a time that might be longer than that for the onset of DRX, Cao et al [114] assessed the effect of dynamic SIP on DRX in steels with high contents of Nb in the range of the current HTP alloy, in their work hot compression deformation tests were carried out at temperatures from 950 to 1100 ◦C and reductions of 60% at strain rates from 0.1 to 0.005 s−1, according to their results, SIP can occur during deformation when the strain rate is lower but cannot delay the starting of dynamic recrystallization because of the longer induction period. Another research carried out by Cho et al [115] reported that SIP during deformation could not prevent DRX, his conclusion is based on the observation of flow curves of torsion tests carried out in a 0.045 % Nb-microalloyed steel at 900°C, different strains and a strain rate of $0.5s^{-1}$.

However, in the current work there is solid of evidence that DRX occurred and yet the PAGBs remained 97% unrecrystallised after the deformation, besides, abundant SIP was observed showing a size distribution of particles large enough to stop the recrystallisation (around 6 nm [116]), even though there is a holding time of one second between the deformation and

quenching, and therefore it cannot be known with accuracy the particle size distribution just after the deformation, it is very likely to have a fraction of strain induced precipitates that coarsen to a size large enough suppress DRX during deformation. Differently to the work published by Cho et al and Cao et al, the strain rate in the current simulations was is significantly larger ($1s^{-1}$) which in consequence delays the onset of DRX, this might allow for SIP have a major influence in the evolution of the deformed austenite grains. As for the curves obtained with the double differentiation method, it can be seen that the fourth inflection point appears at a stress just slightly higher than the critical stress for DRX, this inflection point might be associated with an increase in the strain hardening caused by the stoppage of the recrystallisation followed by precipitation strengthening and work hardening that make the value of $-(\partial\theta/\partial\sigma)$ decrease rapidly. It could be concluded that at 950°C the occurrence of SIP and DRX is almost simultaneous and the precipitation of Niobium can deter the progress of DRX for the recrystallised fraction is too small.

4.5.2. The dynamic transformation of ferrite

The current work supports the dynamic ferrite transformation mechanism proposed by Basabe et al [61] in which the deformation causes the displacive transformation of Widmanstätten ferrite plates that then merge by coalescence and form polygonal grains. The evidence obtained by OM, SEM, SPM and nanoindentation matched well with the extensive research generated around this hypothesis [21], [64], [109], most of the simulations presented a microstructure with regions where dynamically transformed ferrite in form of plates aligned in a single direction and polygonal grains coexisted in the same colony, polygonal grains were observed subjacent to the ferrite plates in the prior austenite grain boundary and also intragranulary due to the coalescence of plates. The dynamic transformation took place in all the deformation temperatures regardless the gradient with respect to Ae_3, however, the volume fraction showed a strong correlation with the extent of recrystallisation as shown in Figure 57.

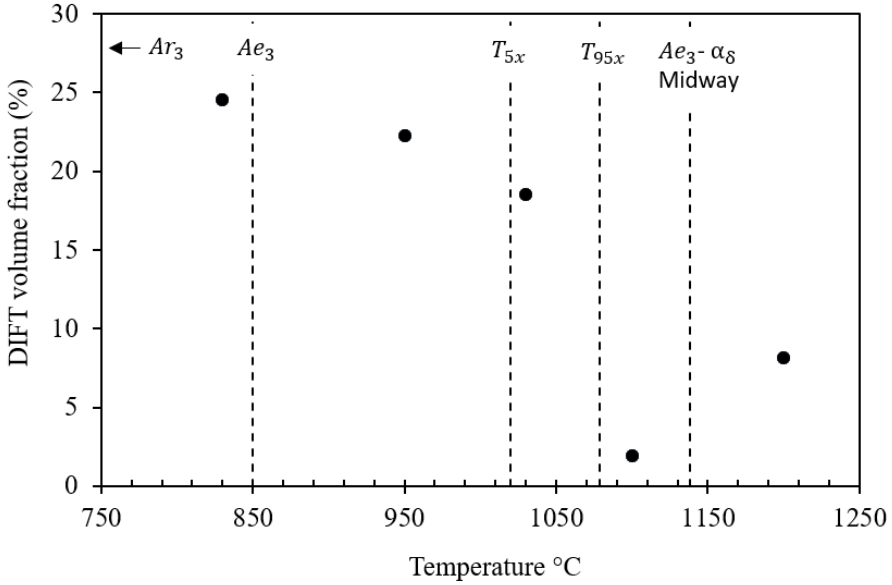

Figure 57. Volume fraction of DIFT as function of the critical and deformation temperatures in the HTP alloy.

In the non-recrystallisation region at 830°C (20°C below the Ae_3) and 950°C (100°C above Ae_3), there was only a subtle decrease of 2.2% in the amount of dynamic transformation as the temperature increased despite the considerable gradient in the deformation temperature, more importantly, the deformation below Ae_3 seems not to have major effect on the acceleration of the dynamic transformation. The microstructures in Figure 45 a) and b) show very similar characteristics; abundant ferrite grains are found along the PAGBs and intragranulary as product of the coalescence of ferrite plates, the wedge shape of the Widmanstätten colonies is significantly distorted which is an indicator of the rapid transformation process favoured by the low temperatures. As the temperature increases to 1030 °C slightly above $T_{5\%}$, the volume fraction of DIFT commence to decrease faster, the micrograph in Figure 45 c) shows Widmanstätten ferrite colonies shaped as sharp wedges, the merging of ferrite plates within the PAGBs appears in a lower extent probably due to a reduction in the driving force for coalesce caused by the insipient recrystallisation.

A substantial fall in the dynamic transformation occurs at 1100 °C in the full recrystallisation zone, only 1.9% of the microstructure is estimated to be DIFT and the rest is primarily bainitic ferrite and some martensite formed during quenching (Figure 45 d)), the dynamically transformed ferrite is difficult to observe either as plates or grains. The decrease in the volume

fraction of DIFT shows strong correlation with the full recrystallisation of the austenite, probably the dynamic transformation is discouraged as the recrystallised fraction increases and consumes the stored energy generated during deformation, since DIFT is also a restoration processes that requires energy, the competition with the recrystallisation affects the amount of DIFT. Another factor influencing the drop in the volume fraction of DIFT at 1100°C is related to the thermodynamics for the γ to α transformation, the lowest driving force for DIFT in whole range of temperatures of the austenite field is found at the midway between Ae_3 and the δ – ferrite phase field [21], at this temperature the Gibbs free energy for the dynamic transformation is the highest and a natural energetic barrier hinders the dynamic transformation, in the HTP alloy the midway between Ae_3 and the α_δ phase field is 1138°C which accounts for the lowest fraction of DIFT in the simulation at 1100°C. Finally, at 1200°C the amount of DIFT increases again as the temperature moves away from the Ae_3 - α_δ midway, nevertheless, the volume fraction is still small (8%) which evidences the influence of the recrystallisation on the decrease of DIFT, the micrograph showed in Figure 45 e) shows ferrite transformation in some PAGBs and the presence of some colonies of very thin Widmanstätten ferrite plates growing within the recrystallised grain.

Grewall et al [21] studied the dynamic transformation of Widmanstätten ferrite in all the austenite phase field in a steel containing 0.06wt%C-0.3wt%Mn-0.01wt%Si subjected to compression at strains of 0.3 and 0.65, their results showed a great correlation between volume fraction of DIFT and the free Gibbs energy barrier to the transformation as illustrated Figure 58 b) and c).

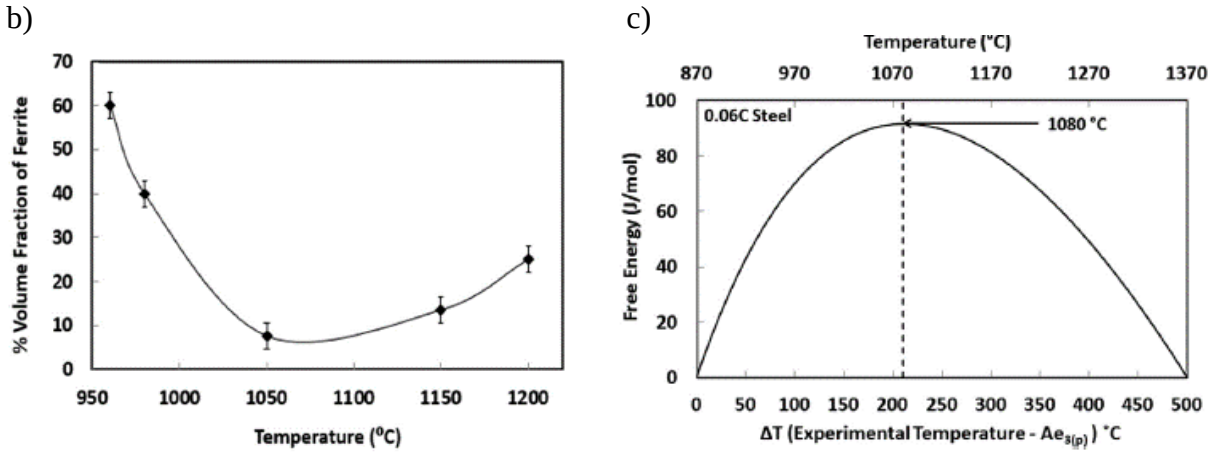

Figure 58. Volume fraction of ferrite a) and estimation of the free energy barrier for the ferrite dynamic transformation in the whole austenite field b) reported by Grewall et al [21].

The current research matches somewhat with the findings reported by Grewall et al; i) a minimum in the volume fraction of DIFT was found close the midway between Ae_3 and α_δ phase field, ii) the amount of ferrite increases as the deformation temperature approaches to any of those temperatures and iii) the volume fraction of DIFT is smaller at higher temperatures. However, the recrystallisation seems to exert a larger influence on the DIFT in HTP alloy since the volume fraction falls more rapidly as the recrystallised fraction increases. DIFT can be considered as restoration mechanism in deformed austenite, the transformation takes places by mechanical activation in which shear accommodation and dilatation work lead to the displacive formation of Widmanstätten ferrite plates within the parent austenite [64], the transformation consumes part of stored energy provided by the deformation and restores the austenite to a certain extent. The dynamic transformation and the recrystallisation show a strong correlation, for instance, the critical strain for DRX is clearly affected by the critical strain for DIFT which appears at lower strains, the expected decrease in the critical strain for DRX as the temperature increases is not clearly fulfilled (see Figure 42 a)) and instead, both critical strains vary in the same fashion. Another example of the correlation of both mechanisms is observed in the sudden drop of the DIFT fraction as the recrystallisation fraction increases. DIFT and RX are restauration mechanisms that operate in tight cooperation, however this correlation has been scarcely studied.

4.5.3. Scanning probe microscopy and nanoindentation, a useful tool for the analysis and quantification of DIFT.

The use of contact scanning probe microscopy has been little exploited in the analysis of steel phases, the very low scanning rate due to mechanical scanning process, the limitation to low magnifications to acquire high resolution images and the slowness to move the probe from one scanning area to another on the specimen, make this methodology unattractive compared to SEM and modern EBSDs which are faster and more flexible scanning techniques. However, the ability of SPM to produce 3D images on the specimen surface can give this technique an important advantage for the phases characterisation. An adequate sample preparation of the specimen prior to the SPM scanning might aid to the identification and quantification of phases that differ in the topography, such is the case of DIFT in the current work.

There is a few research in the microstructural characterisation of steel by SPM, doubtlessly, one of the most relevant contributions of this technique to the understanding of the steel phases is the observation of the surface relief caused by the transformation of extremely thin plates of bainitic ferrite in a carbide free bainitic alloy [117], this research provided evidence by atomic force microscopy (a non-contact SPM method) to understand the displacive nature of the bainitic transformation, in a latter work, the same methodology was used to study the bainite transformed on cooling of the HTP alloy [118]. Pioneer work in the identification of DIFT was carried out by Ahn et al [119] who used SPM, nanoindentation and EBSD to quantify the phases in a microstructure consisting of perlite, and statically and dynamically transformed ferrite in a steel containing Fe–0.1C–1.5Mn–0.25Si–0.05V–0.01Ti–0.04Nb–0.0036N as illustrated in Figure 59, the samples were prepared by the conventional method of grinding and polishing and then etched with 3% Nital solution. The morphology of DIF grains presented by Ahn differs with that found in the current work, probably because the dynamic ferrite was surrounded mainly by static ferrite which must have a similar response to etching, and therefore show similar height in the topography.

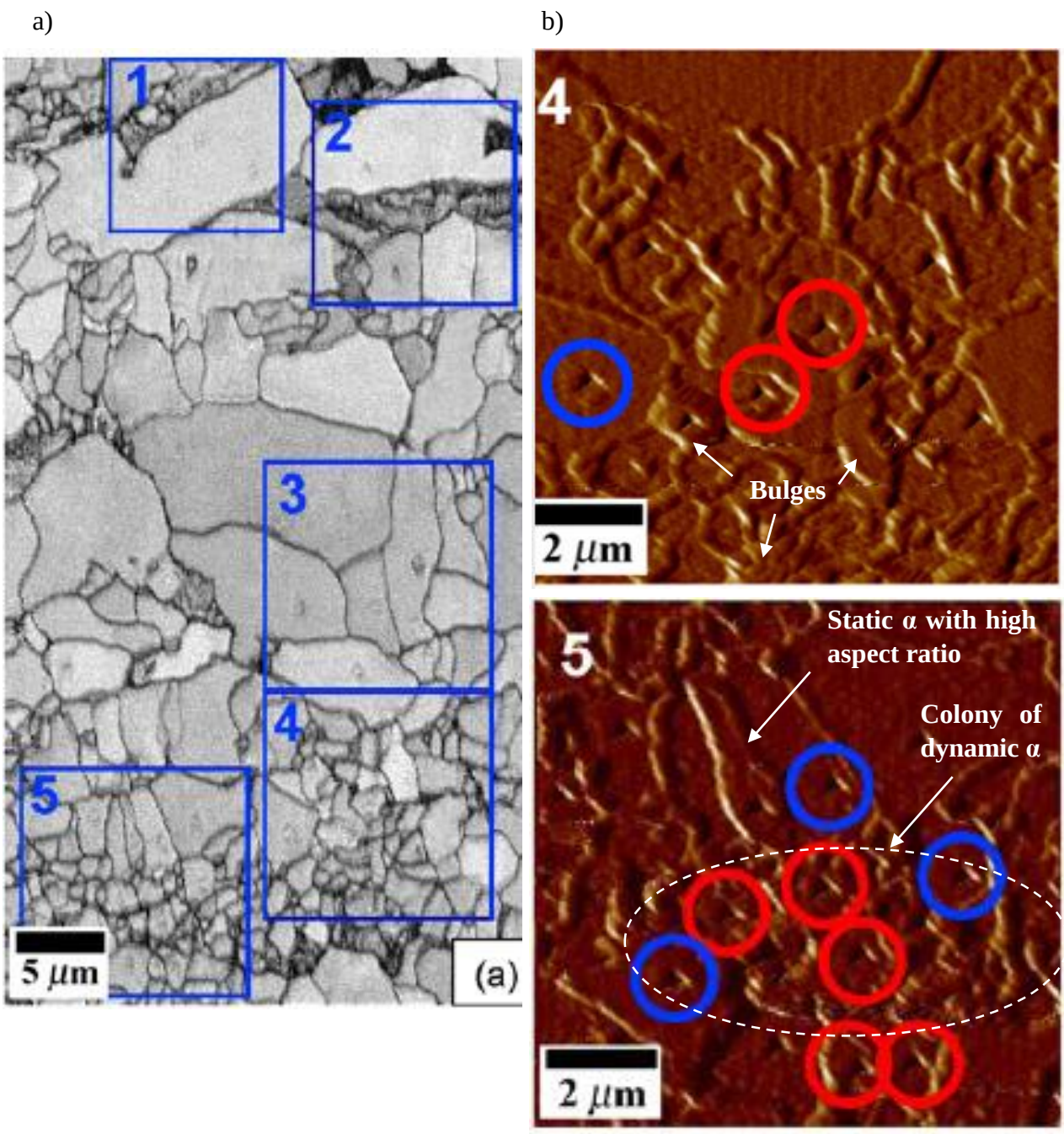

Figure 59. (a) EBSD band contrast map after the indentations and (b) SPM image with indicating indents on dynamically (red circles) and statically transformed ferrite (blue), after Ahn et al [119].

However, some similarities between the current work and Ahn's can be observed comparing the EBSD and SPM images, the region with abundant DIFT appears subtly at higher elevation (mainly in image 5 of Figure 59 b)), and some ultrafine grains observed in EBSD appear in the

SPM image in form of bulges located at junction points and subjacent to the reportedly static ferrite grains with high aspect ratio, such grains with high aspect ratio might be an indicator of the prior transformation of dynamic Widmanstätten ferrite plates that merged and then coarsened during the slow cooling (2°C/s) after deformation. The dynamic ferrite reported lower hardness values than static ferrite, the bulges were also indented as shown in Figure 59 b) image 4 but the results were not reported.

Another research that used EBSD, contact SPM and nanoindentation to differentiate ferrite from martensite in a DP980 dual phase steel was conducted by Zhang et al [120], samples were polished using standard metallographic techniques and then the surface was additionally prepared by two methods; a) chemical-mechanical polishing conducted by vibratory polishing using a 0.05 µm colloidal silica suspension for 60 min, and b) etched with Nital 3%. In SPM both preparation methods showed differences in the topography between the martensite and ferrite, nevertheless, the polishing with silica showed better contrast between the phases and ferrite appeared at heights up to 50 nm. Figure 60 a) and b) shows the match between EBSD and SPM techniques in the detection of phases, martensite appears darker in both maps while ferrite shows a brighter colour, both images were obtained from the same sample position. The validation of phases was done by nanoindentation as shown in Figure 60 c) and d), larger displacements correspond to ferrite since the phase is softer. The average hardness value for the martensite was 8.4 GPa and 4.0 GPa for the ferrite.

The findings in Zhang's work fit with the results obtained in the current research, the electrolytic polishing of the specimens led to a surface with large differences in the height between the ferrite and the hard matrix (either bainite or martensite), in ultrafine grains of diameters of around 1µm the average height was around 140 nm, whereas coarse grains of diameters larger than 4µm presented heights of around 350 nm. It appears that the other works carried out so far about the characterisation of ferrite by SPM converges to some extent with the results presented in this work, it is important to notice that the specimen preparation has a direct influence in the topography of the phases, higher contrasts in the height scale ease the phase quantification, the electrolytic etching produces great contrasts between ferrite and the hard phases.

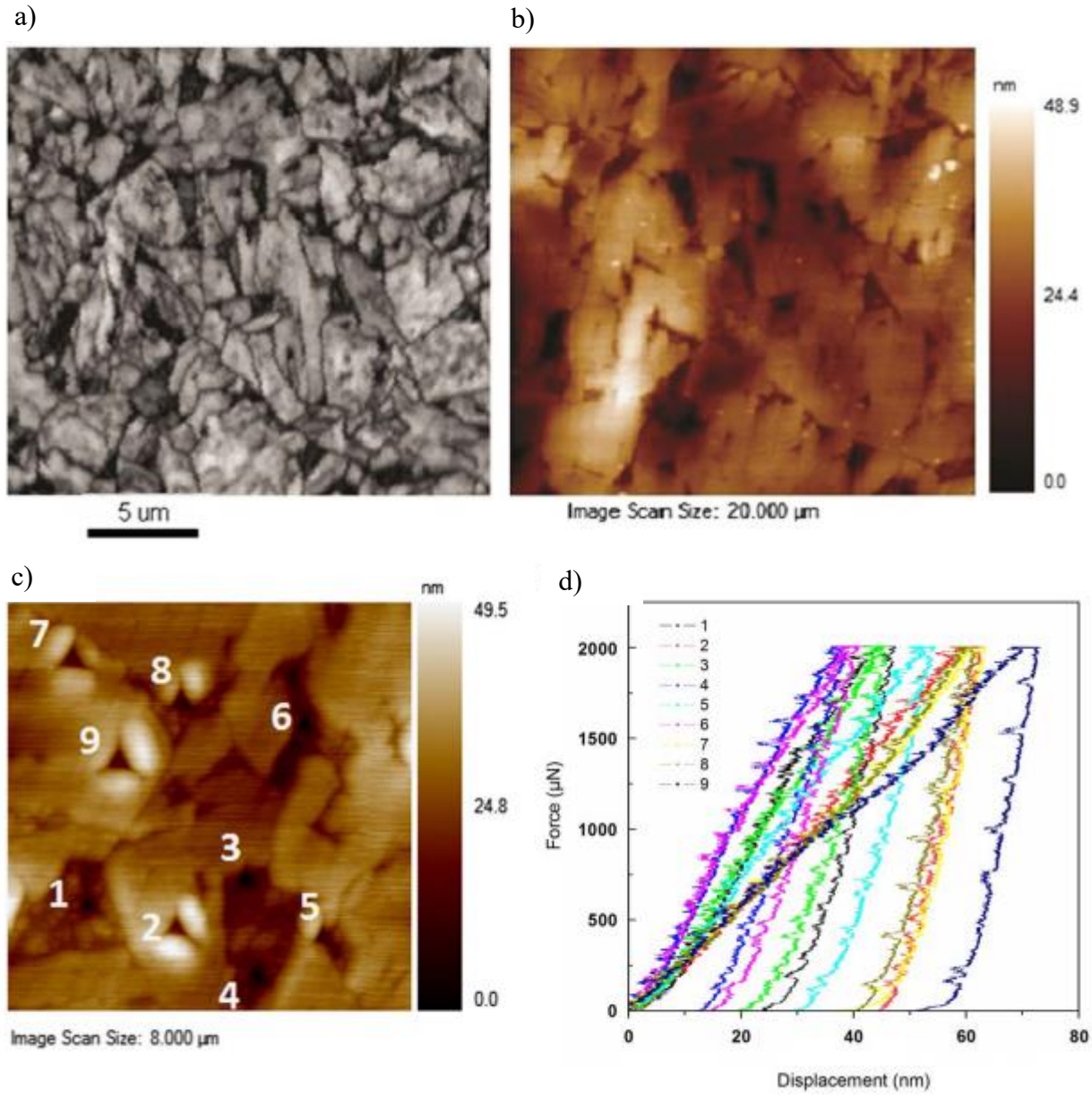

Figure 60. EBSD, SPM and nanoindentation results reported by Zhang et all in a DP980 dual phase steel. EBSD pattern image quality map a), SPM topographic map showing the depth scale bar on the right of the map with units of nanometres (b). SPM image showing indents in zones with different depth d) with their corresponding load and displacement curves d).

As for the nanohardness evaluation, the nanoindentation is not a consistent method to evaluate the hardness of DIFT due to the strong dependence between the hardness and the DIF grain size, however, it is important to remark that the nanoindentation is quite a useful tool for the identification between soft and hard phases, for instance, although the martensite – austenite

(MA) islands also appeared as regions with higher surface height after etching, the hardness is higher than the matrix (Figure 61 a)) and around 10 times higher than in a DIF grain of 2.8µm of diameter (Figure 61 b)).

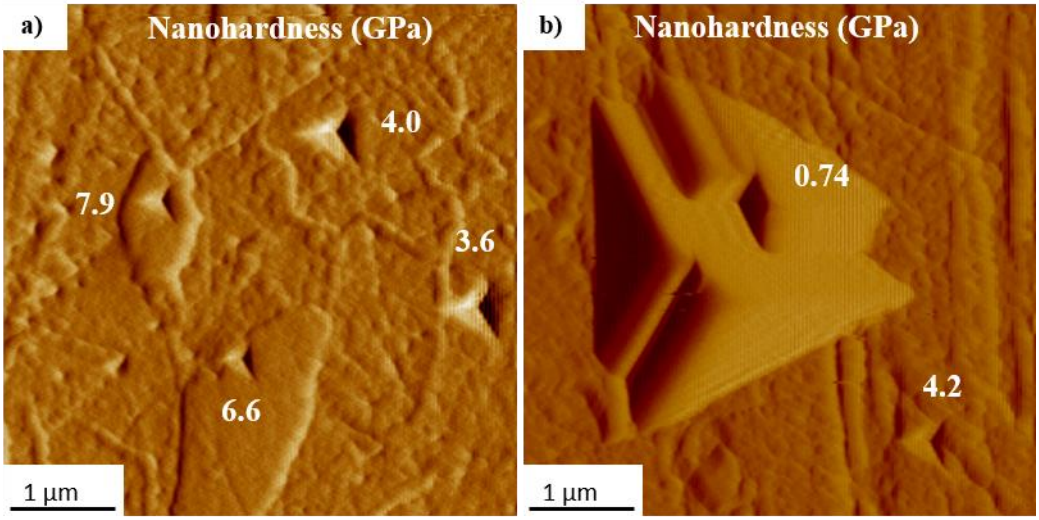

Figure 61. SPM gradient scans showing the difference in hardness between the matrix (bainite), a) MA islands and b) a DIF grain in the simulation at 1100°C.

The combination of nanoindentation and SPM can be a powerful methodology to separate and quantify the DIFT in a hard phase matrix, however, apart from the disadvantages of this methodology described at the beginning of this section, the tip convolution during the SPM scanning brings an additional shortcoming in the observation of the morphology of the DIF grain. Larger DIF grains show greater surface height and consequently are more affected by the tip convolution, for instance, the diameter of the grain showed in Figure 61 b) was measured in the x direction of the SPM image before and after the indentation, since the height of the grain decreased due to the deformation, the diameter changed substantially from 4.3 µm to 2.8 µm after de indentation (35% smaller). Conversely, the size in ultrafine grains is slightly affected by the effect of the tip convolution, Figure 62 shows a grain that changed its size from 790 nm to 760 nm after the indentation (3.8% smaller), thus, this methodology loses accuracy as the average ferrite grain size increases, the volume fractions estimated by SPM in the simulations at high temperatures with apparently coarse grains (1100°C and 1200°C) show an important deviation in the DIFT content, whereas, in simulations at lower temperatures that

showed an average DIF grain size of around 1 µm, the volume fractions were slightly affected by the tip convolution. It is important to recall that during the volume fraction estimation described in Section 3.11.1 a portion of the convolution effect contribution to the ferrite fraction is discriminated, thus, the volume fraction estimated for simulations with ultrafine grains is quite acceptable.

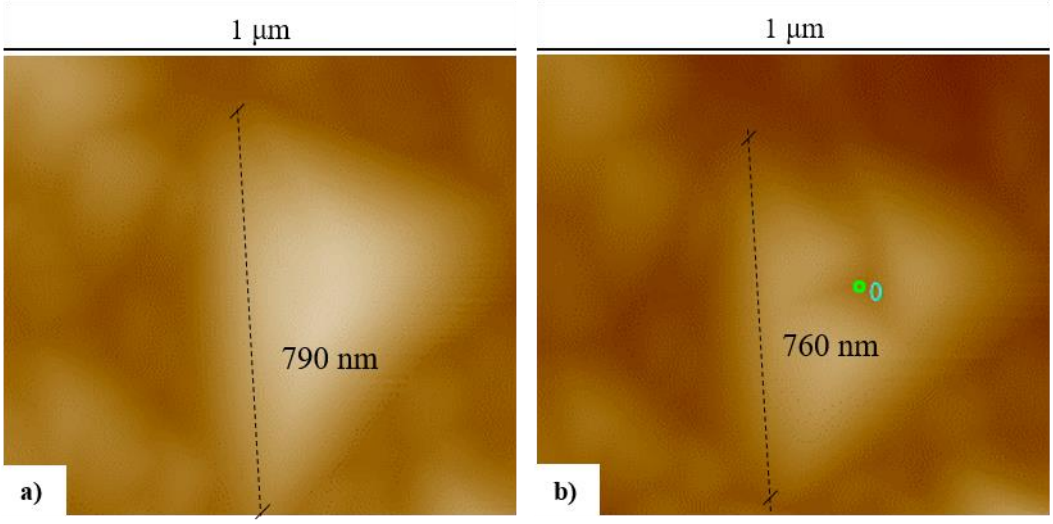

Figure 62. SPM topographic images showing the effect of the tip convolution on the grain size before a) and after b) the indentation.

There are other important drawbacks caused by the tip convolution that affect the morphology of DIF grains in the SPM mapping; the grain boundaries of DIFT cannot be observed, besides, other features on the vicinity of the grain boundary such as small MA islands and cementite carbides observed in SEM (Figure 46) are also hidden within the convoluted ferrite grain, the high values of hardness obtained in the grain boundaries of the convoluted ferrite grains (Figure 31) might be influenced by the presence on MA islands which cannot be seen in the image because of the tip convolution.

Despite the important disadvantages in the operation, imaging and hardness testing with the SPM-nanohardness instrument, the high 3D contrast achieved in the mapping provides a superior advantage for the characterisation of ultrafine ferrite compared to other methods. A frequent practice to quantify DIFT is based on a metallographic method that produce high contrast between ferrite and martensite [21], [58], [68], [72], [70], quenched samples are

prepared with standard metallographic methods and etched with 3% Nital solution, then a second etching with a 10% aqueous sodium metabisulfite ($Na_2S_2O_5$) is performed to enhance the contrast, finally the volume fraction of DIFT is quantified in a software using micrographs. However, the accuracy of this method relies on the capacity to transform only martensite during quenching, any fraction of bainite would cause deviations in the quantification of DIFT since bainite can also reveal light-coloured with both 3% Nital and the with aqueous sodium metabisulfite ($Na_2S_2O_5$) [121], this might represent a challenge in the separation of phases for steels prone to transform bainite during quenching such as low carbon steels, a very precise system of deformation and heat treatment able to provide ultrafast cooling rates immediately after the deformation would be necessary to prevent the bainite formation.

An similar method to estimate the volume fraction of DIFT based on the colour contrast between phases was carried out with optical micrographs (OM), the specimens were etched with 2% Nital but without the etching with 10% aqueous sodium metabisulfite, instead, the contrast between the phases was increased with the software ImageJ as illustrated in Figure 63 a) and b).

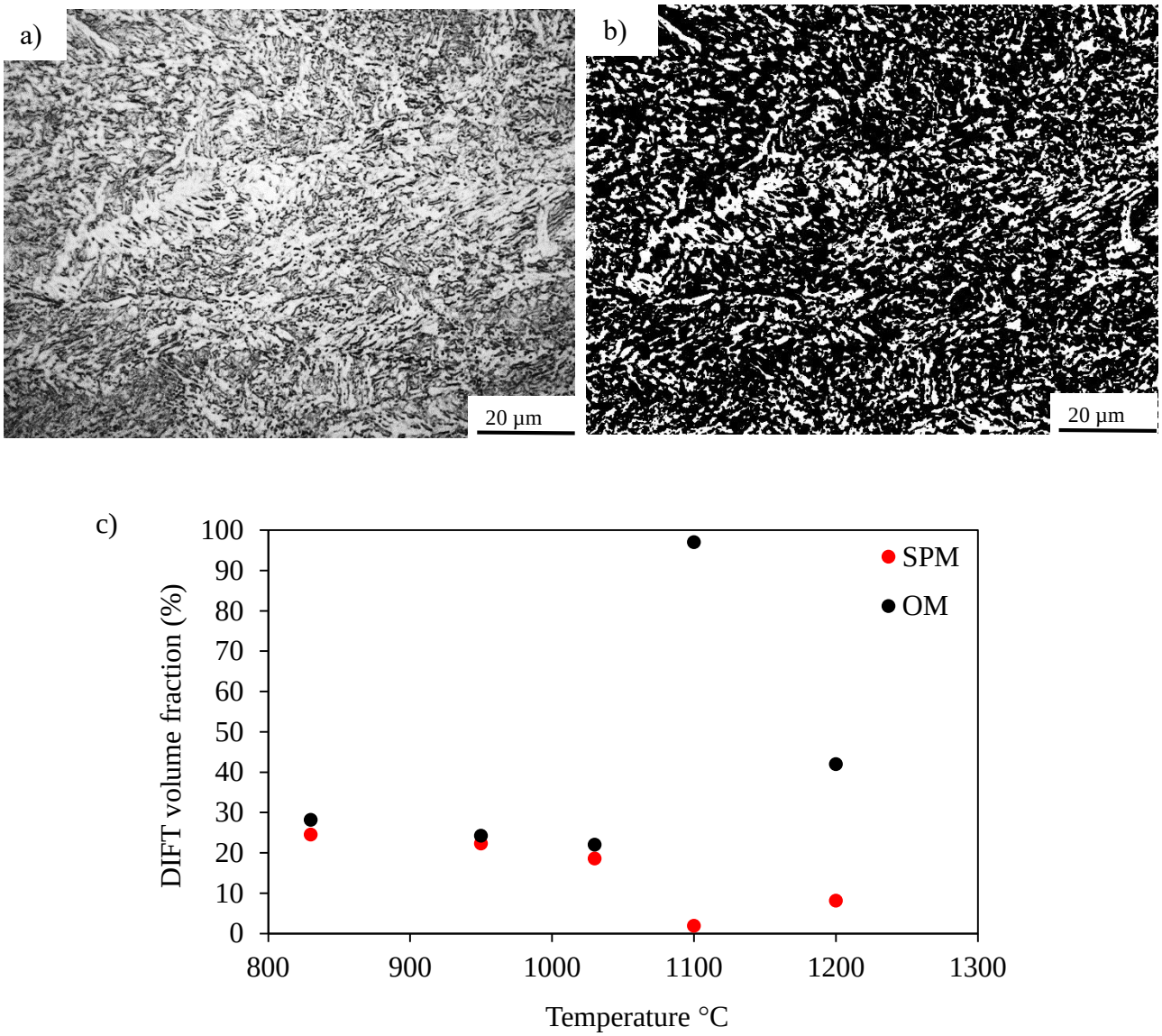

Figure 63. Estimation of the volume fraction of DIFT with optical micrographs. a) Original micrograph corresponding to the simulation at 830°C, b) post-processed image in the software ImageJ and c) comparison between the estimations of the volume fraction of DIFT in SPM and optical microscopy (OM).

The estimation of the volume fraction of DIFT with SPM and optical micrographs shows a good match in the conditions that presented small fractions of bainite (from 830 to 1030°C), however, there is an obvious discrepancy in the amount of DIFT estimated by both methods in the conditions that presented more bainitic transformation as shown in Figure 63 c), particularly at 1100°C where the dominant phase in the microstructure is bainite. The separation of DIFT by metallographic techniques is not accurate when other phases etch light coloured in the

microstructure. The combination of electrolytic etching and SPM scanning on the other hand, easily discriminates DIFT from martensite or bainite, the etching consumes the hard phase layers on the surface at a higher rate, allowing for a great contrast in the height scale between soft and hard phases.

EBSD is also a stupendous method to separate phases in steel, DIFT can be differentiated from bainite and martensite by analysing the internal misorientation within the grains. Since the misorientation in ferrite grains is lower than that in martensite or bainite packets, the quantification of DIFT can be done with grain orientation spread (GOS) maps. However, ferrite grains do not have a constant internal misorientation due to the dynamic transformation, i.e. grains are formed at different strains while the load is still applied to the material, consequently, the amount of accumulated deformation in the grains formed dynamically is not constant, furthermore, fresh and undeformed grains are formed post dynamically in the holding time between the deformation and quenching. This difference in the strain of the grains leads to variations in the aspect ratio and the average internal misorientation and complicates the definition of DIFT grains which is made by the user. Conversely, in SPM the extent of deformation of DIF grains does not affect the quantification of the volume fraction and more importantly, the definition of grains is not ambiguous since the contrast between phases is very high.

4.5.4. Selection of the rough rolling temperature

The selection of the rough rolling temperature is of paramount importance for the whole TMCP since the austenite conditioning starts at this stage, although the current work tested 5 different temperatures at a strain of 0.3 to simulate the rough rolling, for practical reasons the selection of the rough rolling temperature is confined to the highest temperatures where full recrystallisation occurs (1100°C and 1200°C) and lower loads are required to deform the material, however, the simulation below the full recrystallisation temperatures produced valuable information to understand the dynamic transformation of ferrite which is useful for the design of the finish rolling. Considering the benefits and drawbacks in the microstructural evolution between the deformations carried out at 1100°C and 1200°C, it is suggested that the best rough rolling temperature is 1100°C, although this condition showed a poorer performance

in terms of DIFT, the formation of strain induced precipitates might represent an important advantage for further finish rolling. Precipitates formed prior to the finishing passes could serve as immediate pining sites able to stop dynamic recrystallisation without the need of an incubation time, thus, it is probable that higher finishing temperatures are feasible due to the presence of prior precipitates formed during rough rolling.

4.6. Summary

A series of PSCTs were performed at an equivalent strain of 0.3 over a range of temperatures from 830°C to 1200°C in order to simulate the rough rolling of the HTP steel alloy during TMCP. The occurrence of dynamic processes such as recrystallisation, deformation induced ferrite transformation and strain induced precipitation of Nb was analysed using diverse techniques. The highlights of this chapter are summarised as follows:

1. The steel plate was pre-treated with an austenitising heat treatment during 2 hours at 1300°C in order to dissolve the Nb an exploit its benefits as a grain refiner. Most of the Nb was successfully dissolved since NbC precipitates were not observed in the carbon extraction replicas in TEM, however, some coarse cuboidal Ti rich (Ti,Nb)(C,N) were found in the replicas which is an evidence that Nb cannot be fully dissolved in the HTP alloy by the austenitising heat treatment. Nevertheless, the amount of Nb precipitated in the (Ti,Nb)(C,N) can be considered negligible since it must represent an insignificant fraction of the total Nb.

2. The deformation at different temperatures led to microstructures with different degrees of recrystallisation, the observation of the prior austenite grain boundaries showed full recrystallisation at 1200°C and 1100°C, partial recrystallisation at 1030°C and insignificant recrystallisation at 830°C. The deformation at 950°C showed insipient recrystallisation since only a fraction of 3% of recrystallised grains was observed. The PTT diagrams constructed for HTP alloy with Dutta & Sellars model, and the double differentiation method applied to the flow curves gave a good prediction of the final state of austenite in each deformation temperature.

3. The deformation induced ferrite transformation occurred in all the deformation temperatures, the observations in OM, SEM and SPM showed that DIFT obeys the transformation mechanism proposed by Basabe et al, in which the deformation causes the nucleation of Widmanstätten ferrite plates followed by coalescence that transforms the plates into polygonal grains. The volume fraction of DIFT increased as the deformation temperature approached to the Ae_3 or to the δ-ferrite field, at 830, 950 and 1030°C the microstructures presented important amounts of DIFT ranging from 19 to 25%.

4. The contact SPM and nanohardness evaluations are powerful tools for the identification and quantification of DIFT. The electrolytic etching leaves the ferrite grains exposed on a superior height with respect to the matrix allowing for an effective separation and quantification of phases using SPM images. As for nanohardness, single phases can be analysed with high precision due the small size of the indent, ferrite grains showed hardness values significantly smaller than the matrix allowing for a reliable validation of DIFT. However, the accuracy of both methods rely on the ferrite grain size, the imaging in SPM of coarse ferrite grains is severely affected by the tip convolution, an overestimation up to 35% in the grain diameter was detected in grains of around 3μm, conversely, grains of around 1 μm are slightly affected by the tip convolution, thus, contact SPM is a reliable technique if the average grain size is very fine in the order 1 μm. With regards to the nanohardness evaluation, since DIF grains appear as bulges after the electrolytic etching, the method is not a consistent to assess the mechanical properties of DIFT due to the strong dependence of the hardness on the grain size, coarse grains gave unrealistic low values of hardness as result of the inexistent interaction of dislocations with neighbouring grain boundaries.

5. Due to the high content of Nb in the HTP steel alloy, considerable strain induced precipitation can take place even at temperatures as high as 1100°C where full recrystallisation occurs, very fine NbC precipitates with an average diameter of 8.9 nm were observed at such temperature.

Chapter 5. Finish rolling simulation

5.1. Introduction

In this Chapter, TMCP simulations were carried out in order to study the microstructural evolution of the HTP steel alloy in a multipass deformation scheme using two different finish rolling temperatures. The simulations were designed pursuing the occurrence of two phenomena which can notably refine the final microstructure; i) the strain induced precipitation (SIP) of niobium and ii) the strain induced ferrite transformation (DIFT). The former is well known for improving the austenite conditioning by retarding the recrystallisation during the deformation, while the latter provides exceptional grain refinement to the microstructure due to the formation of micrometric ferrite grains.

An important part of this chapter is focused on studying the effect of the finishing temperature on DIFT at temperatures both above the Ae_3 and between Ae_3 and Ar_3. There is a substantial difference in the stability of DIFT in such ranges of temperatures, above the Ae_3 the ferrite is thermodynamically unstable when the load is withdrawn, thus, when the material is maintained at temperatures above the Ae_3 a reverse ferrite to austenite transformation takes place gradually [122]. Conversely, at the metastable austenite region between the Ae_3 and Ar_3, the chemical Gibbs free energy for the γ to α transformation is much lower, thus DIFT is can be stable after the deformation and consequently the reverse transformation does not take place, according research carried out elsewhere DIFT can occur even after the deformation [20], [54].

There is much debate regarding the characteristics of DIFT in the ranges of temperature aforementioned, for instance, it has been reported that DIFT exhibits a polygonal morphology when it occurs between Ae_3 and Ar_3 [59], [71], whereas above the Ae_3, studies have shown that DIFT commences with the formation of Widmanstätten ferrite plates that then coalesce and evolve into polygonal grains [61]. Currently, there is not even a criterion to classify DIFT and different expressions have been used to name such phase, Beladi et al [12] used the term "dynamic strain induced transformation" (DSIT) to call the ferrite transformed dynamically at temperatures between the Ae_3 and Ar_3, while on the other hand, after the research carried out

by Basabe et al [61], [72], the expression “dynamic transformation” (DT) has been extensively used in numerous publications to refer to the plate-like ferrite transformed above the Ae_3. However, it is likely that DSIT and DT might be the same but there is not enough research to confirm it so far. In the current Chapter, several experiments and analysis were performed so as to prove whether DIFT has the same nature in both ranges of temperatures.

Another polemic topic also tackled in the current Chapter, is the transformation mechanism of DIFT. Various hypothesis have been formulated so as to elucidate the transformation mechanisms [20], [55], [59]–[61], nevertheless, there remains a discrepancy amongst researchers. One of most common shortcomings in most of the transformation mechanism proposed so far, is the impossibility to demonstrate whether the alleged DIFT was formed dynamically during the deformation or statically during quenching. In the current work, extensive evidence is provided to demonstrate the presence of DIFT in the microstructure and ambiguities with respect to whether the ferrite is formed dynamically or statically are overcome, besides, a thorough analysis is carried out in EBSD and a new transformation mechanism is formulated to explain DIFT.

5.2. Precipitation-time-temperature diagram for a strain of 0.22

In order to predict the effect of Nb on the recrystallisation during the finish deformation, a PTT diagram for a strain of 0.22 was constructed using the Dutta & Sellars model. After the rough deformation at 1100°C the grains are fully recrystallised and the prior austenite average grain size can be readily measured, this allows for the construction of the PTT diagram applicable for at least the first finishing pass.

According to the PTT diagram shown in Figure 64, the recrystallisation at 950°C and 810°C must be stopped by the precipitation of Niobium. It is important to mention that the diagram was constructed assuming that all the Nb is in solution, however, the rough deformation at 1100°C led to a small amount of Nb precipitation (see Chapter 4), such precipitation could not be accurately estimated and thus, there must be a slight overestimation of the stoppage of the recrystallisation in the diagram.

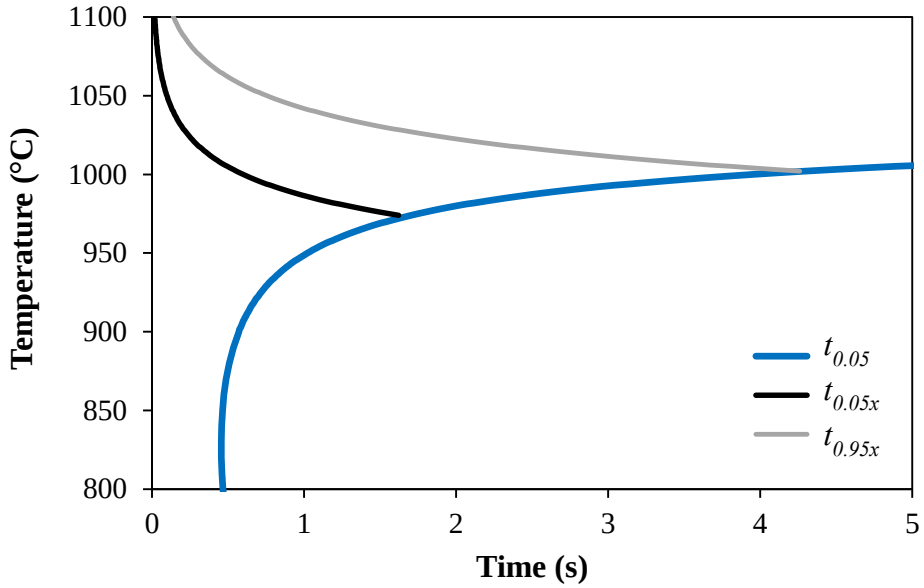

Figure 64. Precipitation-time-temperature (PTT) diagram for a strain of 0.22 and a prior austenite grain size of 25μm.

5.3. Results

5.3.1. X-Rays diffraction

X-Ray diffraction (XRD) was performed in order to obtain the lattice parameters of the main phases present in the microstructure, the test was carried out as a previous step to the EBSD analysis which uses the crystal lattice parameters to solve the EBSD patterns diffracted from the specimen during the test. Two samples with different processing conditions were prepared and analysed following the procedure described in Section 3.10. The first sample was obtained from the steel plate after the austenitising heat treatment, the microstructure in such sample is dominantly martensitic (bct) as previously shown in Chapter 4, the second sample was obtained from a PSC specimen deformed in multiple passes at total accumulated strain of 1.2 (simulation of Figure 93), the microstructure consisted of a mixture of martensite (bct) and around 31% of deformation induced ferrite (bcc).

It is important to remark that the tetragonality of the bct structure depends on the carbon content [123], the ratio between the axes, *c*/a, increases linearly as the carbon increases [124]. The two samples analysed with XRD have substantial differences with regards to the state of the carbon

in the microstructure. In the non-deformed sample, most of the carbon is present as an interstitial solid solution distributed more homogeneously within the martensitic microstructure, the carbon extraction replicas analysed in Section 3.9.1 showed that only few TiNb carbonitrides were not dissolved during the solid solution heat treatment, thus, the amount of interstitial carbon in the martensite phase must be near to the nominal content of carbon in the HTP alloy (0.045%). As for the deformed sample, the amount carbon in solid solution in martensite is expected to be much lower, since the sample underwent a TMCP simulation that led to abundant formation of carbides (mainly SIP of niobium and cementite). More details about the processing and results of the deformed sample are presented in Section 5.3.4.

Despite the significant microstructural differences, the XRD analyses produced almost identical results in both samples, the peaks observed in the diffraction patterns matched well with the main crystallographic planes of the bcc structure of ferrite. In the deformed sample, the difference between the bcc and bct crystal structures is so subtle that cannot be detected in the XRD analysis, the diffraction pattern showed a single peak in each diffracted plane for both structures as shown in Figure 65, this indicates that the peaks of the bcc and bct structures are overlapped at a very similar 2θ angle. For practical purposes for the further EBSD analysis, the ambiguity as to whether the crystal structure of martensite is bcc or bct can be omitted, and it can be assumed that both ferrite and martensite have the same bcc structure. The lattice parameters in the non-deformed and deformed sample were 0.2869 and 0.2872 nm respectively, such difference is insignificant and shows that the amount, distribution and state of the carbon in the HTP alloy has a negligible effect on the crystal lattice.

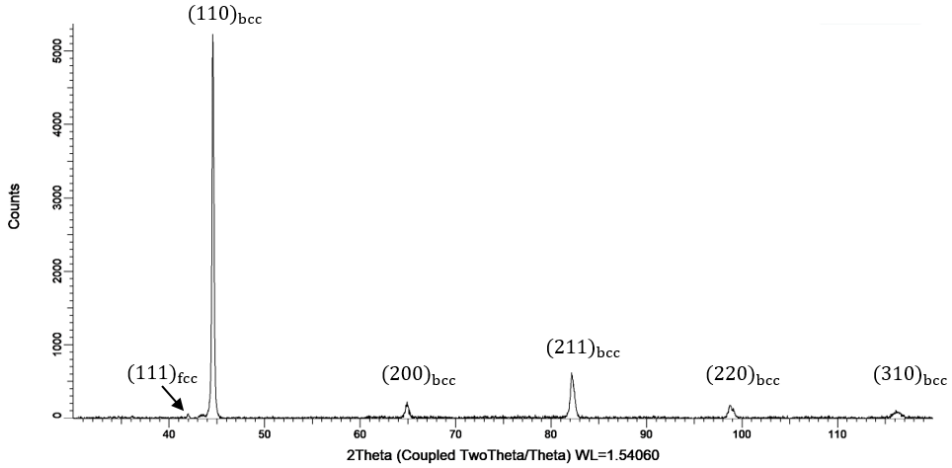

Figure 65. X-Rays diffraction pattern for the sample deformed at an accumulated strain of 1.2.

5.3.2. Finish rolling simulation at 950°C.

5.3.2.1. Flow behaviour and estimation of critical strains for DIFT and DRX

The complete flow curve showing the rough and finish deformations is illustrated in Figure 66, there is an obvious increase in the stress during the finishing passes due to the decrease in the deformation temperature. During the first finishing pass, the stress increases gradually as the specimen is strained, in the following two passes the stress increases quickly at the beginning of the deformation but then it slows down at around 180 MPa, then it increases monotonously until the deformation is stopped. It is important to highlight the drop in the initial flow stress after the first and mostly the second finishing pass, such behaviour in the flow stress indicates that a certain degree of restoration occurred during the holding time between passes. Recrystallisation or recovery can occur during the holding time, however, DIFT is likely to be the main cause of low initial flow stress values, since ferrite is considerably softer than recrystallised austenite [125]. Some similar works [58], [70] have reported lower than expected stress levels in the flow curves due to the occurrence of DIFT during in multipass deformation, such works also studied the HTP alloy using similar temperatures and strains to those used in this research.

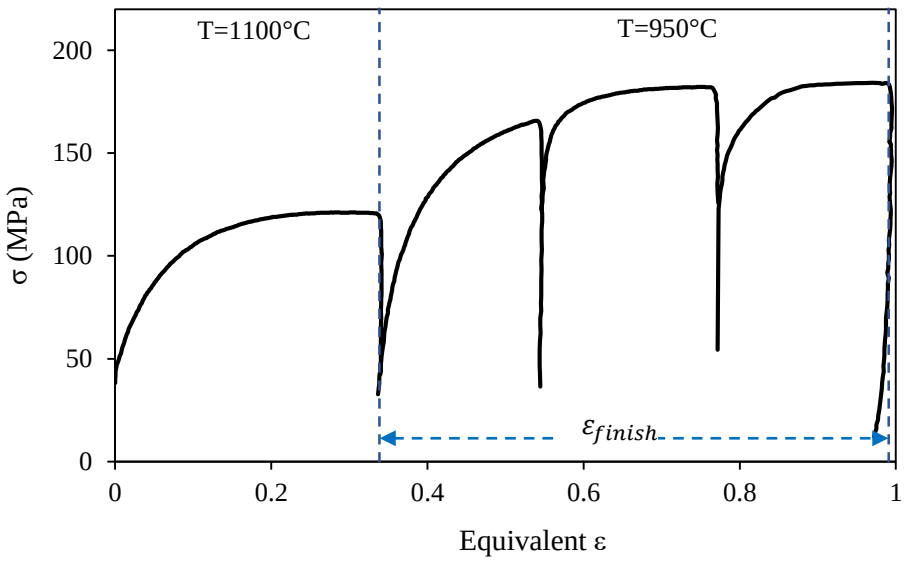

Figure 66. Flow curve showing a roughing pass at a strain of 0.33 at 1100°C followed by three finishing passes at a strain of 0.22 at 950°C applying a strain rate of $10s^{-1}$, a holding time of 10 seconds was added after each finishing pass.

In order to analyse the influence of DIFT on the flow curves during the finish rolling, the softening behaviour of the microstructure was studied following the methodology of the double hit deformation test [35], this technique has been widely used to measure the fraction of softening caused by the static recrystallisation or static recovery of austenite during the interpass time [39], [126], [127]. The method uses the flow stress curves obtained from two different deformation tests performed at constant strain and isothermal conditions. One specimen is deformed continuously to a large strain and the resulting flow curve serves as a reference for the determination of the fractional softening, this test is frequently called "monotonic test". A second specimen is deformed to a constant pre-strain at the same temperature as the monotonic test, then unloaded and held at the deformation temperature for a defined time interval, and then reloaded for a second deformation with equal magnitude of strain, this test is known as "interrupted test". The flow stress curves resulting from both tests are used to estimate the amount of fractional softening obtained during the holding time in the interrupted test.

One of the methods employed for the estimation of the fractional softening was developed by Kwon et al [128], who used a softening parameter X_A based on the area under the flow curves and is expressed as below:

$$X_A = \frac{A_3 - A_2}{A_3 - A_1} \tag{5.1}$$

where A_1 and A_2 are the areas under the flow stress curve of the first and second deformation in the interrupted test respectively, and A_3 is the area under the flow curve in the monotonic test over the strained region equivalent to the second deformation in the interrupted tests.

A monotonic finish rolling test was conducted in order to follow the methodology of the double-hit test, a PSC specimen was deformed in a roughing pass at a strain of 0.3 at 1100°C followed by a single finishing pass at a strain of 0.66 at 950°C (see condition A1, ε_5 in Figure 26,). Note that the only difference between the monotonic finishing test and the TMCP simulation shown in Figure 66, is that the former deforms the specimen to 0.66 of strain in a single finishing pass, whereas the latter, applies the same amount of the deformation but distributed in 3 finishing passes performed at 0.22 of strain.

The segment of the flow curve containing the finishing passes (ε_{finish} of Figure 66) was used as the interrupted test and plotted together with the finishing pass of the monotonic test as shown Figure 67 a). Then the equation 5.1 was used to estimate the fractional softening obtained during the interpass times in the finish rolling simulation as illustrated in Figure 67 b) and c). Note that for the estimation of the fractional softening in the second interpass time, the deformations 1 and 2 in the equation 5.1 correspond to the finishing passes number 2 and 3 respectively.

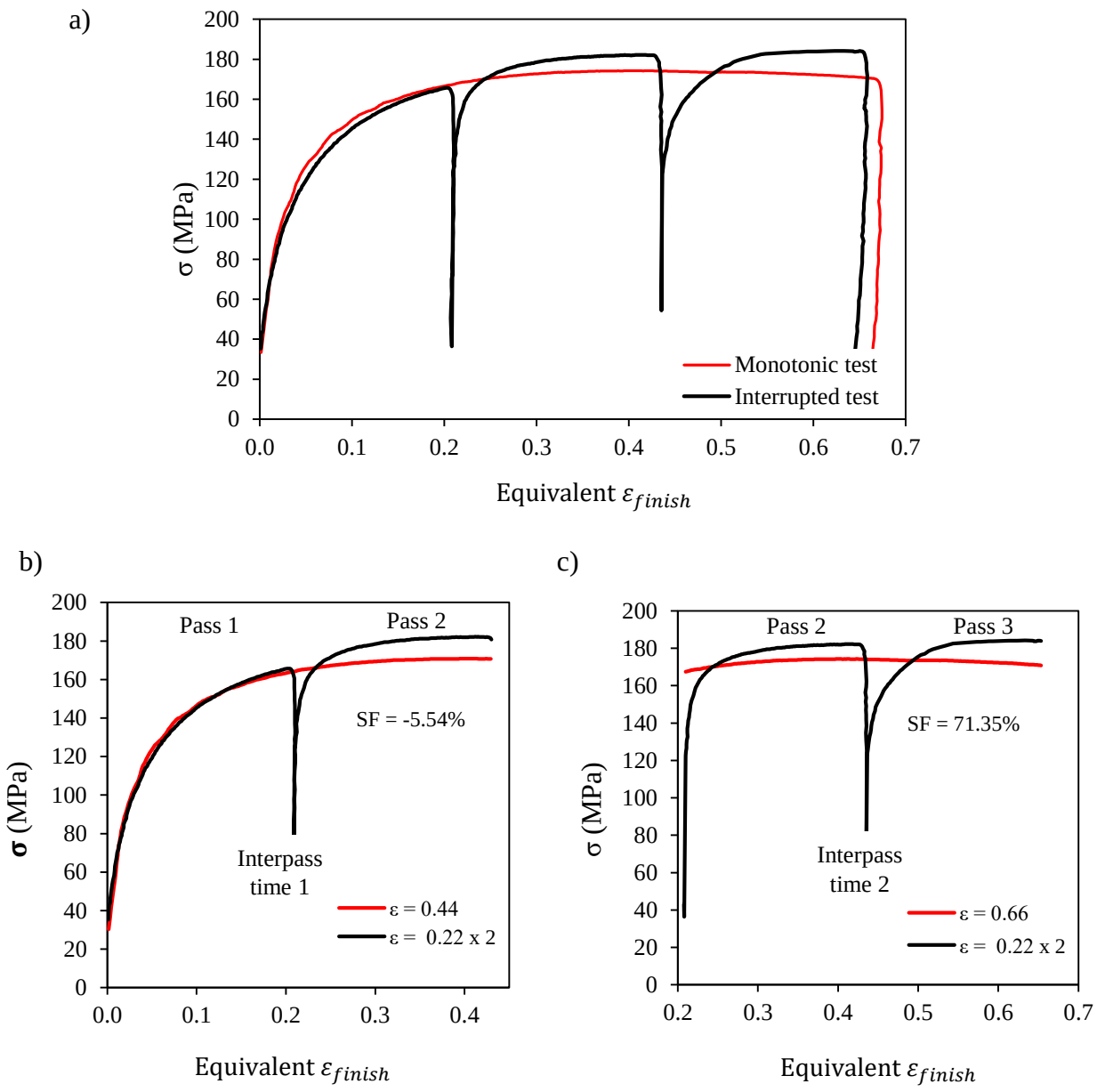

Figure 67. a) Flow stress curves used to estimate the fractional softening of austenite during the interpass times in the finish rolling simulation at 950°C. Softening fraction (SF=X_A·100%) obtained during b) the first and c) second interpass time.

In the second finishing pass the material experienced a subtle hardening of around 6%, whereas in the third pass the behaviour changed drastically since the softening obtained was 71%. Several softening and strengthening mechanisms can operate simultaneously or independently during the deformation or during the holding time; on the one hand, the material is hardened by dislocation strengthening, grain refinement and precipitation strengthening due to SIP of Nb, while in counterpart, recrystallisation, recovery and DIFT restore and soften the deformed microstructure. The subtle hardening in the second finishing pass and the remarkable softening obtained in the third pass, are associated to DIFT during deformation and its subsequent coarsening during the 10 seconds of interpass time.

The critical strains for DRX and DIFT for the rough and finishing passes were determined with the double differentiation method following the steps described in Section 3.4.1. The critical strains for both DRX and DIFT decreases as the number of deformation passes increases as shown in Figure 68, this behaviour is associated to the progressive accumulation of work hardening in the austenite as deformation passes are added. DRX and DIFT can be triggered at very low strains, which is unexpected at least for DRX, since the high content of Nb (either in solution or in form of precipitate) is expected to hinder the recrystallisation.

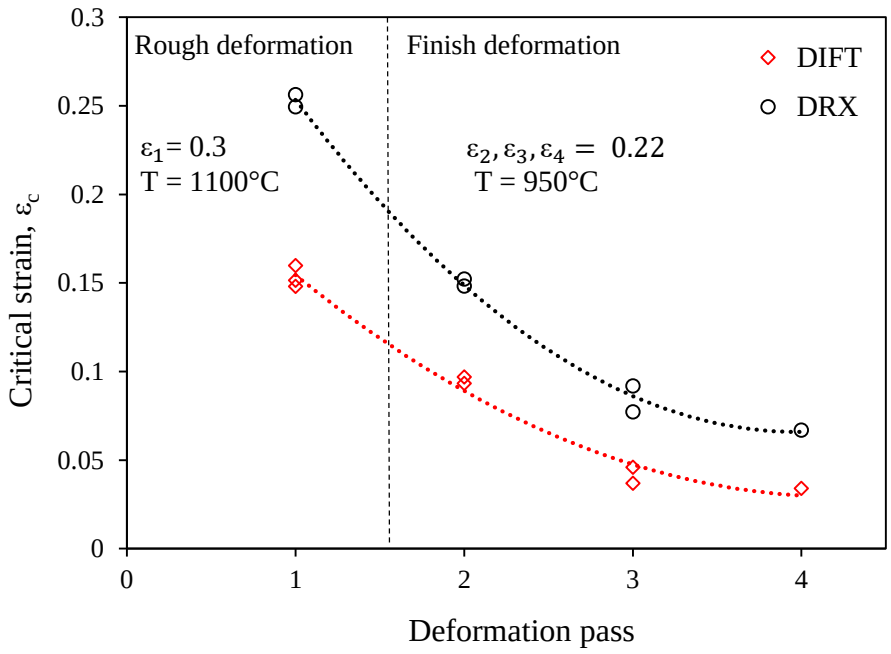

Figure 68. Critical strain for DIFT and DRX at different number of passes. Pass 1 corresponds to the rough deformation at 1100°C and a strain of 0.3, and passes 2, 3 and 4 correspond to the finish deformation at 950°C and a strain of 0.22.

Similar values in the critical strains were reported by Mendez-Fonseca et al [58], in their work, a multipass TMCP was simulated by torsion tests using very similar strains, holding times and chemical composition (HTP alloy), differently to this work, their simulation was carried out under continuous cooling conditions from 920 to 830°C and cooling rates from 0.75 to 15 °C. The authors reported critical strains from around 0.9 to 0.04 for DRX and 0.04 to less than 0.02 for DIFT. In the current work, the critical strains for DIFT and DRX were found at values as low as 0.03 and 0.07 respectively. Other works [69], [70], also studied similar multipass deformation in the HTP alloy, the critical strains for DIFT and DRX reported were quite similar to those reported in the current research.

5.3.2.2. Morphology of the prior austenite grain boundaries.

The evolution of PAGBs during the finish rolling simulation is shown in Figure 69. In the first pass (Figure 69 a) most of the microstructure remains unrecrystallised and the grains exhibit a moderate elongated shape in the rolling direction, however, some polygonal recrystallised grains appear mainly at the boundary junctions of deformed grains, the recrystallised fraction was 12% after the evaluation of several micrographs with the point counting method. Static recrystallisation during the holding time of 10 seconds seems to be insignificant as shown in Figure 69 b), the recrystallisation fraction was almost the same in the conditions with and without the holding time. The second finishing pass produced a highly deformed PAGs as shown in Figure 69 c) and Figure 69 d), the recrystallisation in these conditions was negligible (around 1% in both cases) and the holding time did not affect the morphology of the grains. Finally, the third pass led to significant recrystallisation (20%), Figure 69 e) shows how deformed grains are consumed by new strain-free recrystallised grains.

A summary of the grain size evaluation of the first two finishing passes is presented in Table 8. The PAGBs in the third pass could not be clearly revealed with aqueous picric acid solution after various attempts, thus the average grain size is not reported. Anyway, the extent of recrystallisation in the third pass is significant which means that the microstructure is undesirable for grain refinement purposes. Hereafter the microstructure in the third pass is not analysed for practical purposes.

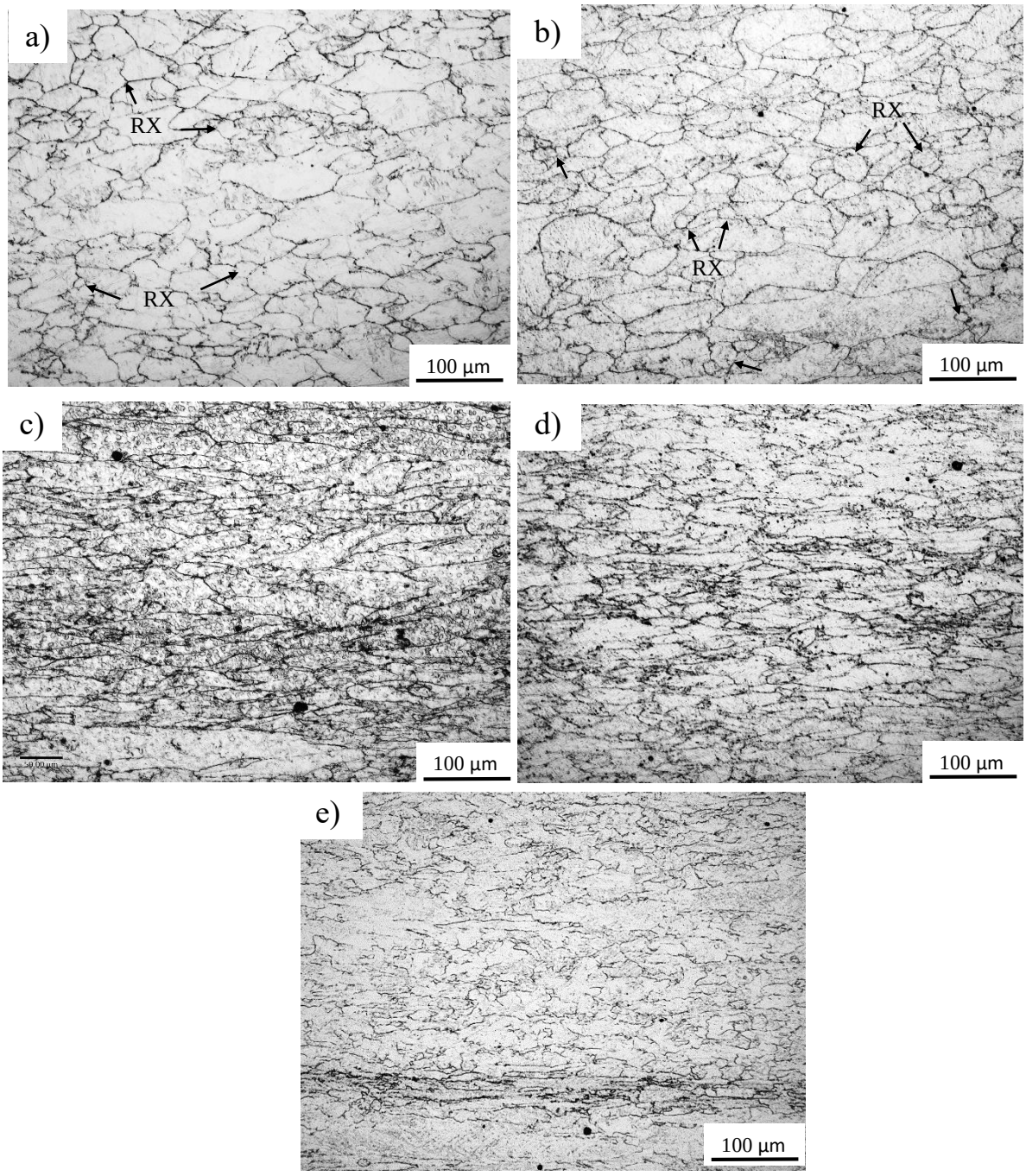

Figure 69. Prior austenite grain boundaries revealed in quenched samples after a) one pass, b) 1 pass + 10 seconds of holding time, c) 2 passes, d) 2 passes + 10 seconds and e) 3 passes + 10 seconds. The arrows in Figure 69 a) and b) indicate recrystallised grains.

Table 8. Prior austenite grain diameter measurements done with the intercept method of ASTM E-112, and recrystallised fraction estimated with the point counting method for the finishing passes at 950°C.

Specimen	Finishing condition	Recrystallised fraction (%)	Average grain diameter (µm)		Aspect Ratio
			Rolling direction	Normal direction	
A1	1 Pass	11.7	48.2	20.3	2.4
A2	1 Pass + 10 seconds	12.6	46.5	18.1	2.6
A3	2 Passes + 10 seconds between passes	1.2	70.4	12.4	5.7
A4	2 Passes + 10 seconds after each pass	1.3	68.4	11.3	6.1
A5	Pass 3 + 10 seconds after each pass	20	-	-	-

5.3.2.3. Microstructure

The microstructure in all the deformation conditions consisted of a mixture of deformation induced ferrite and martensite, DIFT appears in white colour in the optical micrographs whereas martensite appears dark as shown in Figure 70. The austenite grain refinement caused by the deformation provides more nucleation sites for DIFT leading to abundant ferrite formation with both morphologies, i.e. Widmanstätten ferrite plates and polygonal grains. Most DIFT shows intergranular nucleation at the PAGBs although intragranular nucleation is also observed. Widmanstätten ferrite plates appear aligned in a single direction within the prior austenite grains showing a high Schmidt factor, which is an evidence of the dynamic transformation during the application of the load. In the first pass, PAGBs are moderately elongated which allows for the growth of large ferrite plates within the grains as shown in Figure 70 a) and Figure 70 b), besides, polygonal ferrite grains are found primarily at the PAGBs and at the PAGBs junctions. The addition of a holding time after the first pass seems not to have a major effect on the microstructure.

As for the second pass, the deformation results in highly elongated and flattened PAGBs, thus, the growth of plates is confined to shorter lengths. Polygonal ferrite grains appear contouring large extensions of PAGBs. A subtle change in the microstructure can be observed after the holding time as shown in Figure 70 c) and d), ferrite plates exhibit a less sharp aspect and the

amount of polygonal ferrite seems to increase after the holding time. The change in the microstructure might be given by continuous coalescence of plates during the holding time, Figure 70 d) shows that within the colonies of Widmanstätten ferrite the boundaries between plates commence to disappear. The most plausible explanation for such change in the morphology, is the decomposition of plates at a stage prior to the polygonisation of grains. During the holding time after second pass, the deformed austenite stores enough energy to continue the coalescence of plates to some extent, this behaviour is not observed in the holding time after the first pass which means that the coalesce process can occur statically after certain amount of deformation.

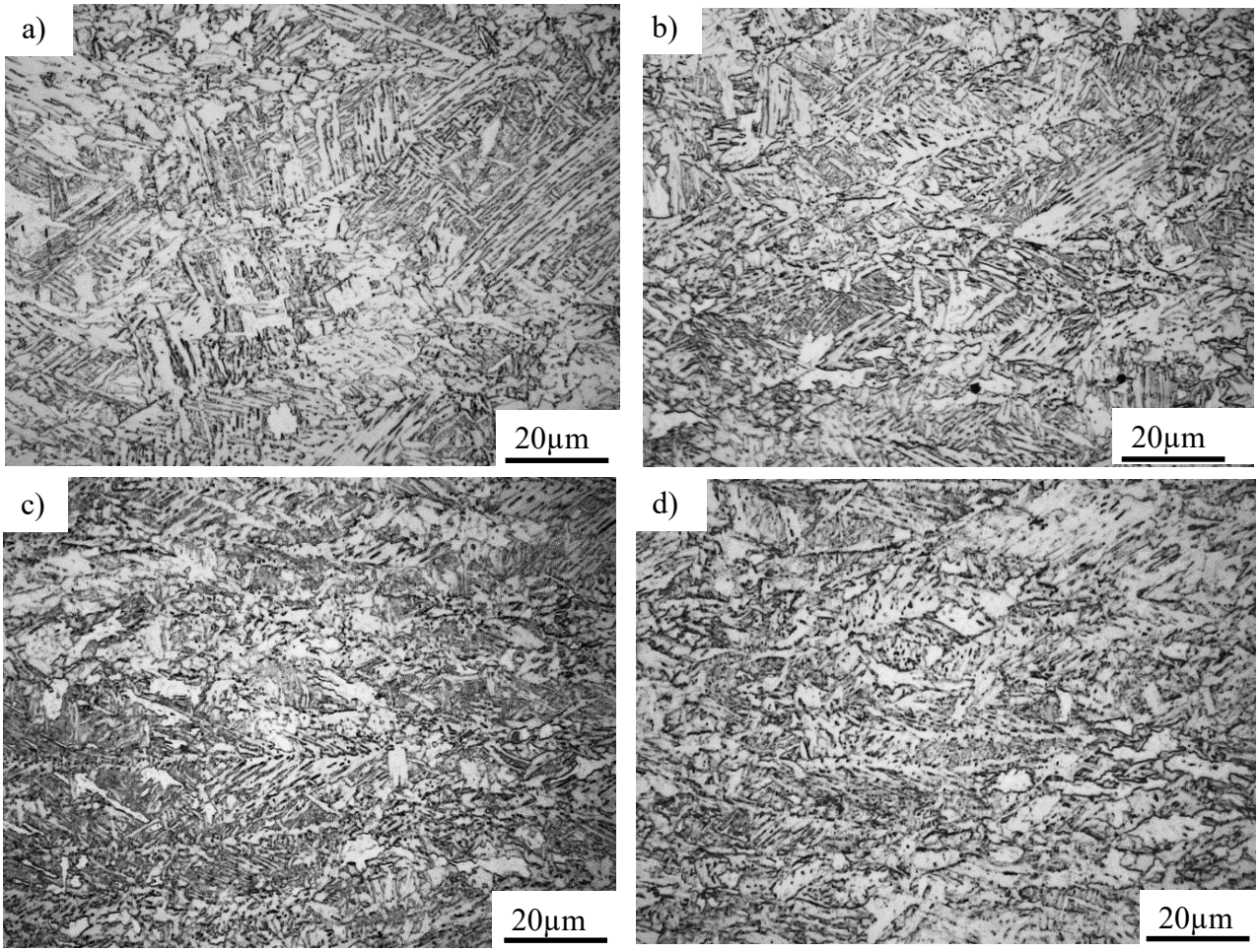

Figure 70. Microstructure revealed in quenched samples after a) one pass, b) 1 pass + 10 seconds of holding time, c) 2 passes + 10 seconds between the passes, d) 2 passes + 10 seconds after each pass.

Two specimens were analysed with the secondary electrons technique in SEM to observe the microstructure in more detail. The first specimen (A2 of Figure 26) was processed with one finishing pass followed by a holding time of 10 s, while the second (specimen A4) included two finishing passes followed by holding times of 10 s after each pass as well, the microstructures for each condition are shown Figure 71 a) and Figure 71 b). The same characteristics observed in the optical micrographs can be observed again in the SEM images. After the first finishing pass the microstructure shows a coarser aspect, abundant colonies of thin and large Widmanstätten ferrite plates appear in all the microstructure and polygonal grains of ferrite are found mainly at the PAGBs. In the specimen deformed in two finishing passes the microstructure was substantially refined, more polygonal grains are formed inter and intragranulary and the ferrite plates have a shorter length.

The coalescence of plates and evolution into polygonal grains can be observed in Figure 71 c), the dashed yellow square in the SEM image shows the stages of DIFT; some fine ferrite plates appear well aligned in a single direction and conserve the initial shape resulting from the dynamic transformation (green arrows), as the coalescence of plates commences, the morphology of ferrite changes into an intermediate shape between plates and polygonal grains (blue arrows), and finally, polygonal grains are formed (red arrow). At the centre of the image, plenty of ferrite grains can be observed, the grains are surrounded by carbides or MA islands as result of the postdynamic diffusion of carbon.

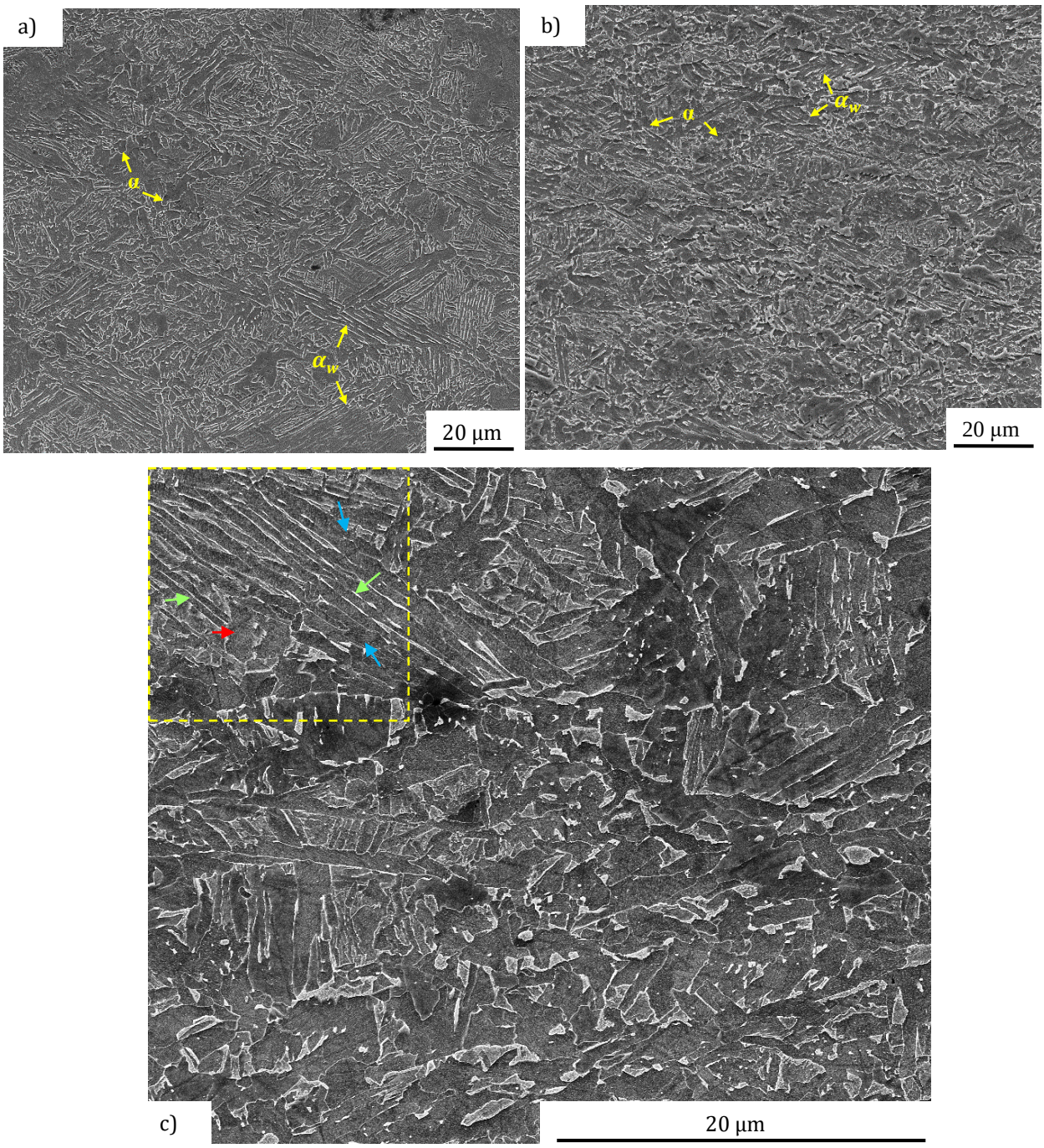

Figure 71. Secondary electrons SEM images showing the microstructure in the simulations that consisted in; a) 1 finishing pass + 10 seconds of holding time (specimen A2) and b) 2 finishing passes + 10 seconds after each pass (specimen A4). c) Microstructure in the specimen A4 observed at 10,000X, the coalescence of plates and polygonisation of ferrite grains can be observed in the dashed yellow square drawn in the image.

5.3.2.4. EBSD analysis

EBSD analysis was carried out in the RD-ND plane of the specimen A4, the sample preparation and the operation of the EBSD instrument was described in Section 3.8.1, the step size used for the analysis was 0.1µm. The index rate achieved was 76%, then the raw data was post-processed in the software HKL Chanel 5 Tango package and the maps were obtained performing a conservative noise reduction of 7%, thus, the maps presented in this section are 83% indexed. The noise reduction consisted in the removal of "wild spikes" (isolated points that could have been incorrectly indexed) and 7% of the zero solutions (non-indexed points), then, an extrapolation filled the removed points with copies of the neighbouring points. The procedure to reduce the noise consisted in replacing the zero solutions by the most common orientation of their 8 neighbouring pixels, then the process was repeated with 7 neighbouring pixels until a final index rate of 83% was attained.

Low quality EBSD patterns cannot be solved by the acquisition software and are saved as zero solutions, an important amount of zero solution pixels comes from factors external to the microstructure, for instance, scratches and pitting formed during or after the specimen preparation, contamination of the sample, etc. However, another significant number of non-indexed points is associated to the microstructure, such as grain boundaries, substructure boundaries and unknown phases. In this simulation, the microstructure possesses multiple features that can cause non-indexed points such as grain and subgrain boundaries, precipitates (all types) and islands of austenite-martensite.

The criterion for the noise reduction was based on the observation of the distribution of the non-indexed points. The noise was reduced until the main scratches generated during the sample preparation almost disappeared, a noise reduction of 7% produced maps with good match with the images observed by secondary electrons in SEM, most the non-indexed points after the noise reduction are located in the regions were grain boundaries, precipitates and islands of martensite-austenite are expected to be found as shown in Figure 73 (the zero solutions appear as black points).

The separation of phases is one of the main difficulties in the analysis of steel in EBSD, the problem arises from the insensitive of the technique to differentiate martensite and bainite from

ferrite by their crystal structure. Ferrite and bainite possess the same body centred cubic (bcc) crystal structure, non-tempered martensite on the other hand, despite having a body centred tetragonal (bct) array, possess lattice parameters quite similar to those in the bcc structures, thus, for practical reasons, the martensite is considered a bcc structure in the EBSD analysis. Attempts to use other crystal symmetries than bcc to evaluate the martensitic patterns have been carried out with poor results [88]. The tetragonality of martensite depends on the carbon content [123], the ratio between the axes, *c*/a, increases linearly with carbon according to the expression $c/a = 1+0.045\%C$ [124]. Thus, as the carbon decreases the ratio c/a tends to the unity, this fact complicates considerably the separation of ferrite from martensite in low carbon steels in EBSD due to the low tetragonality of the bct structure. In the HTP alloy, the difference between the bcc and bct structures is so subtle that cannot be detected in the XRD analysis as discussed in Section 5.3.1. Therefore, the input of crystal structures in the software prior to the acquisition process for the EBSD test is limited only to two arrays; an fcc crystal for the retained austenite and a single bcc structure for ferrite, martensite and even bainite. This implies that the bcc phases cannot be separated by their crystal structure in EBSD since they share the same lattice parameters.

However, despite the very subtle difference in the crystal structure between martensite and ferrite, the diffraction properties of martensite are poorer in EBSD [88]. Such behaviour is generated by the interstitial carbon in martensite which causes a tetragonal distortion in the lattice and in consequence increases the residual stresses in the crystal. Another factor that worsen the diffraction quality in martensite, is the high amount of dislocations introduced in the microstructure during the γ to α' transformation. These factors cause that EBSD patterns (EBSPs) in martensite have lower quality than those in ferrite.

The difference in the diffraction properties can be used to distinguish both phases using quality parameters of the pattern. One of the EBSD techniques able to assess the quality of the EBSPs available the software HKL Chanel 5 Tango package is the Band Slope (BS) analysis. BS is an image quality factor that describes the maximum intensity gradient at the edges of the Kikuchi bands in an EBSP [129], in other words, the BS measures the image quality based on the sharpness of the Kikuchi bands, the higher the BS value, the better the EBSP quality. This technique has been used to separate martensite from ferrite [88], [130] due to the great colour

contrast produced between both phases, in a grey scale image, martensite appears darker than ferrite because of to the low quality of its EBSP.

Figure 72 a) shows a band slope EBSD map of the specimen A4, a clear difference in the contrast between ferrite a martensite can be observed. Ferrite appears in white colour distributed mainly at PAGBs, while martensite is found as laths with darker aspect growing within the PAGBs. Note that most of the ferrite shows an ultrafine grain size and polygonal shape, the grain and subgrain boundaries appear well contoured due to the low quality of the EBSPs diffracted. Some Widmanstätten ferrite can be also observed in the map, however, the high extent of coalescence and polygonisation of plates consumed most of the Widmanstätten ferrite colonies. Additional evidence of the presence of polygonal ferrite and martensite in the microstructure can be obtained analysing the misorientation angle distribution in each phase, for such purpose, two sub-maps were extracted from Figure 72 a), one of the maps was taken from a region dominantly ferritic (red dashed square) and the other from a zone dominantly martensitic (yellow dashed oval), the misorientation profiles of both phases are shown in Figure 72 b). In the case of polygonal ferrite, the frequency of the angular misorientation shows that the microstructure possesses an arbitrary texture, conversely, in martensite the misorientation distribution exhibits a high degree of texturisation, i.e., there is a high frequency only in low and high angle (>50°) boundaries, which is classic from the displacive transformations in steel. Similar misorientation distributions in polygonal ferrite (transformed on cooling) and martensite have been reported somewhere else [88].

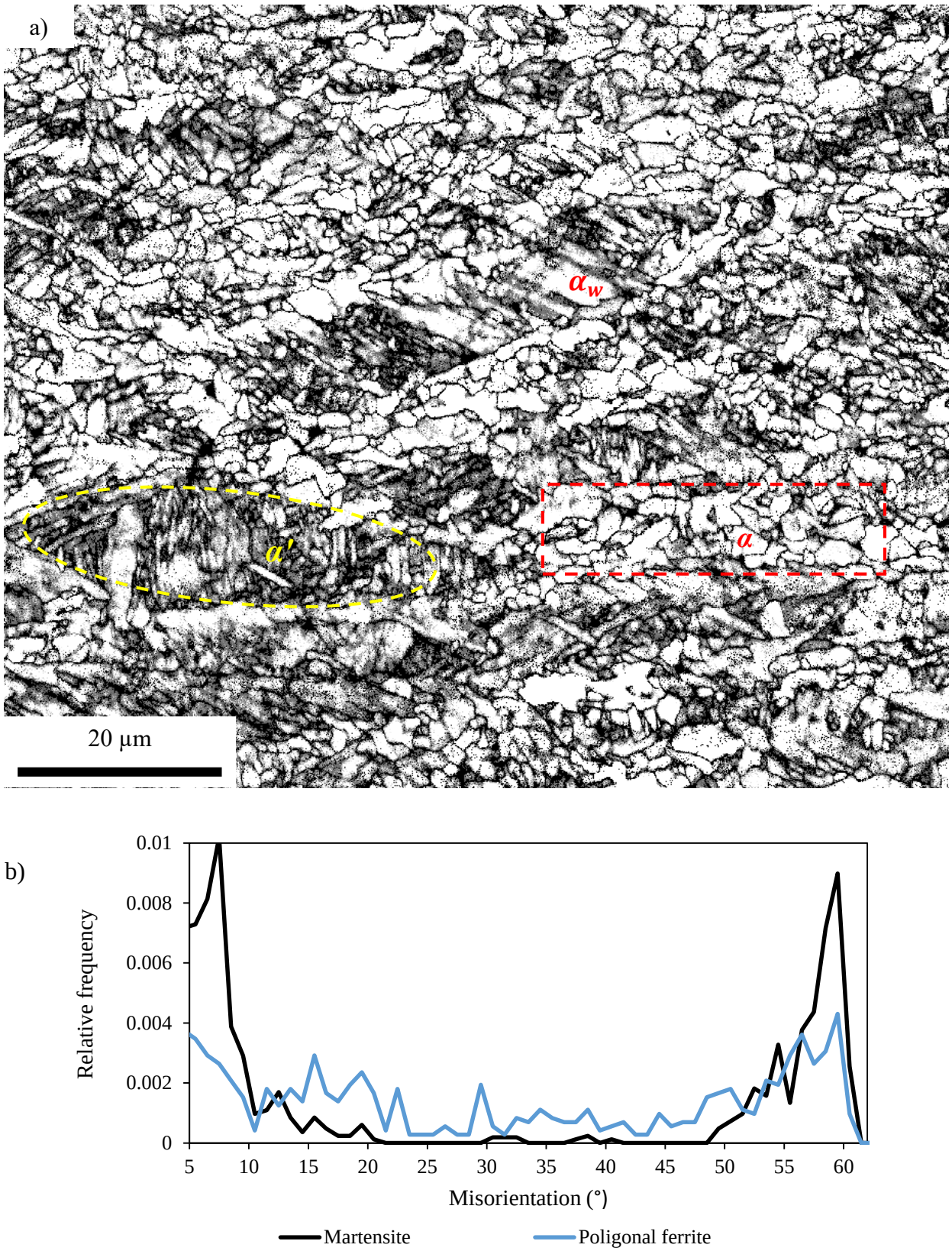

Figure 72. EBSD analysis of the microstructure obtained after the second finishing pass plus 10 seconds of holding time; a) band slope map and b) grain boundaries misorientation distribution of martensite and polygonal ferrite.

It is important to recall that the first stage of DIFT commences with the displacive transformation of Widmanstätten ferrite plates, at this stage the plates have a misorientation distribution similar to that in martensite. Then, when the plates merge and the polygonisation of grains is completed, the misorientation angles between ferrite grains become random and the typical texture of the displacive transformation disappears. A transitory texture appears during the coalesce of plates before the polygonisation of ferrite grains, this form of ferrite will be explained afterwards.

The evolution path from plates to polygonal grains can be understood by analysing the misorientation in the ferritic phase in regions with different morphology. Figure 73 a) shows a band slope (BS) - inverse pole figure (IPF) colouring map made in a region with abundant ferrite (grains and plates). The blue lines in the map represent high angle grain boundaries (HAGBs) that have a misorientation equal or greater than 15°, and the brown lines represent low angle grain boundaries (LAGBs) or substructures with misorientations from 3 to 15°. The black points are non-indexed pixels which are very likely to be carbides or MA islands as explained at the beginning of this Section. As reference, a yellow dashed line was drawn manually in the map to indicate the location of a prior austenite grain boundary. The straight lines b), c) and d) are misorientation measurements done in ferrite regions with different morphology and location. The line b) was drawn within a Widmanstätten ferrite plates colony, the line c) in a wide region of ferrite formed at the PAGB, and the line c) along several ultrafine polygonal grains formed intragranulary.

Two interesting findings arise from the misorientation analysis of the distinct ferrite morphologies. First, in the Widmanstätten ferrite colony the “point-to-origin" misorientation increases gradually with distance as shown in Figure 73 b). And second, the misorientation in the region of ferrite located at the PAGB (Figure 73 c)) shows great similarities with both, the Widmanstätten ferrite and the ultrafine polygonal ferrite (Figure 73 c). This is an evidence of a transitory state in the ferrite that occurs during the coalescence of plates prior to polygonisation of grains. As for the polygonal ultrafine ferrite, the misorientation profiles show a predictable trend as illustrated in Figure 73 d). An explanation of the differences in the misorientation between the distinct morphologies is given below.

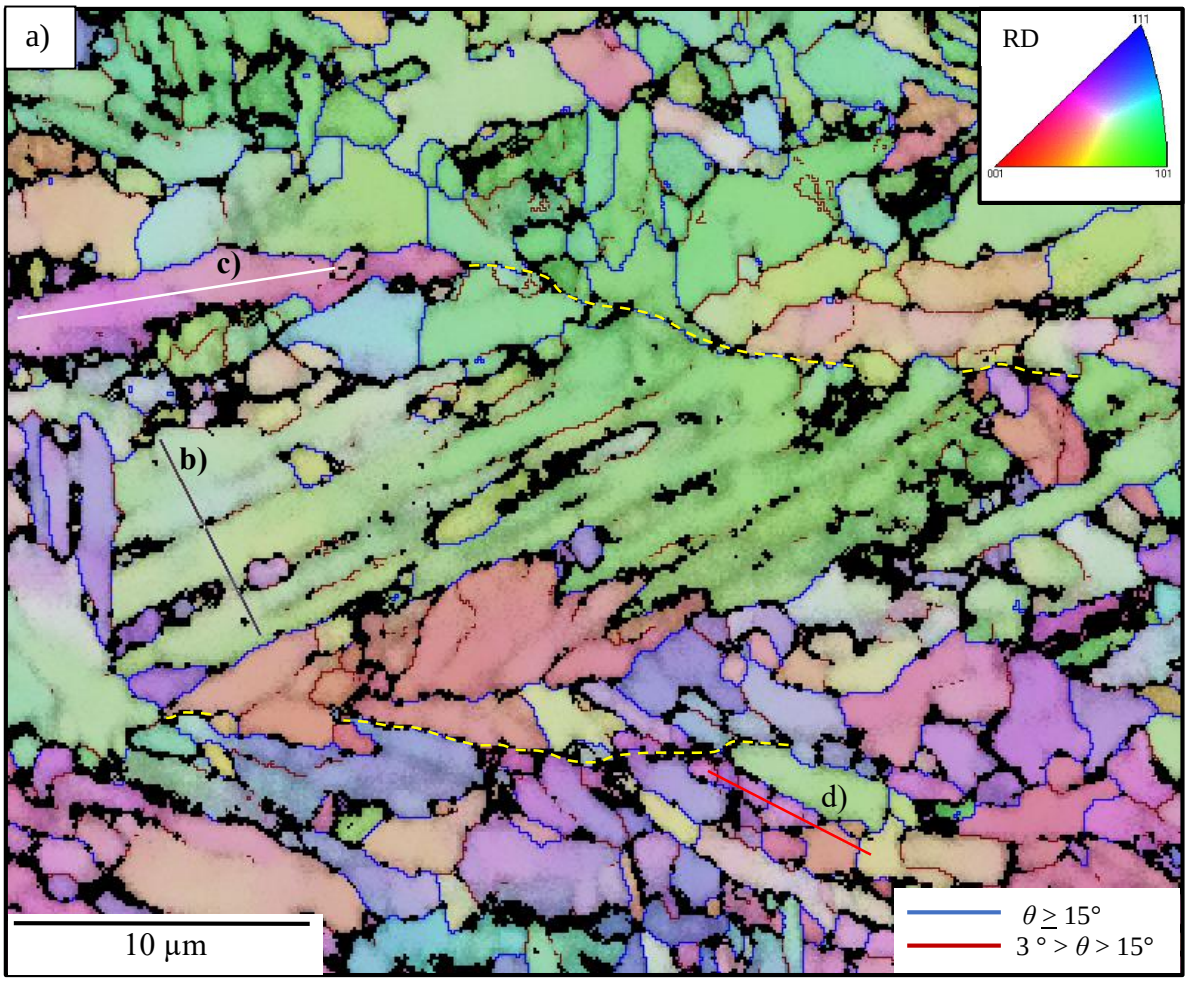
a)
RD
111
001
101
c)
b)
d)
10 µm
θ ≥ 15°
3 ° > θ > 15°

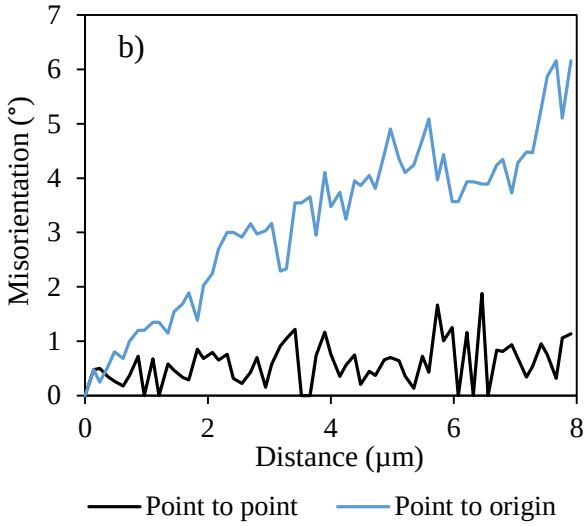
b)
Misorientation (°)
Distance (µm)
Point to point
Point to origin

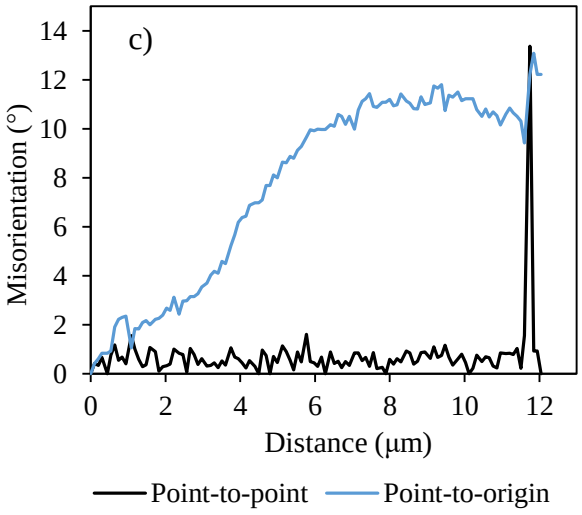
c)
Misorientation (°)
Distance (µm)
Point-to-point
Point-to-origin

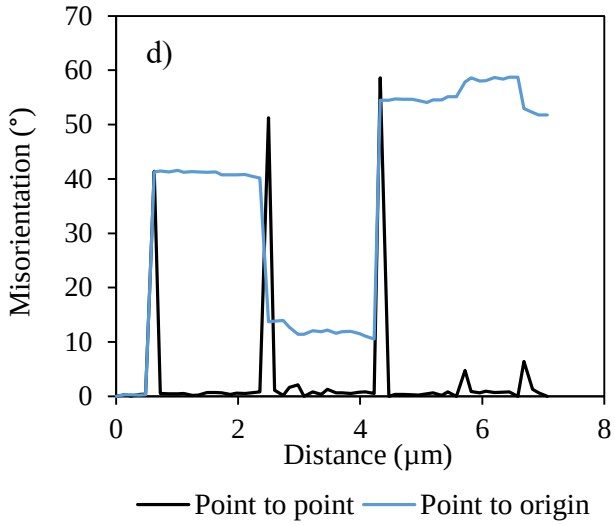

Figure 73. Inverse pole figure and band contrast EBSD map on the RD-ND plane, the grain boundaries appear in blue colour and subgrains in brown. The three lines in the map show the misorientation profile in b) a Widmanstätten ferrite colony, b) a region of ferrite coalescing on the PAGBs and in c) polygonal ferrite grains.

According to research carried out elsewhere [61], [109], DIF plates are unusually thin in the order of 200 nm wide and have very similar orientation between adjacent plates, that is the reason why they are prone to coalesce into grains. In the current work, the boundaries between plates within the Widmanstätten ferrite colony could not be resolved well as shown in the map of Figure 73 a), the step size (100 nm) used in the analysis resulted to be large to resolve individual plates, however, TEM imaging showed that the ferrite plates are around 240 nm wide, these results are presented later in Section 5.3.2.5. As for the orientation in DIFT plates, the "point to point" profile plotted in Figure 73 b) shows that adjacent plates conserve very similar orientation; in a length of 8 µm within a Widmanstätten ferrite colony the misorientation angle does not exceed 2°. The trend in the point-to-point misorientation matches well with the findings reported in the researches aforementioned, however, the point-to-origin profile shows an increase in the misorientation as the distance between plates increases, which is discrepancy with the results presented by Ghosh et al [109].

The misorientation behaviour in both profiles (the point-to-point and the point-to-origin) can be explained by analysing the formation mechanism of Widmanstätten ferrite. According to Basabe et al [61], DIF plates formation follows the mutual accommodation mechanism

proposed by Bhadeshia [131], which states that the formation of Widmanstätten ferrite entails the simultaneous and cooperative growth of a pair of mutually-accommodating plates. During the growth of the pair, each plate exerts approximately opposite shears and consequently much of strain energy is cancelled allowing for the growth of plates. The crystallographic variants involved in the transformation are usually (although not always) similarly oriented in space. The mutual accommodation mechanism was originally formulated to describe the conventional transformation of Widmanstätten ferrite on cooling, below the equilibrium transformation temperature Ae_3. Recently, Jonas et al [64] proposed a mechanism to explain the dynamic transformation of Widmanstätten ferrite caused by deformation above Ae_3, such mechanism is also based on the formation of pairs of ferrite plates. In their model, the application of a shear stress conducts to the formation of a ferrite plate that forces the adjacent austenite to shear along with one of the sides of the plate, then the strained austenite transforms into a second ferrite plate, forming a pair of self-accommodating plates with opposite shears that cancel each other out, the pairs of plates have almost identical orientation [64], [65]. The latter mechanism suits better with the low misorientation observed in the point-to-point profiles reported in papers [61], [109] and in the current work.

As for the point-to-origin profile shown Figure 73 b) in which the misorientation increases with distance along the Widmanstätten ferrite colony, an explanation for this behaviour can be found considering a transformation mechanism that includes the formation of pairs of self-accommodating ferrite plates followed by face-to-face sympathetic nucleation [132] on one of the sides of the pair of plates. In more detail, the formation the colony of plates might follow the next two steps:

1. An initial formation of a pair of self-accommodating ferrite plates following the mechanism proposed by Jonas et al explained above.
2. The sympathetic nucleation of a new ferrite plate at one of the faces of the pair of plates already formed, followed by the formation of another plate to complete a new pair of self-accommodating plates. This process is repeated in a burst of successive formation of pairs of plates. Although adjacent plates have very similar orientation, the continuous nucleation of new plates widens the ferrite colony, and consequently increases gradually the misorientation with respect to the first nucleated plate (the origin).

The mechanism aforementioned describes well the misorientation observed in both profiles within the Widmanstätten ferrite colony. The point-to-point profile confirms that the plates have similar orientation between the adjacent faces, whereas the point-to-origin plot, indicates a successive formation of new plates by sympathetic nucleation, which leads to an increase in the misorientation as more new plates are formed.

With regards to the process in which ferrite plates merge and form polygonal grains, it appears that there is an intermediate and transitory state in the morphology and misorientation of ferrite, in such state, the ferrite can exhibit characteristics of both displacive and reconstructive transformations. In Figure 73 a), the ferrite region that contains the line c) shows a peculiar morphology, despite appearing in the map as a single long grain located on the PAGB, its shape and misorientation indicate that the grain might be instead, a colony of plates in decomposition in a stage prior to the polygonisation. The profiles plotted in Figure 73 c), show that along approximately the first 8 μm the misorientation has a very similar trend to that observed in the colony of Widmanstätten plates (see Figure 73 b)), while in the rest of the graph from 8 to 12 μm, the misorientation is more similar to that in the polygonal ferrite (Figure 73 c)). The peak observed in both profiles at around 12 μm, is due to the presence of a grain boundary of a polygonal grain of around 500 nm diameter. The point-to-origin profile shows a good example of how the misorientation in DIFT is rearranged as the plates transform into polygonal grains.

The coalesce process has been classified as a form of recovery [21], since it involves the removal or dissolution of dislocations located at the boundaries of the plates. The driving force energy that conducts to the coalesce process during the holding time, comes from the deformation stored in the microstructure, and, since the recrystallisation was almost negligible in the specimen evaluated as showed in Section 5.3.2.2, the coalescence of plates and polygonisation of grains, are the main restoration mechanism in operation during the holding time added after the second finishing pass.

The evidence of a transitory state of ferrite, observed in a specimen deformed 100°C above Ae_3 and held isothermally 10 seconds before quenching, indicates that the coalescence of plates and subsequent formation of grains might take place not only dynamically during deformation, but also, post-dynamically during certain holding time. It is important to remark that ferrite is not thermodynamically stable at temperatures above Ae_3, thus, after the deformation, DIFT

commences to retransform into austenite at a certain holding time. Several experiments carried out in isothermal conditions in low and plain carbon steels deformed at temperatures above Ae_3, have demonstrated that the ferrite to austenite reverse transformation starts immediately or few seconds after the deformation [52], [122], [133]. Nevertheless, the addition of Niobium can retard notoriously the reverse transformation, Basabe and Jonas [72] carried out torsion tests on a 0.036 wt% Nb microalloyed steel at a temperature 20 °C above the Ae_3 (856 °C), a strain of 2 and isothermal holding times of 50 s, 100 s, 200 s and 400 s. They showed that the dynamic ferrite was quite stable during the first 200 s of holding time, then the reverse transformation began to happen until the ferrite completely disappeared in around 400 s.

The ability of Nb to slow the ferrite reverse transformation might bring important benefits in terms of mechanical properties, the addition of short interpass holding times can modify the morphology of DIFT and consequently improve the toughness of the alloy. In other words, short holding times will not lead to the ferrite reverse transformation, instead, more Widmanstätten ferrite colonies will evolve into regions of ultrafine polygonal grains, such change in the morphology of ferrite is very positive for the mechanical properties of the material. It is well known that the Widmanstätten ferrite has a detrimental effect on the toughness of steel [134], whereas ultrafine polygonal ferrite causes the opposite effect.

Finally, the misorientation was measured in the region with several ultrafine polygonal ferrite grains, Figure 73 e) shows the profiles obtained from the red line drawn in Figure 73 a), the line crosses the boundaries of four polygonal ferrite grains. In the point-to-point profile it can be seen that the misorientation between grains varies from 5 to 59°, and diameters range from 1 to 1.9 μm. Both profiles show that the misorientation within the individual grains is small and fairly homogeneous, which indicates that the coalescence and polygonisation processes already took place leading the formation new grains free of dislocations.

5.3.2.5. TEM thin foils

Several thin foils were obtained from the specimen A3 of Figure 26 following the procedure described in Section 3.9.2. The specimen corresponds to the simulation that consists of one roughing pass at 1100°C and a strain of 0.3 followed by two finishing passes at 950°C and a strain of 0.22, between the finishing passes a holding time of 10 seconds was added. TEM bright field images were obtained in relevant features of the microstructure. As described along this Chapter, the phases found in the microstructure are mainly martensite and DIFT as shown in the TEM images of Figure 74. Martensite appears in form of dark laths, which indicates the high dislocation density distinctive of as quenched martensite. As for DIFT, the phase shows different morphologies that appear in brighter colour due to the lower dislocation density. Figure 74 a) shows a colony of Widmanstätten ferrite plates merging, a fine ferrite plate is easily observed at the centre of the image, however, most of the plates boundaries cannot be seen due to the removal of dislocations caused by the coalescence. The arrows in the image point out dislocations that form substructures within the ferrite, such substructures are likely to form grain boundaries as the plates merge and evolve into polygonal grains. The formation of DIFT grains can be appreciated in Figure 74 b), at this stage the plate-like morphology disappeared completely, and some ferrite grains show well defined boundaries (see the arrows). Ferrite grains are not precisely polygonal, however, it is important to remember that the complete polygonisation can occur rapidly during the deformation [61], thus the prior polygonal shape can be affected before the withdrawal of the load. The ferrite grains observed in Figure 74 b) show an elongation in the same direction which is likely to be the rolling direction.

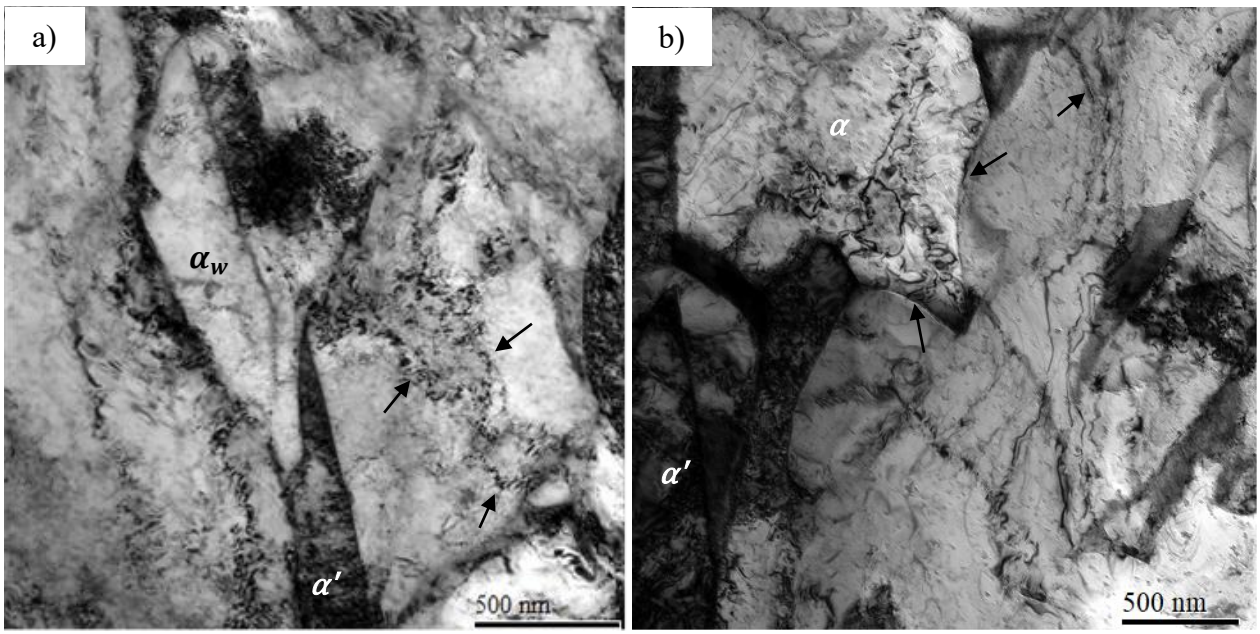

Figure 74. TEM bright field images showing the different morphologies of DIFT. a) A colony of Widmanstätten ferrite plates merging, and b) formation of DIFT grains.

Another important finding observed in the thin foils, is the precipitation in the ferrite phase as shown in Figure 75 a), the precipitates are located at the grain boundary and within the grain. Most precipitates are very fine and have a spherical shape as can be seen in the particle shown in Figure 75 b), however, due to the strong magnetic field emerging from the thin foil, neither EDS nor diffraction patters could be obtained accurately at high magnifications on individual precipitates due to excessive drifting in the TEM imaging.

There is evidence that cementite particles smaller than 20 nm diameter can precipitate intragranulary during DIFT, Weng et al [60] showed a large amount of intragranular cementite precipitation in two low carbon steels containing 0.09%C-0.51%Mn-0.25%Si-0.017%Nb and 0.12%C-0.34%Mn-0.22%Si, the precipitation was similar in both steels despite of the fact that one of them was free of Nb. It is likely that the nanometric particles observed in Figure 75 are cementite precipitates, however, further work is needed to validate their chemical composition.

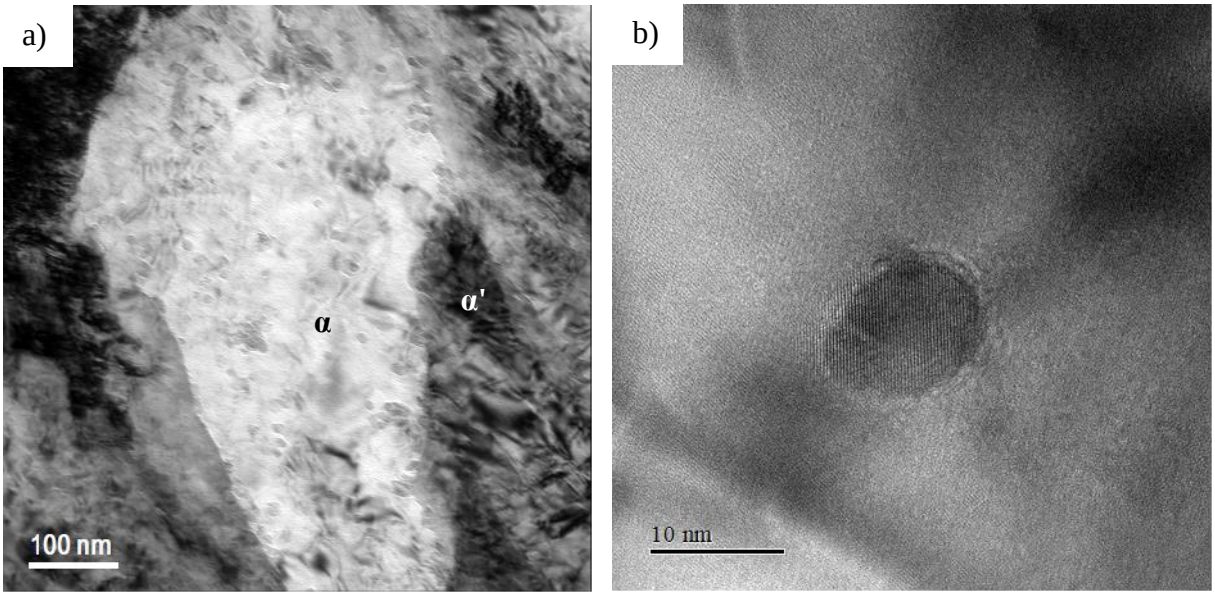

Figure 75. TEM bright field images showing the precipitation in DIFT. a) A grain of ferrite showing intergranular and intragranular precipitation. b) Example of an intragranular precipitate.

5.3.2.6. TEM carbon extraction replicas

The extent of precipitation in the specimen A4 was analysed with carbon extraction replicas and TEM following the procedure described in Section 3.9.1. Figure 76 a) and b) show the carbon replicas after the rough and finish deformations respectively, a substantial increase in the amount of precipitates was observed after the finishing passes, the number of precipitates per unit area increased from $9.1x10^{-5}$ to $2.7x10^{-4}$ particles/nm_2 with the addition of two finishing passes. As for the precipitates size, the average diameters were 8.9 and 5.9 before and after the finish deformation respectively. The increase in the value of precipitates per unit area and the decrease in the average particles size after the finish deformation, indicates that intense strain induced precipitation of very small particles took place. Figure 76 c) shows an example of a Nb precipitate and Figure 76 d) shows the EDS analysis

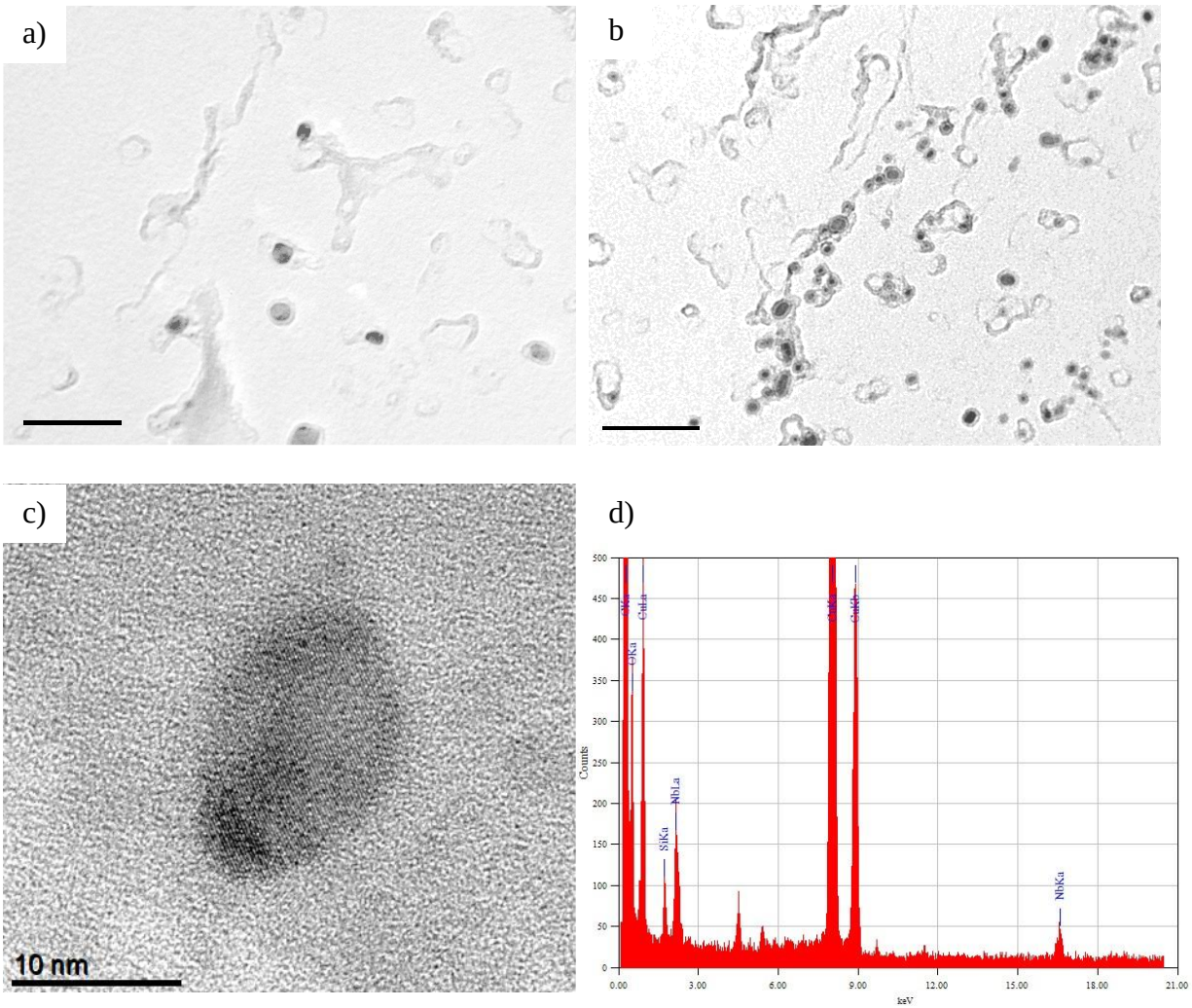

Figure 76. Carbon extraction replicas showing the precipitates a) before the finish deformation and b) after two finishing passes and 10 second of holding time after each pass. c) Example of a nanometric strain induced precipitate of niobium and d) its respective EDS analysis. The peak of Cu in the spectra is from the copper grid supporting carbon replica, and the peak of Si is from the TEM sample holder.

Coarse TiNb(C,N) were also observed in the carbon replicas after finish rolling, the formation of such precipitates is presumed to happen in the early stages of the steel production during or after the solidification as discussed in Section 4.2. The morphology of TiNb(C,N) precipitates commonly appears as coarse cuboid Ti precipitates with spherical Nb precipitates embedded on the surface as result of the epitaxial growth of the latter. However, the presence of Nb on the TiNb(C,N) precipitate is not confined solely to the embedded spherical particle, Figure 77 shows that Nb is also found surrounding the whole surface of the cubic Ti precipitate.

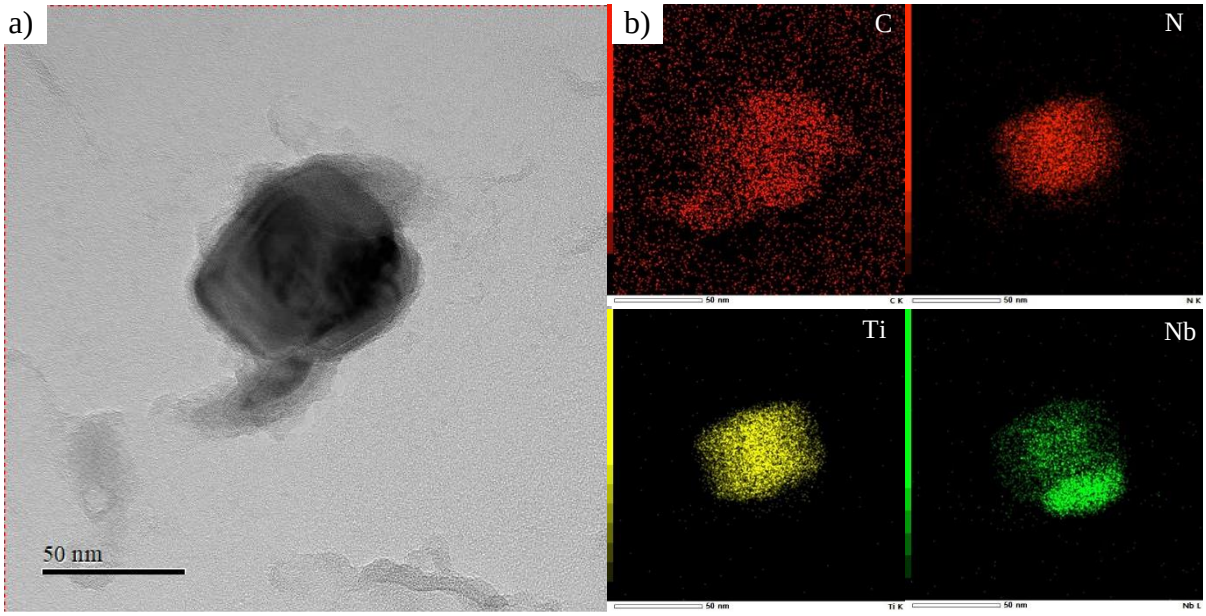

Figure 77. TiNb(C,N) precipitate found in the finish rolling of specimen A4. a) Carbon extraction replica TEM image and b) Scanning TEM (STEM) analysis showing the EDS maps of C, N, Ti and Nb.

5.3.2.7. SPM and nanohardness evaluation

SPM imaging and nanohardness tests were performed on the area of interest in the RD-ND plane of the specimen A4 following the procedure described in Section 3.11. The SPM evaluation revealed a high contrast in the topography between the phases present in the microstructure as shown in as Figure 78. As previously discussed in Section 3.11.1, ferrite exhibits higher surface relief than martensite in the SPM scanning, some examples of DIFT are indicated by yellow arrows in Figure 78 a). In order to evaluate the nanohardness of both phases, three indents were performed in SPM mode in the positions indicated in Figure 78 b), two of them were done on ferrite grains (yellow points) and one on the martensite (red point). The nanohardness values in ferrite were 2.61 and 2.59 GPa, whereas in martensite the nanohardness was 4.8 GPa.

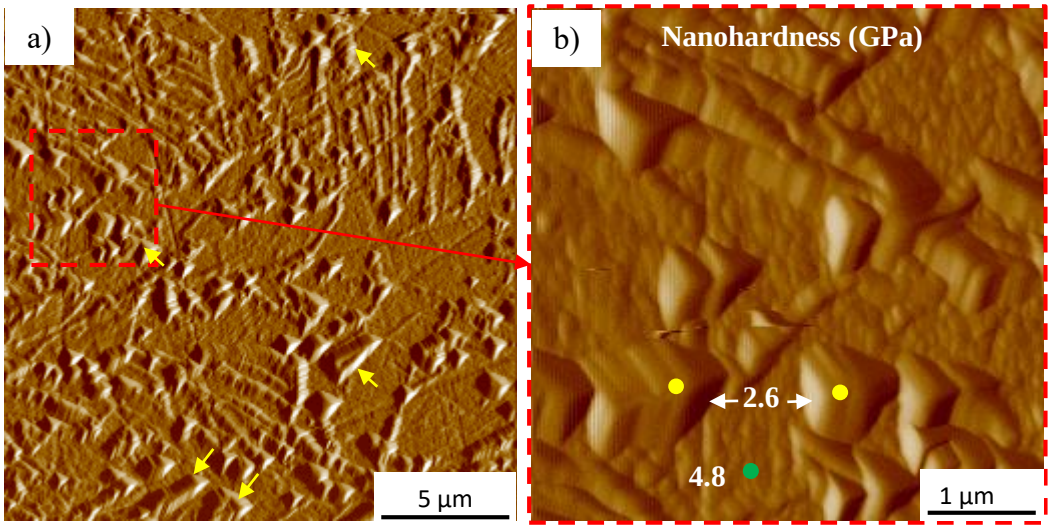

Figure 78. SPM gradient image showing the topography and nanohardness of specimen A4.

Additionally, an extensive nanohardness evaluation (in non-SPM mode) of 225 indents was carried out in a square grid of 15 x 15 indents, the distance between successive points in the grid was 10 µm resulting in a total tested area of 140x140 μm^2. The results are displayed in Figure 79, the bimodal distribution in the nanohardness confirms the mixture of soft DIFT and hard martensite in the microstructure, the peak of DIFT appears in the range from 2.8 to 3.1 GPa, and the one of martensite from 4.5 to 4.9 GPa. Both peaks matched well with the nanohardness values measured in SPM mode in ferrite grains and in the martensitic matrix.

It is important to remark that the distribution displayed in Figure 79 cannot be used to estimate the volume fraction of DIFT, for the probabilities to indent solely the ferrite phase are low in the non-SPM mode evaluation. The measurement of the hardness in ferrite grains requires great precision in the position of the indentation, since at the ferrite grain boundaries the hardness can increase considerably as discussed in Section 4.4.4. Thus, indents must be done at the very centre of the grains to obtain representative hardness values of ferrite, otherwise, the hardness can increase substantially even if the indent barely reaches the ferrite grain boundaries.

The volume fraction of DIFT was estimated with the SPM images following the procedure described in Section 3.11.1 The volume fraction for the specimen A4 was 22.8%.

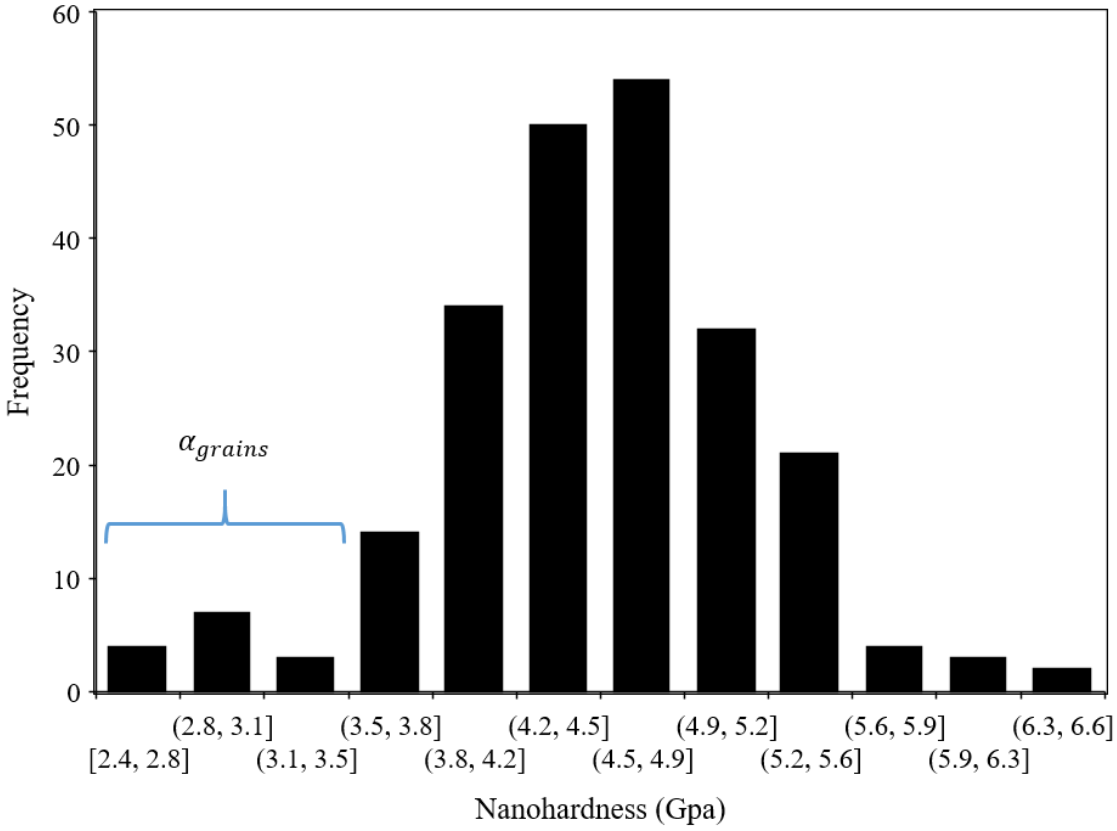

Figure 79. Nanohardness distribution in specimen A4.

5.3.2.8. DIFT quantification.

In Section 4.5.3 it was discussed that SPM scanning can be used to quantify the volume fraction of DIFT with superior accuracy than other methods, however, this evaluation turns out to be very laborious and time consuming, for such reason, in the current Section only the specimen A4 was evaluated with SPM to obtain the volume fraction of DIFT. However, in Section 4.5.3 it was also discussed that the amount of DIFT can be estimated using optical microscope (OM) images of the microstructure etched with 2% Nital, the estimation is good when the microstructure consists solely of martensite and ferrite. In the finishing simulation at 950°C, all the microstructures consisted in a mixture of DIFT and martensite as showed in Figure 70, therefore, the estimation of the fraction of DIFT with OM images can be reliable. Figure 80 shows the evolution of DIFT along the finishing simulation at 950°C, at least 5 OM images of the microstructure at 200x were used to estimate the volume fraction in each condition. In the last condition (Pass 2 + 10 seconds) the fraction of DIFT was calculated with SPM (red point)

as well, it can be seen that both methodologies have a good match in the estimation of the volume fraction.

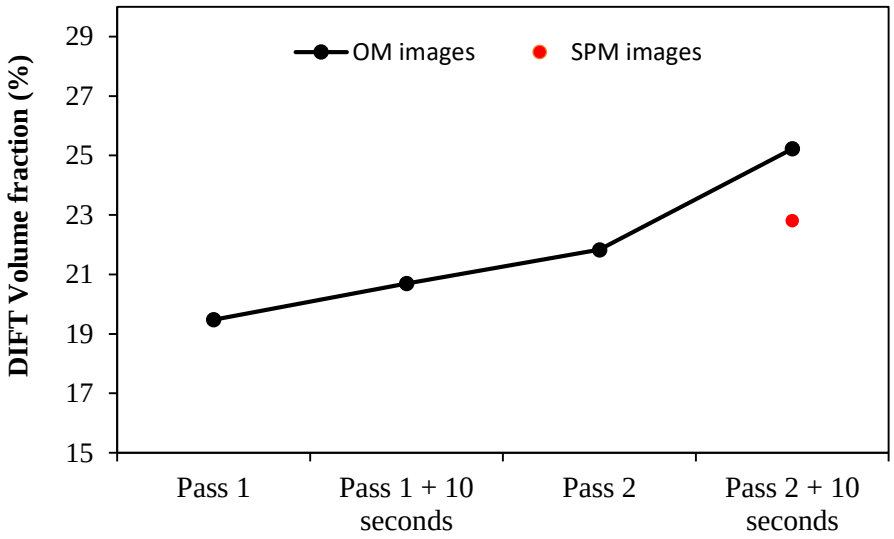

Figure 80. Volume fraction of DIFT in the different conditions of the finish rolling simulation at 950°C.

After the rough deformation the DIFT fraction was barely 2% as previously presented in Chapter 4, then, in the first finishing pass DIFT increased surprisingly to around 19%, which is a substantial change in the microstructure considering that the strain was only 0.22, then, in the following deformation conditions the amount of DIFT increased very slightly. The uneven increase in the volume fraction in the different conditions could be related to the nucleation sites for ferrite plates, although DIFT plates can nucleate intragranulary [72], PAGBs are the preferential sites for the formation of plates as observed in the OM, SEM and SPM analysis. Before the first finishing pass, PAGBs are almost free of DIFT, therefore, a moderate strain of 0.22 can lead to a significant ferrite plates formation due to the large availability of nucleation sites. Then, in the following conditions, since PAGBs are already occupied by DIFT, the availability of preferential nucleation sites is reduced, that is why the fraction of DIFT increases slowly after the first finishing pass. It is also true that during the second finishing pass new grain and subgrain boundaries are formed, such boundaries could also serve as preferential nucleation sites for ferrite plates, however, the reduction of the PAG size probably affects the

ferrite plates formation to some extent, as it occurs in the conventional Widmanstätten transformed on cooling [134].

It is important to remark that DIFT increased during the holding times (although to a small extent), mainly during the second, which is unexpected since ferrite is not thermodynamically stable above the Ae_3, furthermore, new ferrite plates cannot nucleate statically without the application of a load. An explanation for the increase in DIFT during the holding time above the Ae_3 can be deducted analysing the change in the morphology of ferrite, after each finishing pass DIFT and the unrecrystallised austenite store energy due to deformation, and, since the recrystallisation is stopped (as showed in Section 5.3.2.2), the dominant restoration mechanism operating during the holding time is the recovery of DIFT, i.e. the coalescence of plates and polygonisation of grains. Thus, during the holding time the proportion of grains increases as more plates merge, this change in the morphology leads to inaccuracies in the estimation of the volume fraction of ferrite since grains can be easily observed in light microscopy, whereas, ferrite plates are so thin that its volume fraction is unavoidably underestimated.

5.3.3. Finish rolling simulation at 810°C

5.3.3.1. Flow behaviour and estimation of critical strains for DIFT and DRX

The flow curve of the of the specimen B4 is shown in Figure 81, the simulation consisted in one roughing pass at 1100°C and a strain of 0.3 followed by two finishing passes at 810°C and a strain of 0.22, after each finishing pass an isothermal holding time of 10 seconds was added. The curve shows a predictable large increase in the flow stress in the first finishing pass due to the decrease in the deformation temperature, then the stress increases gradually as the specimen is strained in the finishing passes. The flow stress decreases at the beginning of the second finishing pass which is related closely related to DIFT as discussed in Section 5.3.2.1.

The flow behaviour in the simulation at 810°C is very similar to that observed at 950°C, the similarity is such that the critical strains for DIFT and DRX are almost identical between both deformation conditions, it is important to recall that the critical strains are obtained from the

flow curves with the double differentiation method. Figure 82 shows the critical strains for DIFT and DRX in the simulation at 810°C.

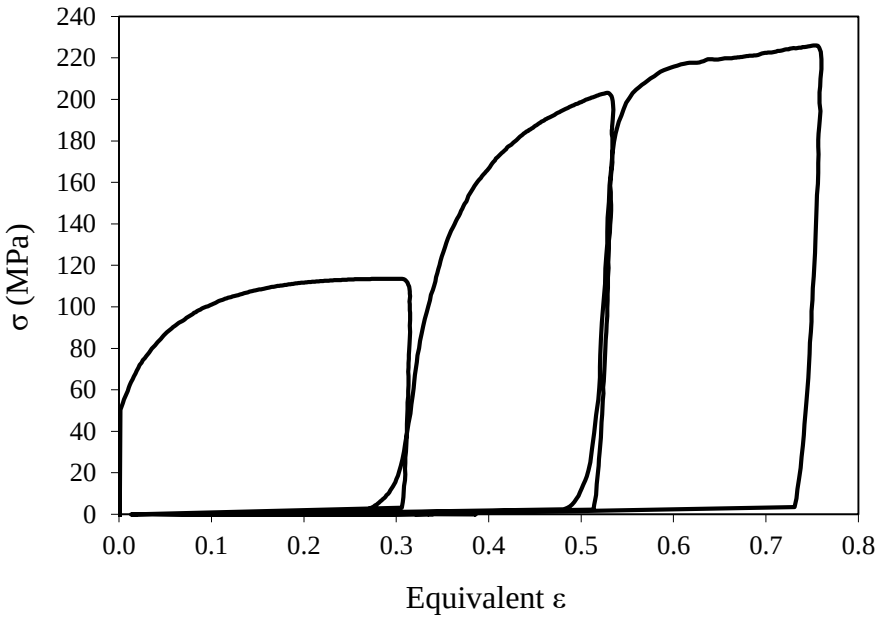

Figure 81. Stress- equivalent strain curve obtained in the PSCT of specimen B4.

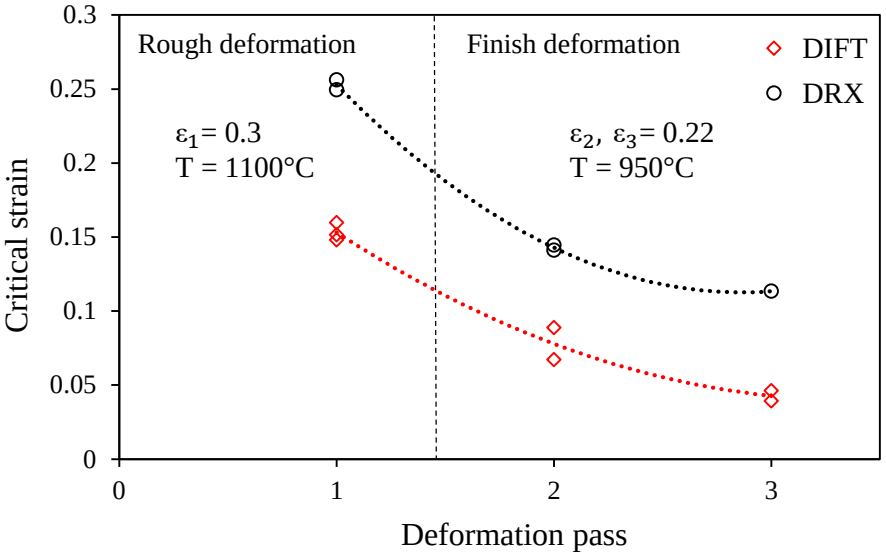

Figure 82. Critical strain for DIFT and DRX at different number of passes.

5.3.3.2. Morphology of the prior austenite grain boundaries.

The evolution of PAGBs in the finish rolling passes can be observed in Figure 83. After the first pass, most PAGs remain deformed as shown in Figure 83 a) and Figure 83 b), nevertheless, some recrystallised grains appear in polygonal shape at the boundary junctions of deformed grains. The holding time has a negligible effect on the amount of recrystallisation, Table 9 shows that the recrystallised fraction is almost the same (around 9%) before and after the deformation, which means that the insipient recrystallisation was effectively stopped during or immediately after the first finishing pass. In the second pass plus the 10 seconds holding time, PAGs exhibit significant deformation and the recrystallised fraction is almost null as shown in Figure 83 c). The PAGBs evolution is very similar in both finish rolling simulations at 810°C and 950°C, although the grain refinement is slightly better at 810°C, surely because of the lower deformation temperature.

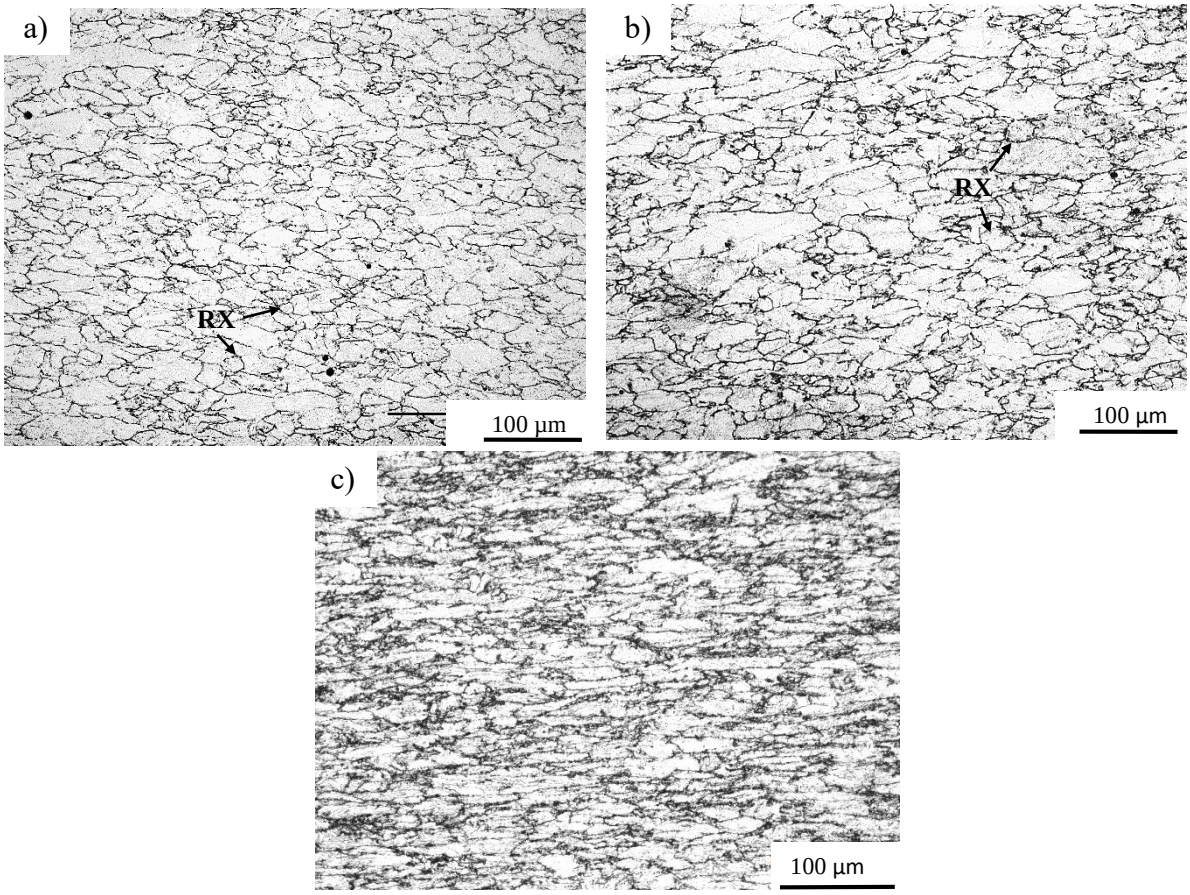

Figure 83. Prior austenite grain boundaries revealed in quenched specimens after a) one pass, b) 1 pass + 10 seconds of holding time and c) 2 passes + 10 seconds of holding after each pass.

Table 9. Prior austenite grain diameter measurements done with the intercept method of ASTM E-112, and recrystallised fraction estimated with the point counting method for the finishing passes at 810°C.

Specimen	Finishing pass	Recrystallised fraction (%)	Average grain diameter (µm)		Aspect Ratio
			Rolling direction	Normal direction	
B1	1 Pass	8.8	49.5	17.11	2.9
B2	1 Pass + 10 seconds	8.5	50.2	17.25	2.9
B4	2 Passes + 10 seconds after each pass	0.5	72.4	11.5	6.3

5.3.3.3. Microstructure

The microstructures of the different conditions simulated at 810°C are displayed in Figure 84, a mixture of deformation induced ferrite and martensite was observed in all the cases. The morphology and distribution of ferrite in the microstructure are about the same reported previously in the simulation A (at 950°C), i.e. ferrite appears as Widmanstätten plates and as polygonal grains, both morphologies can be found mainly growing at the PAGBs but intragranular formation is also observed. Despite the increase of DIFT in the microstructure is not evident from one micrograph to another, the comparison between Figure 84 a) and Figure 84 d) demonstrates that the amount of ferrite increased with deformation.

After the holding times the microstructures show an apparent increase in the amount of polygonal ferrite and a decrease in amount of Widmanstätten ferrite, such change in the morphology of ferrite is caused by the coalescence of plates and evolution into polygonal grains. This observation was also reported in the simulation at 950°C after the second holding time, however, at 810°C a subtle change in the microstructure can be observed after both holding times.

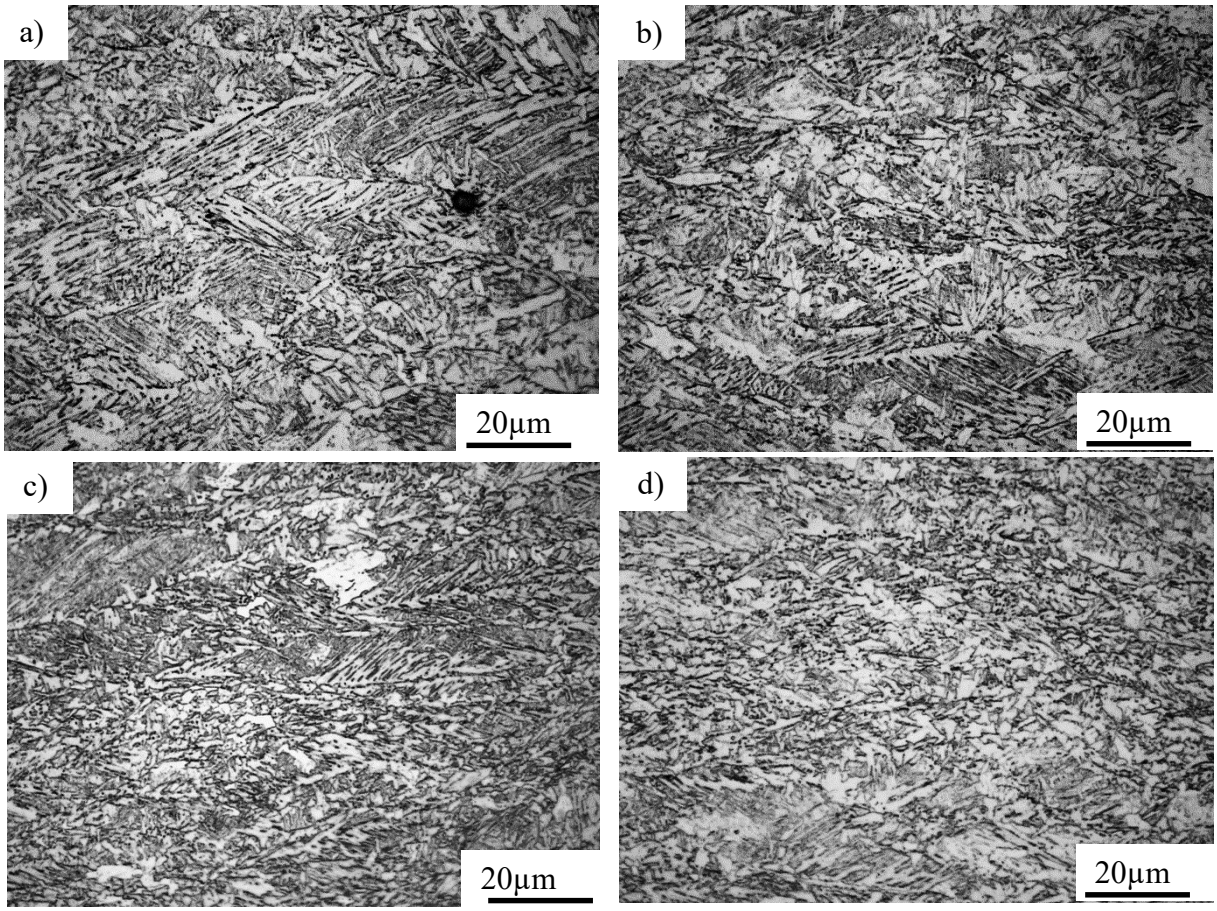

Figure 84. Microstructures revealed in quenched samples after a) one pass, b) 1 pass + 10 seconds of holding time, c) 2 passes + 10 seconds between the passes, d) 2 passes + 10 seconds after each pass.

SEM imaging was performed in the different finish rolling conditions as displayed in Figure 85. In the first finishing pass, the increase in the amount of polygonal ferrite is subtle after the holding time, and most of the ferrite grains appear mainly at the PAGBs as shown in Figure 85 a) and Figure 85 b). In the second pass, the increase in the amount of polygonal ferrite is more notorious, besides, some regions of ultrafine polygonal grains commence to form intragranulary as pointed out by the yellow oval in Figure 85 c). The polygonisation of plates continues during the holding time of the second pass and consequently the presence of intragranular ferrite increases as shown Figure 85 d).

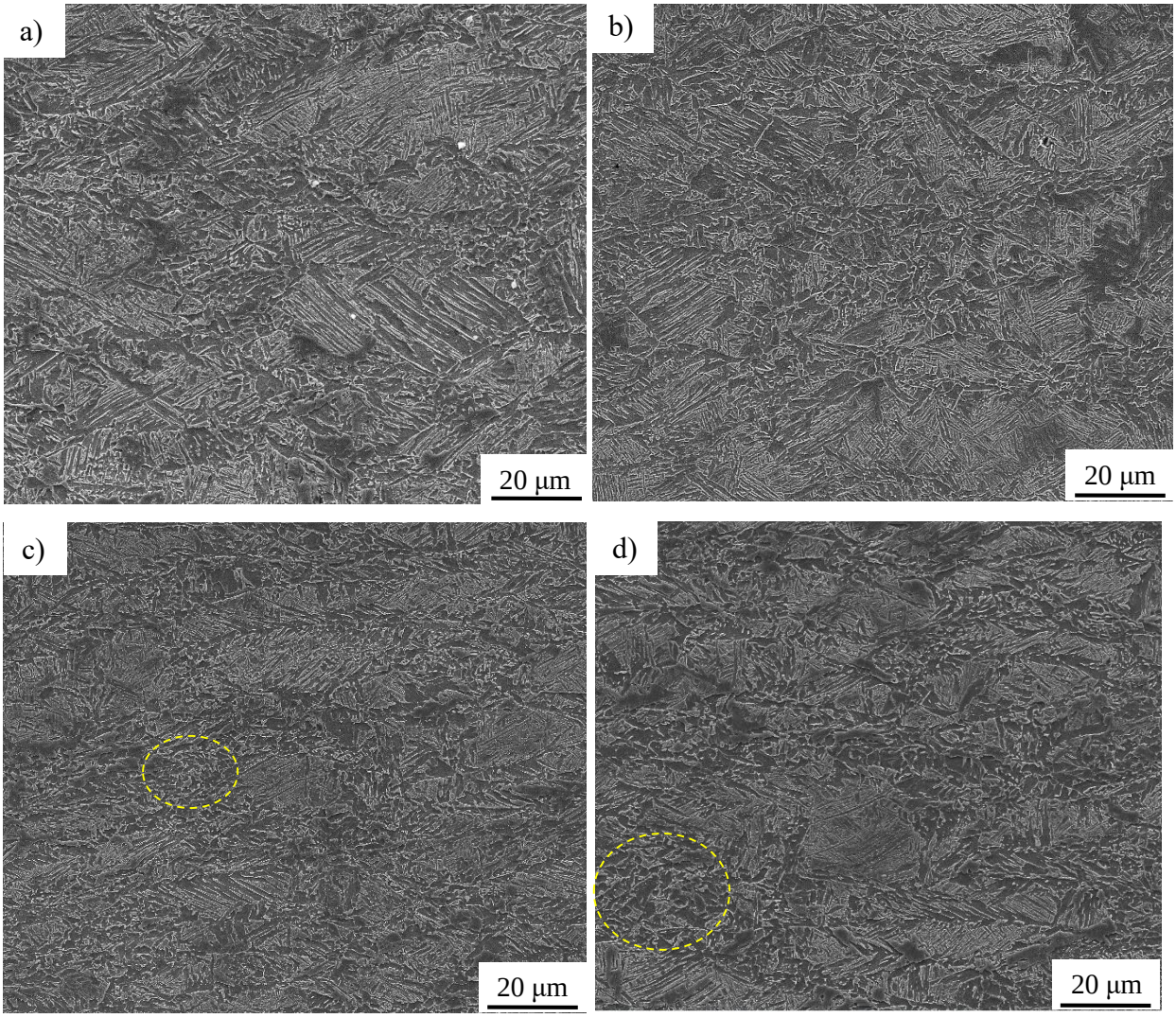

Figure 85. SEM secondary electrons images showing the microstructure in quenched specimens after a) one pass, b) 1 pass + 10 seconds of holding time, c) 2 passes + 10 seconds between the passes, d) 2 passes + 10 seconds after each pass.

The coalescence of plates and subsequent polygonisation of ferrite grains can be observed in more detail in Figure 86, the SEM image shows abundant polygonisation of ultrafine grains, some of them are surrounded by carbides or small martensite-austenite (MA) islands, the grains were formed at PAGBs (α_{inter}) and also intragranulary (α_{intra}). As for the Widmanstätten ferrite plates, the image shows a couple of plates on their way to disappear due to the polygonisation process. Again, the morphology of ferrite observed in SEM coincides with that found in the simulation at 950°C.

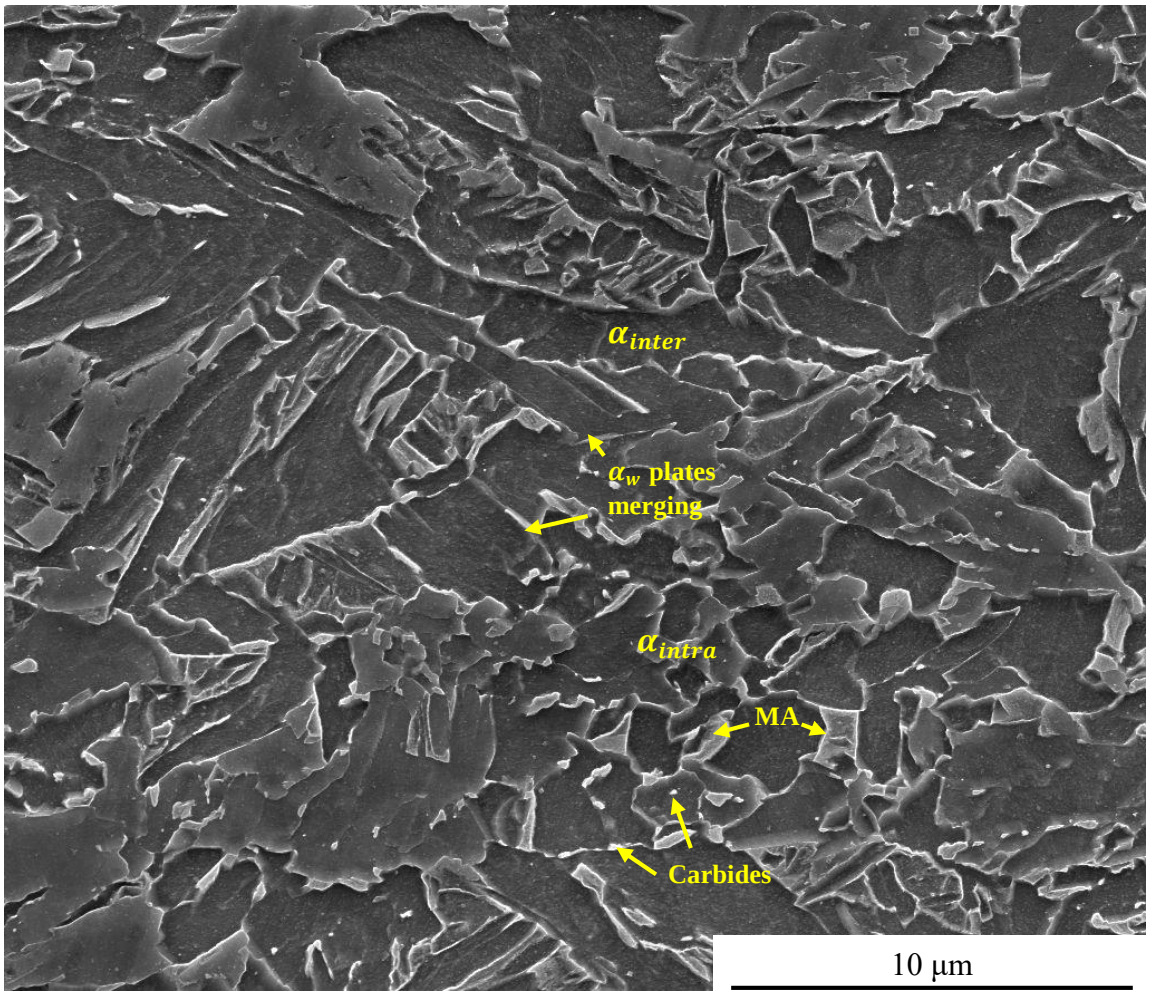

Figure 86. SEM image at 9000 magnifications showing the microstructure in the specimen B4.

5.3.3.4. EBSD analysis

EBSD analysis was performed in the specimen B3, which corresponds to the simulation that consisted in two finishing passes and only one holding time between the passes. The sample preparation and the EBSD test was performed following the procedure described in Section 3.8.1, and the maps were done following the criteria explained in Section 5.3.2.4. The microstructure of the deformed specimen is presented in the image quality maps shown in Figure 87. The band contrast map (Figure 87 a)) shows in great detail the microstructure, the presence of ultrafine polygonal grains and Widmanstätten plates is notorious . As previously discussed in Section 5.3.2.4, ferrite and martensite can exhibit great contrast in the band slope analysis, thus, DIFT can be easily observed in a brighter colour whereas martensite appears dark as shown in Figure 87 b).

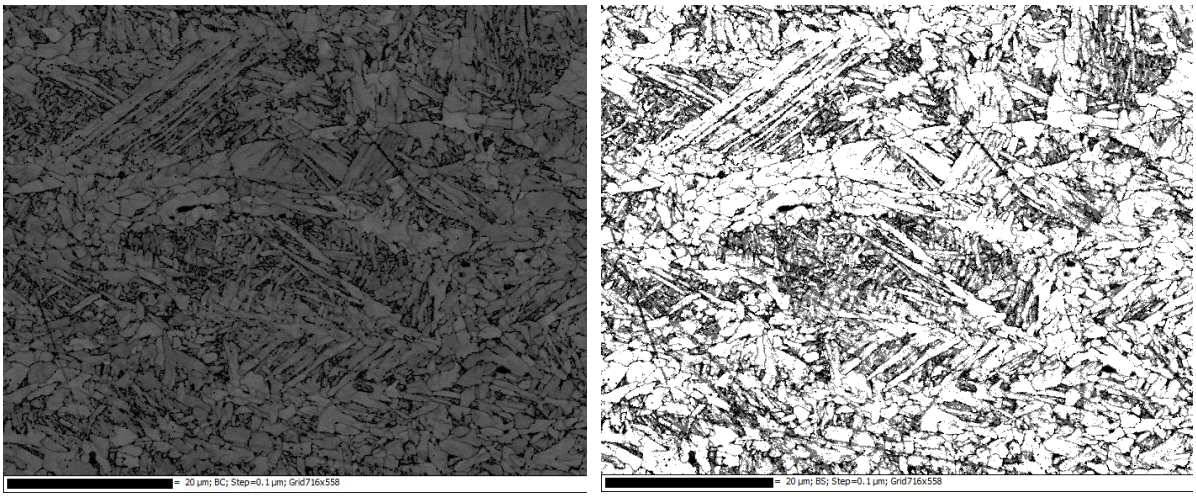

Figure 87. a) Band contrast and b) band slope EBSD maps showing the microstructure in specimen B3.

In order to validate whether DIFT at 810°C possess similar orientation characteristics than at 950°C, misorientation measurements were done in ferrite with different morphologies. Figure 88 a) shows a band slope – inverse pole figure map, in which ferrite plates and grains can be observed. Misorientation measurements were done within a ferrite plate (yellow line in Figure 88 a)) and in a region of ferrite located at a PAGB (white line), their profiles are shown in Figure 88 b) and Figure 88 c) respectively. Both morphologies exhibited the same trends in the misorientation, in the point to point profile the misorientation is very small regardless the increase in the distance, whereas in the point to origin profile, the misorientation increases rapidly with distance.

The same behaviour in the misorientation was also observed at 950°C in ferrite plates and in the transitory morphology of ferrite, i.e. when the plates commence to coalesce to form grains. According to what was discussed in Section 5.3.2.4, such misorientation behaviour might be associated to a face to face sympathetic nucleation mechanism [132] of ferrite plates during deformation. Adjacent plates have very small misorientation, but as new ferrite plates nucleate, the misorientation with respect to the first plate increases gradually as the colony widens. When plates commence to coalesce, a transitory morphology appears before the completion of the polygonisation process, in this transitory state, ferrite exhibits a somewhat polygonal shape but conserves similar misorientation to the plate colony as shown in Figure 88 a) and Figure 88 c).

The findings in the misorientation of ferrite at 810°C confirm that the formation mechanism of DIFT is the same at 810°C and 950°C.

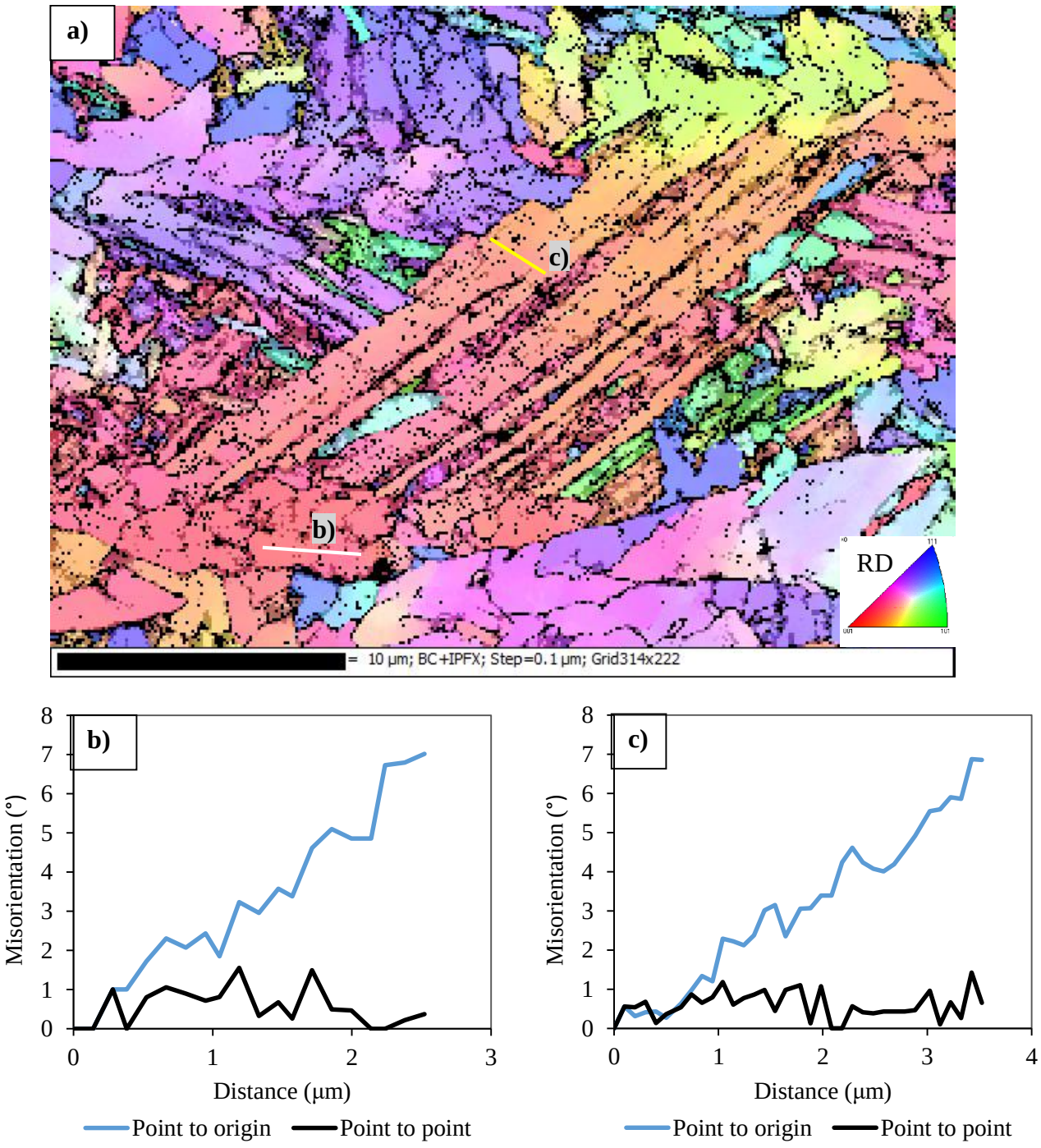

Figure 88. a) EBSD BS-IPF map and misorientation profiles measured a) within a colony of Widmanstätten ferrite and b) in the transitory morphology (between plate and grain) of ferrite.

5.3.3.5. TEM thin foils

TEM bright field imaging was carried out in the specimen B2 (simulation that consisted in one finishing pass at 810°C followed by a holding time of 10 seconds). Figure 89 shows a photo-mosaic of a region in the thin foil where ferrite is the dominant phase. Ferrite appears in form of plates and polygonal grains in bright colour as result of their low dislocations density. The first TEM image in the photo mosaic shows a group of ultrafine polygonal grains with diameters from around 500 nm to 1,700 nm, note that precipitation is found at the grain boundaries and within the grains. As for the ferrite plates, the third image in the mosaic shows a colony of very thin plates with widths from around 190 to 240 nm, most boundaries between the plates are difficult to observe due to the low misorientation between them as previously discussed in the EBSD analysis.

The evidence of ferrite grains and plates in the microstructure in the specimen deformed between the Ae_3 and Ar_3, proves that the mechanism of DIFT is very similar to that proposed by Basabe et al [61] occurring above the Ae_3. However, there is a subtle difference in the plates width between both deformation conditions, at 810°C the plates are thinner with an average width of around 200 nm, whereas at 950°C the plates showed a width of around 240 nm.

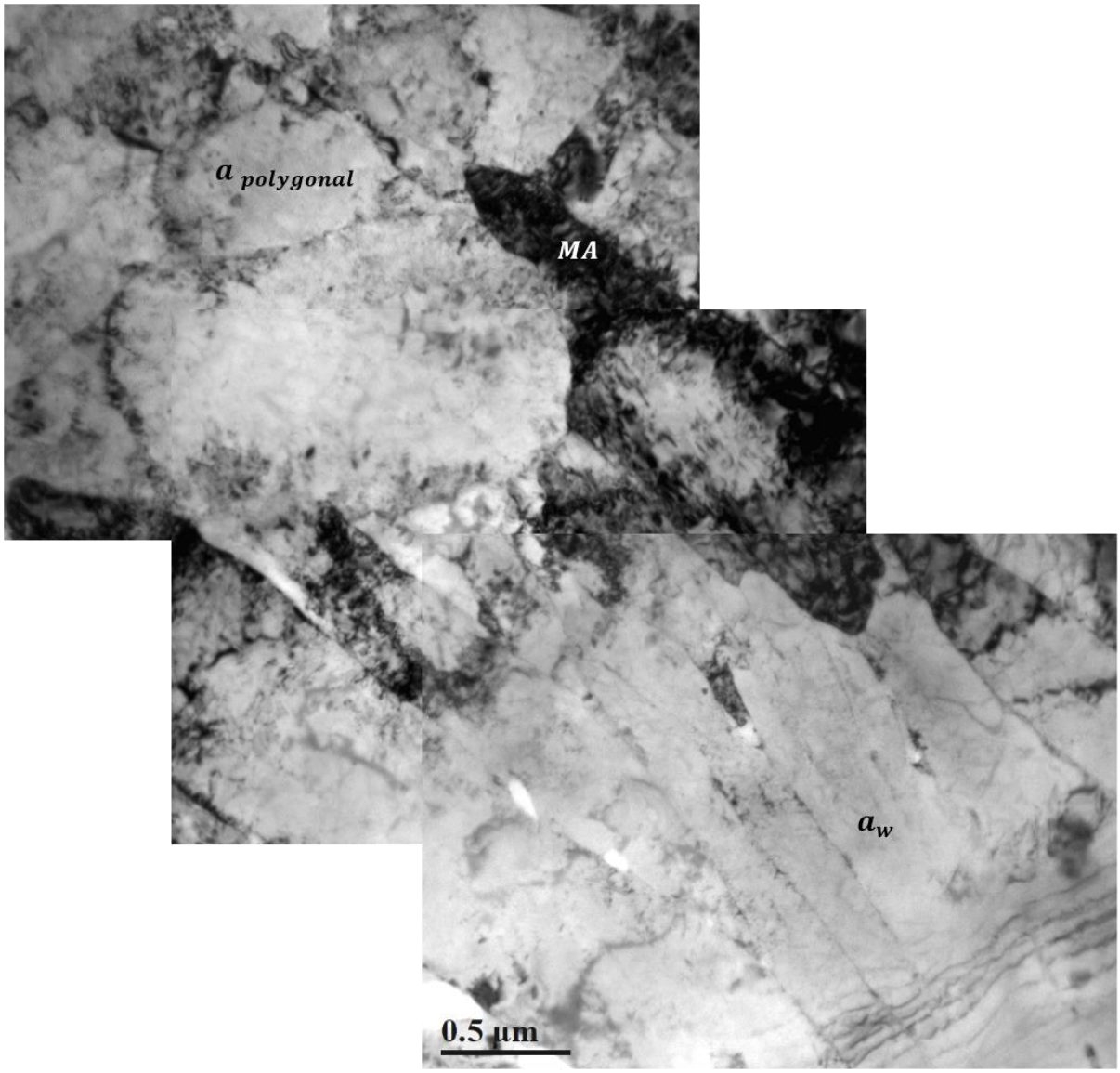

Figure 89. Bright field TEM image showing the presence of ferrite grains and plates.

Another interesting phenomenon captured in the TEM images, is the rearrangement of dislocations between DIFT and the surrounding martensite as pointed out by the yellow arrows in Figure 90. According to Weng et al [60], DIFT is accompanied by the rearrangement of some dislocations to form low angle grain boundaries, in their work, TEM images were presented showing very similar dislocation arrays at the ferrite grain boundaries. Figure 90 also shows what it seems to be ferrite plates coalescing to form a grain, the straight boundary between the martensite and the ferrite and the alignment of dislocations (parallel to the α-α' boundary at distances of around 200 nm) indicates that plates were formed. This morphology of ferrite might be the transitory state reported in the EBSD analysis in Section 5.3.2.4, note

that the morphology of ferrite grains observed in Figure 89 differs from that in Figure 90. In the former the grains show well defined boundaries (probably HAGBs) and there are not traces of former plates within the grain, whereas in the later, ferrite boundaries are not well defined and some arrays of dislocations appear to reduce the misorientation between the ferrite and martensite, besides, the aspect of the grain seems to indicate the former presence of plates.

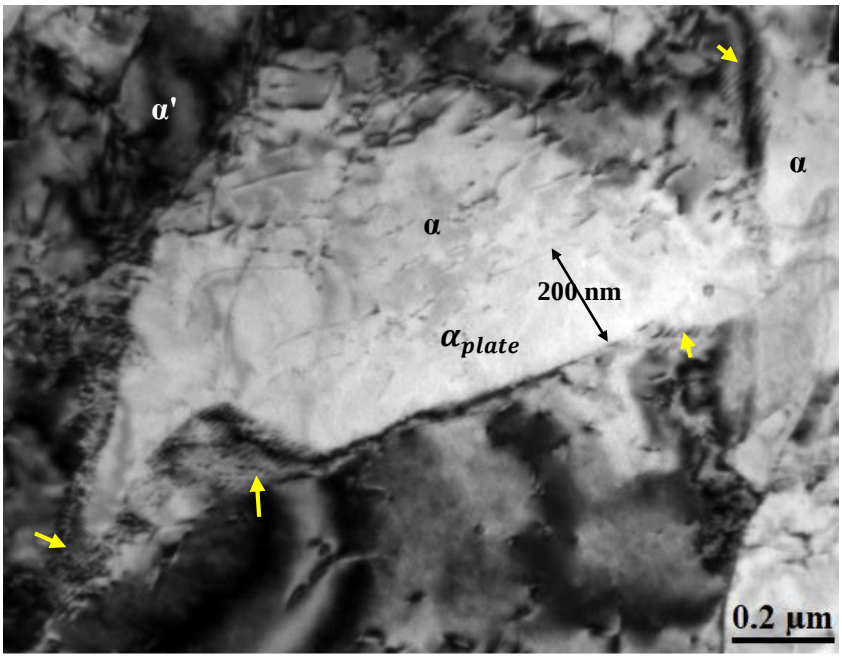

Figure 90. BF TEM image showing the rearrangement of dislocations (yellow arrows) at DIFT grain boundaries.

5.3.3.6. SPM and nanohardness evaluation

An extensive nanohardness evaluation in SPM mode was carried out in selected positions of the microstructure following the procedure described in Section 3.11, the simulation evaluated consisted in one finishing pass at 810°C followed by a holding time of 10 seconds (specimen B2). 15 indents were performed on DIFT grains and the hardness ranged from 1.41 to 2.7 GPa with an average of 2.0 GPa, whereas in martensite the average hardness was 4.79 after 19 indents. An example of the morphology of DIFT grains and their nanohardness values is shown in Figure 91. A more detailed explanation about the findings in the nanohardness – SPM evaluation of specimen B2 can be read in Section 3.11.1. As for the comparison between the

deformation at 950°C and 810°C, the morphology and nanohardness of DIFT is very similar in both conditions.

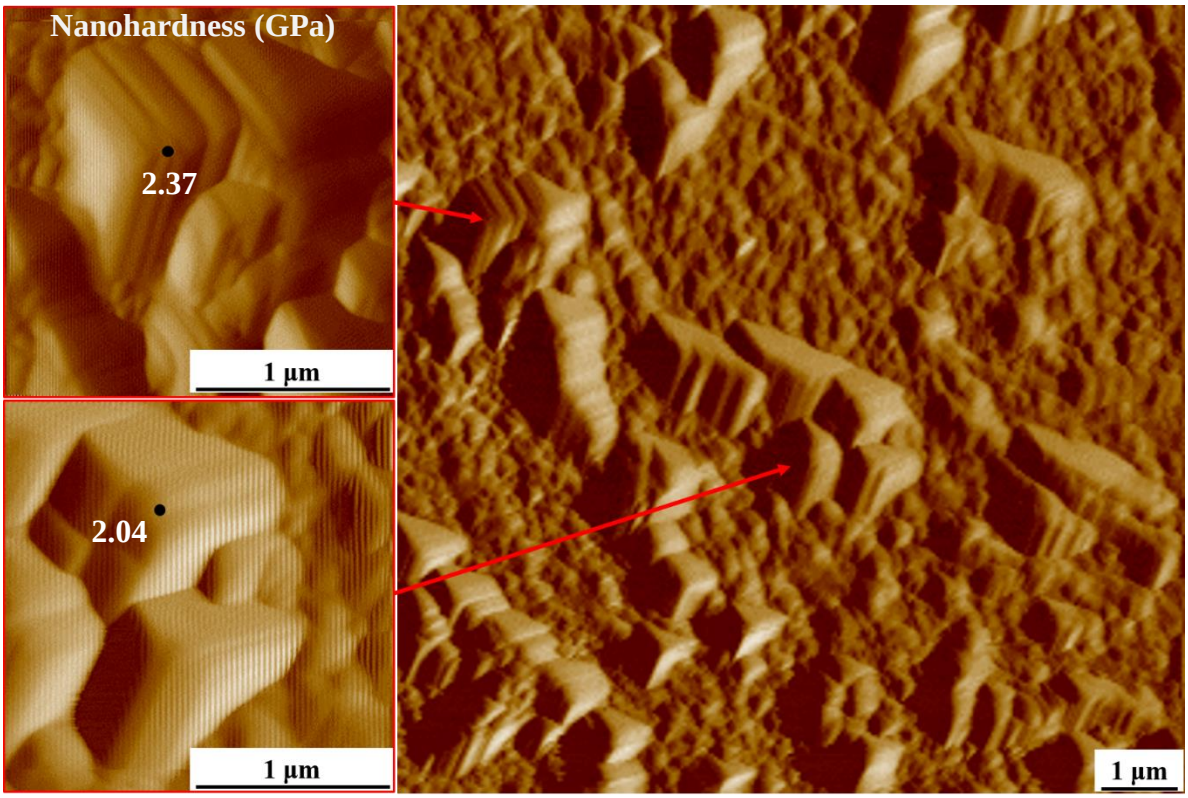

Figure 91. SPM images showing the nanohardness values in two DIFT grains found in the specimen B2.

5.3.3.7. DIFT quantification

The volume fraction of DIFT was estimated using OM images of the microstructure etched with Nital 2% solution, at least 5 images at 200x were used in each deformation condition to obtain the fraction of ferrite. Additionally, the volume fraction in the specimen B2 was obtained with SPM images following the procedure proposed in Section 3.11.1. Figure 92 shows the evolution in the amount of DIFT in the different finish rolling conditions.

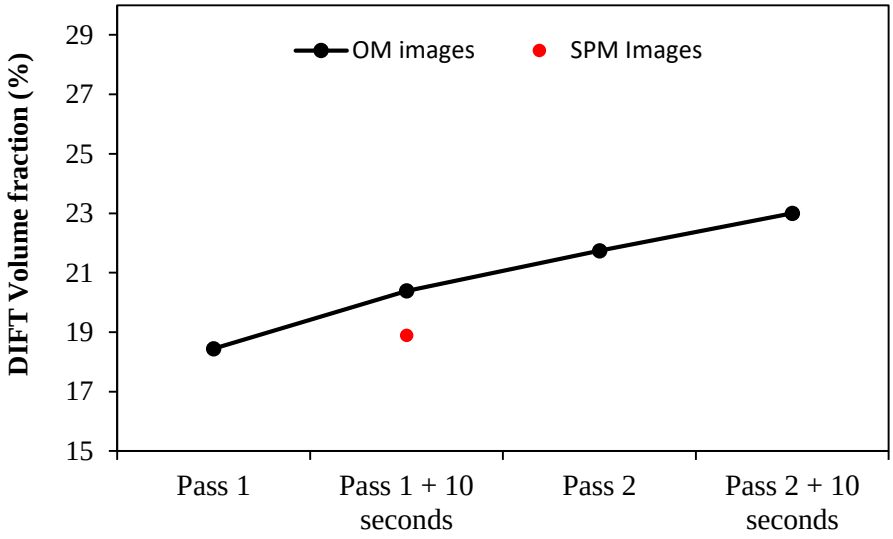

Figure 92. Volume fraction of DIFT in the different conditions of the finish rolling simulation at 810°C.

The finish rolling simulation at 810°C showed very similar results to the simulation at 950°C, the first finishing pass led to a significant fraction of DIFT but then, in the following deformation conditions the amount of DIFT increased very subtly. This behaviour is unexpected regarding that the deformation was performed below the Ae_3 and the conditions for DIFT are supposed to be favourable. It is believed that DIFT increases during the first 10 seconds of holding time when the deformation is performed between the Ae_3 and Ar_3, Dong et al [20] reported an increase from around 15% to 70% in the volume fraction of DIFT after a single holding time of 10 seconds, in their work a steel containing 0.094C-0.29Si-l.42Mn-0.045Nb-0.008Ti-0.0038N (mass%) was deformed by compression at 780°C at a strain of 0.69. Although Dong et al used a larger strain, the chemical composition and deformation temperature are similar to those used in this work, even so, in the HTP alloy the increase in the volume fraction of DIFT after the holding times of 10 seconds was almost insignificant.

5.3.4. Finish rolling simulation at 950°C and 810°C.

A new TMCP simulation was designed based on the best results obtained in the finish deformations at 950°C and 810°C, the simulation consists of a combination of two finishing passes at 950°C plus two passes more at 810°C as shown in Figure 93, again, each finishing pass is followed by a holding time of 10 seconds. The overall equivalent strain applied to the specimen was 1.2 from rough to finish deformation.

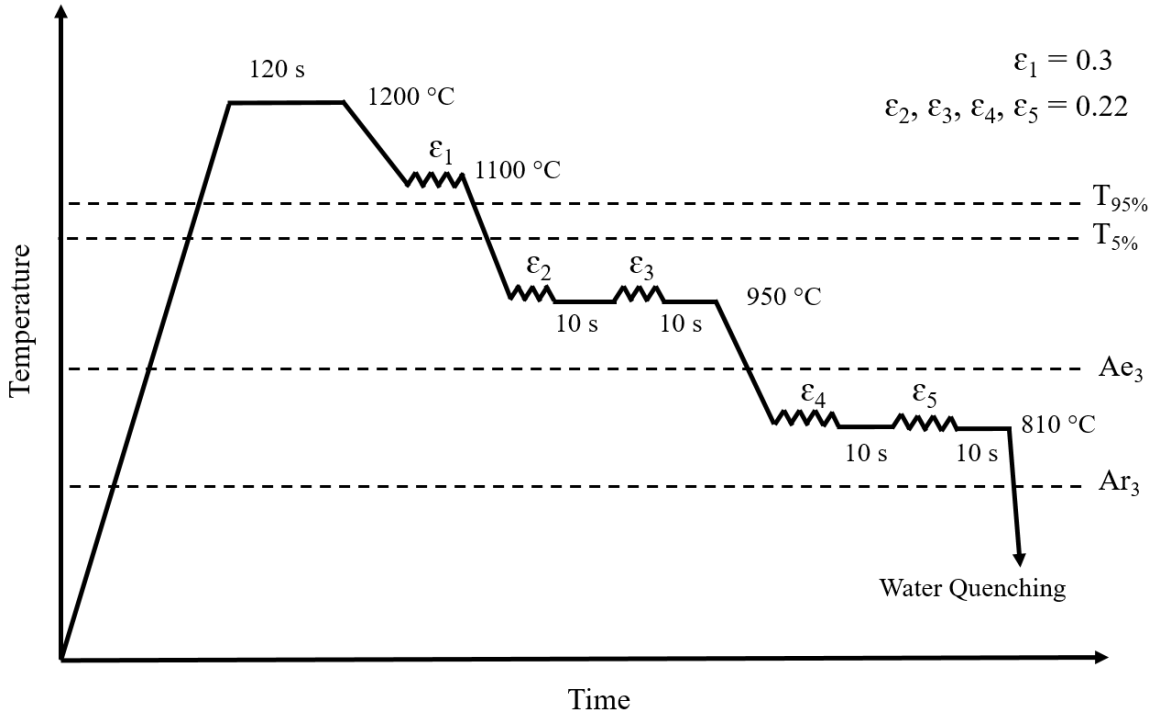

Figure 93. TCMP finish rolling simulation at 950°C and 810°C.

The microstructure exhibited a great grain refinement as shown in the different evaluations presented in Figure 94. Despite of the extensive deformation applied to the specimen the recrystallisation was negligible as can be seen in the PAGBs shown in Figure 94 a), the average PAG length in the rolling and normal directions were 84.3 μm and 8.5 μm respectively, and the aspect ratio was 9.9. As for the microstructure, a 31% of DIFT was estimated with the SPM imaging method described in Section 3.11.1, the refinement achieved can be appreciated in detail in the metallography, SEM image and EBSD band contrast map shown in Figure 94.

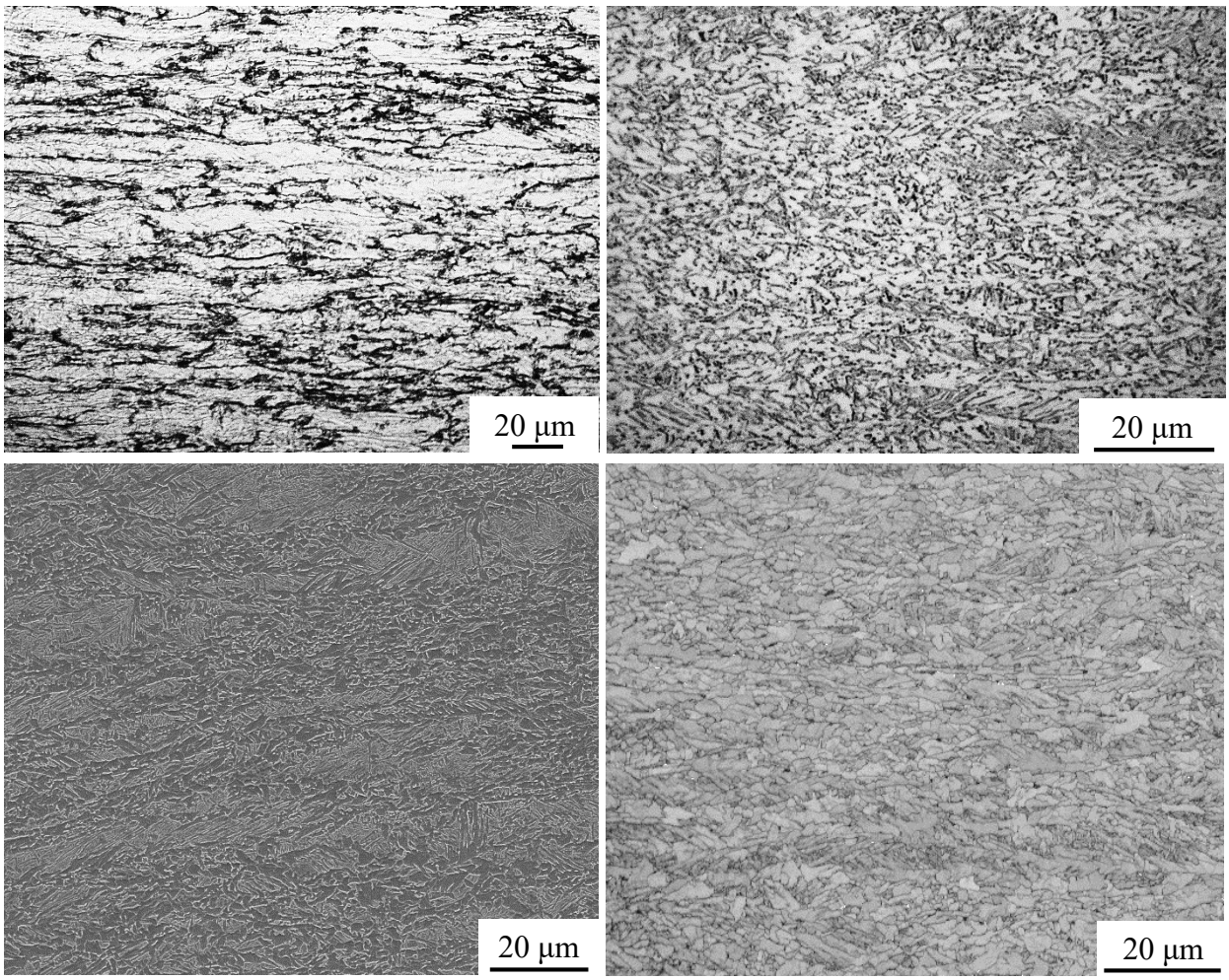

Figure 94. Microstructure of the specimen deformed in four finishing passes ant 950°C and 810°C. a) Prior austenite grain boundaries and microstructure observed in b) light microscopy, c) SEM and d) EBSD band contrast map.

Something important to remark, is that most DIFT shows a polygonal morphology and colonies of Widmanstätten ferrite barely appear, this change in the microstructure results to be very positive for the mechanical properties of the material. It is well known that Widmanstätten ferrite has a detrimental effect on the fracture toughness of steel [134], conversely, ultrafine polygonal ferrite greatly improves the strength and toughness by the grain refinement mechanism.

5.4. Discussion

5.4.1. Recrystallisation behaviour of the HTP alloy during the finish deformation.

The recrystallisation process showed a particular behaviour in the HTP alloy, at both deformation temperatures (950°C and 810°C) the evolution of the prior austenite exhibited the same behaviour during the first two finishing passes. After the first pass, a relatively small amount of recrystallisation was observed at both temperatures as presented in Table 10, surprisingly however, the addition of the holding time caused a negligible effect on the recrystallised fraction. This behaviour indicates that DRX occurred during the first pass (which was validated with the double differentiation method), but it was stopped during or immediately after the deformation, the only mechanism able to stop the recrystallisation is the strain induced precipitation of Nb, although carbon extraction replicas were not obtained in those conditions, it can be assumed that precipitation of Nb took place and prevented static recrystallisation during the holding time.

Table 10. Recrystallisation fraction and critical strains for DRX in the finishing passes at 810°C and 950°C.

Finishing pass	**Recrystallised fraction (%)**		**Critical strain for DRX**	
	950°C	**810°C**	**950°C**	**810°C**
Pass 1	11.7	8.8	0.15	0.14
Pass 1 + 10 seconds	12.6	8.5	-	-
Pass 2	1.2	-	0.08	0.11
Pass 2 + 10 seconds	1.3	0.5	-	-
Pass 3	-	-	0.07	-
Pass 3 + 10 seconds	20	-	-	-

In the second finishing passes at 810°C and 950°C, the recrystallisation was negligible even after the holding time of 10 seconds, PAGBs remained greatly deformed as shown in Figure 69 d) and Figure 83 c). However, the double differentiation method detected the onset of DRX in those conditions, which is inconsistent with the recrystallisation observed in the PAGBs evaluation. Other works [69], [70] have also reported DRX in the HTP alloy under very similar deformation conditions to the second finishing pass of the simulation at 950°C, DRX was also detected with the double differentiation method, however, microstructural evidence was not provided. It is likely that the double differentiation method has detected DRV instead in the second finishing passes at 810°C and 950°C, for the PAGBs observed showed insignificant recrystallisation.

The finish deformation at 950°C led to important recrystallisation after the holding time of the third finishing pass, thus, in order to achieve an optimal grain refinement only two finishing passes should be carried out at 950°C, then, more passes could be added at lower temperatures to attain a better austenite conditioning and avoid the recrystallisation. A proper combination of finishing passes in the temperature range from Ar_3 to $T_{5\%}$ could be the key point to successfully achieve highly refined microstructures in a TMCP, such is the case of the simulation carried at both finishing temperatures 950°C and 810°C in which the prior austenite was remarkably refined as shown in Figure 95 and Figure 96.

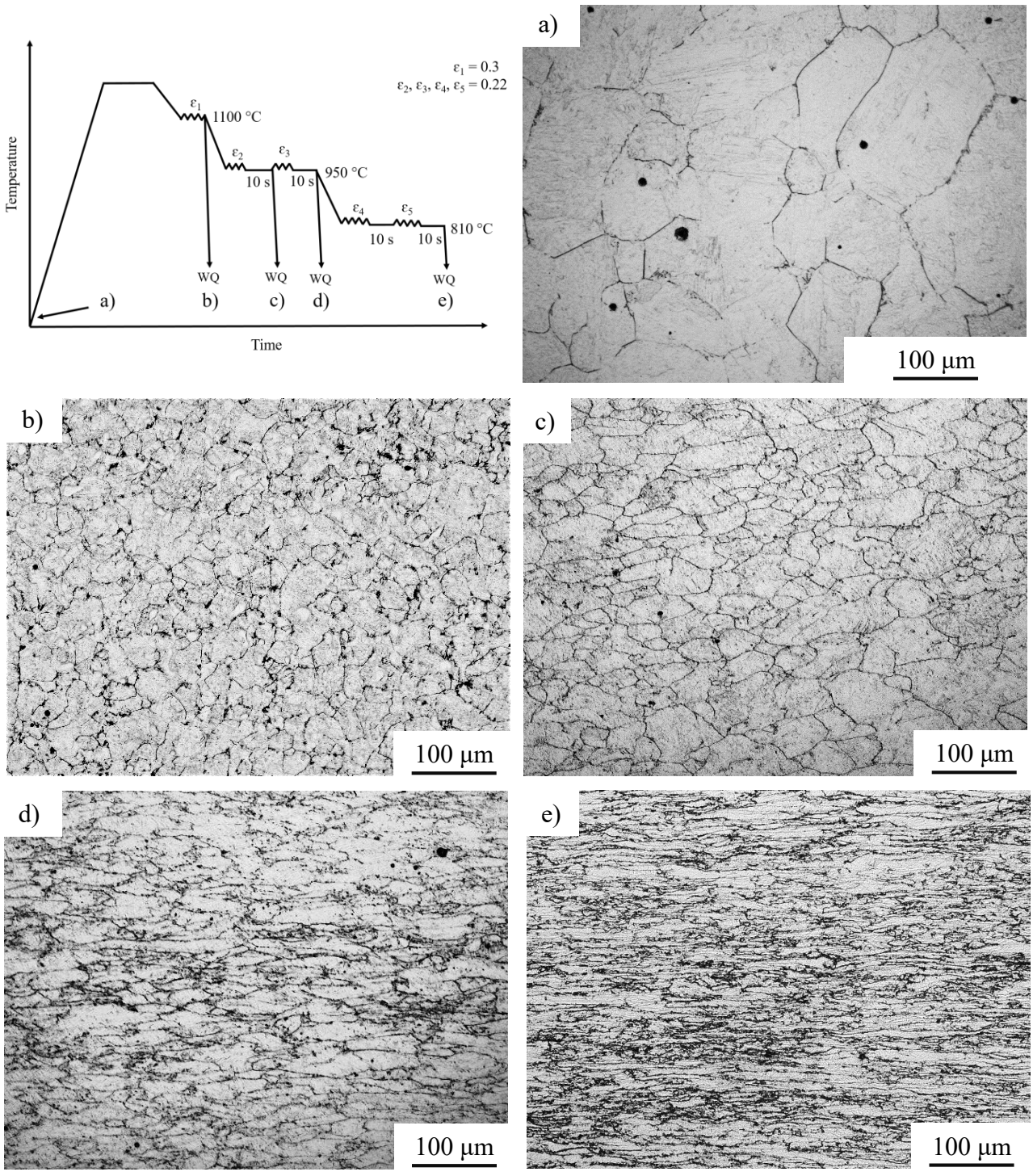

Figure 95. Evolution of prior austenite grain boundaries along the TMCP simulation with finishing passes at 950°C and 810°C.

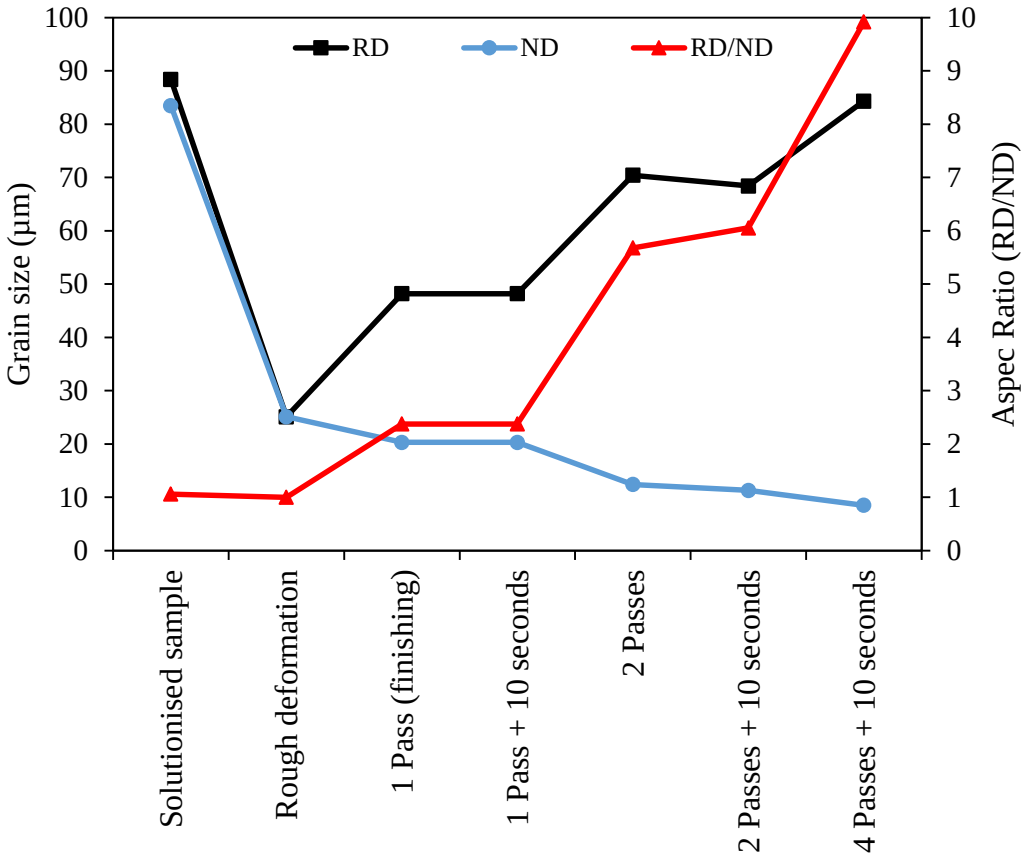

Figure 96. Evolution of the prior austenite grain size in the rolling (RD) and normal (ND) directions and aspect ratio (RD/ND) along the TMCP simulation that consisted in two finishing passes at 950°C and two passes at 810°C.

5.4.2. Characteristics of DIFT at 950°C and 810°C

There are still research gaps to understand the differences (if any) in the mechanism of DIFT above and below the Ae_3 [73], in the current work multiple analysis were carried out in order to answer some of the remaining questions in such matter. After a deep evaluation of DIFT at 950°C (above the Ae_3) and 810°C (between the Ae_3 and Ar_3) with multiple characterisation techniques, it can be concluded that the transformation mechanism is the same at both temperatures. The characteristics highlighted below were observed at both deformation temperatures:

- Formation of very thin Widmanstätten ferrite plates aligned in a single direction showing the influence of the stress during the deformation. Although DIFT plates were 40 nm wider at 950°C (240 nm).
- Coalescence of ferrite plates.
- A transitory state of ferrite that occurs during the coalescence of plates, in which the misorientation is plates-like, but the morphology commences to change to polygonal shape.
- Very similar critical strains for DIFT.
- Intragranular growth of ferrite plates and grains within the PAGBs.
- Intragranular nucleation of carbides within ferrite grains.
- Very similar volume fractions of ferrite at the different deformation conditions.

Note that such characteristics are distinctive of DIFT, and are not reported in proeutectoid ferrite transformed during the cooling of austenite. Another characteristic observed in the EBSD analysis in both deformation temperatures, is the very similar orientation between adjacent ferrite plates, this behaviour has been also reported in dynamically transformed Widmanstätten ferrite plates above the Ae_3 [61], [109] and in conventional Widmanstätten ferrite formed on cooling [135], thus, it seems that the small misorientation between adjacent plates is a general characteristic of Widmanstätten ferrite regardless the transformation mechanism. The misorientation in ferrite plates is usually analysed solely with the "point to point" profile in EBSD, however, the "point to origin" analysis can provide additional valuable information to understand the misorientation within the same phase, after the latter misorientation analysis, in this work it was proposed that DIFT plates form by a face to face sympathetic nucleation mechanism. A comparison in the point to origin misorientation between dynamic and proeutectoid Widmanstätten ferrite, would provide helpful information to understand the differences in the transformation mechanisms in both types of Widmanstätten ferrite.

After the findings reported in the current work, it is suggested to use a single term name the dynamically transformed ferrite above the Ae_3 and between the Ae_3 and Ar_3.

5.5. Summary

Finish rolling simulations at 950°C and 810°C were carried out in order to study the microstructural evolution of the HTP steel alloy when deformed in multiple passes at temperatures both above the Ae_3 and between the Ae_3 and Ar_3. Diverse analyses were performed to characterise the deformation induced ferrite transformation and the remaining prior austenite at different deformation conditions. The most relevant findings are summarised below:

1. The HTP alloy shows a good performance during the first two finishing passes at 950°C and 0.22 of strain, after the deformations the microstructure exhibited an excellent grain refinement and the recrystallisation was prevented even after the holding time of 10 seconds. The prior austenite was well conditioned resulting in an average grain size of 70 µm in the rolling direction and 12 µm in the normal direction, besides, around 25% of the microstructure consisted of DIFT which greatly benefited the microstructural refinement. As for the precipitation of Nb, the two finishing passes followed by holding times conducted to abundant strain induced precipitation of very small particles of around 6 nm diameter, the precipitation went from $9.1x10^{-5}$ particles per nm^2 before finish rolling to $2.7x10^{-4}$ particles per nm^2 after the addition of two finishing passes which is a three-fold increase in the number of particles per unit area. Inconveniently however, the addition of a third finishing pass followed by a holding time of 10 seconds led to a high fraction of recrystallisation, thus, only two finishing passes should be performed at 950 and 0.22 of strain if grain refinement is pursued.

2. The microstructures produced in the finish rolling simulations at 810°C and 950°C are surprisingly similar, the fractions of recrystallisation and DIFT were almost identical at both cases.

3. The DIFT at 810°C and 950°C was analysed with conventional metallography, flow curves, SEM, EBSD, TEM, SPM and nanohardness, it is concluded that the transformation mechanisms is the same at both temperatures since the morphology, topography, misorientation and critical strains for DIFT are almost identical at 810°C and 950°C. DIFT starts with the nucleation of Widmanstätten ferrite plates during the

deformation, plates are very thin and possess similar orientation between adjacent plates. Then during or after the application of the load, plates commence to coalesce and a transitory state of ferrite appears, in such transitory state the ferrite exhibits a somewhat grain-like morphology but a plates-like misorientation. Finally, when the coalescence process is completed, ultrafine polygonal grains from around 0.5 to 2 μm diameter are formed, ferrite forms low and high angle grain boundaries from around 6° to 59°.

4. Considering the best results obtained from the finish rolling simulations at 810°C and 950°C, a third TMCP was designed so as to produce the finest possible microstructure. The simulation consisted of one roughing pass at 1100°C applying a strain of 0.3 followed by four finishing passes at a strain of 0.22, the first two finishing passes were carried out at 950°C, whereas the last two were done at 810°C. A remarkable refinement was observed in the microstructure, PAGBs did not show recrystallisation after the four finishing passes and the average grain size was 84 μm in the rolling direction and 8.5 μm in the normal direction. Furthermore, the volume fraction of DIFT was 30.7% and polygonal grains were the dominant morphology in the ferrite phase.

Chapter 6. Industrial application

The TMCP of the HTP alloy can produce microstructures with an exceptional degree of refinement, a proper combination of strains, number of passes, holding times and deformation temperatures, can lead to an excellent austenite conditioning. Besides, DIFT can be produced in significant amounts which greatly improves the grain refinement in the microstructure. A good combination of rough and finish rolling is paramount to achieve large amounts of deformation without recrystallisation. Below, the results obtained in the rough and finish rolling simulations are discussed and some processing variables are suggested for industrial operations.

6.1. Rough deformation temperature

The rough rolling was simulated at a strain of 0.3 and five different temperatures from 830°C to 1200°C, however, the temperatures of industrial interest are solely 1100°C and 1200°C since the temperature window for the rough rolling of X80 steel plates using the HTP alloy is above 1070°C [136]. In the simulations, a single rough deformation pass caused significant austenite grain refinement by recrystallisation, the PAGS before the rough deformation was 87 μm but the deformations at 1100°C and 1200°C reduced the grain size to 25 μm and 27 μm respectively. The decrease in the deformation temperature to 1100°C produced just a slight improvement in the grain refinement, however, a moderate SIP of NbC with an average diameter of 8.4 nm was observed. Conversely, the deformation at 1200°C did not conduct to SIP.

The response of the HTP alloy to the deformation at 1100°C is rather interesting, normally SIP comes along with the suppression or retardation of recrystallisation [35]. However, due to the high content of Nb in the HTP alloy, SIP can occur even at high temperatures where the full recrystallisation also happens. Such precipitation - recrystallisation behaviour might give an advantage in the further finish rolling process, if the processing time between the rough and finish rolling is not long enough to cause the coarsening of the Nb precipitates, SIP formed

during the rough rolling could improve the resistance to recrystallisation during the finish deformation.

It is true that the SIP during rough rolling decreases the Nb in solution available to precipitate during the subsequent finish rolling, which in consequence reduces the ability of niobium to retard the recrystallisation by solute drag effect. Nevertheless, the benefit of forming fine precipitates prior to finish rolling might outweigh the disadvantages of the reduction of Nb in solution. For instance, during the first finishing pass the precipitates already formed would increase the temperature at which the recrystallisation starts, although there is less Nb in solid solution (which reduces the solute drag effect), Nb precipitates are effective at pinning the grain boundaries. It is commonly accepted that the grain boundary pinning effect is quite superior to suppress the recrystallisation than the solute drag effect [20], [137].

The positive effect of the precipitates formed during rough rolling on the microstructural refinement during the subsequent finish rolling, can be inferred from recrystallisation observed in the first finishing pass at 950°C and 810°C, in both cases, the recrystallisation fraction was about the same after the deformation and after the addition of the 10 seconds holding time, which indicates that the insipient DRX was effectively stopped during deformation. New SIP can nucleate and growth instantaneously during the first finishing pass, however, precipitation requires an incubation time to generate the conditions to stop the recrystallisation. According to the PTT diagram showed in. Figure 39, the incubation time for SIP in the first finishing pass occurs around 0.5 and 1 seconds after the deformations at 810°C and 950°C respectively. If recrystallisation was stopped before the incubation time for precipitation, it is likely that the fine precipitates formed during the rough deformation suppressed the recrystallisation in conjunction with the Nb in solution.

As for DIFT during rough rolling, the SPM evaluation showed that the volume fractions in the simulations at 1200°C and 1100°C were 8.1 and 1.9% respectively. The small amount of ferrite formed at 1100°C is related to a low driving force for dynamic transformation, which is caused by the proximity to the temperature in the midway between the Ae_3 and δ- ferrite phase field (1138°C) [21] as discussed in Chapter 4. It might seem that the deformation at 1200°C is a better condition to improve the microstructural refinement, for the fraction of DIFT is larger, however, two important aspects must be considered; first, DIFT grains are coarser at high

temperatures (see Figure 16 in Chapter 3), at 1200°C the ferrite grain size ranged from 1.5 to 5.8 μm and the average was 2.8 μm, whereas at 830°C, the range was from 0.7 to 1.2 μm and the average was 0.9 μm. And second, it is preferable to end the rough rolling without DIFT so as to increase the number of nucleation sites for finer ferrite during the subsequent finish rolling, a more detailed explanation is given below.

In the finish rolling simulations presented in Chapter 5, it was shown that the largest fraction of DIFT was formed during the first finishing pass, and the subsequent deformations led only to slight increases in the volume fraction of ferrite. The increase in the amount of DIFT in each pass seems to be associated to the availability of ferrite-free PAGBs, during the first pass DIFT was enhanced due to the vast availability PAGBs, whereas in the subsequent deformations, the increase of DIFT was very subtle since most PAGBs were already occupied by the DIFT previously formed during the first finishing pass. The rough deformation at 1100°C led to a very small fraction of DIFT allowing the PAGBs to be available to serve as nucleation sites for DIFT during the finish rolling.

In summary, the rough deformation at 1100°C might bring more benefits than at 1200°C in terms of microstructural refinement, apart from the remarkable austenite conditioning achieved, SIP is triggered and DIFT occurs at very small amounts which improves the grain refinement during subsequent finish rolling.

6.2. Controlling the microstructural evolution during finish rolling

An adequate finish rolling can produce an excellent microstructural refinement in the HTP alloy, large amounts of deformation can be achieved to produce substantial amounts of DIFT and yet prevent the recrystallisation of austenite. Such is the case of the simulation C, in which the specimen was strained to 0.88 below the $T_{0.05x}$ and the recrystallisation after the last finishing pass at 810 was negligible, furthermore, 31% of the microstructure consisted of DIFT.

Due to the nature of DIFT, Widmanstätten ferrite plates and ultrafine polygonal grains unavoidably coexist in the microstructure, which can turn out to be undesirable for the mechanical properties since Widmanstätten ferrite has a detrimental effect on the fracture

toughness of steel [134]. However, the morphology of DIFT can be tailored by combinations of deformation passes plus holding times. The microstructures observed in the finishing simulations suggested that the ratio of polygonal-grains/plates in DIFT increased with the addition of passes and holding times.

Ferrite plates coalesce and evolve into polygonal grains dynamically during deformation in less than a millisecond [72], but it seems that the same process can also occur statically during the holding time at a slower rate. In fact, the ratio polygonal-grains/plates ferrite increased more markedly during the holding times as shown in Figure 97 a). Although the volume fraction of DIFT increases very subtly after the first finishing pass, the proportions of plates and grains in DIFT change rapidly; after the first pass the volume fraction of DIFT was 18.4%, from which 7.7% consisted of grains and 10.7% were plates, but after two passes and two holding times, DIFT increased to 23%, and the fractions of grains and plates changed to 18% and 5% respectively, which means that 78% of the volume fraction of DIFT consisted of ferrite grains and the remaining 22% were plates.

Figure 97 b) shows the evolution in the fractions of DIFT plates and grains in some conditions of the simulation C, it can be seen that after four finishing passes followed by holding times DIFT consists primarily of grains, and only around 4% of the microstructure consisted of ferrite plates.

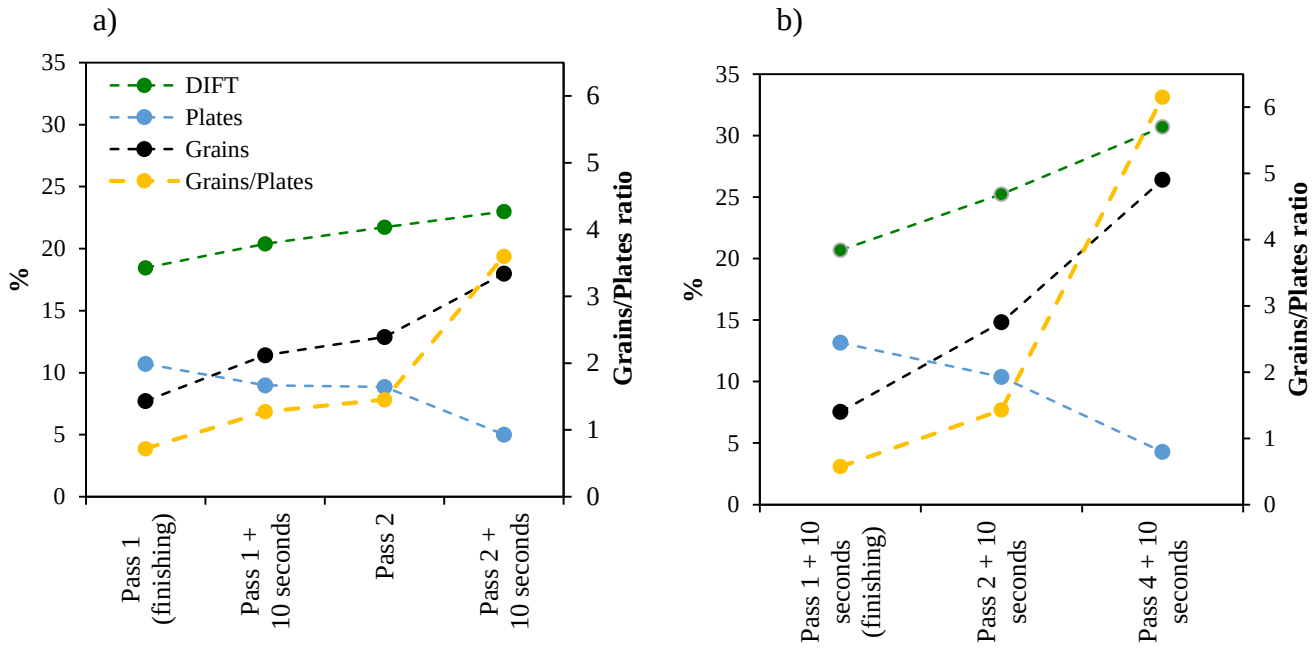

Figure 97. Volume fractions of DIFT, ferrite plates and polygonal grains. a) Simulation A (finishing at 810°C) and b) simulation C (first two finishing passes at 950°C followed by two passes at 810°C). The analysis was done using the point counting method in SEM images at 2000x.

The evolution from plates to grains in the morphology of DIFT, is paramount to achieve high toughness in the final properties of the material, the addition of multiple deformation passes at a small strain combined with holding times appears to be a solution to obtain microstructures where the morphology of DIFT consists primarily in ultrafine polygonal grains.

Various works have achieved large amounts of DIFT with a morphology apparently fully polygonal, particularly in TMCP simulations where the deformation took place slightly above the Ae_3 [72], [105], [133], [138] or between the Ae_3 and the Ar_3 temperatures [106], [139]. However, in such works the ferritic transformation was induced in a single deformation pass at large strains from 0.6 to 2, that accounts for the polygonal morphology of DIFT. Basabe et al [72], reported that single strains below 0.5 led to a plate-dominated microstructure, whereas above 0.5, the microstructure consisted primarily of polygonal ferrite grains, their experiments were carried out at the Ae_3 temperature, and 20°C and 60°C above the Ae_3. It is also expected

that there is a threshold strain in which the morphology of DIFT becomes dominantly polygonal at deformation temperatures between the Ae_3 and the Ar_3.

From and industrial perspective, high reductions are difficult to achieve in a single deformation pass in TMCP, particularly during the finish rolling where the reductions are relatively small for good shape control [59]. Thus, the combination of small deformations followed by short holding times during the finish rolling, might be the key point to produce microstructures highly refined with remarkable austenite conditioning and significant amounts of ultrafine polygonal ferrite grains.

In summary, the microstructural evolution during the deformation of the HTP alloy can be controlled to obtain the finest possible microstructures, for such purpose the following recommendations should be considered:

1. Perform rough rolling at temperatures in which the austenite can be remarkably refined by recrystallisation and the amount of DIFT is small. This will provide the conditions for an optimal finish rolling in which most of DIFT takes place in the finishing passes resulting in an ultrafine ferrite grain size. The deformation at 1100°C suits well with such purposes, besides, SIP of Nb also occurs at such temperature which probably improves the resistance to recrystallisation in the subsequent finish rolling.

2. Design a sequence of finishing passes in the range of temperatures between the $T_{0.05X}$ and the A_{r3}, in which each pass leads to a microstructure that consists of deformed austenite plus DIFT. A good starting temperature can be 950°C which exhibits an excellent grain refinement after the first two finishing passes, then, the deformation temperatures must decrease gradually so as to preserve the unrecrystallised austenite. Since the transformation mechanism of DIFT seems to be same in the temperature ranges above the Ae_3 and between the Ae_3 and Ar_3, the window for finish deformation can be quiet ample, and deformations can be performed in both temperature ranges to produce the same microstructures.

3. If large deformations cannot be performed during finish rolling, multiple finishing passes should be carried out at low strains followed by holding times of 10 seconds. Low strains (greater than σ_c) conduct to DIFT with a morphology that consists primarily

of Widmanstätten ferrite plates which is a microstructure with detrimental effects on the toughness of the steel, however, the continuous addition of deformation passes followed by holding times leads to the evolution in the morphology of DIFT from plates to ultrafine polygonal grains. The latter, greatly improves the strength and toughness of the steel by the grain refinement mechanism. Another benefit achieved with the addition of holding times of 10 seconds, is the notable increase in the SIP of Nb which remarkably retards or suppresses the recrystallisation process.

In the current work, the strain of 0.22 used in the finishing passes led to good results, the critical strain for DIFT was easily reached in each pass and DIFT consisted mainly of polygonal ultrafine grains after the second finishing pass. Besides, the amount of DIFT increased progressively as finishing passes were added, a volume fraction of 31% of DIFT was obtained after four passes in the simulation C.

6.3. Limitations of the TMCP

As previously explained in Section 3.4, the rolling variables used for the simulations of this research replicate reasonably well the rolling conditions that take place during the real TMCP of steel plates for welded linepipe grades (such as the X80 HTP), however, the TMCP designs have some limitations that hinder the realization of more realistic simulations of the rolling process.

It is important to first understand the industrial context of the fabrication of steel plates for welded linepipe steel grades through TMCP. An accepted industrial practice is to perform rough rolling with reductions between 20 to 35% per pass at temperatures above 1070°C, the deformation can accumulate up to 60% of reduction depending on the number of passes. Then, after rough rolling the slabs are transferred to the finish rolling mill where the passes are commonly executed with gradually decreasing reductions per pass from 40% to 10% within a temperature window that ranges from 50~100°C below the $T_{95\%}$ to 20~70°C above the Ar_3, generally the accumulated reduction during finish rolling can be as much or even more than 70% [83]. The true strains applied in each pass during both rough or finish rolling can vary from 0.05 to 0.35 and the strain rates can go from 1 to 40 s^{-1}, the latter is not constant during

the period of hot reduction and usually decreases with the progress of deformation [82]. The number of passes depends on the percentage of reduction pursued in final thickness of the plates, and the deformations are performed in different ranges of temperatures according to the stage of the process; during rough rolling the deformations are carried out at high temperatures above the non-recrystallisation temperature of austenite ($T_{95\%}$ or also called T_{nr}), the objective in this stage of the process is to apply relatively large reductions at temperatures in which the deformed austenite recrystallises completely between the rolling passes, such recrystallisation leads to austenite grain refinement. Conversely, during finish rolling smaller reductions (per pass) are applied to the steel plates until the final thickness and length are achieved, the passes are executed at lower temperatures in order to prevent the recrystallisation of austenite, after finish rolling the austenite ends in "pancake" shape, i.e. deformed and elongated along the rolling direction.

The strains, strain rates, temperatures, interpass times and cooling and heating rates used in the simulations of this research match well with those used in the industrial TMCP in plate-mills, however, due to the characteristics of the PSCT the real industrial conditions cannot be completely reproduced at laboratory scale. For instance, the number of passes that can be applied to the PSC specimen during the TMCP simulations is far fewer than the number of passes used in the rolling mills, after around 3 deformations the specimens tend to fall down from the grippers during the application of the load and consequently the tests fail. The maximum number of passes achieved in the simulations of this work was 5 (1 roughing and 4 finishing passes in simulation C) which is significantly smaller than the typical number of passes used during the controlled rolling of plates. The TMCP of plates for welded pipes using the HTP alloy usually performs around 4 to 6 roughing passes and 5 to 7 finishing passes depending on the percentage of reduction pursued from the slab to the final plate [83], [140].

Performing TMCP simulations with less deformation passes than those used in the industry does not reproduce with accuracy the microstructural evolution achieved in the real processes, for the austenite conditioning and the volume fractions of DIFT and SIP strongly depend on the number of passes and holding times of the process, however, the simulations provide an excellent description of the evolution of the microstructure of the HTP alloy in a TMCP. The final microstructure of the HTP alloy resulting from a TMCP with more roughing and finishing passes could be inferred from the results obtained in the current simulations.

For instance, it is very likely that the microstructure undergoes only slight changes if more roughing passes (between 3 to 5) at 1100°C are added, based on the evidence reported in other works about the austenite grain refinement obtained during the multipass rough rolling of Nb microalloyed steels [82], [141], the addition of more roughing passes at 1100°C to the TMCP simulations would not lead to austenite grains significantly finer than those observed in the single pass rough rolling simulation at 1100°C reported in Chapter 4. On the other hand, DIFT is also expected to experience only subtle changes with the addition of more roughing passes at 1100°C, in Chapter 4 it was evidenced and discussed that the rough deformation led to almost insignificant DIFT when the deformation took place at such temperature due to the low driving force for the dynamic transformation at the midway temperature between Ae3 and δ- ferrite phase field. Thus, the addition of more roughing passes at 1100°C surely would increase the volume fraction of DIFT during rough rolling but the increase would probably be slight.

The behaviour of the strain induced precipitation of Nb in a multipass rough rolling at 1100°C might also be inferred from the results obtained in the single pass rough rolling simulation. In Chapter 4 it was shown that SIP can occur even at 1100°C in moderate amounts ($9.1x10^{-5}$ particles/nm^2) and in Chapter 5 it was demonstrated that the SIP formed during rough rolling improves the resistance to recrystallisation of austenite in the subsequent finishing passes. Thus, the addition of roughing passes to the TMCP simulations would surely increase the amount of SIP during rough rolling and consequently improve the performance of the HTP alloy during the finish rolling.

As for the addition of more finishing passes in the TMCP simulations, as long as the added passes are conducted below the initiation of recrystallisation temperature i.e., below 950°C after the second finishing pass, the microstructural refinement will be even better since the aspect ratio of the deformed austenite increases with the number of passes, meaning that austenite conditioning is improved. The addition of more finishing passes followed by holding times also entails the formation of higher volume fractions of DIFT with a dominant polygonal morphology, which in consequence can greatly improve the final strength and toughness of the material.

Another limitation of the TMCP designed in this work is related to capacities of the different types of rolling mills. In a plate-mill such designs might be very useful to study the microstructural evolution during TMCP, as aforementioned, most of the rolling variables used in the simulations match well with those used in the plate-mills. However, due to the holding times of 10 seconds added after each finishing pass, the TMCP designs do not simulate well the rolling conditions in mills where the interpass times are significantly shorter, such as the strip-mills where the interpass times ranges from 5 to less than 1 second in the tandem finish mills. However, is important to remark that the manufacture of the X80 steel grade using the HTP alloy commonly takes place in plate-mills where the interpass times during the finish rolling range from 8 to 20 s [82], [85].

The use of relatively long interpass times during finish rolling can bring remarkable benefits to the grain refinement, Peng et all [46], [142], [143] demonstrated that the addition of isothermal holding times of 10 seconds during the finish rolling of Nb microalloyed steels brings important benefits to the microstructural refinement, the holding times led to an important increase in the volume fraction of SIP which in consequence prevented the recrystallisation of the deformed austenite, furthermore, the volume fraction of DIFT also increased after the holding times resulting in a final microstructure that consisted of a mixture of highly refined austenite and ultrafine ferrite. In strip-mills the benefits of longer interpass times are lost, thus polygonisation of DIFT is mainly achieved by the multiple deformations that take place in tandem finish mills.

Chapter 7. Conclusions

7.1. Austenitising Treatment.

1) The austenitising heat treatment was effective to dissolve the niobium in the steel plate from which the PSC specimens were obtained for the simulations. After holding the plate for 3 hours at 1300°C most of the niobium precipitates were dissolved, then the subsequent quenching of the hot plate in cold water allowed to keep the niobium in solid solution at room temperature, which means that the niobium was available to precipitate during the rolling simulations.

   The observation of carbon extraction replicas in TEM showed that the microstructure was free of Nb(C,N) after the austenitising heat treatment, however, some coarse and cuboid TiNb(C,N) were found in the replicas, such precipitates are very stable and cannot be dissolved at 1300°C which is consistent with what is reported in the literature. Nevertheless, only a few TiNb(C,N) precipitates were observed, meaning that the amount of non-dissolved Nb was negligible after the austenitising treatment.

7.2. Single pass rough rolling

1) The rough deformation at a strain of 0.3 led to full recrystallisation as of 1100°C. The prior austenite was remarkably refined in a single pass, the initial PAGS was 87 μm before the rough deformation but it was reduced to 25 and 27 μm after the deformations at 1100°C and 1200°C respectively. At lower temperatures PAGs are partially recrystallised (at 1030°C) or practically unrecrystallised (at 950°C and 830°C), such microstructures are undesirable for real rough rolling processes since the austenite is work hardened and consequently high loads would be necessary to perform more deformations, thus, the rough rolling at temperatures below 1100°C is impractical for real applications. However, for research purposes the rough rolling simulations at low

temperatures produced very useful results to understand the effect of temperature on the deformation induced ferrite transformation.

2) For industrial applications, the deformations at 1100°C and 1200°C could be good choices to perform rough rolling, at both temperatures the austenite was successfully refined via recrystallisation. However, the deformation at 1100°C showed two additional characteristics that could be favourable for the microstructural refinement during the subsequent finish rolling. First, SIP of NbC occurred during the deformation at 1100°C, the precipitates had an adequate size (8 nm in average) and an even distribution that might improve the resistance to recrystallisation at lower temperatures during the finish rolling. Second, DIFT was barely observed in the deformation at 1100°C, only 2% of the microstructure consisted of DIFT whereas at 1200°C the DIFT fraction was 7%. It is preferable to avoid DIFT during the rough rolling since ferrite grains are coarser at higher temperatures, if PAGBs are free of DIFT after the rough rolling, large amounts of finer ferrite grains (around 18%) can be formed in the first finishing pass.

3) The peak stress was not reached in any of the flow curves of the five rough rolling simulations, meaning that substantial dynamic recrystallisation did not happen. However, the double differentiation method detected the onset of DRX as of 950°C, which indicates that at 1100°C and 1200°C the recrystallisation was rapidly completed in the delay of 0.5 seconds that there is between the deformation and the quenching stage. On the other hand, a large fraction of recrystallisation was observed at 1030°C, whereas at 950°C the recrystallised fraction was minimal. Thus, it can be concluded that the double differentiation method detected well the onset of DRX.

7.3. Multipass finish rolling

1) The HTP steel alloy showed an excellent microstructural refinement after two finishing passes at 950°C, a notable austenite conditioning was achieved and the recrystallisation was prevented even after the second holding time of ten seconds. PAGs remained highly elongated in the rolling direction with an average length of 68.4 μm and an aspect

ratio of 6.1. Furthermore, an estimated volume fraction of 25% of DIFT was observed in the microstructure. Inconveniently however, the addition of a third pass followed by a holding time of 10 seconds led to a large fraction of recrystallisation. Therefore, an adequate design of finish rolling should not include more than two finishing passes at 950°C (followed by holding times of 10 s) if grain refinement is pursued.

2) The finish rolling simulation of two passes at 810°C showed surprisingly similar characteristics than that at 950°C, the evolution of DIFT and PAGBs was quiet similar in both deformation temperatures although the austenite refinement was slightly better at 810°C.

3) The best microstructural refinement was achieved in the TMCP simulation that consisted of four finishing passes; two passes at 950°C and two more at 810°C, each finishing pas followed by a holding time of 10 s. The final microstructure exhibited an outstanding grain refinement, for the recrystallisation was imperceptible and the prior austenite remained highly deformed. PAGs showed an average length of 84.3 μm in the rolling direction and an aspect ratio of 10. Furthermore, the microstructure contained 31% of DIFT with a dominant polygonal grain morphology and the ferrite grains were rather fine with diameters from around 1 to 2 μm.

   TMCP can be designed to obtain highly refined microstructures with great austenite conditioning and large amounts of ultrafine DIFT grains, a key point to achieve this, is to perform multiple finishing passes at successively decreasing temperatures from below the $T_{0.05x}$ to above the Ar_3.

7.4. Characteristics of DIFT

1) Through multiple analyses it was confirmed that DIFT follows the transformation mechanism proposed by Basabe et al, in which the deformation causes the formation of Widmanstätten ferrite plates than then coalesce and form grains. The plates are atypically thin and appear aligned in a single direction showing the influence of the stress applied during the deformation.

2) DIFT follows the same transformation mechanisms at 950°C and 810°C, several characteristics were surprisingly similar in the ferrite observed at both deformation temperatures such as the morphology, topography, internal misorientation, critical strains for DIFT and the volume fractions as a function of the accumulated strain. These findings fill a knowledge gap as to whether the dynamic formation of ferrite is the same above the Ae_3 and between the Ae_3 and the Ar_3.

3) The misorientation within Widmanstätten ferrite colony exhibits a peculiar characteristic; the misorientation between adjacent plates is very small, whereas in non-adjacent plates, the misorientation increases gradually as the distance between plates increases (when the plate colony widens). This behaviour in the internal misorientation can help unveil the transformation mechanism in the Widmanstätten ferrite colony, it is proposed that DIFT involves the formation of pairs of self-accommodating plates and face to face sympathetic nucleation at the sides of the pairs of plates.

4) During the coalescence of plates prior to the full polygonisation of grains an intermediate and transitory state of the ferrite appears, in such state the ferrite exhibits a somewhat grain-like morphology but its internal misorientation is plate-like. This finding obtained by EBSD analyses provides a robust validation of the stages (proposed by Basabe et al) that occur during the dynamic transformation of ferrite.

5) In a single pass deformation, the volume fraction of DIFT shows a strong dependence with the deformation temperature, the closer to the Ae_3 temperature or to the γ-phase field, the larger the amount of DIFT. In the rough rolling simulations at a strain of 0.3, large amounts of ferrite were formed when the deformations were performed close to the Ae_3 temperature (850°C); at 830, 950 and 1030°C, the volumes fractions of DIFT were 25, 22 and 19% respectively. Then, a sudden drop in the amount of ferrite (2%) was observed at 1100°C, this is due to the proximity to the midway temperature (1140°) between Ae_3 and the γ-phase field in which the thermodynamic conditions for DIFT are unfavourable. Finally, at 1200°C the amount of ferrite increased again to 7% since the deformation temperature started to approach to the γ-phase field (1430°C).

6) In a multipass deformation scheme (finish rolling simulations), the amount of DIFT increases with the addition of passes, whereas the addition of holding times allows for the evolution of ferrite from plates into polygonal grains. Thus, as passes and holding times are added the volume fraction of DIFT increases and the ferrite becomes dominantly polygonal. Besides, the first deformation pass plays a paramount role in the volume fraction of DIFT since the largest amount of ferrite is transformed in such pass. This behaviour can be associated to the availability of ferrite-free PAGBs, although DIFT can nucleate and growth intragranulary, PAGBs are the preferential sites for the ferrite nucleation. Before the first finishing pass most PAGBs are ferrite-free and thus abundant ferrite transformation can take place on the grain boundaries, however, in the subsequent finishing passes the transformation is substantially minor since a large fraction of PAGBs is already occupied by DIFT. That explains why the volume fraction of DIFT greatly increases after the first finishing pass but then it increases slightly in the subsequent passes.

   A clear example of the characteristics of DIFT aforementioned can be appreciated in the finish rolling simulation at 810°C. Before the first finishing pass the initial amount of DIFT was 2%, thus, most PAGBs were free of DIFT at that stage of the simulation. Then, after the first finishing pass the volume fraction of DIFT largely increased to 19.4%, from which 7.7% were ferrite gains and the remaining 10.7% were ferrite plates, meaning that the morphology of DIFT consisted primarily of plates. However, after the holding time of 10 seconds the volume fractions of ferrite grains and plates changed to 11.4 and 8.9% respectively, which means that morphology of DIFT evolved from a plate-dominated microstructure into one consisting primarily of polygonal grains. In the second pass, DIFT subtly increased to 21.7% and the amounts of grains and plates changed to 12.8 and 8.8%, then, the second holding time increased substantially the ferrite grains/plates ratio, for the volume fractions of polygonal grains and plates in DIFT were 18 and 5% respectively.

7.5. Testing methods to evaluate DIFT

1) The nanoindentation test is not a consistent method to characterise the mechanical properties of DIFT since the nanohardness of ferrite showed a strong dependence with the grain size, which is incoherent. Such dependence is caused by the topography of the phases revealed in the microstructure after the electrolytic etching; ferrite grains appear at substantially higher elevations (up to around 500 nm high) with respect to the martensitic matrix, the larger the grain size the greater the height. Ferrite grains with greater heights show significant lower nanohardness values due to the lack of material around them, during the indentation large grains are deformed freely without the interaction of dislocations at the grain boundaries which conducts to a substantial drop in the nanohardness.

   Nevertheless, although the nanohardness test is not a reliable method to characterise the mechanical properties of DIFT, the difference in the nanohardness between ferrite and martensite is notable, thus, the identification of ferrite within the microstructure is quiet easy. The average nanohardness value in martensite is at least two times greater than that in ferrite, for instance, in the specimen B2 of the finish rolling simulation at 810°C the average nanohardness values of ferrite and martensite were 2.0 GPa and 4.79 GPa respectively.

2) The electrolytic etching of the specimens with the solution I1 of ASTM E1558 and the evaluation with contact-SPM scanning, produce images with a topography that shows great contrasts between ferrite and martensite in the microstructure, both phases can be readily separated by simply setting a threshold in the height scale in the 3D SPM image. This new methodology shows notorious advantages versus other methods to quantify ultrafine ferrite, for the images show high resolution and very fine grains can be easily separated from the matrix. However, the operation of the SPM instrument and the acquisition of images is very laborious and time consuming, which is an important disadvantage if multiple specimens need to be evaluated.

Chapter 8. Future work

Based on the results obtained and the work encompassed so far, the following points are proposed as a further work:

8.1. Controlled cooling after the finish rolling simulations.

The current work carried out a thorough evaluation and analysis about the microstructural evolution during the deformation of austenite, however, a complementary work about the transformation of deformed austenite on cooling is necessary to obtain a final microstructure applicable to a high strength steel grade (such as X80 or X100). The author suggests to design a controlled cooling able to transform the remaining deformed austenite into acicular ferrite after the finish rolling simulations, as reference, the work carried out by Haitao et al [79], [144]–[148] (who used the current HTP alloy) might be quite useful to find a cooling rate suitable to transform the remaining deformed austenite into acicular ferrite. The combination of ultrafine polygonal DIF with acicular ferrite can be promissory for the final mechanical properties of the material, for acicular ferrite is also well known as a very fine microstructure that improves the strength and toughness of steel [149]. The research about the effect of the combination of both microstructures on the final mechanical properties of the steel is very scarce, this topic might be a fruitful area of research.

8.2. Study of the strain induced precipitation of Nb at the different stages of the TMCP simulations.

A systematic study of stain induced precipitation of Nb along the whole TMCP simulation is still needed, although in this work the SIP was analysed in some stages of the simulation A, it is worthwhile to study and quantify the precipitation after each finishing pass and holding time at different temperatures. It is well known that the SIP of Nb plays a very important role in the retardation of the recrystallisation, this topic has attracted much of attention due to its relevance in the development of fine-grained steels and numerous papers have been published so far. However, the effect of SIP on DIFT has been scantly studied, some studies have revealed that

the addition of Nb to the steel also retards the reversal α to γ transformation [72], nevertheless, there has not been research to study the correlation between SIP and DIFT in a TMCP.

8.3. Evaluation of DIFT in Atomic Force Microscopy (AFM).

A novel methodology to observe and quantify DIFT was proposed in the current work, the contact-SPM imaging resulted to be very useful to separate the ferrite phase from martensite. However, due the tip convolution effect caused by the interaction between Berkovich tip and the very small features of DIFT, the mapping of the topography of ferrite grains was affected in an important extent. It is thus suggested to use AFM to observe the topography of DIFT after the electrolytic etching, the acquisition of high resolution images with a sharper probe would reveal the ferrite grain boundaries much more accurately, besides, the DIFT quantification will be better.

References

[1] Y. M. Kim, S. Y. Shin, H. Lee, B. Hwang, S. Lee, and N. J. Kim, "Effects of molybdenum and vanadium addition on tensile and charpy impact properties of API X70 linepipe steels," *Metall. Mater. Trans. A Phys. Metall. Mater. Sci.*, vol. 38, no. 8, pp. 1731–1742, 2007.

[2] D. K. Matlock, G. Krauss, and J. G. Speer, "New microalloyed steel applications for the automotive sector," *Mater. Sci. Forum*, vol. 500–501, pp. 87–96, 2005.

[3] N. A. McPherson, "Through process considerations for microalloyed steels used in naval ship construction," *Ironmak. Steelmak.*, vol. 36, no. 3, pp. 193–200, 2009.

[4] M. Z. S. Khan and I. A. Burch, "Effect of seawater on the fatigue life and crack growth behaviour of a new microalloyed steel for submarine hull application," *Int. J. Fatigue*, vol. 14, no. 5, pp. 313–318, 1992.

[5] D. K. Matlock and J. G. Speer, "Microalloying concepts and application in long products," *Mater. Sci. Technol.*, vol. 25, no. 9, pp. 1118–1125, 2009.

[6] C. Ouchi, "Development of steel plates by intensive use of TMCP and direct quenching processes," *ISIJ Int.*, vol. 41, no. 6, pp. 542–553, 2001.

[7] W. Morrison, "Overview of microalloying in steel," *Proc. Vanitec Symp.*, pp. 25–35, 2000.

[8] T. N. Baker, "Microalloyed steels," *Ironmak. Steelmak.*, vol. 43, no. 4, pp. 264–307, 2016.

[9] D. G. Stalheim, "The use of high temperature processing (HTP) steel for high strength oil and gas transmission pipeline applications," *Iron Steel*, vol. 40, pp. 699–704, 2005.

[10] K. Hulka and J. M. Gray, "High temperature processing of line-pipe steels," *Proc. Int. Symp. Niobium*, pp. 87–612, 2001.

[11] C. Shang and F. Guo, "The state of the art of long distance gas pipeline in China," *Int. Gas Res. Conf. Proc.*, vol. 2, no. 1, pp. 723–729, 2017.

[12] D. Stalheim, "The evolution, review and optimization next steps related to the high temperature processing (HTP) alloy design for pipeline steels in china," in *Conference, International Pipeline Technology.*, 2010.

[13] W. Wang, Y. Shan, and K. Yang, "Study of high strength pipeline steels with different microstructures," *Mater. Sci. Eng. A*, vol. 502, no. 1–2, pp. 38–44, 2009.

[14] W. J. Nie, W. F. Xin, T. M. Xu, P. J. Shi, and X. B. Zhang, “Enhancing the toughness of heavy thick X80 pipeline steel plates by microstructure control,” *Adv. Mater. Res.*, vol. 194–196, pp. 1183–1191, 2011.

[15] M. C. Zhao, B. Tang, Y. Y. Shan, and K. Yang, “Role of microstructure on sulfide stress cracking of oil and gas pipeline steels,” *Metall. Mater. Trans. A Phys. Metall. Mater. Sci.*, vol. 34 A, no. 5, pp. 1089–1096, 2003.

[16] M. C. Zhao, Y. Y. Shan, F. R. Xiao, K. Yang, and Y. H. Li, “Investigation on the H2S-resistant behaviors of acicular ferrite and ultrafine ferrite,” *Mater. Lett.*, vol. 57, no. 1, pp. 141–145, 2002.

[17] Y. Zhong, F. Xiao, J. Zhang, Y. Shan, W. Wang, and K. Yang, “In situ TEM study of the effect of M/A films at grain boundaries on crack propagation in an ultra-fine acicular ferrite pipeline steel,” *Acta Mater.*, vol. 54, no. 2, pp. 435–443, 2006.

[18] E. O. Hall, “The deformation and ageing of mild steel: II Characteristics of the Lüders deformation,” *Proc. Phys. Soc. Sect. B*, vol. 64, no. 9, pp. 742–747, 1951.

[19] N. J. Petch, “The cleavage strength of polycrystals,” *J. Iron Steel Inst*, vol. 174, no. 1, pp. 25–28., 1953.

[20] H. Dong and X. Sun, “Deformation induced ferrite transformation,” in *Ultrafine grained steels*, Y. Weng, Ed. Metallurgical Industry Press, 2009, pp. 86–135.

[21] R. Grewal, C. Aranas, K. Chadha, D. Shahriari, M. Jahazi, and J. J. Jonas, “Formation of Widmanstätten ferrite at very high temperatures in the austenite phase field,” *Acta Mater.*, vol. 109, pp. 23–31, 2016.

[22] S. L. Semiatin, Ed., *Metalworking: Bulk Forming*, Volume 14. ASM International, 2005.

[23] F. J. Humphreys and M. Hatherly, *Recrystallisation and related annealing phenomena*, Second Edi. 2004.

[24] L. A. Reed Hill Robert E., Reza Abbaschian, *Physical metallurgy principles*, Fourth Edi. 2009.

[25] C. M. Sellars, “Recrystallization of metals during hot deformation,” *Philos. Trans. R. Soc. London. Ser. A, Math. Phys. Sci.*, vol. 288, no. 1350, pp. 147–158, 1978.

[26] K. Huang and R. E. Logé, “A review of dynamic recrystallization phenomena in metallic materials,” *Mater. Des.*, vol. 111, pp. 548–574, 2016.

[27] J. E. Burke and D. Turnbull, “Recrystallization and grain growth,” *Prog. Met. Phys.*, vol. 3, no. C, pp. 220–292, 1952.

[28] B. López and J. M. Rodriguez-Ibabe, “Recrystallisation and grain growth in hot working

of steels," in *Microstructure evolution in metal forming processes*, L. Jianguo, D. Balint, and M. Pietrzyk, Eds. Woodhead Publishing in Materials, 2012, p. 403.

[29] W. B. Morrison, "Microalloy steels - The beginning," *Mater. Sci. Technol.*, vol. 25, no. 9, pp. 1066–1073, 2009.

[30] C. I. Garcia, M. Hua, K. Cho, and A. J. DeArdo, "On the strength of microalloyed steels - An interpretive review," *Metall. Ital.*, vol. 101, no. 10, pp. 35–42, 2009.

[31] H. Spindler, M. Klein, R. Rauch, A. Pichler, and P. Stiaszny, "High strength and ultra high strength hot rolled steel grades - Products for advanced aplications," in *Super High Strength Steels (SHSS): International Conference*, 2005.

[32] J. R. Davis, *Alloying: understanding the basics*. 2001.

[33] A. J. DeArdo, "Microalloyed steels : fifty years of progress - An interpretive review," no. January 2008, 2016.

[34] Zener C. quoted by Smith C.S., "Introduction to grains, phases, and interfaces - an interpretation of microstructure," *Trans. AIME*, vol. 175, no. 15, pp. 15–51, 1948.

[35] A. J. DeArdo, "Niobium in modern steels," *Int. Mater. Rev.*, vol. 48, no. 6, pp. 371–402, 2003.

[36] B. Dutta and C. M. Sellars, "Effect of composition and process variables on Nb(C, N) precipitation in niobium microalloyed austenite," *Mater. Sci. Technol. (United Kingdom)*, vol. 3, no. 3, pp. 197–206, 1987.

[37] B. Dutta, E. Valdes, and C. M. Sellars, "Mechanism and kinetics of strain induced precipitation of Nb(C,N) in austenite," *Acta Metall. Mater.*, vol. 40, no. 4, pp. 653–662, 1992.

[38] E. J. Palmiere, C. I. Garcia, and A. J. De Ardo, "Compositional and microstructural changes which attend reheating and grain coarsening in steels containing niobium," *Metall. Mater. Trans. A*, vol. 25, no. 2, pp. 277–286, 1994.

[39] E. J. Palmiere, C. I. Garcia, and A. J. DeArdo, "The influence of niobium supersaturation in austenite on the static recrystallization behavior of low carbon microalloyed steels," *Metall. Mater. Trans. A Phys. Metall. Mater. Sci.*, vol. 27, no. 4, pp. 951–960, 1996.

[40] P. Yan and H. K. D. H. Bhadeshia, "The austenite – ferrite transformation in enhanced-niobium , low-carbon steel," vol. 31, pp. 1066–1076, 2015.

[41] E. K. Storms and N. H. Krikorian, "The niobium-niobium carbide system," *J. Phys. Chem.*, vol. 64, no. 10, pp. 1471–1477, 1960.

[42] B. G. Baker and J. Nutting, "Precipitation processes in steels, special report 64," in

Institute, Iron and Steel, 1959.

[43] G. Kurdjumov and G. Sachs, "Over the mechanisms of steel hardening," *Z. Phys*, 1930.

[44] A. Iza-Mendia, M. A. Altuna, B. Pereda, and I. Gutiérrez, "Precipitation of Nb in ferrite after austenite conditioning. Part I: Microstructural characterization," *Metall. Mater. Trans. A Phys. Metall. Mater. Sci.*, vol. 43, no. 12, pp. 4553–4570, 2012.

[45] R. Okamoto, A. Borgenstam, and J. Ågren, "Interphase precipitation in niobium-microalloyed steels," *Acta Mater.*, vol. 58, no. 14, pp. 4783–4790, 2010.

[46] P. Gong, E. J. Palmiere, and W. M. Rainforth, "Characterisation of strain-induced precipitation behaviour in microalloyed steels during thermomechanical controlled processing," *Mater. Charact.*, vol. 124, pp. 83–89, 2017.

[47] S. S. Hansen, J. B. V. Sande, and M. Cohen, "Niobium carbonitride precipitation and austenite recrystallization in hot-rolled microalloyed steels," *Metall. Trans. A*, vol. 11, no. 3, pp. 387–402, 1980.

[48] S. H. Park, S. Yue, and J. J. Jonas, "Continuous-cooling-precipitation kinetics of Nb(CN) in high-strength low-alloy steels," *Metall. Trans. A*, vol. 23, no. 6, pp. 1641–1651, 1992.

[49] Y. Chen, D. Zhang, Y. Liu, H. Li, and D. Xu, "Effect of dissolution and precipitation of Nb on the formation of acicular ferrite/bainite ferrite in low-carbon HSLA steels," *Mater. Charact.*, vol. 84, pp. 232–239, 2013.

[50] P. Gong, E. J. Palmiere, and W. M. Rainforth, "Dissolution and precipitation behaviour in steels microalloyed with niobium during thermomechanical processing," *Acta Mater.*, vol. 97, pp. 392–403, 2015.

[51] H. Yada, Y. Matsumura, and K. Nakahima, "United States Patent 4466842. Ferritic steel having ultra-fine grains and a method for producing the same." 1984.

[52] H. Yada, Y. Matsumura, and T. Senuma, "Massive type transformation induced by hot deformation in low carbon steels. In: Proceedings of the international conference on martensitic transformation.," *JIM*, pp. 515–20, 1986.

[53] Y. H, M. Y, and S. T., "A new thermomechanical heat treatment for grain refining in low carbon steels," in *Proceedings of the 1st conference on physical metallurgy of thermomechanical processing of steels and other metals, ISIJ, THERMEC-88.*, 1988, pp. 200–7.

[54] H. Dong and X. Sun, "Deformation induced ferrite transformation in low carbon steels," *Curr. Opin. Solid State Mater. Sci.*, vol. 9, no. 6, pp. 269–276, 2005.

[55] H. Yada, C. M. Li, and H. Yamagata, “Dynamic γ→α transformation during hot deformation in iron-nickel-carbon alloys,” *ISIJ Int.*, vol. 40, no. 2, pp. 200–206, 2000.

[56] C. Aranas, S. F. Rodrigues, R. Grewal, and J. J. Jonas, “Ferrite formation above the Ae3 temperature during the torsion simulation of strip rolling,” *ISIJ Int.*, vol. 55, no. 11, pp. 2426–2434, 2015.

[57] S. F. Rodrigues, C. Aranas, and J. J. Jonas, “Dynamic transformation during the simulated plate rolling of a 0.09% Nb Steel,” *ISIJ Int.*, vol. 57, no. 6, pp. 1102–1111, 2017.

[58] N. Mendes-Fonseca, S. F. Rodrigues, B. Guo, and J. J. Jonas, “Dynamic transformation during the simulated hot rolling of an API-X80 steel,” *Steel Res. Int.*, vol. 90, no. 8, pp. 1–8, 2019.

[59] P. D. Hodgson and H. Beladi, “Dynamic strain-induced ferrite transformation (DSIT) in steels,” in *Phase transformations in steels. Volume 1: Fundamentals and diffusion controlled transformations*, vol. 1, E. Pereloma and D. V. Edmonds, Eds. Woodhead Publishing in Materials, 2012, pp. 527–554.

[60] Y. Weng, X. Sun, and H. Dong, “Overview on the theory of deformation induced ferrite transformationa,” *Symp Ultrafine Grain Struct (ISUG2005), Beijing Metall. Ind. Press*, vol. 2, no. 1, pp. 9–15, 2005.

[61] V. V. Basabe, J. J. Jonas, and C. Ghosh, “Formation of Widmanstätten ferrite in a 0.036% Nb low carbon steel at temperatures above the Ae3,” *Steel Res. Int.*, vol. 85, no. 1, pp. 8–15, 2014.

[62] C. Ghosh, V. V. Basabe, and J. J. Jonas, “Determination of the critical strains for the initiation of dynamic transformation and dynamic recrystallization in four steels of increasing carbon contents,” *Steel Res. Int.*, vol. 84, no. 5, pp. 490–494, 2013.

[63] C. Ghosh, V. V. Basabe, J. J. Jonas, S. Yue, and X. Y. Xiong, “Dynamic transformation behavior of a deformed high carbon steel at temperatures above the Ae3,” *ISIJ Int.*, vol. 53, no. 5, pp. 900–908, 2013.

[64] J. J. Jonas and C. Ghosh, “Role of mechanical activation in the dynamic transformation of austenite,” *Acta Mater.*, vol. 61, no. 16, pp. 6125–6131, 2013.

[65] J. J. Jonas, Y. He, and G. Langelaan, “The rotation axes and angles involved in the formation of self-accommodating plates of Widmanstätten ferrite,” *Acta Mater.*, vol. 72, pp. 13–21, 2014.

[66] J. J. Jonas, C. Ghosh, X. Quelennec, and V. V. Basabe, “The critical strain for dynamic

transformation in hot deformed austenite," *ISIJ Int.*, vol. 53, no. 1, pp. 145–151, 2013.

[67] S. F. Rodrigues, C. Aranas, T. Wang, and J. J. Jonas, "Dynamic transformation of an X70 steel under plate rolling conditions," *ISIJ Int.*, vol. 57, pp. 162–169, 2017.

[68] S. F. Rodrigues, C. Aranas, B. Sun, F. Siciliano, S. Yue, and J. J. Jonas, "Effect of grain size and residual strain on the dynamic transformation of austenite under plate rolling conditions," *Steel Res. Int.*, vol. 89, no. 6, pp. 1–7, 2018.

[69] S. F. Rodrigues *et al.*, "Dynamic phase transformation behavior of a Nb-microalloyed steel during roughing passes at temperatures above the Ae3," *Metals (Basel).*, vol. 9, no. 3, 2019.

[70] H. B. Palhano *et al.*, "Strain-induced ferrite formation during steckel mill simulations with varying roughing pass schedules," *Metals (Basel).*, vol. 9, no. 8, pp. 1–16, 2019.

[71] H. Beladi, G. L. Kelly, A. Shokouhi, and P. D. Hodgson, "The evolution of ultrafine ferrite formation through dynamic strain-induced transformation," *Mater. Sci. Eng. A*, vol. 371, no. 1–2, pp. 343–352, 2004.

[72] V. V. Basabe and J. J. Jonas, "The ferrite transformation in hot deformed 0.036% NB austenite at temperatures above the Ae3," *ISIJ Int.*, vol. 50, no. 8, pp. 1185–1192, 2010.

[73] C. Ghosh, C. Aranas, and J. J. Jonas, "Dynamic transformation of deformed austenite at temperatures above the Ae3," *Prog. Mater. Sci.*, vol. 82, pp. 151–233, 2016.

[74] H. Beladi, G. L. Kelly, and P. D. Hodgson, "Ultrafine grained structure formation in steels using dynamic strain induced transformation processing," *Int. Mater. Rev.*, vol. 52, no. 1, pp. 14–28, 2007.

[75] C. Aranas, T. Wang, and J. J. Jonas, "Effect of interpass time on the dynamic transformation of a plain c-Mn and a Nb microalloyed steel," *ISIJ Int.*, vol. 55, no. 3, pp. 647–654, 2015.

[76] P. J. Hurley, P. D. Hodgson, and B. C. Muddle, "Analysis and characterisation of ultra-fine ferrite produced during a new steel strip rolling process," *Scr. Mater.*, vol. 40, no. 4, pp. 433–438, 1999.

[77] A. Ali and H. K. D. H. Bhadeshia, "Nucleation of Widmanstätten ferrite," *Mater. Sci. Technol. (United Kingdom)*, vol. 6, no. 8, pp. 781–784, 1990.

[78] N. Saunders, Z. Guo, X. Li, A. P. Miodownik, and J. P. Schillé, "Using JMatPro to model materials properties and behavior," *Jom*, vol. 55, no. 12, pp. 60–65, 2003.

[79] H. Zhao, "Effect of austenite deformation and continuous cooling on microstructure evolution in a pipeline steel," PhD Thesis. The university of Sheffield, 2016.

[80] M. S. Loveday *et al.*, “Measurement of flow stress in hot plane strain compression tests,” *Mater. High Temp.*, vol. 23, no. 2, pp. 85–118, 2006.

[81] L. Sun, “PhD Thesis: The effects of strain path reversal on austenite grain subdivision, recrystallisation and phase transformations in microalloyed steel,” 2012.

[82] I. Tamura, C. Ouchi, T. Tanaka, and S. Hiroshi, *Thermomechanical processing of high-strength low-alloy steels*. Butterwoths, 1988.

[83] R. Revie, Ed., *Oil and gas pipelines: integrity and safety handbook*. Wiley, 2015.

[84] F. Siciliano, D. G. Stalheim, and J. M. Gray, “Modern high strength steels for oil and gas transmission pipelines,” *Proc. Bienn. Int. Pipeline Conf. IPC*, vol. 3, pp. 187–195, 2009.

[85] S. Hashmi, Ed., “Assessing properties of conventional and specialized materials,” in *Comprehensive materials processing*, Volume 1., Elsevier, 2014, p. 246.

[86] B. Dutta, E. J. Palmiere, and C. M. Sellars, “Modelling the kinetics of strain induced precipitation in Nb microalloyed steels,” *Acta Mater.*, vol. 49, no. 5, pp. 785–794, 2001.

[87] ASTM Standards, Ed., *ASTM E112. Standard test methods for determining average grain size*, vol. 03.01. 2010.

[88] L. Ryde, “Application of EBSD to analysis of microstructures in commercial steels,” *Mater. Sci. Technol.*, vol. 22, no. 11, pp. 1297–1306, 2006.

[89] A. W. Wilson, J. D. Madison, and G. Spanos, “Determining phase volume fraction in steels by electron backscattered diffraction,” *Scr. Mater.*, vol. 45, no. 12, pp. 1335–1340, 2001.

[90] O. Engler and V. Randle, *Introduction to texture analysis*, Second Edi. 2010.

[91] D. B. Williams and C. B. Carter, *Transmission electron microscopy: a textbook for materials science*. Springer, 2009.

[92] ASTM Standards, Ed., *ASTM E1558-09. Standard guide for electrolytic polishing of metallographic specimens*, vol. 03.01. 2014.

[93] W. C. Oliver and G. M. Pharr, “An improved technique for determining hardness and elastic modulus using load and displacement sensing indentation experiments,” *J. Mater. Res.*, vol. 7, no. 6, pp. 1564–1583, 1992.

[94] R. Howland, L. Benatar, and C. H. S. P. M. T. Echniques, “A practical guide to scanning probe microscopy,” *ThermoMicroscopes*, p. 80, 2000.

[95] C. A. Schneider, W. S. Rasband, and K. W. Eliceiri, “NIH Image to ImageJ: 25 years of image analysis,” *Nat. Methods*, vol. 9, no. 7, pp. 671–675, 2012.

[96] J. C. Russ and T. D. Robert, *Practical stereology*, Second. New York, 2000.

[97] B. Bhushan and O. Marti, "Scanning probe microscopy. Principle of operation, instrumentation, and probes," in *Handbook of Nanotechnologie*, 4th ed., Springer, 2017, pp. 573–617.

[98] A. C. Fischer-Cripps, *Introduction of contact Mechanics*, 2nd ed. Springer, 2007.

[99] ASTM Standards, Ed., *ASTM E384-05a. Standard test method for microindentation hardness of materials*, vol. 14. 2005.

[100] K. Zhu, O. Bouaziz, C. Oberbillig, and M. Huang, "An approach to define the effective lath size controlling yield strength of bainite," *Mater. Sci. Eng. A*, vol. 527, no. 24–25, pp. 6614–6619, 2010.

[101] S. Zheng, C. Davis, and M. Strangwood, "Elemental segregation and subsequent precipitation during solidification of continuous cast Nb-V-Ti high-strength low-alloy steels," *Materials Characterization*, vol. 95. pp. 94–104, 2014.

[102] S. G. Hong, K. B. Kang, and C. G. Park, "Strain-induced precipitation of NbC in Nb and Nb-Ti microalloyed HSLA steels," *Scr. Mater.*, vol. 46, no. 2, pp. 163–168, 2002.

[103] M. Tarafder, P. Sinha, A. Kundu, M. Strangwood, and C. Davis, "Fractal based correlations for Nb microalloyed steel undergoing static recrystallization," *Mater. Charact.*, vol. 85, pp. 92–99, 2013.

[104] E. I. Poliak and J. J. Jonas, "A one-parameter approach to determining the critical conditions for the initiation of dynamic recrystallization," *Acta Mater.*, vol. 44, no. 1, pp. 127–136, 1996.

[105] X. Sun, H. Luo, H. Dong, Q. Liu, and Y. Weng, "Microstructural evolution and kinetics for post-dynamic transformation in a plain low carbon steel," *ISIJ Int.*, vol. 48, no. 7, pp. 994–1000, 2008.

[106] J. K. Choi, D. H. Seo, J. S. Lee, K. K. Um, and W. Y. Choo, "Formation of ultrafine ferrite by strain-induced dynamic transformation in plain low carbon steel," *ISIJ Int.*, vol. 43, no. 5, pp. 746–754, 2003.

[107] X. Quelennec and J. J. Jonas, "Simulation of austenite flow curves under industrial rolling conditions using a physical dynamic recrystallization model," *ISIJ Int.*, vol. 52, no. 6, pp. 1145–1152, 2012.

[108] C. Aranas, T. Nguyen-Minh, R. Grewal, and J. J. Jonas, "Flow softening-based formation of Widmanstätten ferrite in a 0.06%C steel deformed above the Ae3," *ISIJ Int.*, vol. 55, no. 1, pp. 300–307, 2015.

[109] C. Ghosh, V. V. Basabe, J. J. Jonas, Y. M. Kim, I. H. Jung, and S. Yue, “The dynamic transformation of deformed austenite at temperatures above the Ae3,” *Acta Mater.*, vol. 61, no. 7, pp. 2348–2362, 2013.

[110] W. D. Nix and H. Gao, “Indentation size effects in crystalline materials: A law for strain gradient plasticity,” *J. Mech. Phys. Solids*, vol. 46, no. 3, pp. 411–425, 1998.

[111] M. G. Wang and A. H. W. Ngan, “Indentation strain burst phenomenon induced by grain boundaries in niobium,” *J. Mater. Res.*, vol. 19, no. 8, pp. 2478–2486, 2004.

[112] R. L. Higginson and C. M. Sellars, *Worked Examples in Quantitative Metallography Dedication*. London: Maney, 2003.

[113] T. A. Davenport, R. E. Miner, and R. A. Kot, “The hot deformation of austenite,” *Metall. Soc. AIME. New York*, 1977.

[114] Y. bin Cao, F. ren Xiao, G. ying Qiao, X. bing Zhang, and B. Liao, “Quantitative research on effects of Nb on hot deformation behaviors of high-Nb microalloyed steels,” *Mater. Sci. Eng. A*, vol. 530, no. 1, pp. 277–284, 2011.

[115] S. H. Cho, K. B. Kang, and J. J. Jonas, “Dynamic, static and metadynamic recrystallization of a Nb-microalloyed steel,” *ISIJ Int.*, vol. 41, no. 1, pp. 63–69, 2001.

[116] I. Weiss and J. J. Jonas, “Dynamic precipitation and coarsening of niobium carbonitrides during the hot compression of HSLA steels,” *Metall. Trans. A*, vol. 11, no. 3, pp. 403–410, 1980.

[117] M. J. Peet and H. K. D. H. Bhadeshia, “Surface relief due to bainite transformation at 473 K (200 °c),” *Metall. Mater. Trans. A Phys. Metall. Mater. Sci.*, vol. 42, no. 11, pp. 3344–3348, 2011.

[118] P. Yan and H. K. D. H. Bhadeshia, “Mechanism and kinetics of solid-state transformation in high-temperature processed linepipe steel,” *Metall. Mater. Trans. A Phys. Metall. Mater. Sci.*, vol. 44, no. 12, pp. 5468–5477, 2013.

[119] T. H. Ahn *et al.*, “Small-scale mechanical property characterization of ferrite formed during deformation of super-cooled austenite by nanoindentation,” *Mater. Sci. Eng. A*, vol. 523, no. 1–2, pp. 173–177, 2009.

[120] F. Zhang, A. Ruimi, and D. P. Field, “Phase identification of dual-phase (DP980) steels by electron backscatter diffraction and nanoindentation techniques,” *Microsc. Microanal.*, vol. 22, no. 1, pp. 99–107, 2016.

[121] G. Vander Voort, “Indentifying isothermally-transformed steel microstructural constituents,” in *Solutions for materials preparation, testing and analysis*, vol. 5, no. 4,

Buehler, Ed. 2015, p. 5.

[122] Y. Chen and Q. Chen, “Dilatometric investigation on isothermal transformation after hot deformation,” *J Iron Steel Res Int*, vol. 10, pp. 46–8, 2003.

[123] N. Seljakow, G. Kurdjumow, and N. Goodtzow, “Eine röntgenographische Untersuchung der Struktur des Kohlenstoffstahls,” *Zeitschrift für Phys.*, vol. 45, no. 5–6, pp. 384–408, 1927.

[124] H. K. D. H. Bhadeshia and R. Honeycombe, *Steels microstructure and properties*, Third Edit. 2006.

[125] S. Seetharaman, *Fundamentals of metallurgy*. Boca Raton Boston New York Washington, DC: Woodhead Publishing Limited, 2005.

[126] B. Dutta and E. J. Palmiere, “Effect of prestrain and deformation temperature on the recrystallization behavior of steels microalloyed with niobium,” *Metall. Mater. Trans. A Phys. Metall. Mater. Sci.*, vol. 34 A, no. 6, pp. 1237–1247, 2003.

[127] J. S. Perttula and L. P. Karjalainen, “Recrystallisation rates in austenite measured by double compression and stress relaxation methods,” *Mater. Sci. Technol.*, vol. 14, no. 7, pp. 626–630, 1998.

[128] O. Kwon and A. J. DeArdo, “On the recovery and recrystallization which attend static softening in hot-deformed copper and aluminum,” *Acta Metall. Mater.*, vol. 38, no. 1, pp. 41–54, 1990.

[129] A. Day and P. Trimby, *Channel 5 manual*. HKL technology, 2001.

[130] J. Y. Kang, S. J. Park, and M. B. Moon, “Phase analysis on dual-phase steel using band slope of electron backscatter diffraction pattern,” *Microsc. Microanal.*, vol. 19, no. SUPPL. 5, pp. 13–16, 2013.

[131] H. K. D. H. Bhadeshia, “A rationalisation of shear transformations in steels,” *Acta Metall.*, vol. 29, no. 6, pp. 1117–1130, 1981.

[132] H. I. Aaronson *et al.*, “Sympathetic nucleation: an overview,” *Mater. Sci. Eng. B*, vol. 32, no. 3, pp. 107–123, 1995.

[133] Z. Liu, D. Li, S. Lu, and G. Qiao, “Thermal stability of high temperature deformation induced ferrite in a low carbon steel,” *ISIJ Int.*, vol. 47, no. 2, pp. 289–293, 2007.

[134] R. L. Bodnar and S. S. Hansen, “Effects of Widmanstätten ferrite on the mechanical properties of a 0.2 pct C-0.7 pct Mn steel,” *Metall. Mater. Trans. A*, vol. 25, no. 4, pp. 763–773, 1994.

[135] D. Phelan and R. Dippenaar, “Widmanstätten ferrite plate formation in low-carbon

steels," *Metall. Mater. Trans. A Phys. Metall. Mater. Sci.*, vol. 35 A, no. 12, pp. 3701–3706, 2004.

[136] C. Shang, "Development of high performance structural plate steels by China in the last 10 years," in *Procedings of the international symposium on emerging challenges for metals and materials. Engineering and technology*, 2009, pp. 211–217.

[137] J. G. Speer and S. S. Hansen, "Austenite recrystallization and carbonitride precipitation in niobium microalloyed steels," *Metall. Trans. A*, vol. 20, no. 1, pp. 25–38, 1989.

[138] L. Hao, M. Sun, N. Xiao, and D. Li, "Characterizations of dynamic strain-induced transformation in low carbon steel," *J. Mater. Sci. Technol.*, vol. 28, no. 12, pp. 1095–1101, 2012.

[139] G. Chen, W. Yang, S. Guo, and Z. Sun, "Characteristics of microstructural evolution during deformation-enhanced ferrite transformation in Nb-microalloyed HSLA steel," *J. Univ. Sci. Technol. Beijing Miner. Metall. Mater. (Eng Ed)*, vol. 14, no. 1, pp. 36–40, 2007.

[140] Y. Yuqun, Y. Huang, Y. Yongkuan, W. Daoyuan, W. Yonglong, and D. G. Stalheim, "The development of X80 steel plate and coil for the 2nd west-east pipeline project," in *Proceedings of IPC 2008, 7th International Pipeline Conference*, 2008, pp. 1–9.

[141] Q. Y. Sha, Z. Q. Sun, and L. F. Li, "Refinement of coarse grained austenite in Nb-V-Ti microalloyed steel during roughing rolling," *Ironmak. Steelmak.*, vol. 42, no. 1, pp. 74–80, 2015.

[142] P. Gong, "The precipitation behaviour and the formation of deformation induced ferrite during a new type of thermomechanical processing," PhD Thesis. The University of Sheffield, 2016.

[143] P. Gong, L. Sun, B. P. Wynne, E. J. Palmiere, and W. M. Rainforth, "The effect of thermomechanical controlled processing on recrystallisation and subsequent deformation-induced ferrite transformation textures in microalloyed steels," *J. Mater. Sci.*, vol. 53, no. 9, pp. 6922–6938, 2018.

[144] H. Zhao and E. J. Palmiere, "Influence of cooling rate on the grain-refining effect of austenite deformation in a HSLA steel," *Mater. Charact.*, vol. 158, no. June, 2019.

[145] H. Zhao and E. J. Palmiere, "Effect of austenite grain size on acicular ferrite transformation in a HSLA steel," *Mater. Charact.*, vol. 145, no. June, pp. 479–489, 2018.

[146] H. Zhao, B. P. Wynne, and E. J. Palmiere, "Conditions for the occurrence of acicular

ferrite transformation in HSLA steels," *J. Mater. Sci.*, vol. 53, no. 5, pp. 3785–3804, 2018.

[147] H. Zhao and E. J. Palmiere, "Effect of austenite deformation on the microstructure evolution and grain refinement under accelerated cooling conditions," *Metall. Mater. Trans. A Phys. Metall. Mater. Sci.*, vol. 48, no. 7, pp. 3389–3399, 2017.

[148] H. Zhao, B. P. Wynne, and E. J. Palmiere, "Effect of austenite grain size on the bainitic ferrite morphology and grain refinement of a pipeline steel after continuous cooling," *Mater. Charact.*, vol. 123, pp. 128–136, 2017.

[149] Y. E. Smmith, A. P. Coldren, and R. L. Cryderman, "Mn-Mo-Nb acicular ferrite steels with high strength and toughness," *Climax Molybdenum Co. Ltd*, pp. 119–142, 1972.